

Taras Shevchenko National University of Kyiv
Ministry of Education and Science of Ukraine
Taras Shevchenko National University of Kyiv
Ministry of Education and Science of Ukraine

Qualifying scientific work
on manuscript rights

VOITSEKHOVSKYI VADYM VADYMOVYCH

UDK 524.1+524.3+524.7

THESIS

**ACCELERATION AND PROPAGATION OF ULTRA
HIGH ENERGY COSMIC RAYS IN THE LOCAL
UNIVERSE**

Specialisation - 104 Physics and Astronomy

Discipline - 10 Natural Sciences

The thesis for obtaining the scientific degree of Doctor of Philosophy

The dissertation contains the results of own research. The use of ideas, results and texts of other authors are linked to the appropriate source.

_____ V.V.Voitsekhovskyi

Scientific supervisor: Prof. Hnatyk Bohdan Ivanovych, Doctor of Physical and Mathematical Sciences



Kyiv - 2022

АНОТАЦІЯ

Войцеховський В.В. Прискорення та поширення космічних променів надвисоких енергій в Локальному Всесвіті. - Кваліфікаційна наукова праця на правах рукопису.

Дисертація на здобуття наукового ступеня доктора філософії за спеціальністю 104 – фізика та астрономія - Київський національний університет імені Тараса Шевченка, МОН України, Київ, 2022

Встановлення джерел космічних променів надвисоких енергій (КПНВЕ, $E > 10^{18}$ eV) залишається однією з основних невирішених проблем сучасної астрофізики. Космічні промені (КП) таких енергій становлять виключний інтерес не тільки для астрофізики, але і для фізики елементарних частинок в цілому, оскільки земні прискорювачі не мають можливості прискорювати протони чи ядра важчих елементів до енергій понад 10^{20} eV, які ми детектуємо з відкритого космосу. Дослідження таких частинок дозволить краще розуміти стандартну модель елементарних частинок та фізичні процеси, які відбувались у ранньому Всесвіті. Та незважаючи на більш ніж столітню історію фізики космічних променів, нам досі невідомі ні джерела КПНВЕ, ні механізми прискорення КП в них. Це викликано головно викривленням траєкторій заряджених частинок в магнітних полях та енергетичними втратами внаслідок взаємодії з фоновим випромінюванням.

Дисертаційна робота присвячена пошуку та дослідженню джерел КПНВЕ, а також аналізу фізичних процесів генерації нетеплового радіо-, гама- та нейтринного випромінювання в потенційних класах джерел КПНВЕ, оскільки ці випромінювання є непрямими вказівками на прискорення релятивістських частинок у відповідних об'єктах.

Літературний огляд в даній роботі широко охоплює сучасну фізику КП.

Описано сучасні методи їх детектування та історію досліджень укупі з характеристиками минулих, діючих та майбутніх обсерваторій. Вказано основні характеристики КП, такі як хімічний вміст, спектр та анізотропія. Детально розглянуто теоретичні моделі прискорення частинок та виділено астрофізичні джерела здатні забезпечувати умови для цих механізмів прискорення. В кінці розділу обґрунтовано складність визначення джерел КПНВЕ та шляхи розв'язання цих проблем.

Дослідження щодо прямого пошуку потенційних джерел КПНВЕ було розділено на дві частини, в кожній з яких використовувались різні підходи до вирішення поставленої задачі. Спочатку використовуючи сучасні дані про космографію Локального Всесвіту було розглянуто низку джерел великомасштабної структури Всесвіту, від яких ми можемо очікувати на Землі потік КПНВЕ різної інтенсивності. Заряджені частинки рухаючись крізь міжгалактичний простір викривлюють свою траєкторію, а також взаємодіють з фоновим випромінюванням втрачаючи енергію та змінюючи початковий хімічний вміст. На основі аналізу довжин вільного пробігу та відхилення в магнітних полях було зроблено теоретичні оцінки кутів відхилення та послаблення потоку КПНВЕ від розглянутих джерел Локального Всесвіту. Отримані оцінки дозволили виділити потенційні астрофізичні джерела з оптичною товщиною щодо послаблення потоку КП внаслідок енергетичних втрат $\tau \leq 2$, а сумарне відхилення в магнітних полях не перевищує ~ 1 рад від точки детектування на небесній сфері. Виявлені потенційні джерела можуть бути використані в майбутньому для їх багатоканального аналізу.

Друга частина прямого пошуку потенційних джерел використовувала принципово інший підхід. Було написано програмний код, який використовуючи сучасну модель Галактичного магнітного поля, розраховував зворотню траєкторію руху зарядженої частинки. Для пошуку потенційних джерел КПНВЕ вздовж відтворених траєкторій задетектованих на Auger та TA подій було

сформовано вибірку потенційних джерел в Локальному Всесвіті, яка включає активні ядра галактик (АЯГ), галактики зі спалахом зореутворення, параметризований каталог радіо галактик, каталог магнетарів та скупчень галактик. Також ми обмежились розглядом подій тільки з гранично високими енергіями (КПГВЕ, $E > 10^{20}$ eV), щоб зменшити вплив магнітного поля. За допомогою написаного програмного забезпечення було вперше розраховано зворотні траєкторії КПГВЕ та отримано координати виходу частинки з Галактики. Додавши до цих нових координат розмазування у випадковому міжгалактичному магнітному полі, було обмежено регіони на небесній сфері, з яких ці частинки могли прилетіти до спостерігача. Проведений порівняльний аналіз отриманих областей потенційного прискорення з вибірками потенційних джерел завершився виділенням конкретних джерел. Проведена робота дозволяє вибирати пріоритетні об'єкти для майбутніх досліджень потенційних джерел високоенергетичних частинок.

В роботі також проведені дослідження механізмів прискорення та очікуваних характеристик КП в їх потенційних джерелах: скупченнях галактик, АЯГ та магнетарах.

Внаслідок великих розмірів та наявності магнітних полів, час виходу космічного променя зі скупчень галактик є більшим за габлівський час. Внаслідок цього, скупчення галактик слугують великими резервуарами КП, де ці заряджені частинки поширюються по всьому об'єму, переприскорюються, втрачають енергію на випромінювання, та повторюють цей цикл. Енергетичні втрати космічних променів маніфестують себе у нетепловому гама- чи нейтринному випромінюванні. Отже реєстрація випромінювання певних характеристик від скупчень галактик є достовірними вказівками на те, що в даних об'єктах відбувається прискорення частинок. В даній роботі вперше проведено чисельне моделювання породженого КП нетеплового гама- та нейтринного випромінювання від скупчень галактик Волосся Вероніки та Геркулес. На основі отриманих

результатів зроблено оцінки перспективи їх спостереження в існуючих (Fermi-LAT, LHAASO, IceCube) та майбутніх обсерваторіях (CTA, IceCube-Gen2).

Розміщені в скупченнях галактик АЯГ, в джетах яких прискорюються заряджені частинки, можуть вносити суттєвий вклад в загальну енергетику КП скупчень галактик та формувати в скупченнях нову популяцію КП з енергіями понад 10^{18} еВ. Внаслідок такого вкладу, спектр випромінювання від скупчень галактик суттєво модифікується стаючи більш жорстким. В роботі досліджені можливі прояви таких породжених в АЯГ високоенергетичних КП в спектрах нетеплового гама- та нейтринного випромінювання від скупчень галактик Волосся Вероніки та Геркулес. Додатковим тестом на присутність в скупченнях лептонного компонента КП, прискореного в релятивістських струменях АЯГ, є синхротронне випромінювання. Нами досліджено зв'язок синхротронного та високоенергетичного рентгенівського та гама-випромінювання в радіогучних АЯГ на різних стадіях їх активності, що дає змогу прогнозувати спалахи активності АЯГ за змінністю їх нетеплового випромінювання.

Ще одним перспективним типом потенційних джерел КПНВЕ є магнетари, адже такі об'єкти зустрічаються і у нашій Галактиці. Недавні роботи вказують на можливість прискорення заряджених частинок до десятків чи навіть сотень ЕеВ в об'єктах з помірно релятивістськими транзієнтними джетами чи у гігантських магнетарних спалахах. Так само як у випадку скупчень галактик, високо- та дуже-високо енергетичне (ГеВне, ТеВне) гама-випромінювання від цих об'єктів генерується внаслідок взаємодій прискорених КП, а отже вказує на можливість прискорення частинок в даних об'єктах та дозволяє досліджувати їх властивості. В даній роботі показано, що Галактичний магнетар SGR1900+14 є потенційним джерелом триплету КПЕВЕ. Проведено моделювання нетеплового гама-випромінювання від магнетара SGR190+14 та побудовано теоретичні моделі еволюції цього об'єкта. В рамках побудованих моделей пов'язаних з магнетаром залишку Наднової/ магнетарно-вітрової туманності пояснено спосте-

режні прояви даного магнетара у всіх діапазонах електромагнітного спектру, оцінено перспективи його спостережень та спостережень інших подібних транзієнтних об'єктів діючими та майбутніми гама-обсерваторіями та детекторами КПНВЕ.

Ключові слова: космічні промені, скупчення галактик, магнетари, активні ядра галактик, гама-промені, нейтрино

ABSTRACT

Voitsekhovskiy V. V. Acceleration and propagation of ultra high energy cosmic rays in the Local Universe. - Qualifying scientific work on the rights of manuscript.

The thesis for obtaining the scientific degree of Doctor of Philosophy by specialization 104 - physics and astronomy - Taras Shevchenko Kyiv National University, MES of Ukraine, Kyiv, 2022

Establishing the sources of ultra high energy cosmic rays (UHECRs, $E > 10^{18}$ eV) remains one of the main unsolved problems in modern astrophysics. Cosmic rays (CRs) of such energies are of exceptional interest not only for astrophysics, but also for particle physics in general, since terrestrial accelerators do not have the ability to accelerate protons or nuclei of heavier elements to energies above 10^{20} eV, which we detect from outer space. The study of such particles will provide to us a better understanding of the standard model of elementary particles and the physical processes that occurred in the early universe. Despite the more than century-old history of cosmic ray physics, we still do not know the sources of UHECRs, nor the mechanisms of acceleration of CRs in them. This is caused mainly by the deflection of the trajectories of charged particles in magnetic fields and energy losses due to interaction with background radiation.

Dissertation work is devoted to search and investigation of CR sources, as well as analysis of physical processes of generation of non-thermal radio-, gamma-ray and neutrino emission in potential classes of UHECR sources, since this emission is indirect indication of the acceleration of relativistic particles in the respective objects.

The literature review in this work broadly covers state-of-the-art CR physics. Modern methods of CR detection and the history of research are described together with characteristics of past, current and future observatories. The main characteri-

stics of CRs, such as chemical composition, spectrum and anisotropy are indicated. Theoretical models of particle acceleration are considered in detail and astrophysical sources capable of providing conditions for these acceleration mechanism are identified. At the end of the chapter, the complexity of determining the sources of UHECR and the ways of solving these problems are substantiated.

Research on the direct search for potential sources of UHECR was divided into two parts, each of which used different approaches to solving the task. First, using modern data on the cosmography of the Local Universe, a number of sources of the large-scale structure of the Universe were considered, from which we can expect a various intensity UHECR flow on the Earth. Charged particles moving through intergalactic medium deflect their trajectories, and also interact with background radiation, losing energy and changing the initial chemical composition. Based on the analysis of mean free path and deflections in magnetic fields, theoretical estimates of the angles of deviation and weakening of the UHECR flow from the considered sources of the Local Universe were made. The obtained estimates made it possible to single out potential astrophysical sources with optical thickness $\tau \leq 2$ in terms of weakening the CR flow due to energy losses, and the total deviation in magnetic fields does not exceed ~ 1 rad from the detection point on the celestial sphere. The identified potential sources can be used in the future for their multi-messenger analysis.

The second part of the direct search for potential sources used a fundamentally different approach. Using a modern model of the Galactic magnetic field we have written a program code that calculates backward trajectory of the charged particle. For searching of sources of UHECR along the reproduced trajectories of Auger and TA events was formed a sample of potential sources in the Local Universe, which includes active galactic nuclei (AGN), starburst galaxies, a parameterized catalog of radio galaxies, a catalog of magnetars and galaxy clusters. We also limited ourselves to the consideration of events with extremely high energies only (EHECR, $E > 10^{20}$

eV) in order to reduce the influence of the magnetic field. With the help of the written software, the backward trajectories of the EHECR were calculated for the first time and the coordinates of the exit of the particle from the Galaxy were obtained. The regions on the celestial sphere from which these particles could fly to the observer were limited by adding to these new coordinates the smearing in the random intergalactic magnetic field. The conducted comparative analysis of the obtained areas of potential acceleration regions with samples of potential sources ended with the selection of specific sources. The work carried out makes it possible to select priority objects for future research of potential sources of high-energy particles.

In the work, the acceleration mechanisms and expected characteristics of CRs in their potential sources: galaxy clusters, AGN and magnetars are also studied.

Due to the large size and the presence of magnetic fields, the exit time of cosmic rays from galaxy clusters is longer than the Hubble time. As a result, galaxy clusters serve as large reservoirs of CRs, where these charged particles spread throughout the volume, accelerate, lose energy through radiation, and repeat this cycle. Energy losses of CRs manifest themselves in non-thermal gamma-ray or neutrino emission. Therefore, the registration of radiation of certain characteristics from clusters of galaxies is a reliable indication that particles are accelerated in these objects. In this work, for the first time, numerical modeling of non-thermal gamma-ray and neutrino emission generated by CRs from the Coma and Hercules galaxy clusters was carried out. Based on the obtained results, the prospects of their observation in existing (Fermi-LAT, LHAASO, IceCube) and future observatories (CTA, IceCube-Gen2) were evaluated.

AGN that are located in galaxy clusters can make a significant contribution to the total energetics of CRs of galaxy clusters and form a new population of CRs with energies above 10^{18} eV. As a result of such a contribution, the spectrum of radiation from galaxy clusters is significantly modified, becoming more rigid. This work investigates the possible manifestations of such high-energy CRs generated in the active

galactic nuclei on the spectra of non-thermal gamma-ray and neutrino emission from the Coma and Hercules clusters. Synchrotron radiation is an additional test for the presence in clusters of the lepton component of the CRs accelerated in relativistic jets of the AGN. We have investigated the relationship between synchrotron and high-energy X-ray and gamma-ray emission in radio-loud AGN at different stages of their activity, which makes it possible to predict outbursts of AGN activity based on the variability of their non-thermal radiation.

Magnetars are another promising type of potential sources of UHECR, because such objects are also found in our Galaxy. Recent works indicate the possibility of acceleration of charged particles to tens or even hundreds of EeV in objects with moderately relativistic transient jets or in giant magnetar flares. Just as in the case of galaxy clusters, high- and very-high energy (GeV, TeV) gamma-ray emission from these objects is generated due to the interactions of accelerated CRs, and therefore indicates the possibility of particle acceleration in these objects and allows them to be studied. This paper shows that the Galactic magnetar SGR1900+14 is a potential source of the EHECR triplet. Non-thermal gamma-ray emission from the SGR190+14 magnetar was simulated and theoretical models of the evolution of this object were constructed. Within the framework of constructed models related to the magnetar of the remnant Supernova/magnetar-wind nebula, the observational manifestations of this magnetar in all ranges of the electromagnetic spectrum were explained. The prospects of its observations and observations of other similar transient objects by existing and future gamma-ray observatories and detectors of UHECR were evaluated.

Keywords: cosmic rays, galaxy clusters, magnetars, active galactic nuclei, gamma rays, neutrinos

List of publications

1. B. Hnatyk, R. Hnatyk, V. Zhdanov, V. Voitsekhovskiy // Unveiling the nature of the unidentified gamma-ray sources 4FGL J1908.6+0915e, HESS J1907+089/HOTS J1907+091, and 3HWC J1907+085 in the sky region of the magnetar SGR 1900+14 // MNRAS, 2022 - Vol. 514, Issue 1. – P. 762-779. <https://doi.org/10.1093/mnras/stac1304>, Paper Q1, Scopus
2. R. Hnatyk, V. Voitsekhovskiy // Gamma-ray and neutrino radiation from Coma cluster (A1656) // Ukr.J.Phys., 2022 - Vol.67, No.2, pp. 102-109. <https://doi.org/10.15407/ujp e67.2.102>, Paper Q4, Scopus
3. V. Voitsekhovskiy // Prospects for gamma-ray observations of Hercules cluster // Advances in Astronomy and Space Physics, 2021 - Vol. 11, Issue 1-2, PP. 13-18
<https://doi.org/10.17721/2227-1481.11.13-18>, Web of Science
4. E. Fedorova, B. Hnatyk, A. Del Popolo, A. Vasylenko, V. Voitsekhovskiy // Non-Thermal emission from radio-loud AGN jets: radio vs x-rays // Galaxies, 2022 - 10(1), 6, Paper Q2, Scopus
5. R. Hnatyk, V. Voitsekhovskiy // Extremely high energy cosmic rays: observations and potential sources // PoS(ICRC2021)464 (<https://pos.sissa.it/395/464/pdf>), Conference Paper, Scopus
6. B. Hnatyk, R. Hnatyk, V. Zhdanov, V. Voitsekhovskiy // High energy and very high energy gamma-ray emission from the magnetar SGR 1900+14 outskirts // PoS(ICRC2021)672 (<https://pos.sissa.it/395/672/pdf>), Conference Paper, Scopus
7. R. Hnatyk, V. Voitsekhovskiy // Extremely high energy cosmic rays: potential sources // Kinematics and physics of celestial bodies, 2020 - 36(3), p. 47-68, Paper Q4, Scopus
8. V. Voitsekhovskiy, B. Hnatyk, Yu. Kudrya // Acceleration and propagation of ultra high energy cosmic rays in local Universe // Visnyk of Kyiv national university of Taras Shevchenko. Astronomy, 2018 - 2, p. 33-36

Contents

Acronyms	14
Introduction	15
1 Cosmic rays: observations, characteristics, potential sources and acceleration mechanisms	20
1.1 Introduction	20
1.2 Detection technique and modern type of detectors	20
1.2.1 First large surface observatories	21
1.2.2 Pierre Auger Observatory	22
1.2.3 Telescope Array	22
1.2.4 Future Detectors	23
1.3 The main characteristics of Cosmic Rays: chemical composition, fluxes, spectrum, anisotropy	24
1.3.1 Chemical composition	25
1.3.2 Spectrum	27
1.3.3 Anisotropy	28
1.4 Acceleration mechanisms	31
1.4.1 Fermi mechanism of 2nd order	33
1.4.2 Diffusive shock acceleration (1st order Fermi mechanism)	34
1.5 Source types	37
1.5.1 Galactic sources	39
1.5.2 Extragalactic sources	40
1.5.3 Exotic models	42
1.6 Search for sources and problems of identification	42
1.6.1 Trajectory deflections	43
1.6.2 Energy losses	44
1.7 Conclusions and unsolved problems	45
2 Potential sources of ultra-high energy cosmic rays	48
2.1 Introduction	48
2.2 State-of-the-art problems in UHECR physics	49
2.3 Influence of ISM and IGM on the propagation of UHECR, energy losses	50

2.4	Model of Galactic and extragalactic magnetic fields	51
2.5	UHECRs in the Local Universe	53
2.5.1	Large-scale structure of the Universe	55
2.5.2	Expected characteristics of UHECR from potential sources in the Local Universe	57
2.6	EHECRs observed by detectors PAO and TA	59
2.7	Surveys of potential sources of EHECR	61
2.8	EHECR trajectory recovery	63
2.9	Correlation of EHECR events with potential sources	65
2.10	Conclusions	70
3	Galaxy clusters as reservoirs of cosmic rays	72
3.1	Introduction	72
3.2	Formation of galaxy clusters	72
3.3	Galaxy cluster content and distribution parameters	73
3.4	Dark matter in galaxy clusters	76
3.5	Signatures of cosmic ray acceleration in galaxy clusters	77
3.6	AGN in galaxy clusters and their influence on cosmic rays	79
3.6.1	Physics of radio-loud AGN	79
3.6.2	Spectral energy distribution of the radio loud AGN	80
3.6.3	Spectral Fitting of the AGN Sample	82
3.6.4	Interconnection of Radio and X-ray Spectra in the AGN Sample	86
3.7	Modelling of gamma-ray emission using MINOT	88
3.8	Hercules galaxy cluster	89
3.9	Coma galaxy cluster	93
3.10	Conclusions	95
4	Transient sources of EHECR in the Galaxy and Local Universe based on example of magnetar SGR1900+14	98
4.1	Introduction	98
4.2	Looking for Galactic transient sources of UHECR	99
4.3	Sky region around the magnetar SGR1900+14 in different bands	100
4.3.1	Sky region around SGR 1900+14 in the γ -ray band	100
4.3.2	Sky region around SGR 1900+14 in the radio band	102
4.3.3	Sky region around SGR 1900+14 in the optical/infrared band	103

4.3.4	Sky region around SGR 1900+14 in the X-ray band	104
4.4	Expected signatures of PWNe, SNRs and SFRs in the sky region around SGR1900+14	104
4.4.1	PWNe, SNRs and SFRs as CR accelerators	105
4.4.2	Energy requirements for γ -ray sources in the region of SGR 1900+14 . .	109
4.4.3	Modelling of the spectral energy distribution (SED) for the SGR 1900+14 region in SNR model	111
4.4.4	Modelling of the SED for the SGR 1900+14 region in PWN model . . .	113
4.5	HE – VHE gamma-ray emission from SGR 1900+14 region - possible sources . .	116
4.5.1	Supernova Remnants	116
4.5.2	Star formation region	118
4.5.3	Pulsar wind nebulae	119
4.5.4	Source confusion	122
4.6	Conclusions	123
5	Overall conclusions	125
6	References	126
7	Appendix	140

Acronyms

- AGN** - Active galactic nuclei
- CMB** - Cosmic microwave background
- CR** - Cosmic ray
- DM** - Dark matter
- DSA** - Diffusive shock acceleration
- GC** - Galaxy cluster
- GMF** - Galactic magnetic field
- GRB** - Gamma-ray burst
- GZK** - Greisen-Zatsepin-Kuzmin
- EAS** - Extensive air shower
- EGMF** - Extragalactic magnetic field
- EHECR** - Extreme-high energy cosmic ray
- IC** - Inverse Compton
- ICM** - Intracluster medium
- IGM** - Intergalactic medium
- ISM** - Interstellar medium
- SBG** - Starburst galaxy
- SFR** - Star formation region
- SNR** - Supernova remnant
- SSC** - Synchrotron self-Compton
- SW** - Shock wave
- TA** - Telescope Array
- PAO** - Pierre Auger Observatory
- PWN** - Pulsar wind nebulae
- UHECR** - Ultra-high energy cosmic ray

Introduction

Justification of the choice of research topic. The search for sources of ultra-high energy cosmic rays (UHECR, $E > 10^{18}$ eV) is one of the most significant unsolved problems in high energy astrophysics. The observed high degree of isotropy of the UHECR intensity as a result of the impact of extragalactic and Galactic magnetic fields, coupled with the significant uncertainty in their chemical composition (atomic masses) as a result of indirect detection, makes it impossible to link observed events to their sources and establish acceleration mechanisms.

There are elaborated theoretical mechanisms of acceleration that can accelerate UHECR particles to energies through all their spectrum. We also know about astrophysical objects where such conditions can be met, e.g. active galactic nuclei (AGN), starburst galaxies (SBGs), galaxy clusters (GCs), magnetars, tidal disruption events, i. e. objects where strong shock waves or transient jets are occurring. Therefore studying itself of particles that was producing in such rich diversity of astrophysical objects can give us more deep understanding of this objects - sources of CRs.

Besides of this exceptional interest to the sources of UHECR, CRs are the most energetic particles in the Universe that we have detected yet. For comparison maximal energy of detected CR is $3.2 \cdot 10^{20}$ eV, that significantly exceeds the highest energy reached on the Large Hadron Collider (7 TeV).

Therefore investigation of UHECRs can provide us with more deeply understanding of particle physics, astrophysics of compact objects, non-stationary processes in the Universe and provide a unique probe of new physics beyond the Standard Model.

Connection of the program with scientific programs, topics, grants. The thesis work was performed while studying at the Department of Nuclear Physics, Faculty of Physics, Taras Shevchenko National University of Kyiv. The acquirer also worked as an engineer at the Astronomical Observatory of Kyiv University within the scientific projects - 16BF023-01 "Fundamental physics and models of high energy astrophysical processes 19BF023-01 "High-energy phenomena and active processes in astrophysical and cosmological systems based on multi-messenger observations" and 22BF023-04 "Multi-messenger investigations of generation of cosmic rays and non-thermal emission in the relativistic jets of astrophysical objects". In addition, part of the research described in this work was carried out within the framework of the scientific project 10F "Research of sources of X-ray and gamma-ray emission and prospects of their observations in CTA".

The purpose and tasks of the research. The aim of the work is to study the influence of the intergalactic and interstellar medium on the propagation of UHECR from potential sources, the establishment of sources of extremely high energy cosmic rays (EHECR, $E > 10^{20}$ eV), as well

as the study of the possibilities of acceleration of UHECR in galaxy clusters and magnetars based on the analysis of secondary non-thermal gamma-ray and neutrino emission.

To realize this aim, the following tasks were set:

- Estimation of characteristic maximum distances to the EHECR sources in the Local Universe due to EHECR energy loss lengths.
- Calculation of the backward trajectories of the detected by Auger and TA EHECR events in the Galactic (GMF) and extragalactic magnetic field (EGMF) and search for their potential sources in the Local Universe.
- Modeling of the non-thermal gamma-ray and neutrino emission from cosmic rays in galaxy clusters taking into account the contribution of AGN accelerated CRs to the overall CR energy balance and spectra; estimation of perspectives for their study by existing (Fermi-LAT, LHAASO, IceCube) and future detectors(CTA, IceCube-Gen2).
- Analysis of the mechanisms of generation of leptonic CR non-thermal radio- and gamma-ray emission in radio loud AGN jets.
- Analysis of UHECR acceleration and non-thermal gamma-ray emission from relativistic jets in transient sources: A case study of Galactic magnetar SGR1900+14

Object of research: cosmic rays of ultra-high and extremely high energies; potential sources of UHECR and EHECR: galaxy clusters, magnetars, active galactic nuclei; non-thermal electromagnetic radiation.

Research methods: analytical investigation of CR acceleration and propagation mechanisms, numerical modeling of the propagation of the EHECR in galactic and extragalactic magnetic fields, modeling of non-thermal gamma-ray and neutrino emission.

Scientific novelty of the obtained results:

1. Based on the analysis of EHECR energy loss lengths and deviations in magnetic fields the estimation of characteristic maximum distances to the EHECR sources in the Local Universe has been improved.
2. For the first time the calculation of the backward trajectories of the detected by Auger and TA EHECR events in the Galactic (GMF) and extragalactic magnetic field (EGMF) was made and the potential sources of these EHECR events in the Local Universe were determined.

3. For the first time, a numerical simulation of contribution of AGN to non-thermal gamma and neutrino emission from galaxy clusters Coma and Hercules was carried out, and the prospects of their observation by existing (Fermi-LAT, LHAASO, IceCube) and future observatories (CTA, IceCube-Gen2) were evaluated.
4. For the first time we have selected the subsample of radio loud AGN with similar spectral indices of radio synchrotron and X-ray inverse Compton emission as a signature of multi-wavelength leptonic CR jet emission.
5. For the first time the connection of the Galactic magnetar SGR1900+1 with the detected by Auger and TA EHECR triplet is substantiated and the observed multiwavelength emission from the magnetar SGR1900+14 region is explained in the frame of the magnetar- connected Hypernova remnant/magnetar wind nebula.

Practical significance of the obtained results.

1. A number of sources of the large-scale structure of the Universe have been identified, the UHECR flux from which is expected to be high enough, and the deviation in magnetic fields is weak enough, for the reliable detection of these UHECR on Earth, which can be used for further multi-messenger analysis of these potential sources.
2. Based on the calculation of backward trajectories of the EHECR, astrophysical objects that can be the sources of relevant events are selected, which allows to choosing priority objects for future studies of potential sources of high-energy particles.
3. The obtained fluxes of gamma- and neutrino emission make it possible to estimate the energy contribution from cosmic rays to the total energy deposit of galaxy clusters, and also justify the prospects of observations of Coma and Hercules cluster in future missions (CTA, IceCube-Gen2)
4. The joint analysis of non-thermal radio and X-ray spectra of active galactic nuclei, carried out in this work, opens up possibilities for separating the contributions to electromagnetic radiation from jet and corona disk, and clarifies the radiation processes in AGN, which can serve as a test for future observations.
5. Constructed models of the evolution of the magnetar SGR1900+14 can be used to explain the radiation from similar transient objects, as well as to assess the possibilities of accelerating the UHECR in magnetars.

Personal contribution of the acquirer. Primarily, the choosing of the subject and methods of research, interpretation of results and their generalization in all works was carried out by the author together with his scientific supervisor Prof. Hnatyk Bohdan. Among the above list of the author's publications, the recipient's contribution to each work is as follows. The work [3] was performed by the author completely independently. In works [2,5,7], the acquirer was engaged in writing the code, modeling and interpreting the obtained results, and writing the publications in close collaboration with his colleague and co-author Dr. Hnatyk Roman. Also, the recipient took an active part in the formulation and solving the problem, interpretation and discussion of the obtained results, preparing tables and overall in the preparation of publications [1,4,6,8]. All talks on the conferences from the list of "approbation of the results" was prepared and performed by the author.

Approbation of the results. Obtained in the work results was reported on the next conferences and seminars:

- 28th Cracow EPIPHANY Conference on Recent Advances in Astroparticle Physics (Cracow, 2022)
- 37th International Cosmic Ray Conference (Berlin, 2021)
- 10th International Conference on New Frontiers in Physics (Crete, 2021)
- Astronomy in Lviv University (Lviv, 2021)
- Astronomy and Physics in Kyiv University (Kyiv, 2021)
- 28th Young Scientists Conference on Astronomy and Space Physics (Kyiv, 2021)
- 11th Young Scientists Conference Problems of Theoretical Physics (Kyiv, 2020)
- Astronomy and Physics in Kyiv University (Kyiv, 2020)
- 27th Young Scientists Conference on Astronomy and Space Physics (Kyiv, 2020)
- Astronomy and Physics in Kyiv University (Kyiv, 2019)
- 26th Young Scientists Conference on Astronomy and Space Physics (Kyiv, 2019)
- Science seminar in the Insitute of Astronomy and Astrophysics of Tubingen University
- Science seminars

Publications.

Results of this thesis was published in the 8 papers in scientific journals, among which 1 paper is in Q1 journal (*MNRAS*), 1 paper is in Q2 journal (*Galaxies*), 2 papers are in Q4 journal (*Kinematics and Physics of Celestial Bodies, Ukrainian Journal of Physics*), 2 papers based on conference material in journals indexed by Scopus (*Proceedings of Science*), 1 paper in journal indexed in Web of Science (*Advances in Astronomy and Space Physics*), and 1 paper is in Ukrainian profile scientific journal (*Bulletin of Taras Shevchenko National University of Kyiv. Astronomy*).

1 Cosmic rays: observations, characteristics, potential sources and acceleration mechanisms

1.1 Introduction

Cosmic rays are charged particles (protons, heavy nuclei, positrons and electrons) and neutrinos, that fill interstellar and intergalactic medium mostly isotropic. These particles are constantly bombarding Earth's atmosphere. The history of cosmic ray physics develops more than hundred years. In 1912 Victor Hess using balloon experiments discovered that ionisation intensity becomes higher with altitude above the Earth's surface. Based on these results he made an assumption that this ionisation is caused by extraterrestrial nature. He has obtained Nobel prize in 1936 for this discovery. It was originally thought that this phenomenon has electromagnetic nature. From this assumption we have today's name of this - Cosmic rays. But in the 1930s the true nature of CR was revealed, after observations of deflection of these particles in magnetic fields scientists understood that CR are charged particles. Next centuries, before constructing of first powerful accelerators, CRs were the main object of study for the high energy physics. Particularly, positrons and muons were discovered in CR fluxes. Now the physics of CRs facing mainly the problem of finding sources for such energetic particles. In the next section we will discuss state-of-the-art data in CR physics.

1.2 Detection technique and modern type of detectors

First cosmic rays were detected in ionisation chambers that were carried by air balloons. These very first detectors used principle of ionisation calorimeter. Later, the fact that our atmosphere also behaves like calorimeter, was used for evolving of more powerful detection techniques of energetic particles. Number of CR particles with energy higher than 10^{14} eV that reach our atmosphere is not enough for being detected by small detectors on air balloons. To investigate such energetic particles we need to use physical process called extensive air showers (EAS). The cascade of reactions are developed due to the interaction of incoming particle with an atmosphere atoms. The final products of such reactions can cover the large areas of the Earth's surface, Fig. 1 .

There are three basic types of EAS detection. Surface arrays for detailed study of particles quantity in the EAS, Cherenkov detectors and fluorescence detectors that can register fluorescence of excited Nitrogen atoms. Fluorescence technique allows to build full picture of EAS development due to possibility of detecting it from the sides [1].

⁰<https://www.mpi-hd.mpg.de/hfm/CosmicRay/Showers.html>

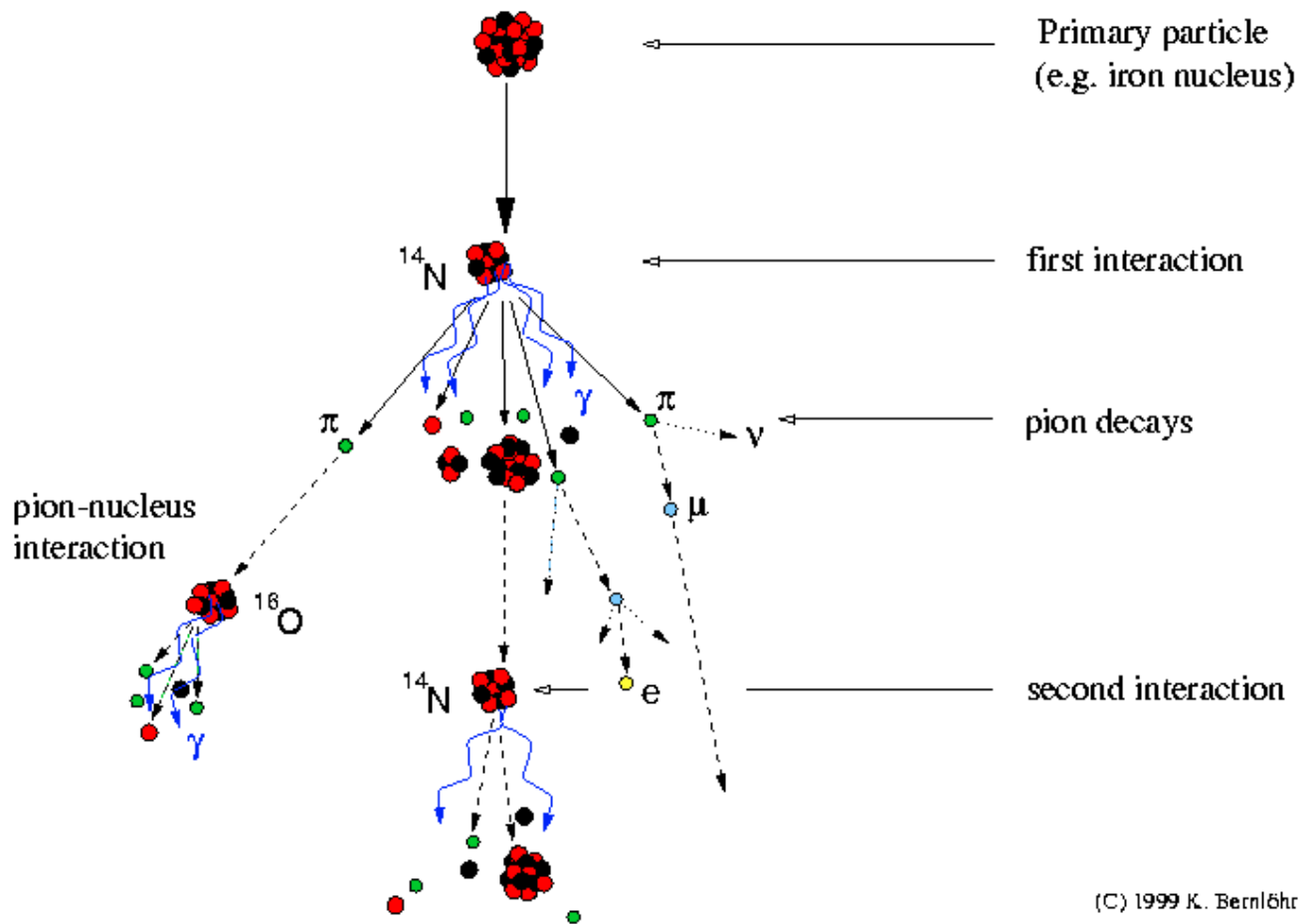


Fig. 1: Sketch that goes deep into development of EAS due to the interaction of incoming energetic heavy nuclei and atmosphere atom ^{14}N . Fig. from www.mpi-hd.mpg.de

1.2.1 First large surface observatories

Akeno Giant Air Shower Array (AGASA) was the largest detectors operating during the 1990s, the 100km^2 ground scintillator array in Japan (Chiba et al 1992), and the High Resolution Fly's Eye (HiRes) pair of fluorescent telescopes operating in Utah (USA) until 2006 [2]. During their work, AGASA achieved an exposure of $1.6 \times 10^3\text{km}^2$ ster year, while HiRes surpassed this result twice. The HiRes telescope consists of two sections spaced 12.6 km apart. At the heart of the detectors is an analog of direct digital converters, that is, in fact, the telescope can create a video of the development of EAS. The Fly's Eye project is known for registering the event with the highest energy so far, $E = 320\text{EeV}$ [3]. The HiRes experiment also conducted the first observations of the Greisen-Zatsepin-Kuzmin limit (GZK suppression).

1.2.2 Pierre Auger Observatory

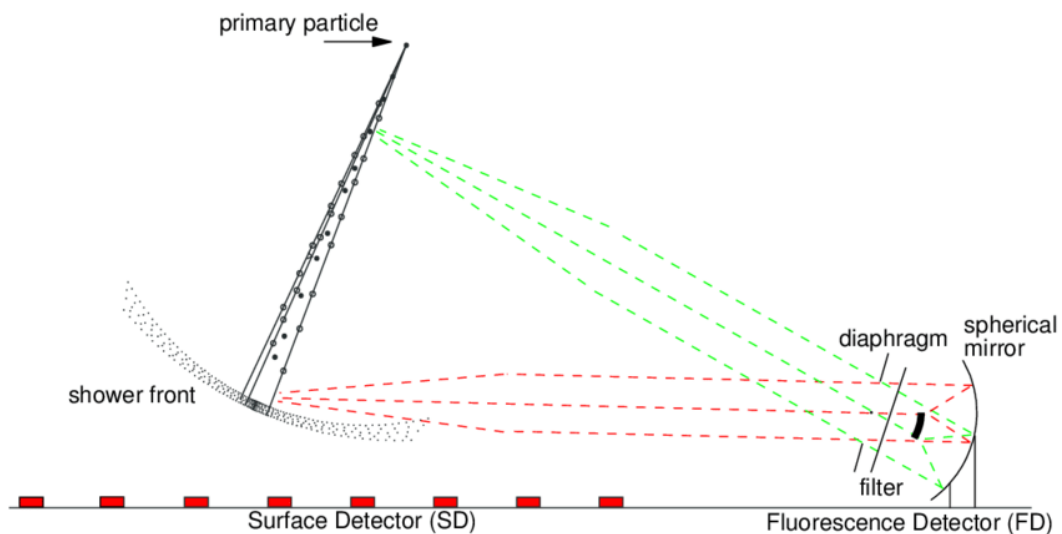


Fig. 2: Hybrid technique of detection as it used by PAO. One can see two types of detectors - surface detectors and fluorescence detectors. Credit: PAO

One of the biggest surface observatories is Pierre Auger Observatory (PAO). It was built in Argentina on the surface of approximately 3000 km^2 by collaboration of 18 countries. The built was start in 2002, and this obseratory was fully finished in 2008. But some observations took place even in 2007. The main feature of this project is using of hybrid technique of detection 2. There are two types of detectors on the territory of the observatory. First type is the water tanks that can register Cherenkov light of CR secondary particles that penetretate this tanks. Surface detectors form the grid with 1.5 km distance between its nods. All atmosphere above this territory is observe by second type of detectors - 4 fluorecence detectors. This principally other detectors are registering ultra-violet light induced by exciting atoms of Nitrogen. This hybrid method provides two independent paths for CR detection ¹.

1.2.3 Telescope Array

The next step of CR experiment evolution in Utah is the Telescope Array. The observatory uses, a hybrid technique of detection and is designed to detect EAS induced by UHECR. An array of terrestrial scintillation detectors detects EAS when it reaches the Earth's surface, while the fluorescent detectors measure the scintillation light generated in the atmosphere. TA observes CRs with energies above 10^{18} eV . Surface detectors in the amount of 500 pieces, evenly distributed over an area of 762 km^2 at a distance of 1.2 km from each other, Fig. 3 . Each ground-based detector

¹<https://www.auger.org>

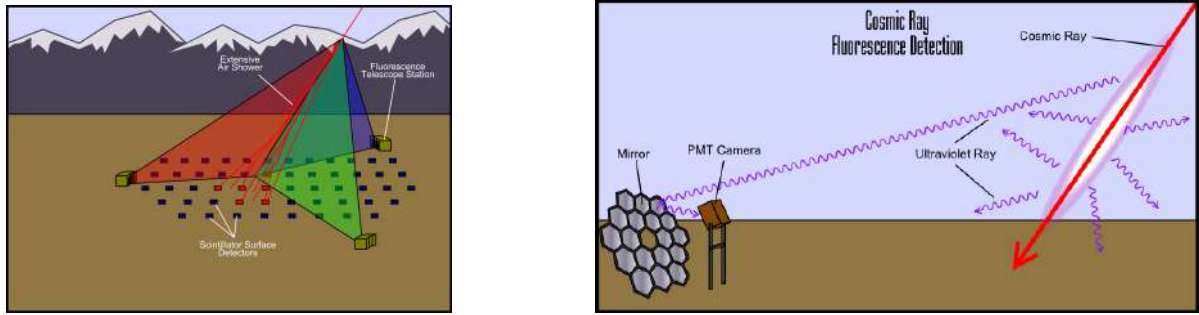


Fig. 3: Left: Hybrid detection technique in the Telescope Array project. Right: Fluorescent emission excited by the EAS and its detection in the Telescope Array project. Credit: TA

weighs 250 kg and consists of a battery, two layers of scintillation detectors and electronics. In addition, there are three stations located in a triangle with sides of 30 km. At these stations there are 12-14 telescopes ².

1.2.4 Future Detectors

A number of observatories are also planned to be launched, the exposure and resolution of which will significantly exceed the existing detectors. In particular, back in 1981, the idea was proposed to measure the fluorescent radiation of EAS using UV telescopes aboard orbital satellites. Their fundamental difference from AMS-type detectors is that the latter detect particles from outer space.

Such new type orbital detectors include future JEM-EUSO and POEMMA projects. JEM-EUSO is the first orbital experiment of this type to be launched in the early third decade of the 21st century. Designed for detecting UHECRs. The history of this detector dates back to the 2000s under the lead of the European Space Agency (ESA), which planned to place it on the ISS. However, in 2004 the project was closed due to technical and financial difficulties. Over time, the mission was transferred to the Japanese JEM module, where it is now planned to launch. The instrument consists of a set of 3 large Fresnel lenses with a diameter of 2.65 m that transmit a signal to the detector, consisting of 137 modules, each of which is an array of 48x48 photomultipliers. Registration will take place in the range of 300-450 nm, the time resolution for photon registration is 2.5 μs [4].

To summarise the data on CR observatories Fig. 4 demonstrates exposure time of past, modern and future detectors.

²<http://www.telescopearray.org>

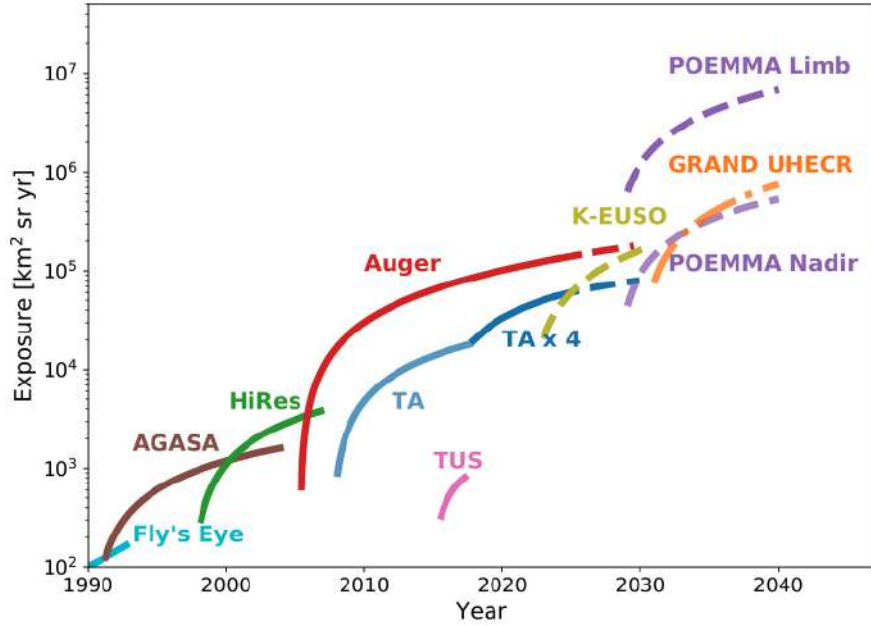


Fig. 4: Evolution of CR detector exposure as a function of time. Future experiments are marked with dashed lines. Fig. from [5]

1.3 The main characteristics of Cosmic Rays: chemical composition, fluxes, spectrum, anisotropy

Cosmic rays that penetrate top of the our atmosphere includes all nuclei and stable charged particles with lifetimes of about 10^6 years and longer. There are so-called primary particles - those particles that have been accelerated in astrophysical sources, and secondary - those particles that are the products of the interactions of the primary CRs. Therefore, protons, helium, electrons as well as all the heavier nuclei to iron that were synthesized in the stars are the primary CRs. Lithium beryllium and boron nuclei (which are not common end products of stellar nucleosynthesis) are secondaries. Positrons and antiprotons are mostly of secondary origin. Whether any part of these antimatter particles is among the primary CRs remains an open question [1].

One of the main measurable characteristics of CRs are their intensity. CR flux are suppressed by solar modulation effect at the energies below GeV. Above this energies the intensity of the CR flux can be approximately presented by a power law:

$$I(E) \propto E^{-\gamma} \quad (1)$$

where γ is the differential spectral index which is typically lying between 2.7 and 3.3.

If we consider energy range from several GeV to subPeV energies, the intensity of primary

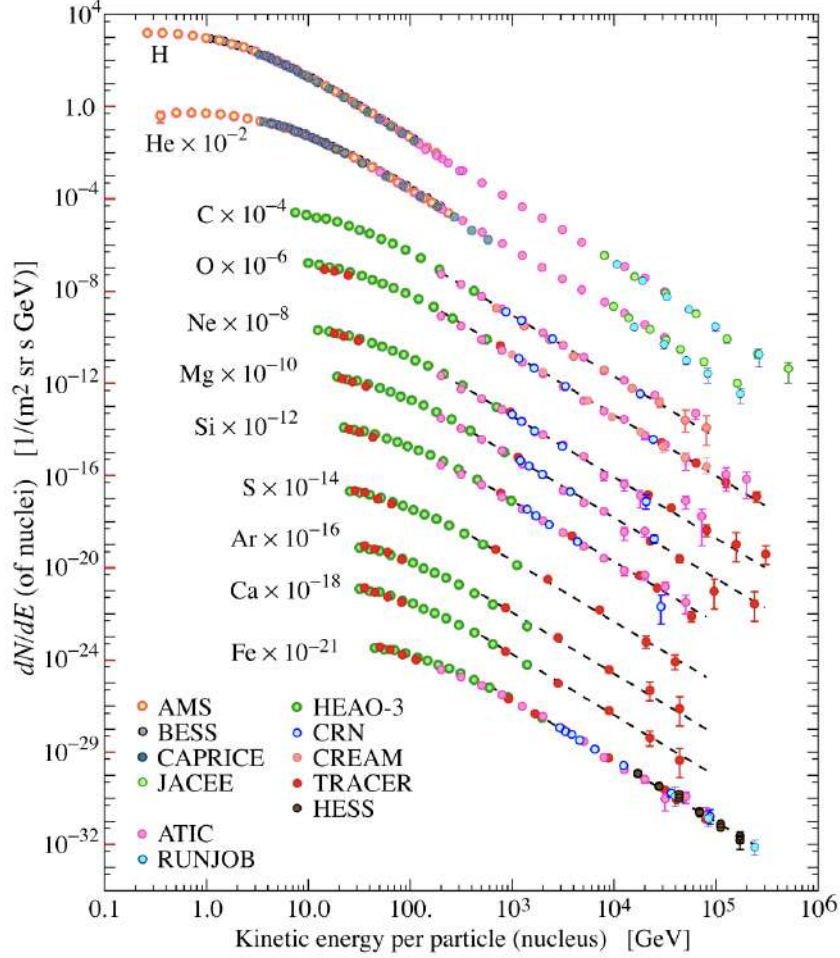


Fig. 5: Hadronic component of CRs as it arrives on the Earth [6].

CRs can be approximately given by:

$$I_N(E) \approx 1.8 \times 10^4 (E/1\text{GeV})^{-\gamma} \left[\frac{\text{nucleons}}{\text{m}^2 \text{ s sr GeV}} \right] \quad (2)$$

where E is the energy per nucleon and $\gamma (\equiv \alpha + 1) = 2.7$. There are approximately 79% of free protons in this energy range. If we will look to higher and higher energies, the fraction of heavier nuclei will grow, but overall intensity are falling down to very small quantities. For example particles with energies $E > 10^{11}\text{GeV}$ are extremely rare, less than one particle per square kilometer per century.

1.3.1 Chemical composition

Lets have a look into chemical composition of wide energy ranged CR flux. CRs are mainly protons ($\sim 90\%$) and heavier nuclei. Electron/positron flux on the top of atmosphere is relatively small (tens of particles per million). Flux of the hadronic component of CRs based on the observations of different obsrvatories are shown on the Fig. 5. The relative abundance of CR

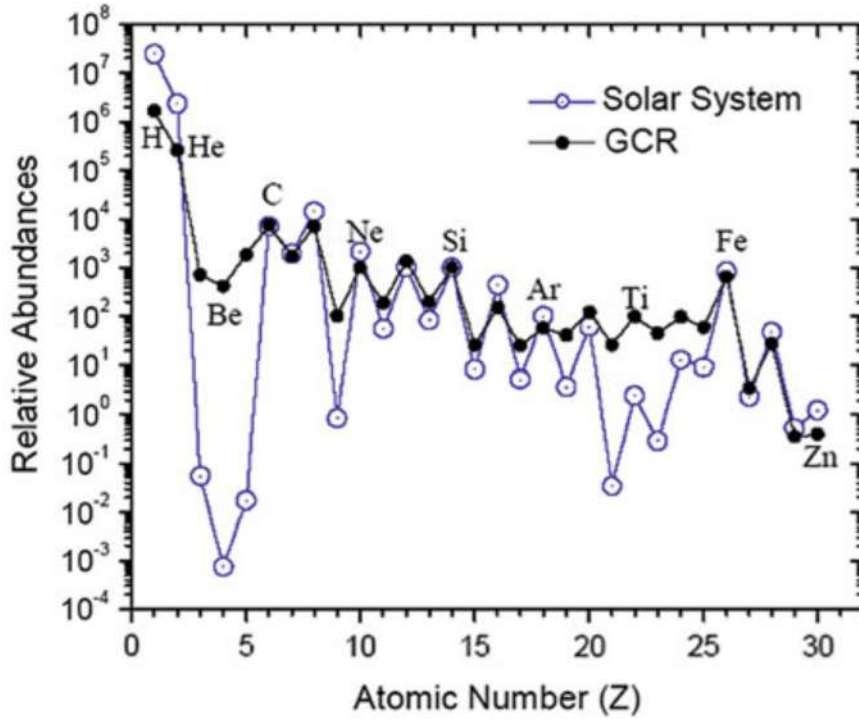


Fig. 6: Relative abundance of the main hadronic components present in the cosmic rays arriving at Earth and in the Solar System. Both are normalized to the abundance of Si = 103, and the relevant energy range is a few hundreds MeV/nucleon. Credit: ACE archives

species is shown on the Fig. 6. The main features can be summarise as follows [7]:

- the abundance of nuclei of carbon, oxygen, silicone and iron groups is approximately the same in the number of CP and in the solar system;
- light elements as Lithium, Beryllium and Boron are much more abundant in CR flux in comparison to Solar System
- elements between Calcium and Ferrum are more abundant in CR flux
- Helium and Hydrogen presented in less quantities relative to the heavy elements

Distribution of different elements in the CR flux is not much different from the typical chemical composition of Solar System. Some features, such as 2nd and 3d listed above, can be the result of nuclei spallation due to the interaction of CRs with ISM. In such interaction nuclei of CR are fragmented into nuclei with atomic and mass numbers that are smaller of primary composition.

At the energies of several TeV and below, chemical composition of CR can be established by comparing of measurements of particle momentum and information from Cherenkov detectors. At higher energies during detection of EAS this task is more complicated. One of the main parameter

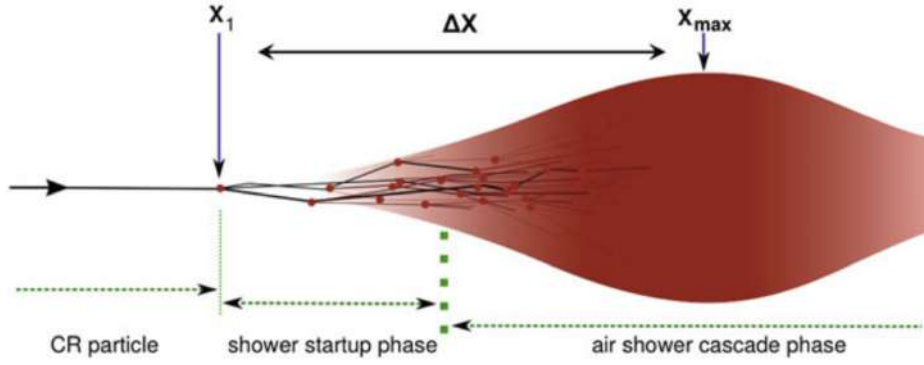


Fig. 7: Schematic overview of EAS and measuring X_{max} parameter. Credit: Doctoral thesis of R. Ulrich

that helps to derive chemical composition of initial particle is X_{max} [g/cm^2] - the depth of maximum number of secondary particle in the EAS. X_{max} can be measured as sum of depths of primal interaction X_1 and distance of EAS evolution ΔX , Fig. 7:

$$X_{max} = X_1 + \Delta X \quad (3)$$

This method is based on the fact that cross section of nuclei is growing with their atomic number.

1.3.2 Spectrum

Energetic spectrum of CRs has the similar shape as typical spectrum of energetic particles from the Galactic and extragalactic non-thermal sources. In the energy range above $E > 10^9$ eV, where CR spectrum is not affected by solar wind, it can be expressed by power-law distribution:

$$N(E)dE = KE^{-\gamma}dE \quad (4)$$

where spectral index γ is varying $\approx 2.5 - 3.1$. At the energy around 10^{15} eV we observe some break in CR spectrum which usual are referred as knee, where the spectral index becomes equal ≈ 3.1 . This feature corresponds to the limit of Galactic accelerators for protons. If we divide the overall spectrum to different components for each type of nuclei, we will see that the knee in the energy spectrum for helium lies on the higher energies that for protons. And for other nuclei their spectra is shifted towards higher energy with increasing element number. Therefore the main idea here is in the fact that steepening of the spectra of different CR species causes the knee in the all particle spectrum [8]. Kascade-Grande experiment also stated that steepening of the spectrum at the energies around 8×10^{16} is observed together with transition to heavier nuclei [9].

Next spectrum feature is second knee, that is observed at the energies around 400 PeV, and characterised by the steepening of the spectrum from 3.1 to 3.3. So-called ankle, next feature at the energies 5×10^{18} eV, is respective for more hard spectrum. One of the possible explanation is the start of dominating of extragalactic CRs on the galactic CRs [10]. But a lot of discussion still ongoing. Particularly in [11] ankle is because of transition from Galactic origin to extragalactic. But in models of proton dominating, ankle is produced because of energy loses on pairs creating [12], or as result of reactions $p\gamma \rightarrow e^+ + e^-$ on the CMB [13]. But ankle explanation as transition from Galactic to extragalactic can be justified even in proton dominating models [14]. Therefore there are no essential contribution from Galactic CRs on the energies above 10^{18} eV if this interpretation is correct.

In 1965 was the discovery of cosmic microwave background (CMB), a sharp cut-off of the CR spectrum was theoretically predicted due to inelastic collisions of charged CR particle with background photons [15; 16]. The energy threshold for photo-pionic birth processes is $5 \text{ times } 10^{19} \text{ eV}$. Therefore, the number of CRs above this energy should fall sharply, which in practice means a rapid cut-off of the spectrum. A similar result of the collapse of the spectrum is also given by the theory of photodisintegration of heavy nuclei in the mixed content model [17]. However, experiments on UHECR observations also detected particles with energies above 10^{20} eV [10; 18].

The spectrum of all CR particles built on the basis of observations of various observatories is shown in Fig. 8. The differential energy spectrum is multiplied by $E^{2.6}$ in order to conveniently show all the features of its shape, such as the knee or ankle.

In addition to general spectrum features mentioned above, there are one more interesting feature of electron/positron spectrum at low energies. The orbital experiments PAMELA [19] and AMS-02 [20] measured that the ratio of positrons to electrons increases with energy for the energy range above 10 GeV. This structure of the electronic spectrum, as well as the increase in the total share of positrons, may be associated with contributions from individual nearby sources (supernova remnants or pulsars) [21]. Other explanations for this effect include [22] propagation effects or dark matter decay/annihilation processes [23]. Significant differences in the measurements of the relative proportion of electrons/positrons below ~ 10 GeV are explained by differences in the charge-dependent effects of solar modulation present near the Earth during the measurement.

1.3.3 Anisotropy

The difficulty of determining the directions to the CR sources mainly caused by the effect of Lorentz force in all-permeating magnetic fields. A charged particle with momentum p and charge $q = eZ$, moving in the magnetic field B , under the action of the Lorentz force begins to move

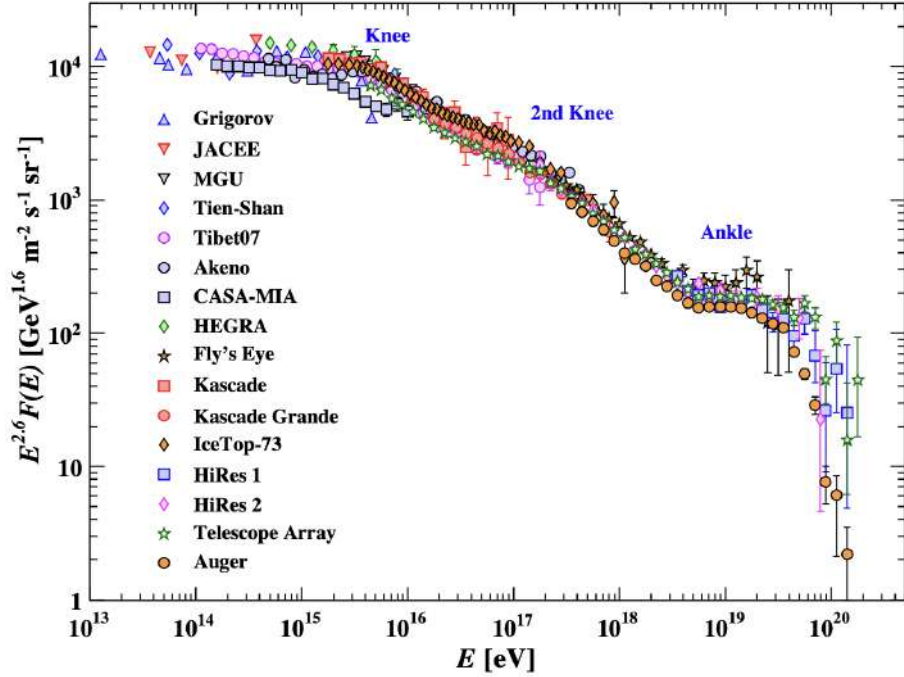


Fig. 8: Experimental spectrum of CR based on EAS as a function of energy. Intensity is multiplied by $E^{2.6}$ for better visualization of the results. Fig. from [1]

along a spiral trajectory with radius:

$$r_L(p, B) \simeq \frac{p}{qB} \simeq 1 \left(\frac{p/Z}{10^{15} \text{eV}} \right) \left(\frac{B}{\mu\text{G}} \right)^{-1} \text{ pc} \quad (5)$$

For intermediate energies of CRs, the radius of gyration is much less than the distance of a few hundred parsecs to the nearest source, in this case SN, and even less than the typical scale of the turbulence of the Galactic magnetic field - $l \sim 100$ pc. Due to this fact, only relatively high-energy protons and nuclei fly into the vicinity of the Earth without undergoing strong distortion in magnetic fields.

Therefore the distribution of CRs on the celestial sphere is close to isotropic at most energies due to diffuse propagation in magnetic fields. Milagro [24], Ice Cube [25], and the Tibet-III array have observed anisotropy at 10^{-3} for TeV CRs, probably as a result of close sources. There is also another type of anisotropy in the distribution of CRs at such energies, which is associated with the movement of the Solar System through the space. It is called by its pioneers - the Compton-Getting effect [26], and its amplitude is determined by:

$$\delta = (\alpha + 2) \frac{w}{v} \quad (6)$$

where α is an indicator of the differential energy spectrum of CR, w is the speed of the Sun, v is the speed of particles. Taking into account the different relative velocities of the Sun, we obtain

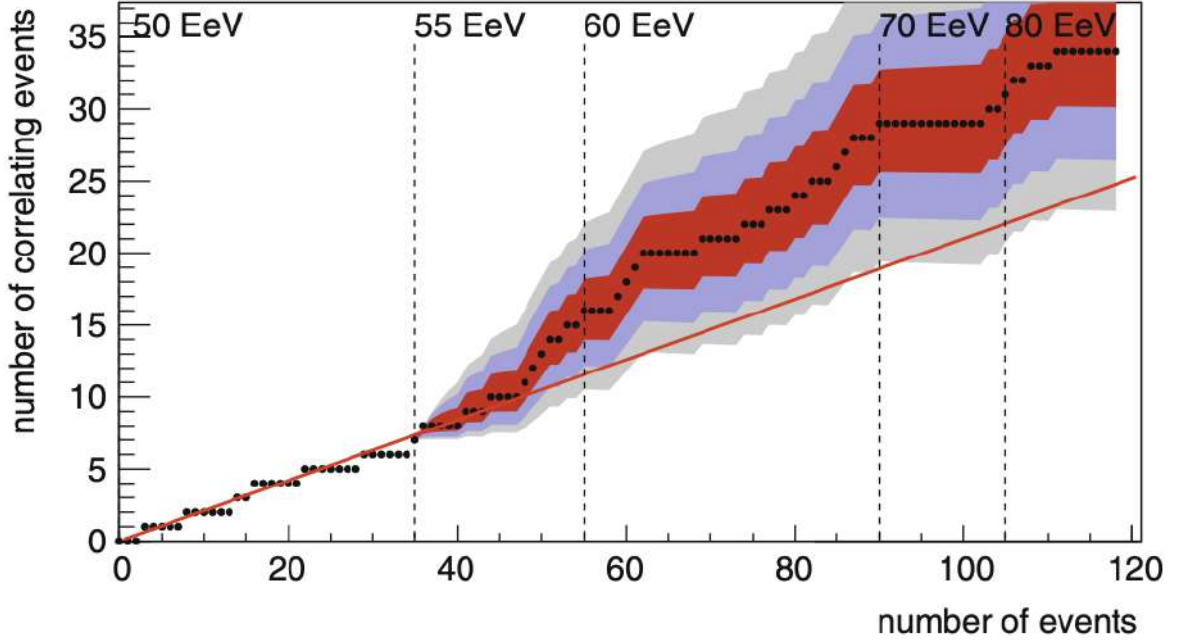


Fig. 9: Energy-ordered correlation of events above 57 EeV with the Véron-Setti Véron (VCV) AGN catalog as observed by the PAO until June 2011. The red line represents the correlation in the case of an isotropic distribution. Credit: PAO collaboration

values within $\delta \sim 10^{-4} - 10^{-3}$.

At higher energies, the anisotropy is manifested on a larger scale, due to the smaller gyroradius of the particles, and hence greater preservation of the initial direction. Based on the formula 5, one can determine the gyroradius of CR for different values of rigidity R . The corresponding values are listed in the table 1. Comparing these values with the thickness of the galaxy's disk (approximately 300 pc) and the halo radius (3-10 kpc), we can conclude that protons with energies above 10^{19} eV have a gyroradius 10 times larger than the size of the galaxy, and therefore will not be effectively trapped by the Galactic magnetic field. In the Galactic magnetic field, the CR with extreme high energies $E \sim 10^{20}$ eV deviate very weakly and, as a result, propagate quasi-ballistically, retaining to a greater or lesser extent the initial direction to the source.

The search for an anisotropy in the region of ultrahigh energies was carried out by the PAO and TA collaborations. In the southern galactic hemisphere, Pierre Auger's collaboration reports a correlation of events above 57 EeV with the Verona-Setti Verona catalog of the order of 33 %, with 21 % expected according to the isotropic distribution [27]. PAO data also indicate a visible cluster of events with energies above the GZK in the direction of the nearest known radio galaxy Centaurus A (NGC 5128) [28]. The significance of this fact, however, is difficult to quantify, as this knowledge is derived from observations, and the probability of such an accumulation in the

Rigidity R [V]	Proton gyroradius [pc]	Ferrum gyroradius [pc]
10^{15}	0.36	0.014
10^{17}	36	1.4
10^{19}	3.6	140
10^{21}	360000	14000

Tab 1: Larmor radius r_L of protons and iron nuclei in a magnetic field with amplitude 3×10^{-6} G (typical value of magnetic field in our Galaxy)

isotropic distribution is only a few percent [29]. Two of the observed events correlate with the core of the galaxy. If this is a real surplus, then it is somewhat unexpected, because although Centaurus A is the third strongest radio source in the sky in the center of which is the BH weighing about $55 M_{\odot}$ and the nearest radio galaxy to us at a distance of only $\simeq 3.6$ Mpc. It is by nature an elliptical radio galaxy with relatively low power [30]. A comparison with the minimum power required to accelerate the particles to the required energy (the ratio 18), calls into question the ability of Centaurus A to accelerate CRs to the energies of UHECR. Alternatively, the UHECR observed in the Centaurus A direction may be born mainly at the sources of the Centaurus GC, which in turn is part of the Hydra-Centaurus GC that extends directly behind Centaurus A. In the northern hemisphere, the TA collaboration reported observations of so-called 'hot spot', for events above 57 EeV, in the direction of the constellation Ursa Major with a diameter of $30^{\circ} - 40^{\circ}$ with a post-trials statistical significance of this excess with respect to an isotropic distribution 3.4σ [31].

1.4 Acceleration mechanisms

The main equation of motion for charged particles in electromagnetic fields is the following expression:

$$\frac{d}{dt}(\gamma m \mathbf{v}) = e(\mathbf{E} + \mathbf{v} \times \mathbf{B}) \quad (7)$$

In most astrophysical objects, static electric fields cannot be maintained due to the extremely high electrical conductivity of plasma - any electric field dissipates quickly due to the surrounding movement of free charges. Therefore, the electromagnetic mechanism of acceleration of the CRs can be associated only with non-stationary electric fields, for example, strong electromagnetic waves or time-varying magnetic fields. No work is performed on the particle in a constant magnetic field,

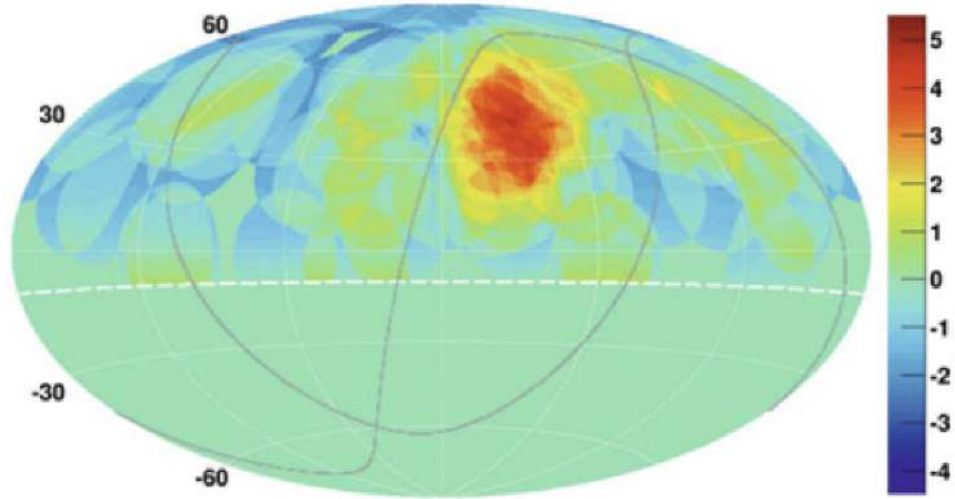


Fig. 10: Events with energy over 57 EeV were observed by Telescope Array until May 2014. The color scale represents the importance of detection. The area of the 'hot spot' is well visible. Fig. from [32]

but if the magnetic field changes over time, the work can be performed by an induced electric field, which is given by one of Maxwell's equations: $\text{rot}\mathbf{E} = -\partial\mathbf{B}/\partial t$ [7].

At the scientific conference in 1933, Zwicky and Baade put forward a revolutionary hypothesis: massive stars end their lives with explosions that destroy them, which in turn generate CRs. It took another 16 years before Fermi was able to develop a model that could explain this hypothesis. In the next sections we will briefly discuss main ideas of Fermi theory.

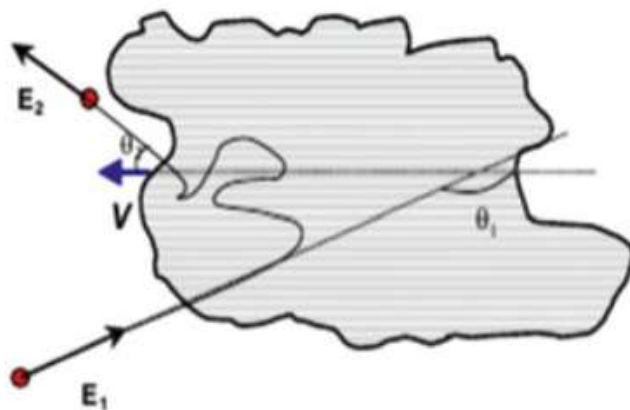


Fig. 11: Scattering of a charged particle on an interstellar clouds. Fig. from [33]

1.4.1 Fermi mechanism of 2nd order

The Fermi mechanism was first proposed in 1949 as a stochastic method by which particles after collisions with clouds in the interstellar medium (ISM) can be accelerated to high energies (Fermi, 1949). In the original Fermi version, charged particles are reflected on "magnetic mirrors" that are associated with the irregularities in the Galaxy's magnetic field. Mirrors are assumed to move randomly at a typical velocity V , and Fermi showed that particles stochastically gain energy in these reflections. If particle remains in the acceleration region for some characteristic time τ_{esc} , then particle spectrum shows power-law behavior. This mechanism can also take place in shock waves, which may be related to gravitational collapse, e.g. star collapse or conditions in the vicinity of black holes. It is assumed that the mirror has infinite mass, and therefore its velocity $\beta = V/c$ does not change in the collisions. Let consider this mechanism in more details. Assume the charged particle with energy E_1 (velocity v) in the laboratory frame of reference is reflected from the moving boundary between regions with different densities Fig. 11. Angles θ_1 and θ_2 are the angles between the initial and final direction of the particle and the velocity of the cloud.

The energy of the particle E_1^* in the reference frame of the cloud is given (neglecting the mass of the particle relative to its kinetic energy):

$$E_1^* = \gamma E_1 (1 - \beta \cos \theta_1) \quad (8)$$

In the reference frame of the scattering cloud $E_1^* = E_2^*$ (analog of the collision with the wall), so in the laboratory reference frame, the energy of the particle after the collision will be equal to:

$$E_2 = \gamma E_2^* (1 + \beta \cos \theta_2) \quad (9)$$

Next steps is to calculate mean fraction of energy $\langle \frac{\Delta E}{E} \rangle$, that is taken in acceleration process. I refer the interested reader to a wonderful book of Malcolm Longair [7] where all calculations are presented. Here is discussed only the final result:

$$\langle \frac{\Delta E}{E} \rangle \simeq \frac{4}{3} \beta^2 \quad (10)$$

As one can see, energy change depends on the second order of velocity, therefore this mechanism is known as the second-order Fermi acceleration mechanism. However, it is facing a bunch of problems. In particular, the random velocities of interstellar clouds in the Galaxy are very small compared to the speed of light, $\beta \leq 10^{-4}$. In addition, the average free path for scattering CRs in the ISM is about 0.1 pc, so the number of collisions will be about a few per year, which will lead

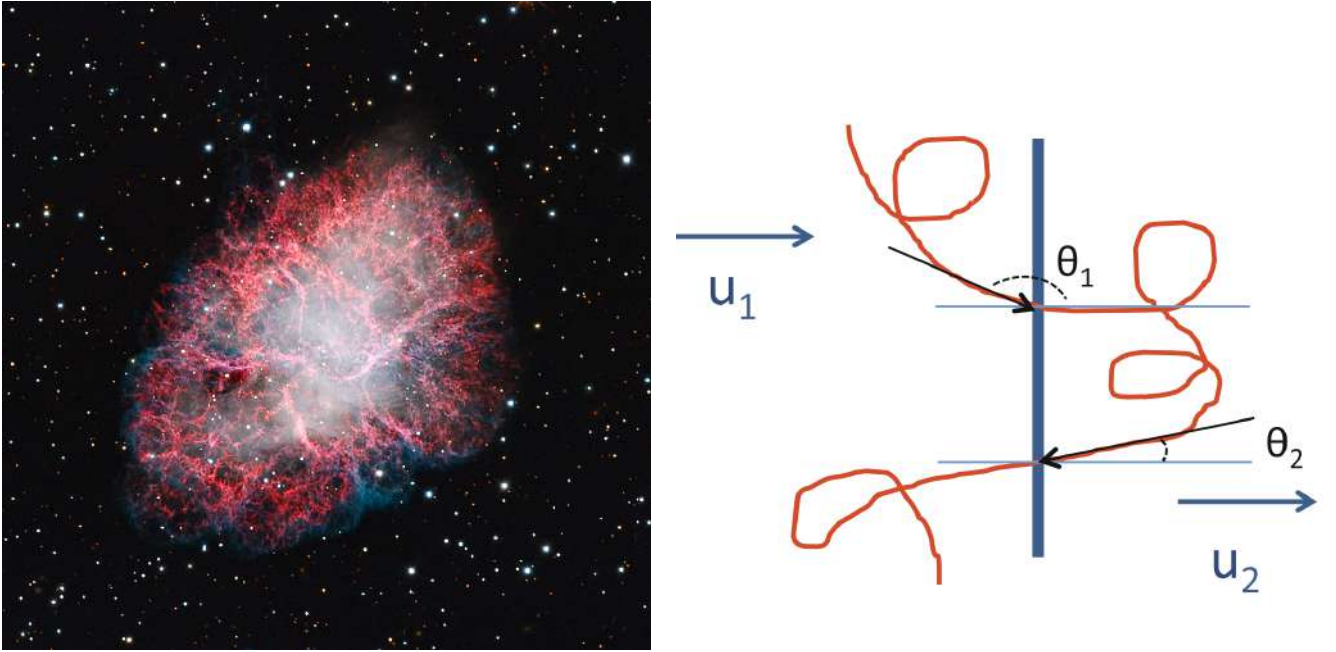


Fig. 12: Left: Crab Nebula Supernova Remnant from the Mount Lemmon SkyCenter Schulman Telescope. Courtesy Adam Block. Right: Schematic overview of the acceleration process. Vertical blue line is the shock front, red curve is CR trajectory. Fig. from [34]

to a very slow increase in particle energy. Therefore, due to all the difficulties, this mechanism cannot explain the whole energy spectrum of the CRs.

1.4.2 Diffusive shock acceleration (1st order Fermi mechanism)

In the presence of shock waves there is an acceleration on diffuse shock waves (DSA), during which the increase in energy is proportional to the 1st order of velocity β . The fundamental difference between this process and the previous one is that the directions of the shock waves are not randomly distributed, but strongly correlated - the so-called plane wave approximation [7]. Lets consider the shock wave (SW) generated by a supernova explosion, for example one like in the Crab Nebula, Fig. 12, which propagates at supersonic speed by amassing up gas and creating a region of increased density (compression factor ~ 4) with a locally flat front of the SW.

In the SW reference frame, the medium in front of the SW (upstream) penetrates the SW front at a rate of \vec{u}_1 , and the shock gas (downstream) is removed at a rate of \vec{u}_2 (Fig. 12). Thus, in the laboratory frame of reference, a particle flying into the shock front from region 1 to region 2 is in frontal collision with a high-density magnetized gas moving with velocity $V = \vec{u}_1 - \vec{u}_2$. The charged particle can undergo a large number of elastic scatterings inside this medium (due to a turbulent magnetic field), as a result of which its initial direction will change to the opposite and it will cross the SW front repeatedly.

Now the angles θ_1 and θ_2 between the initial and final direction of motion of the particle and SW, are limited by certain geometric conditions. In particular, the initial angle θ_1 is in the range from 90 to 270 degrees, and $\theta_2 \in (-90^\circ; 90^\circ)$. Omitting mathematical calculations, we can get the expression for energy change in case of such acceleration mechanism:

$$\frac{\Delta E}{E} \simeq \frac{4}{3}\beta = \epsilon \quad (11)$$

Turbulent magnetic fields on both sides of the SW cause the particle to cross the front many times. As a result, the particle gains more and more energy. In each such cycle, the particle receives a small fraction of the energy ϵ . After n cycles, the energy of the particle will be:

$$E_n = E_0(1 + \epsilon)^n \quad (12)$$

Using this fact, as well as the probability of leaving the acceleration region P_i , we can derive the relation for the energy, that has power-law form:

$$\frac{dN}{dE} \propto \left(\frac{E}{E_0}\right)^{-\gamma} \quad (13)$$

where γ is the power index:

$$\gamma = \alpha + 1 \quad (14)$$

and α can be expressed as:

$$\alpha = -\frac{\ln(1 - P_i)}{\ln(1 + \epsilon)} \cong \frac{P_i}{\epsilon} \quad (15)$$

Therefore, the Fermi mechanism predicts that the energy spectrum of the CRs demonstrate power-law behaviour, with an approximately constant value of power index. In the case of supersonic SW, power index $\gamma \sim 2 - 2.3$ [34]. In observations, the spectrum of CRs is more flat due to the effects of CR propagation in the Galactic magnetic field.

Similar to the above-mentioned Fermi mechanism of the 1st order, the linear effect of energy acceleration is also achieved in the processes of reconnecting magnetic field lines. Magnetic reconnection occurs when two magnetic fluxes of opposite polarity collide. The converging magnetic field lines annihilate on the discontinuity surface creating a so-called current sheet. The fast reconnection (reconnection with $V_R \sim V_A$) destroys the magnetic field topology and releases magnetic energy during a short period of time, which can explain explosive radiation (such as sun or star outbreaks) [36]. The acceleration of particles in the regions of reconnecting is due to the advective electric field which is created in the current sheet perpendicular to the XY plane, Fig. 13. This electric

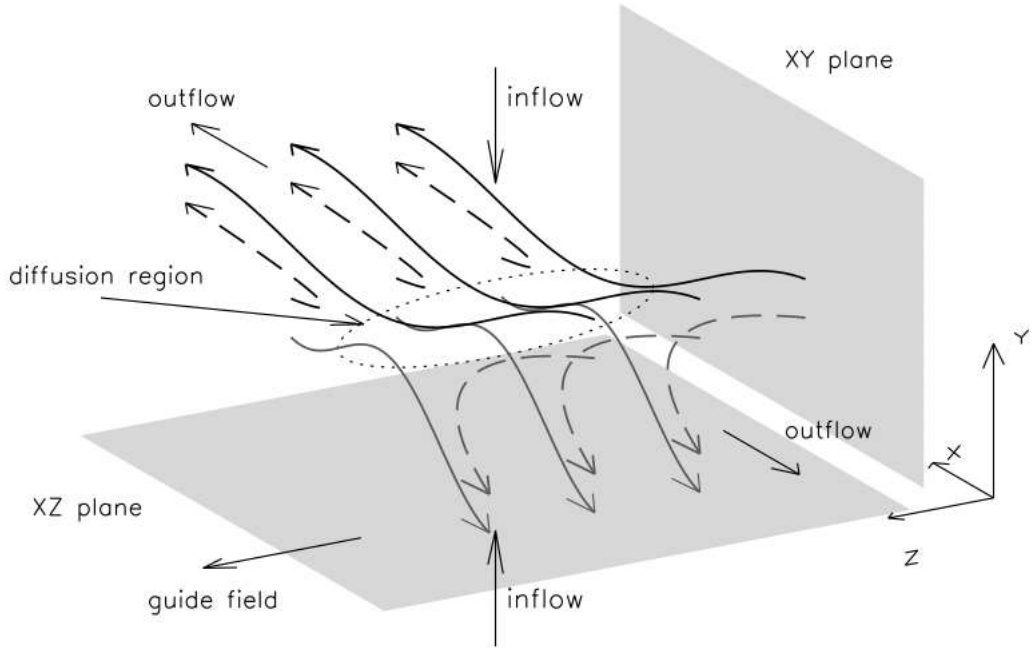


Fig. 13: Schematic 3D visualization of reconnection of magnetic field lines. In the diffusion region, the magnetic field lines are merged, and their combination (dotted lines) is ejected along the X-axis. Particle acceleration occurs in the z-axis direction). Fig. from [35].

field creates the conditions for linear acceleration along the z axis [37]. Similar to the acceleration on shock waves experienced by a charged particle trapped between perturbed (post SW) and undisturbed (pre SW) regions, [38] (model GL05) suggested that a similar mechanism could occur when a particle is between two regions with similar direction of magnetic field lines, that are merged with velocity V_R . They showed that when a particle is reflected in both directions due to frontal collisions with magnetic fluctuations in the current sheet, its energy increases by $\langle \Delta E/E \rangle \sim 8/3 \cdot V_R/c$, which provides the first order Fermi acceleration.

In some cases, in particular due to the turbulence [39], V_R may be of the order of the local Alfvén velocity V_A . In particular, in the vicinity of relativistic sources $V_R \simeq V_A \simeq c$, and therefore the mechanism of acceleration due to magnetic reconnection is even more effective [40; 41; 38]. If charged particles are accelerated in such electric fields, their spectrum is very hard. Switching of magnetic field lines is a fairly common phenomenon in astrophysical objects, and therefore it is quite expected that a significant proportion of CRs is accelerated due to this mechanism. In particular, this possibility is discussed in solar flares [42; 43], terrestrial magneto-tails [44; 45], as well as in Galactic and extragalactic systems where UHECRs are accelerated, such as the jet accreting systems [46; 40; 38; 41], in compact objects, such as AGN and gamma burst [47; 40; 48], and even in pulsar wind nebulae (PWN) [49].

Source	Magnetic field	Size	Max energy [eV]
SNR	30 μG	1 pc	10^{16}
AGN	300 μG	10^4 pc	$> 10^{21}$
Gamma burst	10^9 G	10^{-3} au	10^{21}

Tab 2: Typical values of size and magnetic fields in the potential sources of CR acceleration, as well as the maximum achievable energy [7].

1.5 Source types

CR sources must meet certain requirements in order to be able to accelerate charged particles to certain energies. The maximum possible energy of particle acceleration in the magnetic field B and in the region of acceleration of linear dimensions l can be obtained from the following considerations, that was made originally by Syrovatskii. In this work we follow Longair discussion of this problem [7]. As was mentioned above, in astrophysical sources can be produced induced electric fields, that obey Maxwell's first equation:

$$\nabla \times \mathbf{E} = -\frac{\partial \mathbf{B}}{\partial t} \quad (16)$$

If velocity of SW denotes by u , this equation can be re-expressed in such form:

$$\frac{E}{l} \sim \frac{B}{l/u} \quad (17)$$

Thus the energy of a particle with charge ze accelerated in induced electric fields is:

$$E_{max} = \int zeE \, dx = zeBul \quad (18)$$

Using this expression, it is possible to make estimates of the ability to accelerate CR in different astrophysical objects to order of magnitude. For example, taking the typical parameters of the young supernova remnant - $B = 30\mu\text{G}$, $u = 10^4$ km/s and $l \sim 1$ pc, we can determine the rough upper limit on the energy of CR accelerated in supernova remnants, e.g. $E_{max} \sim 10^{16}$ eV. Some typical values are listed in the Table 2.

If we talk about CRs with energies below 10^{18} eV, it is believed that it is mainly of galactic origin, accelerated by shock waves in various astrophysical objects, which will be discussed later in this section. However, there are still not clearly where particles with the highest energies $E \sim 10^{19} - 10^{20}$ eV can be accelerated. It is convenient to visualise expression 18 in way of diagram. The original diagram was firstly presented by Hillas in 1984, but here one can see adapted figure

due to recent astrophysical discoveries, Fig. 14. The main axes are magnetic field strength and linear size of accelerator. This figure shows only the maximum achievable energy in a particular type of source, but it is very important not to forget about the various mechanisms of acceleration, as well as energy losses in the source. The maximum achievable energy should also be limited if we can neglect collisions of CRs with background. In such case the acceleration time t_{acc} should be not only less than the time of leaving the area t_{esc} , but also less than the time of energy losses t_{loss} . Also, the shock wave may have a finite lifetime, during which the particle must have time to gain maximum possible energy. In the next sections we will discuss different types of possible sources in more detail.

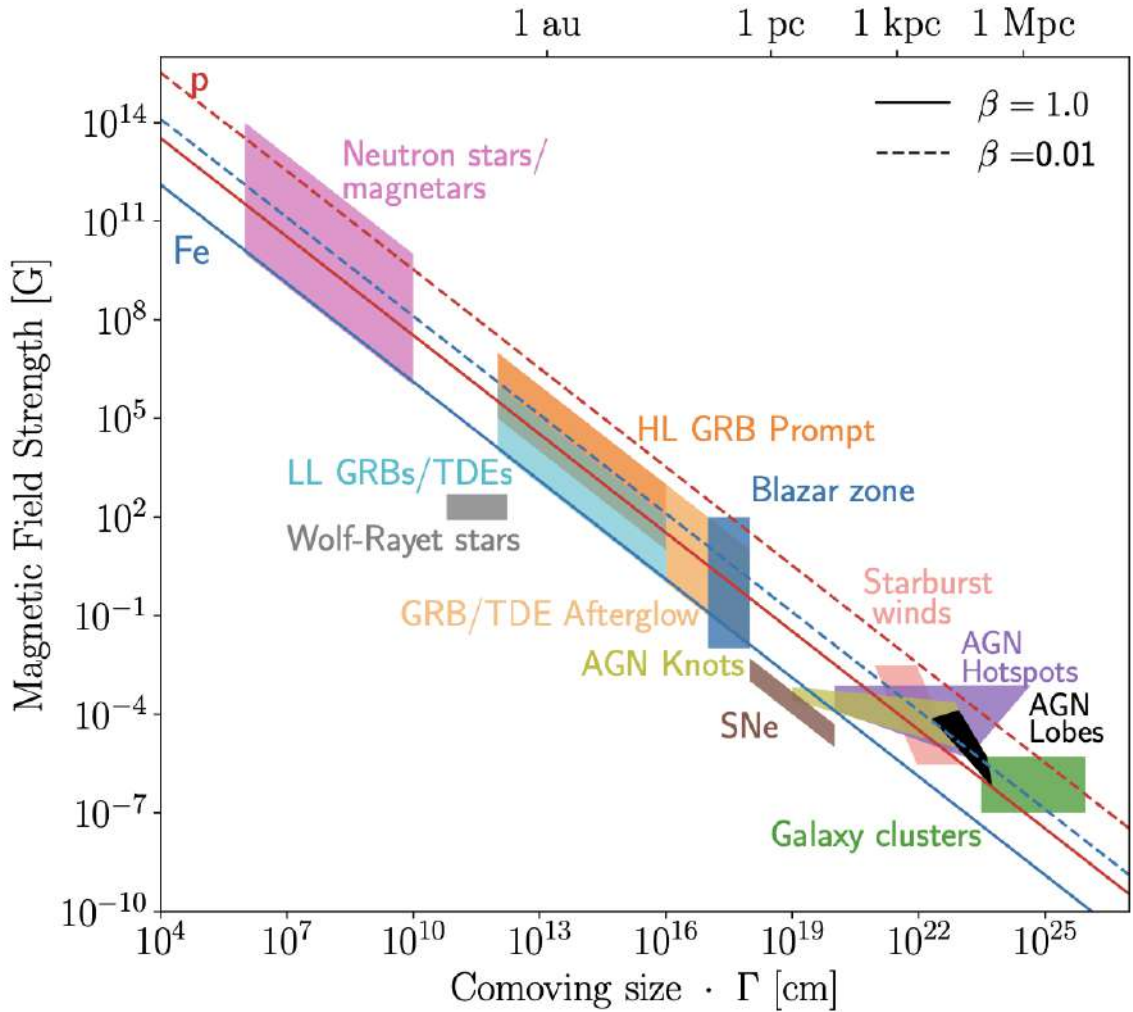


Fig. 14: The Hillas diagram represents astrophysical objects that are potential cosmic ray accelerators in a two-dimensional figure, where the linear dimensions of the accelerator are plotted on the X-axis and the magnetic field strength is plotted on the Y-axis. Maximum energy values correspond to diagonal lines can be implemented either in very large areas or in compact sources with a large magnetic field. Typical SW velocities range from $\beta \sim 1$ to $\beta \sim 1/100$. Figure from [5]

1.5.1 Galactic sources

CRs with energies above $\sim 1\text{GeV}$ must be of non-solar origin. The average energy density of the CRs should be homogeneous in most of the Galaxy. If CRs have universal feature, than they must have constant density throughout the Universe. An interesting fact is that the average energy density of CRs, ρ_{CR} , have the same order of magnitude as density of the of CMB. However, it is difficult to find any causal relationship in such an equality, so most likely it is a coincidence [34]. SNRs are one of the main candidates to the role of sources of Galactic CRs [50; 51]. On the one hand, this is motivated by the fact that the supernova shell dropped due to the explosion forms a SW with the ISM, which can accelerate CRs due to the Fermi 1st order mechanism up to PeV energies [52]. Quantitatively, this fact can be deduced from the relation 18 by substituting the typical physical parameters of the slipped of shell. On the other hand, this follows from purely energetic reasons, which will be discussed in the next paragraph.

CRs accelerated in the Galactic sources must recover those CRs that were lost as a result of their diffusive exit from the Galaxy in order to maintain the observational intensity of the Galactic CRs $j(E)$. Then the total luminosity of the CR Galactic sources must satisfy $L_{CR} = (4\pi/c_0) \int dEdVT_{res}(E)^{-1}Ej(E)$, where T_{res} is the average confinement time of a CR with energy E in the Galactic disk with a volume of V . This parameter can be determined from the average column density of ISM $X(E)$, which are traversed by Galactic CR with energy E . The interaction of primary CR particles with gas leads to the formation of different secondary grades of CR particles. After making some algebra, that can be checked in detail in the book of Sigl [34], we obtain necessary CR luminosity of Galactic sources:

$$L_{CR} \sim 1.5 \times 10^{41} \text{ erg s}^{-1} \quad (19)$$

Therefore, such luminosity of CR sources in our Galaxy would be enough to explain the observed flux of CRs. Now let's compare this value with the average kinetic energy of the shell of expelled gas. SN explosions happen about once every 30-100 years, and each of these explosions transfer to the shell about of 10^{51}erg in the form of kinetic energy. Such values give the luminosity $\sim 10^{42}\text{erg c}^{-1}$. So even if only 10% of the total kinetic energy of a supernova explosion is transformed into the energy of relativistic particles, this will be enough to explain most CRs, at least from a purely energetic point of view. These estimates were first made by Ginzburg and Syrovatsky in 1964. Taking into account the fact of observation of secondary gamma rays from this objects, one can make an assumption that SNR are the main Galactic sources of CR, at least in the energy range up to the knee.

At the moment, SNR is easily observed in the TeV range. Observed radiation are generated mainly by hadronic mechanism. This mechanism involves the interaction of accelerated protons or nuclei with the surrounding gas [53]. The corresponding cross section σ_{pp} for such reactions remains almost constant for different energies, and therefore the spectrum of secondary particles repeats the spectrum of primary ones. That is, the decay products have the same spectrum shape as the CRs from which they were formed. This fact makes gamma rays ideal candidates for studying CR acceleration sites.

The decisive test for establishing SNR as galactic sources of CRs would be the detection of neutrinos formed by the decay of charged pions, which can be formed only as a result of the above-mentioned hadronic interactions, in particular $p+p \rightarrow \pi^0 + \dots$ and $p+\gamma \rightarrow p+\pi^0$. Despite the fact that such detections are still lacking, the Fermi LAT experiment recently registered a characteristic feature of the decay of neutral pions in the gamma spectrum of two SNR - IC 443 and W44, in the range between ~ 100 MeV and ~ 100 GeV [54], which is called the pion bump. This feature is peculiar only to the decay of pions, and can not be as result of IC or bremsstrahlung, which may provide a higher flux at energies ~ 100 MeV. Fermi LAT observational data strongly suggest that these SNRs contribute to the galactic flux of CRs. In addition to SNR, there may be other galactic objects that have all the conditions to accelerate CRs. These are primarily objects with transient jets, which are described in more detail in the section 4. Binary objects with accretion disks also satisfy all the conditions to accelerate CRs, and moreover such objects are presented in our Galaxy.

1.5.2 Extragalactic sources

Active galactic nuclei According to modern theories, in the center of each galaxy is a supermassive black hole (SMBH) with mass $\sim 10^6 - 10^{10} M_\odot$. For example, in the center of our Galaxy, there is a BH with a mass of approximately $\sim 4 \times 10^6 M_\odot$, which was detected not only by the orbital motions of the surrounding stars, but even in the latest observations of Event Horizon Telescope. In about 1 % of cases, these SMBHs are active, i.e. it shows powerfull emission and have signs of accretion. Such objects are called active galaxy nuclei (AGN). As mentioned in above section, PAO observed an excess in UHECR flux in the direction of the Cen A, so this makes this radio galaxy and other similar objects as good candidates for particle accelerators. Cen A demonstrates activity also in the gamma-rays, which was detected by H.E.S.S telescopes [55]. However, this component of radiation can not be explained by interactions of electrons. This TeV gamma-rays can be generated due to the pion decay, which were produced by accelerated protons [56]. This fact is already a clear indication of the possibility to accelerate particle in the AGN [28].

Another potential site for particle acceleration near the center of AGN may be the corona of the accretion disk around central BH, where energy is transferred through the aforementioned magnetic reconnection [57].

Gamma-ray burst Another potential extragalactic sites for CR acceleration are GRBs. GRBs are one of the most powerful explosions in the Universe, that are emitting electromagnetic energy of the order of 10^{53} erg during tens of seconds. The main energy fluence is released at MeV energies, although some of the closer observed gamma-ray bursts reach hundreds of GeV, such as GRB130427A, detected by the Fermi LAT telescope [58]. The radiation flux shows variability on time scales up to milliseconds. Due to such a short time, the area of the central object should have stellar size.

In the Fireball model, optically thick plasma of leptons, photons, and baryons expands until this region became transparent for the gamma rays. Because different parts of the expansion front form shells that move at different speeds, these shells collide, generating SWs, which can accelerate particles due to 1st order Fermi acceleration. There occurs SW due to interaction of external layers with undisturbed ISM also. There are presented the corresponding calculations of the energy capability of GRBs to accelerate UHECR [34]. Here one can see the final result of estimations:

$$E_{max} \lesssim 1.6 \times 10^{21} \left(\frac{\varepsilon_0}{\text{MeV}} \right) \left(\frac{\epsilon_B}{\epsilon_e} \right)^{1/2} \left(\frac{10^{52} \text{erg s}^{-1}}{L_\gamma} \right)^{1/2} \frac{1}{f} \left(\frac{\Gamma}{300} \right)^3 \left(\frac{t_v}{0.01c} \right) \text{ eV} \quad (20)$$

As can be seen from this relation, GRBs are potentially capable of accelerating CRs to the highest detected energies.

Shock waves due to the formation of structures The formation of large structures in the Universe can lead to the formation of large-scale SW with sizes exceeding tens of MPC [59]. Such SWs form accretion fluxes and can generate magnetic fields. The maximum achievable energies of CRs in such SW depend on the size of SW. For 50 Mpc or more, the maximum energies can exceed 10^{20} eV if the average amplitude of the extragalactic magnetic field is in the region of $10^{-9} G$ [60], while the SWs themselves generate a magnetic field of the order of μG . One of the problems that arises when accelerating particles on large-scale SW is that such processes are relatively slow, and therefore accelerated particles suffer severe energy losses due to pairproduction and hadronic interaction, which significantly limits the maximum achievable energy of CRs [61].

Galaxy clusters There are observed magnetic field with an average amplitude of $5 \mu G$ and sizes up to 500 kpc in GCs [62]. According to the formula (18), such a magnetic field in such large volume can accelerate CRs to energies even above 10^{20} eV . This probability was discussed in [63] with the conclusion that the large size of such system together with the corresponding energy

losses provides the limit on the maximum acceleration energies to 10^{19} eV. Moreover, recent TA observations have recorded an excess of events with an energy of $E \geq 10^{19.4}$ eV towards the center of the Perseus Pisces supercluster [64]. The Perseus Pisces cluster is 70 Mpc away and it is the closest GC in the northern hemisphere.

Pulsars. Pulsars are presented in our and other galaxies. They are the smallest acceleration sites in the Hillas diagram 14 among those sources that can accelerate protons to energies 10^{20} eV. In such cases, in addition to the usual DSA model on the SW, direct acceleration in strong electrostatic potential generated on the surface of the neutron star, magnetic reconnection or giant flares is often taken into account. This idea has further development in the section 4.

Tidal disruption events. Stars intersecting the tidal radius of a SMBH are destroyed, and large quantity of debris starts to accrete on the central BH. If the destruction occurs outside the BH event horizon, a bright flash of thermal radiation is generated, and in some cases a jet is formed [65; 66]. So far, only a small number of TDEs with jets have been registered, while the total number of known and TDE candidates is approaching one hundred. Black holes of intermediate masses can also destroy stars due to tidal forces. Tidal compression can trigger nuclear combustion of white dwarf nuclei, leading to supernova explosions, and as a consequence the acceleration of CR up to ultrahigh energies [67; 68; 5].

1.5.3 Exotic models

In addition to the above widely accepted potential sources, there is a fundamentally different type of objects that can provide an observational flux of CR, at least in theory. This is the so-called top-down mechanism, when CRs are the products of decay of more energetic particles. In contrast to the bottom-up mechanism, where the formation of CRs is the result of acceleration from lower to higher energies. The main idea in the top-down approach is the formation of observational CRs as a result of the decay of very massive X particles with mass M_X of the order of $\sim 10^{25}$ eV.

The main difference between top-down and bottom-up models, is the flat spectrum and other chemical composition. In top-down models, massive X particles break down into a chain of all known elementary particles. As a result, the CR flux that was formed in such processes must contain much more gamma rays and neutrinos [61].

1.6 Search for sources and problems of identification

After the acceleration, CRs leave the source and move through the intergalactic and interstellar space before we detect them. The space through which CRs are moving is filled with matter,

magnetic fields, and radiation, all of which are targets for interactions with charged particles. Particles distort their trajectories due to the Lorentz force. By the time they reach the solar system, CRs lose their initial direction to the source, depending on particle energy. CR nuclei are producing secondary particles during interaction with matter and radiation. Electrons in magnetic fields are generating synchrotron radiation, and produce photons through Inverse Compton (IC) mechanism due to interaction with background light. All these processes state hard task to find sources of CRs.

1.6.1 Trajectory deflections

Faraday rotation measurements of polarisation give clear indications of the presence of magnetic fields with nonzero amplitude all throughout the Universe. Based on these measurements, certain models of Galactic (GMF) and Extragalactic magnetic fields (EGMF) are built [69; 70; 71; 72]. In the general case, the magnitude of the magnetic field in the Galaxy is several μG , and the EGMF varies between $10^{-15} - 10^{-9}$ G. Large-scale magnetic fields have a cellular structure [73]. In each such cell there are approximately equally oriented magnetic field lines, which randomly change their direction from one cell to another at a distance l_c , which is called the coherence length. The presence of magnetic fields in the universe limits our ability to directly study the sources of charged particles, as they can deflect quite strongly in such fields, Fig. 15. As one can see from left part of Fig. 15, neutrino and photons do not deflect in magnetic fields, and therefore can be good probes for indirect search of CR sources.

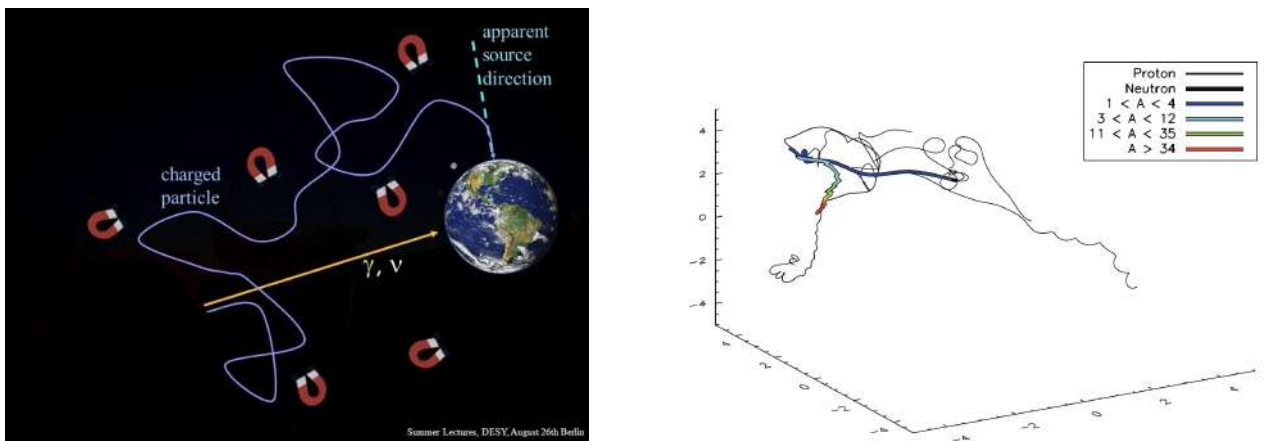


Fig. 15: Left: Sketch of CR trajectory from source to observer. It is clearly shows how much the initial direction to the source can be lost. Credit: DESY. Right: Typical CR particle trajectory with energy $10^{21}eV$ in typical values of EGMF Fig. from [34]

To estimate a deflection angles in the GMF, we can use the relation 27 from next section. For

calculations we can use the typical values of parameters $l_c \sim 10pc$, $B_{rms} \sim 5\mu G$, $d \sim 10kpc$. The value obtained in this way is approximately equal to:

$$\theta(E) \sim 0.5^\circ Z(10^{20}eV/E) \quad (21)$$

Thus, protons with GZK energies are deflected by only a few degrees, while heavier nuclei from the iron group demonstrate deflection as much as tens of degrees. From this point we can conclude that GMF completely destroys the initial trajectory of heavy nuclei after their entry into our Galaxy, which makes it impossible to directly track the direction of arrival of such CRs. This phenomenon creates the so-called magnetic lensing effect, which significantly

Large-scale EGMF is more difficult to analyze than GMF due to lower amplitude. So far, we do not have good enough experimentally proven EGMF models. But we can study the effect of such a magnetic fields on UHECR using the results of numerical modeling. The most well-known techniques in this case are the magnetohydrodynamic approach [74; 75] and the Euler hydro-N-body code [76]. In all such numerical approaches to EGMF modeling, magnetic fields roughly trace the large-scale structure of the universe, that means they are stronger in denser regions. The typical trajectory of UHECR in such simulated fields is shown on the right side of Fig. 15. As can be seen from the two figures shown above, magnetic fields have a decisive influence on the shape of the trajectory of a charged particle. Due to all-permeating magnetic fields, the apparent direction to the source of CRs is not a real direction. To take into account the effects of magnetic fields on the CRs, we can use a number of different approaches that improve our ability to track the movement of the CR. In particular, we can consider events with the highest energies to reduce influence of magnetic field. This will allow us to more confidently determine its source due to lower degree of deflection. Also, taking into account modern models of the magnetic field, it is possible to simulate the movement of a particle through them, and trace its trajectory to the source in some approximation. This method is called backward trajectories. Both of the above mentioned methods have been used in this work.

1.6.2 Energy losses

But magnetic fields are not the only problem that interrupts us from determining CR sources, but also energy losses. Moving up trough the spectrum of CRs to higher energies, various processes of energy loss starts to take effect. The creation of electron-positron pairs is a process that is beginning to play a significant role at relatively lower energies than others. A photon moving in the field of the nucleus can produce electron-positron pairs. This process has an energy threshold E_{thpp} :

$$E_{thpp} = \frac{m_e(m + m_e)}{\varepsilon} \simeq 4.8 \times 10^{17} A \left(\frac{\varepsilon}{10^{-3}eV} \right)^{-1} eV \quad (22)$$

where $\varepsilon \sim 10^{-3}eV$ corresponds to the energy value of a typical CMB target photon. The coefficient of inelasticity is very small, $\eta \sim 10^{-3}$, so the birth of pairs can be considered as a continuous process of energy loss [77].

Next lets consider the reaction of the birth of pions $N + \gamma \rightarrow N + \pi$. In CR physics this is causing so-called GZK effect. In the ultrarelativistic approximation $\beta \rightarrow 1$ the energy threshold for the nucleon N is given by a head-on collision with a photon of energy ε :

$$E_{th\pi} = \frac{m_\pi(m_N + m_\pi/2)}{2\varepsilon} \simeq 3.4 \times 10^{19} \left(\frac{\varepsilon}{10^{-3}eV} \right)^{-1} eV \quad (23)$$

As in the previous case, the main targets are CMB photons with $\varepsilon \sim 10^{-3}eV$. The GZK effect is beginning to play a significant role for UHECR. The process of birth of pions involves both electromagnetic and strong interactions. This process is the result of creation Δ -resonances when protons reach threshold energy for the birth of pions.

$$p + \gamma \rightarrow \Delta^+ \rightarrow \begin{cases} n + \pi^+ \text{ with branching ratio } 1/3 \\ p + \pi^0 \text{ with branching ratio } 2/3 \end{cases} \quad (24)$$

The inelasticity coefficient is from $\sim 20\%$ to $\sim 50\%$ depending on the interaction energy. As the energy increases, the proton will lose more of its initial energy.

Photodisintegration is another important process of energy loss for CR nuclei. This is the phenomenon of spallation of primary nucleus into lighter nuclei. Photodisintegration can be divided into two energy ranges depending on the photon energy in the rest system of the nucleus. At relatively low energies of 30 MeV, the emitting of one or two nuclei dominates, which is also called the giant dipole resonance. At higher energies, more nuclei can be emitted in one colliding [34].

On the Fig. 16 one can see the mean free path for different nuclei species. Figure takes into account all the processes of the above interactions, except the birth of pairs. It is clear from this Fig. that the mean free path for protons and iron nuclei is approximately the same at the energies $\sim 10^{20}$ eV, while the nuclei of intermediate masses move a much shorter distance without collisions.

1.7 Conclusions and unsolved problems

One of the main tasks of CR physics today is to establish the sources and mechanisms of acceleration of UHECR. Due to our technical capabilities we can only observe the arrival directions, spectra and chemical compositions of the CR flux on the Earth. However, even these observations

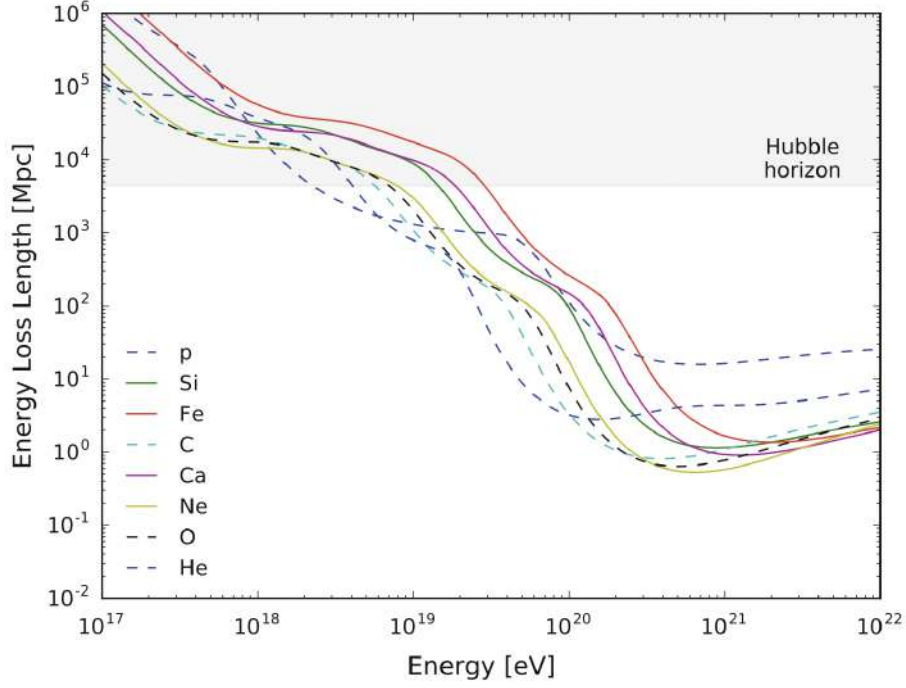


Fig. 16: Energy loss length as function of energy. This is the result of CRPropa modelling. Fig. from [34].

are somewhat distorted due to the peculiarities of the propagation of charged particles throughout the Universe. First of all, we still cannot determine the acceleration sites of UHECR due to the strong deflection of charged particles in magnetic fields. Despite the fact that PAO already registers some correlation with close extragalactic sources, other modern detectors have not yet succeeded in this field.

There are a number of approaches to solve this problem, some of which have been used in this work. In particular, I considered events only with the highest energies detected so far $E > 10^{20}$ eV. Such approach allows to minimize the influence of magnetic field because the gyroradius of particle is inversely proportional to particle energy. In some cases EHECR can reach even quasi-ballistically regime of propagation.

Another approach involves the use of modern models of the GMF and EGMF to simulate the trajectory of particle that moving through such configurations. In this work was used JF12 model of magnetic field.

But finding the initial direction of the CR arrival does not mean finding the source itself. After all, the acceleration sites of EHECR must meet certain criteria, which are also one of the unsolved problems of modern astrophysics. Indirect indications on the acceleration sites of CR are secondary emission due to the interactions of accelerated particles with the background. Therefore, the analysis of gamma and neutrino emission as well as the analysis of possibilities for observing

potential sources in this bands, play a key role in our understanding of the EHECR acceleration. The possible fluxes of gamma emission and neutrinos from the nearest large matter concentrations, such as GC Coma and Hercules was analyzed in this work. The expediency of their observations by modern and future detectors is substantiated.

Of particular value are recent indications for the possibility of transient sources to accelerate CRs to energies $E > 10^{20}$ eV. After all, such sources are also presented in our Galaxy, and therefore the particles generated by them do not have time to be strongly deflected by magnetic fields, and are at distances less than GZK cut-off. In this work, one of such objects - the magnetar SGR1900+14 - was studied in detail, and models of its evolution and radiation were built.

2 Potential sources of ultra-high energy cosmic rays

2.1 Introduction

Determining the nature and origin of UHECRs is one of the outstanding challenges in cosmic ray physics. The high degree of isotropy of the observed UHECR intensity, caused primarily by the deviations of the UHECR trajectories in EGMF and GMF, as well as the significant uncertainty in their chemical composition (atomic mass), make it impossible to trace the observed events to their sources and determine the mechanisms for their acceleration. There are two techniques to lessen the effect of magnetic deflection: taking into account EHECR events and contemporary models of the GMF to adjust its effect on the EHECR trajectory. In this study, the effect of Galactic and random extragalactic magnetic fields is accounted for when adjusting the observed arrival directions of EHECRs from PAO and TA detector data. New celestial positions of EHECRs are compared to samples of potential sources used by the PAO, including 17 AGN with powerful gamma-ray emission (from the 2FHL catalog) and 23 SBGs (radio-flux-selected), as well as samples of 42 radio-galaxies from a parameterized catalog of radio-galaxies and magnetars. Taking into account the energy loss length of the nuclear component (H, He, C, Si, Fe) of EHECRs in the extragalactic environment and the expected typical distances to potential sources (~ 100 Mpc for H and Si-Fe and ~ 50 Mpc for He and C), the astrophysical objects that could be sources of relevant events were identified. The probable acceleration processes in the selected objects are investigated, as well as the contribution of hypothetical Galactic sources to the observed EHECR flux.

The distribution of matter in the Local Universe (up to ~ 100 Mpc), especially in the region of the Virgo supercluster (~ 20 Mpc), is very heterogeneous and includes all elements of the large-scale structure: galaxies and their clusters, superclusters, filaments, layers, and voids. It is expected that the distribution of the EGMF corresponds to the distribution of the density of baryonic matter. EHECRs from extragalactic sources undergo significant deviations in the EGMF, making it difficult to find their sources. In addition, UHECR flux is suppressed due to the photodisintegration of nuclei during interaction with background microwave and infrared radiation. In this section was evaluated the influence of these factors on the propagation of UHECR particles from sources in the Local Universe, in particular, the mean free path and the magnetic deviation of H(p), He, O, Si, and Fe nuclei are studied. For potential sources of EHECR in the Local Universe, the types and energies of nuclei that can reach the Earth and at the same time maintain the connection of the arrival directions with the position of the source within ~ 1 rad

have been estimated.

2.2 State-of-the-art problems in UHECR physics

In recent years, astronomy has experienced revolutionary changes: the detection of gravitational waves from merging black holes and neutron stars in binary stellar mass systems laid the foundation for gravitational-wave astronomy as a new branch of experimental astronomy and opened a new era of multimessenger astronomy, i.e., observation of astronomical objects in channels of electromagnetic and gravitational radiation. The observation of high-energy ($E = 270$ TeV) neutrinos with spatial and temporal reference to the gamma-ray burst of blazar XS 0506+056 (redshift $z = 0.34$) ushered in the era of high-energy neutrino astronomy (only neutrinos from the Sun and the supernova SN1987A with energies on the order of several MeV had been detected until then). At the same time, cosmic ray astronomy (with the exception of solar cosmic rays) is still waiting to be developed. CRs are high-energy particles that enter the Earth's atmosphere at kinetic energies significantly exceeding their rest energy (~ 1 GeV for a proton) with a quasi-power-law energy spectrum $F(E) = kE^{-\gamma}$, where the exponent $\gamma = \gamma(E)$ depends on the energy and varies between 2.6 and 3.2 [78]. In the energy range $E \geq 4 \times 10^{19}$ eV, there is a sharp decrease in the CR flux, which may be due to the aforementioned GZK cut-off due to the interaction of the proton component with the cosmic microwave background [79; 80; 78] or a physical restriction on the maximum attainable energies in space accelerators (so far, the upper energy limit is still determined by CR detected in 1993 with an energy of 3.2×10^{20} eV [81; 82]).

The main reason why astrophysical objects that are the sources of CRs have not yet been determined is associated with the deviation of trajectories to the extent of diffusion propagation of charged CR particles in the GMF and EGMF. The observed CR flux with energies up to 10^{18} eV can provide the acceleration of ISM particles at shock fronts of Galactic supernova remnants through the first-order Fermi mechanism [78; 83]. However, UHECRs are not captured by the GMF [84] and should be accelerated in extragalactic sources [85; 78; 86]. Potential extragalactic sources of UHECRs include AGN [59; 87], cosmological GRBs [88; 89; 90], SBGs, [84; 91], newborn millisecond pulsars and magnetars [92; 93; 94], phenomena of tidal disruption of stars in the gravitational fields of supermassive black holes [87; 95], and magnetar giant flares (also observed in our Galaxy) [96].

The search for UHECR sources is complicated by the difficulties with finding the atomic mass of particles entering the atmosphere from the results of observations of EAS generated by them, in particular, from the estimates of the average depth of the shower maximum $\langle X_{max} \rangle$ and its

fluctuations σX_{max} . The Auger data indicate that the average mass $\langle A \rangle$ decreases with increasing UHECR energy to $\log(E/\text{eV}) \approx 18.3$ until the dominance of light elements (H + He) and further increases to $\langle \ln A \rangle \approx 2 - 3$ (C-N-O) in the last bin of the FD-spectrum, $\log(E/\text{eV}) = 19.7 - 19.8$ (35 events) [97; 98]. At the same time, the TA data on $\langle X_{max} \rangle$ and σX_{max} are consistent both with the dominance of light elements for all UHECRs in the QGSJET II-04 hadron interaction model and with the contribution of heavy nuclei, in particular, 75% H + He, 17% N, 8% Fe [99].

2.3 Influence of ISM and IGM on the propagation of UHECR, energy losses

Significant energy losses, mainly due to the photodisintegration of complex nuclei and photopionic loss of protons (GZK- cutoff of the spectrum), limit the distance to astrophysical sources of EHECRs to 100 Mpc. On the other hand, a decrease in the distance to the sources with an increase in the EHECR energy significantly reduces the influence of the extragalactic magnetic field on the deviation of their trajectories, increasing the fraction of observed events that have preserved a correlation with the source.

The main processes of energy loss for protons and heavier nuclei are the birth of pions and photodisintegration, respectively. This is manifested in the spectrum cut-off at energies above $10^{10.6} \text{GeV}$. If the interaction energy in the CMS exceeds $\epsilon_{thr} \approx 140 \text{MeV}$, the process of pion formation occurs, as a result of which protons lose energy [15; 16]. Such processes lead to a reduction in the initial number of accelerated CR nuclei that have left the source, and therefore the observer on Earth cannot detect particles accelerated in sufficiently distant sources. The distances to potential sources from which CR can reach us depend on the charge number and significantly limits the EHECR ranges, limiting the distance to potential sources to values on the order of 100 Mpc for protons and heavy nuclei (Si, Ca, Fe) and to 50 Mpc for intermediate nuclei (He, C-N-O), taking into account their secondary origin from the photodisintegration of heavier nuclei. On the Fig. 17 is demonstrated energy loss length for protons and iron nuclei in the radiation field with energy $\epsilon_0 = 1 \text{meV}$ and number density $n_0 = 400 \text{cm}^{-3}$, which corresponds to the monochromatic approximation of CMB [100]. In the case of photodisintegration, the stripped nuclei Ni(Ai, Zi) will have the Lorentz factor of the initial nuclei $N0(A0, Z0)$ and energy $E(\text{Ni}) = (\text{Ai}/A0)E(A0)$ (for iron $\text{Fe}(56.26)$, $E(\text{Ni}) = (\text{Ai}/56)E(\text{Fe})$) [101; 102; 103; 104].

Deviation of UHECR in magnetic fields also leads to time delays relative to the ballistic trajectory of the light beam, which can be estimated as [105]:

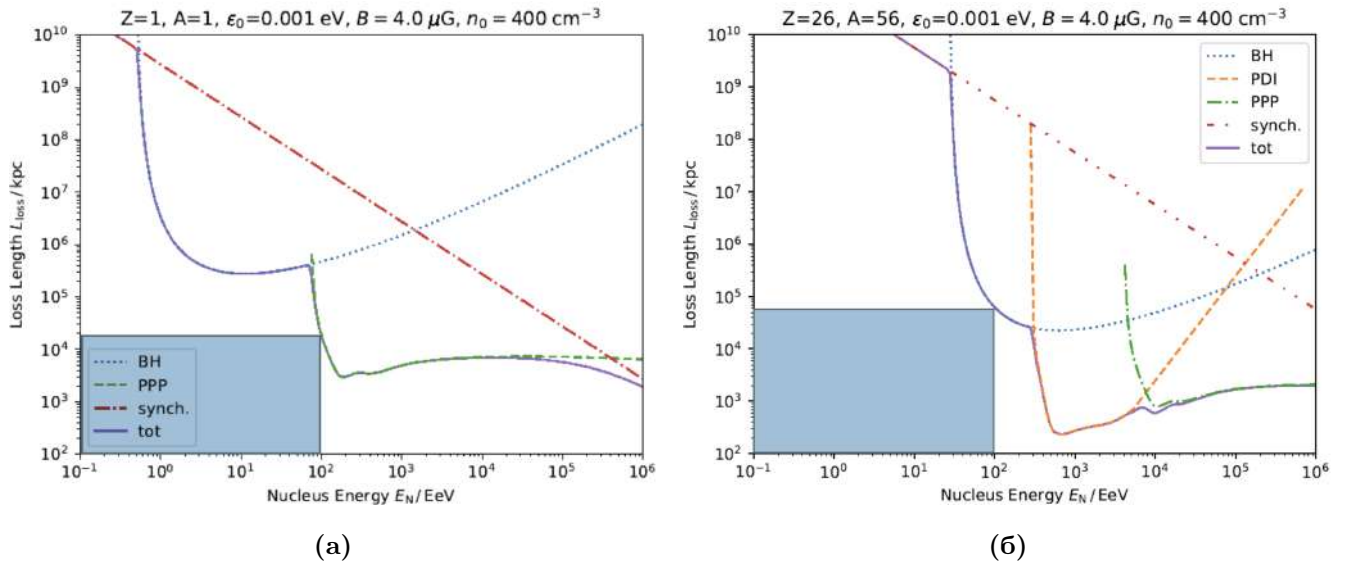


Fig. 17: Energy loss length for $Z=1$ (right) and $Z=26$ (left). Blue region denotes loss length for respective nuclei with energy $E = 10^{20} \text{ eV}$. Figure adapted from [100]

$$\tau(E, d) \simeq 1.5 \times 10^3 Z^2 \left(\frac{E}{10^{20} \text{ eV}} \right)^{-2} \left(\frac{d}{10 \text{ Mpc}} \right)^2 \left(\frac{l_c}{1 \text{ Mpc}} \right) \left(\frac{B_{\text{rms}}}{10^{-9} \text{ G}} \right)^2 \text{ years} \quad (25)$$

The phenomenon of such a time delay has interesting consequences for the acceleration of CR in transient sources that show a variability shorter than the parameter $\tau(E, d)$. The spectrum of such sources will be strongly distorted, showing peaks at higher energy values, which are not present in the real spectrum of the source. This will be due to the fact that high-energy particles propagate quasi-ballistically and reach the observer much earlier than less energetic ones, which diffuse in the magnetic fields and are therefore registered later. This can be especially actual for GRBs or magnetar giant flares [34].

2.4 Model of Galactic and extragalactic magnetic fields

To model the magnetic field of the Galaxy, in this work was used the Jansson&Farrar 2012 model (JF12), which is based on an analytical approximation of observations of the Faraday rotation of synchrotron radiation in the Galaxy plane [69]. GMF is presented in the form of two independent contributions - regular and random. The regular GMF, in turn, consists of the magnetic field in the disk and the halo, as well as X-components. The random GMF is represented by contributions from the disk and the halo. During calculations of backward trajectory of CR, was determined the contribution from each of the above components.

Fig. 18 demonstrates magnitude of different components of Galactic magnetic field. Left and right panel can provide the comparison of disk component of the random field (left panel) versus

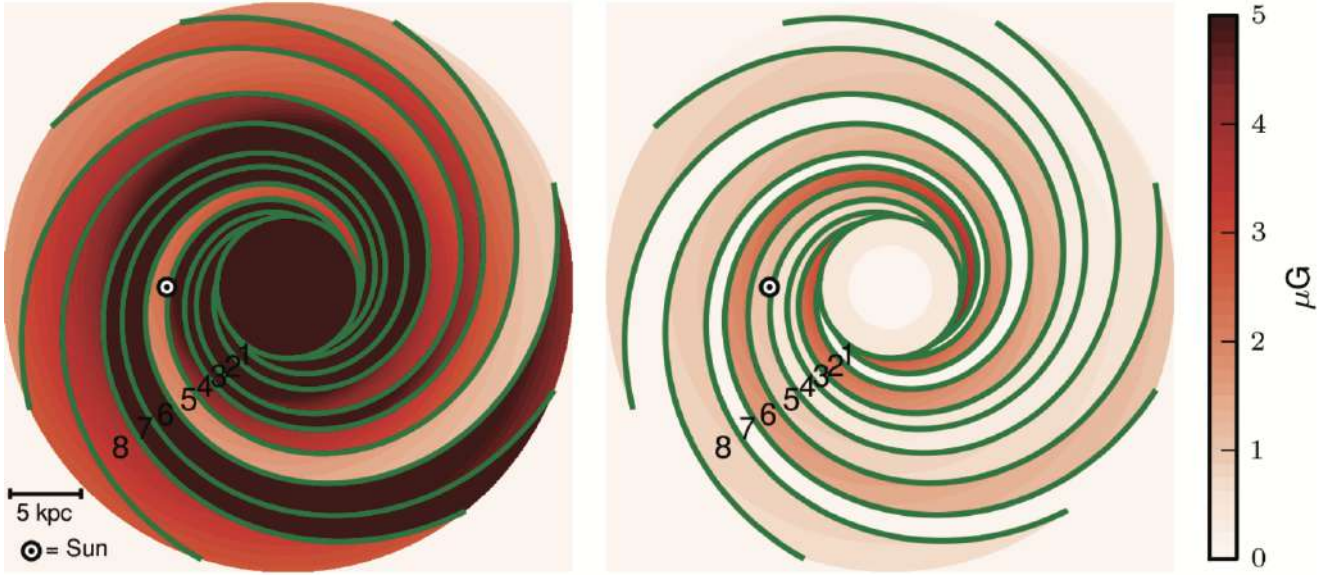


Fig. 18: Left: random component of Galactic magnetic field in the spiral arms. Right: regular component of Galactic magnetic field in spiral arms. Fig. from [70].

coherent disk field (right panel). The average rms strength for random disk component is around $6.6 \mu\text{G}$, but it depends on considering different arms. Every number on the scheme denotes separate region with separate values of magnetic field. The strength of disk component strongly varies from arm to arm. In general case magnitude of random component is higher than regular. In this work was considered deflection in random Galactic magnetic field as smearing circles with opening angle Θ_{random} :

$$\Theta_{random}^2 = \frac{2}{9} \left(\frac{Ze}{E} \right)^2 l_c \int B^2 dl \quad (26)$$

For regular component was used more complicated analysis. I traced backward trajectory of the particle through the different configuration of magnetic field in every arm and took into account orientation and strength of respective magnetic field contribution.

But before entering our Galaxy, CR particles are moving through the IGM that are permitted by EGMF. There are several models that describes the nature of such fields, their distribution and magnitude. Distribution of EGMF should trace density profile of barionic matter because of frozen-in effect. The lowest values of magnetic field in voids are determined either by primordial field $B_{void} \leq 10^{-9} \text{G}$, that was generated in the earliest Universe, or by contribution of Galactic wind $B_{void} \leq 10^{-12} \text{G}$. Typical values of magnetic field that are observing inside GC are $B \sim 10^{-6} \text{G}$. Therefore upper border for the fields inside filament and voids are $B_f \leq 10^{-8} \text{G}$ and $B_{void} \leq 10^{-9} \text{G}$, respectively [72].

In this work averaged rms strength of EGMF was taken as 10^{-10}G and with coherence length

as $l_c = 1\text{Mpc}$ [72]. The CR particle that are moving in such fields will change its direction to the value that depends on distance and energy of particle.

The magnitude of deflection of extragalactic CRs in magnetic fields is still not clearly known. But one can use some analytical approximations. For example, in the non-resonant scattering regime ($r_g \gtrsim l_c$) and in the approximation of small angles of deviation $\theta(E, d) \ll 1$, the root-mean-square angle of deflection of a CR with energy E and charge Ze after passing distance d is calculated according to [34]. The final angle of deflection can be calculated as:

$$\theta(E, d) \simeq 0.8^\circ Z \left(\frac{E}{10^{20}\text{eV}} \right)^{-1} \left(\frac{d}{10\text{Mpc}} \right)^{1/2} \left(\frac{l_c}{1\text{Mpc}} \right)^{1/2} \left(\frac{B_{rms}}{10^{-9}\text{G}} \right) \quad (27)$$

In this case, the angle of deflection is formed due to random movements with a step length $\sim l_c$, and the contribution from different cells is added quadratically.

Therefore, CRs of extragalactic origin on their way to us are deflected in various types of magnetic fields. Firstly their trajectories are distorted in weak, randomly oriented EGMF. But due to long distance of travel in such fields, the effect of distortion accumulates and can become significant. After entering our Galaxy, CR particle enters complicated configuration of GMF. This fields are stronger than intergalactic, and only particles with the highest energies can move quasi-ballistically in such fields.

2.5 UHECRs in the Local Universe

First of all was decided to consider more general approach for the search of potential sources of UHECR. The observed isotropy of the UHECRs flux indicates the dominance of the extragalactic component of the UHECRs and the significant deviation of the UHECRs trajectories in the EGMF up to the diffusion mode of their propagation, when the distance to their sources significantly exceeds the mean free path (scale of dispersion) of the UHECR in the EGMF [72]. However, for UHECR, which are at the top of the energy spectrum of cosmic rays (the maximum energy of detected cosmic rays is equal to $E = 3 \cdot 10^{10}$ eV) and for cosmologically close sources - in the Local Universe (LU, up to ~ 100 Mpc) - it can be expected, that their motion through EGMF should have no time to enter the diffusion regime. That means that we can expect so-called ballistic regime in this case, when the deflections of the UHECR trajectories in the EGMF will not be too large and the directions of their arrival on the celestial sphere will correlate with the positions of the sources within $\sim 1\text{rad}$ ($\sim 57^\circ$). Therefore, one of the most promising method in the search for UHECR sources, is searching for correlations of the arrival directions of UHECR with potential extragalactic sources in the Local Universe.

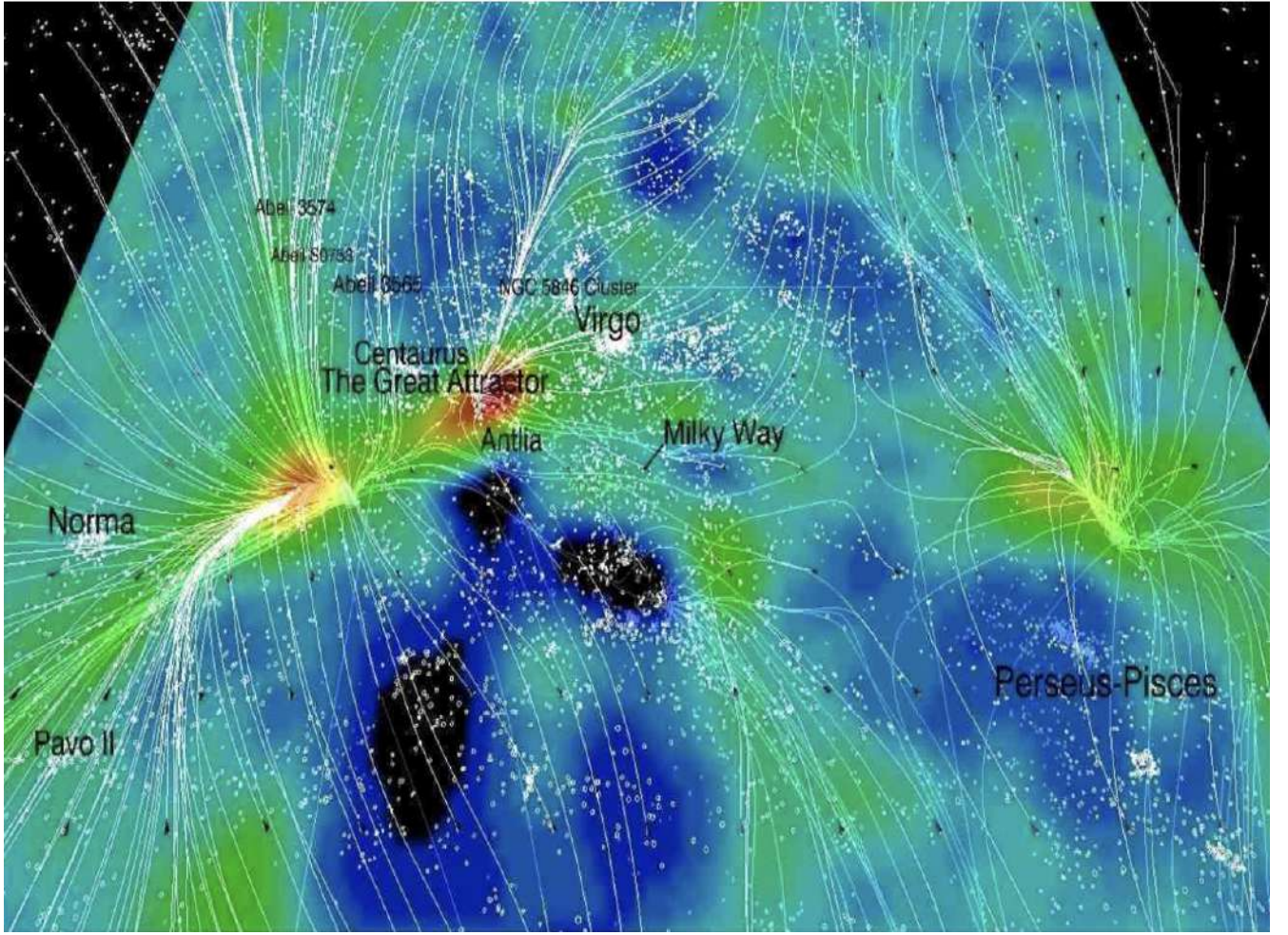


Fig. 19: Large-scale structure of the Local Universe based on the Wiener filter analysis. White dots locate galaxies from the V8k catalog that lie within considered slice $SGZ=0$. White lines identify streamlines of motion and colors means overall density with a progression from blue in voids to red in the regions of highest density. Fig. from [106]

The distribution of matter in the Local Universe, in particular in the region of the Virgo Supercluster (VSC), is highly heterogeneous and includes all elements of the large-scale structure: galaxies and their clusters, superclusters, filaments and sheets (in particular, Local Group resides in the Local Sheet, which in turn are part of the Local Filament, low density regions - voids [107; 108]. The distribution of potential sources of UHECR - AGN, SBGs, and the distribution of magnetic fields in the LU should follow the distribution of baryonic matter. LU is dominated by the Great Attractor (GA, 80 Mpc), Perseus-Pisces Supercluster (PPS, 70Mpc) and VSC (16.5 Mpc), Fig. 19 [109; 107; 106]. In order to estimate the prospects of detecting UHECR from potential sources in the LU, in this work was estimated the characteristics of different nuclei types in CR flux that can reach the Earth, and at the same time can maintain the connection of the arrival directions with the position of the source within ~ 1 rad.

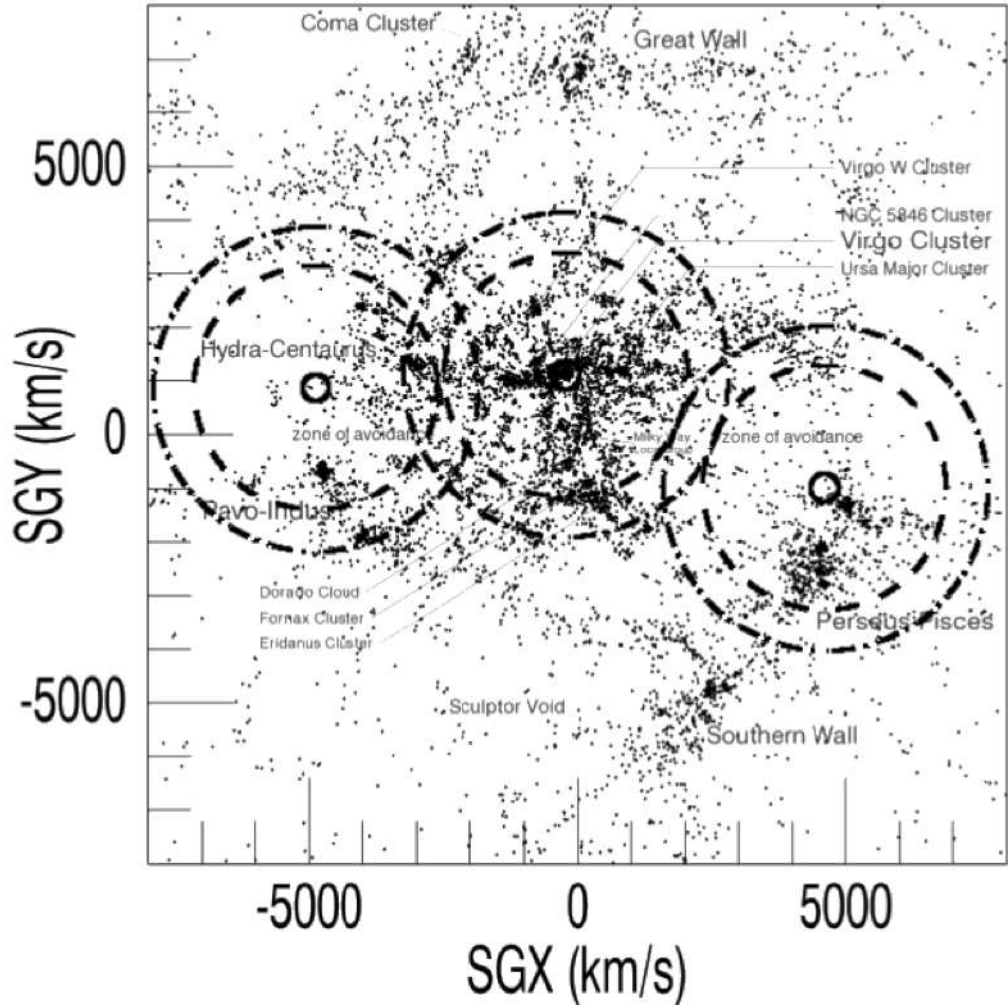


Fig. 20: Large-scale structures of the Local Universe and mean free path for EHECR in the IGM for representative groups of nuclei O (solid line), Si (dashed line), Fe (dashed-points line). Distances in the units $1 \text{ Mpc} = 100h^{-1} \text{ km/s}$. Figure adapted from [106]

I calculated expected angles of deflection for UHECRs from this element of large-scale structure in the Local Universe, using EGMF model described in the section 2.4. Results for this angles are presented in the Table 3. We are assuming that UHECRs still preserve a connection with the source of their acceleration if their deflections do not exceed $\sim 1 \text{ rad}$, i.e., the condition for entering the diffusion regime.

2.5.1 Large-scale structure of the Universe

Local Universe - the region $\sim 100 \text{ Mpc}$ around our Galaxy - is about twice the size of the average distance between GCs (GCs - the largest gravitationally bound systems in the Universe), so it contains all the typical elements of the large-scale structure of the Universe. At its smallest scale, our Galaxy and its distant counterpart, M31 (the Andromeda Nebula, 770 kpc), along with several

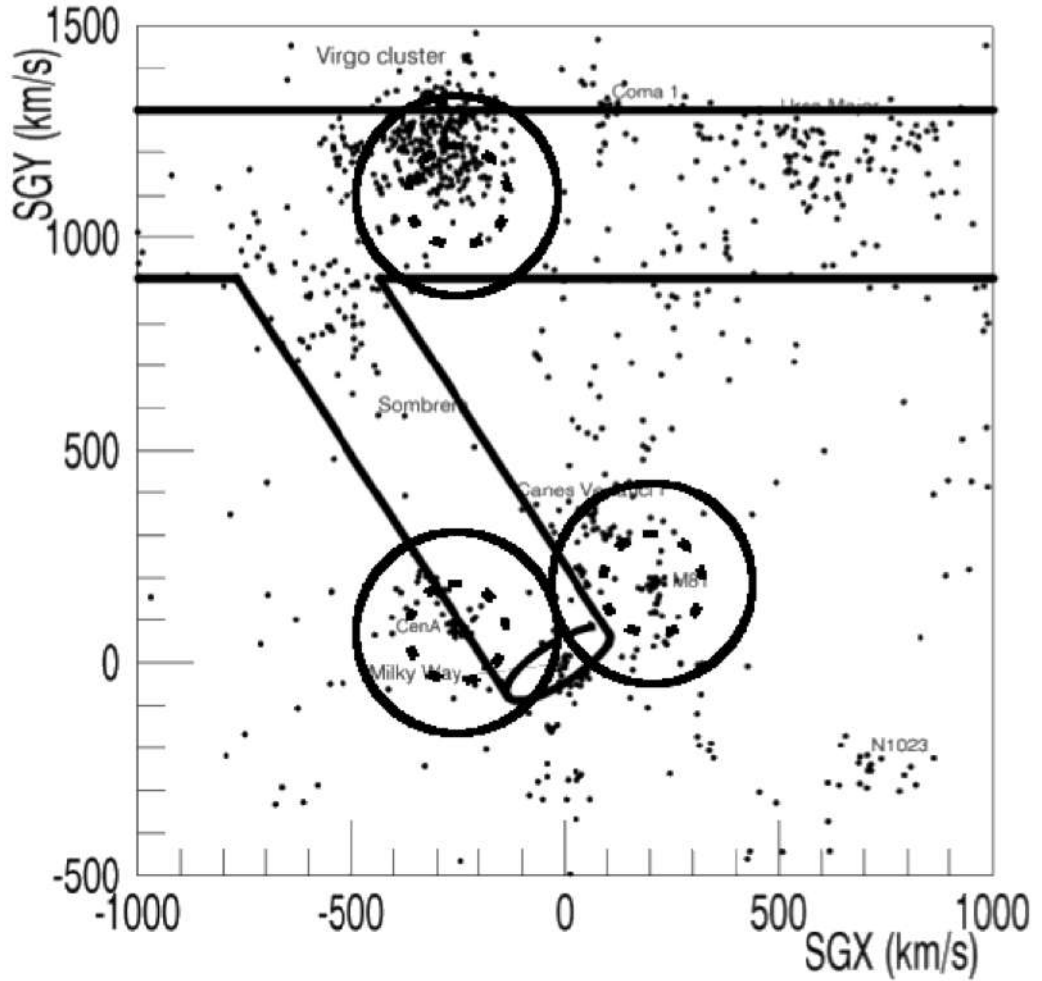


Fig. 21: Virgo cluster together with Local filament and mean free path for CR. Solid line denotes Oxygen (for $E = 10^{19}$ eV) and dashed for He. Distances in the units $1 \text{ Mpc} = 100h^{-1} \text{ km/s}$. Figure adapted from [106]

dozen dwarf galaxies, forms the Local Group of galaxies. Together with similar groups of galaxies Centaurus A/M83 ($\sim 4 \text{ Mpc}$) and M81 ($\sim 3.6 \text{ Mpc}$, contains M81 and M82), and some others, the Local Group is included into the Local Sheet – a pancake-like concentration of galaxies with radius - $\sim 5 \text{ Mpc}$, and thickness - $\sim 1.5 \text{ Mpc}$ [108; 110]. The Local Sheet is a part (thickening) of the Local Filament - a cylindrical region (radius $\sim 2 \text{ Mpc}$) of increased concentration of galaxies, which stretches from the Fornax cluster to the Virgo cluster and “flows in” (along the Local Filament there is a real flow of plasma of the IGM) into a more powerful filament, which includes the Virgo cluster and connecting the two largest concentrations of matter in the LU - the GA (at a distance 80 Mpc from the LG) and the PPS (70 Mpc from the LG). At the same time, the Virgo GC forms the central part of the Virgo Supercluster (radius 20 Mpc), on the periphery of which resides the LG [107; 109].

As already mentioned above, the extragalactic potential sources of UHECRs - AGN and SBGs - will be more often found in regions of increased baryon concentration, in our case we expect the presence of potential sources of UHECRs in the Virgo cluster (closest mass concentration) and in the Great Attractor and Perseus-Pisces superclusters (highest concentrations masses in the Local Universe).

2.5.2 Expected characteristics of UHECR from potential sources in the Local Universe

EGMF weaken or even suppress UHECR fluxes from distant sources due to a significant deflection of their trajectories, without changing the energy of the UHECR themselves. At the same time, UHECR lose energy when interacting with photons of intergalactic background radiation (mainly CMB and infrared). At the characteristic length $\Lambda = c \cdot \tau_{interaction}$ of energy loss by protons or nuclear photodisintegration, the intensity of the UHECR flux decreases by a factor of e , so that for a source at a distance D the optical thickness of the intergalactic medium will be equal to $\tau = D/\Lambda$, and the initial intensity of the flux will decrease by a factor of $\exp(-\tau)$, from the expression 28.

$$I = I_0 \exp\left(-\frac{D}{\Lambda}\right) \quad (28)$$

We will assume that UHECR from sources in the Local Universe can be registered (can reach the Earth) when the intensity of the flux decreases by no more than $\exp(-2)$ (when $\tau < 2$), and are identified with the source when their deviations in the EGMF do not exceed 1 rad (see Table 3) and (Fig. 20 - 21).

The two main processes that accompany the propagation of UHECR in the IGM – deflection of UHECR trajectories up to the diffusion regime and energy loss/photodisintegration due to interaction with background electromagnetic radiation – hide the astrophysical sources of observed UHECRs in the Local Universe. If we introduce the criterion that promising sources for the observed UHECRs will be those from which the UHECRs deviate in the EGMF by no more than 1 rad and for which the optical thickness of the intergalactic medium does not exceed 2, then for the representative light groups (H (Z=1), He(Z=2)), intermediate (O(Z=8), Si(Z=14)) and heavy (Fe(Z=26)) nuclei from the data in Table. 3 we can draw the following conclusions:

1. Virgo Cluster - among UHECRs with energies $E = 5 \cdot 10^{19}$ eV, that are moving through the void with typical characteristic of magnetic field, the most promising one for detection are nuclei of H (protons), O, Si, Fe. For higher energies $E = 10^{20}$ eV we are losing information

Potential sources	Characteristics of UHECR	H(p)	He	O	Si	Fe
UHECR	$E = 5 \cdot 10^{19}$ eV					
Virgo A + void	Angle of deflection (deg)	2.1	4.1	16.4	28.8	53.4
	Optical depth	0.01	5.5	0.8	0.4	0.3
Virgo A + Local Filament	Angle of deflection (deg)	14.5	29	116.2	>180	>180
	Optical depth	0.01	5.5	0.8	0.4	0.3
Great Attractor	Angle of deflection (deg)	4.2	8.5	33.9	59.3	110.1
	Optical depth	0.07	>10	3.5	1.5	1.3
Perseus-Pisces	Angle of deflection (deg)	3.9	7.8	31.3	54.9	101.9
	Optical depth	0.06	>10	3	1.3	1.1
	$E = 10^{20}$ eV					
Virgo A + void	Angle of deflection (deg)	1.1	2.1	8.2	14.4	26.7
	Optical depth	0.1	>10	>10	1.2	0.8
Virgo A + Local Filament	Angle of deflection (deg)	7.2	14.5	58.1	101.7	>180
	Optical depth	0.1	>10	>10	1.2	0.8
Great Attractor	Angle of deflection (deg)	2.1	4.2	16.9	29.6	55
	Optical depth	0.4	>10	>10	5.4	3.7
Great Attractor	Angle of deflection (deg)	1.9	3.9	15.7	27.4	50.9
	Optical depth	0.4	>10	>10	4.6	3.1

Tab 3: Characteristic of UHECR from potential sources in Local Universe

about O. But if we consider the case of UHECR propagating in the Local Filament with higher value of magnetic field, we can expect sufficient detectable conditions only for protons.

2. Great Attractor - for energies $E = 5 \cdot 10^{19}$ and $E = 10^{20}$ eV only protons are promising nuclei for detection on the Earth.

3. Perseus-Pisces Supercluster - among UHECR with energies $E = 5 \cdot 10^{19}$ eV the most promising ones are H and Si. Only protons remains for energies $E = 10^{20}$ eV.

2.6 EHECRs observed by detectors PAO and TA

At present, UHECRs are mainly detected by the two largest facilities: PAO array in the Southern Hemisphere [111] and TA in the Northern Hemisphere [112]. Despite the rich observational material, no reliable data have yet been obtained regarding the correlation between the UHECR arrival directions and potential sources. The Auger detector registered only the dipole component of large-scale anisotropy with an amplitude of 6.5% in the distribution of UHECRs with an energy $E > 8$ EeV [113], while the TA detector registered a harder UHECR spectrum of the polar region of the celestial sphere ($24.8^\circ < \delta < 90^\circ$) in comparison with the spectrum of the equatorial region ($-16^\circ < \delta < 25.8^\circ$): the spectrum breaks at $lg(E/eV) = 19.85 \pm 0.03$ and $lg(E/eV) = 19.59 \pm 0.06$, respectively [114]. At medium angular scales, both detectors registered “hot spots” (using different minimum energies of samples to equalize the total UHECR fluxes: $E_{TA} \geq 53.2 EeV$, $E_{PAO} \geq 40 EeV$) in their respective hemispheres: in a 15° -radius circle around $\alpha = 9^h 30^m, \delta = +54^\circ$, and in a 20° -radius circle around $\alpha = 12^h 40^m, \delta = -50^\circ$, at the levels of 1.5σ and 2.2σ , respectively (post-trial significance, [113]).

At small angular scales, a search is conducted for correlations between the UHECR arrival directions and the celestial coordinates of potential sources of various classes. The analysis of the 15-year Auger data series revealed a significant correlation with samples of starburst galaxies, γ -AGN, and galaxies from the Swift-BAT and 2MRS catalogs 4.5σ , 3.1σ , 3.7σ , 3.72σ respectively, for UHECRs with $E \geq 40$ EeV at an angular distance $\theta \leq 15^\circ$ from potential sources) along with excess events around the AGN Cen A and starburst galaxy NGC 253 [115].

As noted above, the main reason for the loss of correlation between the arrival directions of UHECRs and their sources is the deviation of the trajectories of charged particles, which make up the vast majority (if not all) of CRs in extragalactic and Galactic magnetic fields. For this reason, we examine in our study potential sources of the EHECRs, that was detected by the Auger and TA detectors, for which the above correlations with potential sources become insignificant [115], and there are no reliable estimates of chemical composition [99; 97; 98].

The published data of EHECR observations with the coordinates of the events include only six such events for Auger (from January 2004 to March 2014) [116] and ten events for TA (from May 2008 to May 2014) [32; 117]. The number of the TA events exceeds the Auger data despite a significantly smaller total aperture ($5400 \text{ km}^2 \text{ sr year}$ for TA and $51753 \text{ km}^2 \text{ sr year}$ for Auger); this is due to systematic errors in determining the energy of detected events in each of the detectors (14% in Auger and 21% in TA). A comparative analysis of the UHECR spectra from the Auger and TA detectors requires a systematic shift of the UHECR energies by $+5.2\%$ for Auger and -5.2% for TA up to 10^{19} eV and a further energy-dependent systematic shift of 10% for Auger and -10%

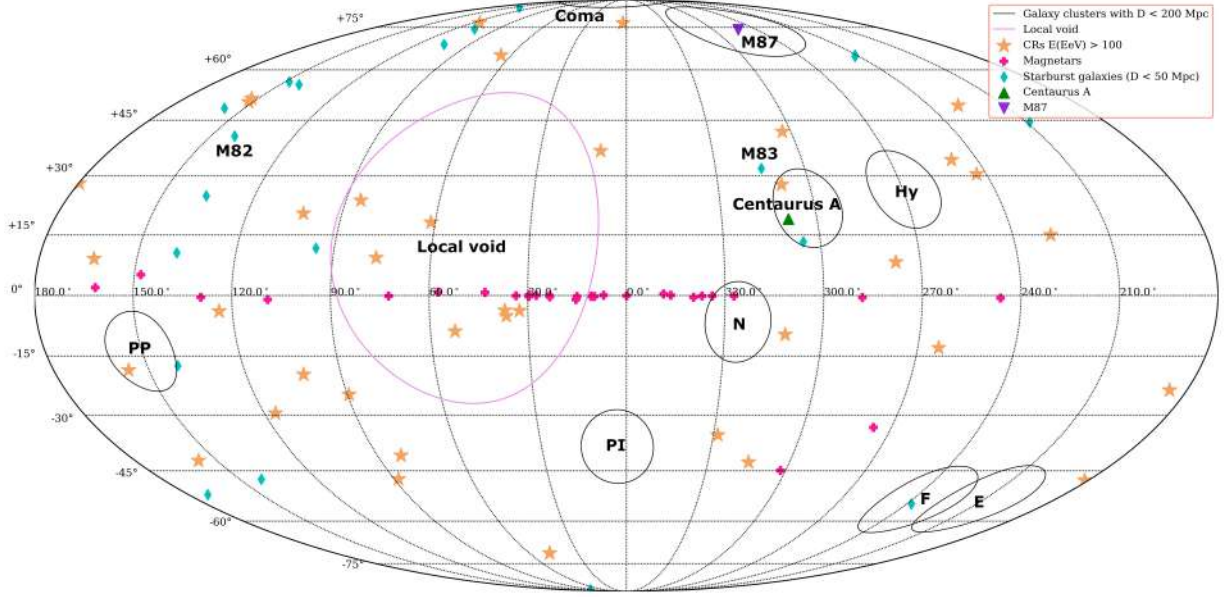


Fig. 22: Distribution of EHECRs (crosses) together with the positions of galaxy clusters and superclusters in the Local Universe (up to 100 Mpc) in Galactic coordinates. C is the Centaurus Supercluster, Co is the Coma Cluster, E is the Eridanus Cluster, F is the Fornax Cluster, Hy is the Hydra Supercluster, N is the Norma Supercluster, PI is the Pavo–Indus Supercluster, PP is the Perseus–Pisces Supercluster, UM is the Ursa Major groups, V is the Virgo Cluster. The dashed line is the Local Void that borders the Local Group.

for TA per decade at high energies [114]. By modeling the observational UHECR spectra of the Auger detector, the value of the calibration coefficient for the energy spectrum $k_{Auger} = 1.15...1.26$ was obtained [118], [119]. For this reason, we use in our study a sample of 11 Auger events with $E > 10^{20}$ eV obtained after calibrating the initial sample [116] at $k = 1.2$. At the same time, the initial TA sample [117] is supplemented with the data on new 12 TA events with energies $E > 10^{20}$ eV from Fig. 5 [120], which are attributed the minimum energy $E > 10^{20}$ eV. The new sample contains 22 events, including a doublet $l = 151^\circ$, $b = 51^\circ$ (two events within the angular separation of the detector 1.4°), and a triplet of events in the region $32^\circ < l < 37^\circ$, $-4.7^\circ < b < -3.3^\circ$ (the Auger + TA doublet and the event at a distance of 3.7° from it) [120]. In addition, we included in the consideration the event registered in 1993 by the Fly’s Eye detector with a record-high energy thus far $(3.2 \pm 0.9) \cdot 10^{20}$ eV with arrival coordinates $\alpha = 85.2 \pm 0.2^\circ$, $\delta = 48_{-6.3}^{+5.2^\circ}$, (Galactic coordinates $l = 163.4^\circ$, $b = 9.6^\circ$) and EAS maximum depth $X_{max} = 815_{-53}^{+60}$ g/cm² [81].

The distribution on the celestial sphere of the EHECR sample formed in such a way is shown in Fig. 22 together with the positions of clusters and superclusters of galaxies that determine the large-scale distribution of mass in the Local Universe (within 100 Mpc): Centaurus Supercluster (C, 60 Mpc), Coma Cluster (Co, 90 Mpc), Eridanus Cluster (E, 30 Mpc), Fornax Cluster (F, 20 Mpc),

Hydra Supercluster (Hy, 50 Mpc), Norma Supercluster (N, 65 Mpc), Pavo–Indus Supercluster (PI, 70 Mpc), Perseus–Pisces Supercluster (PP, 70 Mpc), Ursa Major groups (UM, 20 Mpc), and Virgo Cluster (V, 20 Mpc).

In the model of the EHECR acceleration in astrophysical objects — AGN, GRBs, SBGs, etc. — one would expect a correlation of the EHECR arrival directions with the elements of a large-scale structure, i.e., galaxy clusters and superclusters forming a supergalactic plane, and anticorrelation with the position of the Local Void, the region of the near absence of galaxies with Galactic coordinates of the center $l = -47.7^\circ$, $b = +11.0^\circ$, which borders the Local Group and extends to 40–60 Mpc [51, 52]. However, such correspondence is not confirmed from Fig. 22 EHECRs also do not exhibit excesses in the vicinity of the AGN Cen A ($l = 309.5^\circ$, $b = 19.41^\circ$) [116] and the hot spot ($l = 177.1^\circ$, $b = 49.6^\circ$) [64] found in the Auger and TA data at lower energies $E \geq 40$ EeV. With reservation regarding the relatively small number of recorded events, we can make a preliminary conclusion from Fig. 22: the EHECR distribution is close to that expected in the case of intermediate (C-N-O) and heavy (Fe group) nuclei deflected by the magnetic field of the Galaxy. An alternative version of the dominance of light nuclei (H + He) in the EHECR flux with quasi-ballistic trajectories does not explain the events from the Local Void.

2.7 Surveys of potential sources of EHECR

To check the correlations of EHECR events with potential sources we used several types of acceleration sites. The EHECR arrival directions corrected for the influence of the galactic magnetic field were compared with the samples formed in [121]:

- **sample A:** gamma-ray active AGNs (γ AGN: 17 blazars and radio-galaxies at a distance of up to 250 Mpc from the Fermi-LAT 2FHL catalog with an integrated flux of 50 GeV to 2 TeV as an estimate (proxy) for the expected UHECR flux; in particular, Cen A, M87, Mrk 421, Mrk 501, etc.);

- **sample B:** starburst galaxies (SBGs, 23 galaxies at a distance of up to 250 Mpc with a flux of over 0.3 Jy at 1.4 GHz as an estimate (proxy) for the expected UHECR flux; in particular, seven Fermi-LAT gamma-ray sources (M82, NGC253, etc.))

In addition, the following samples were considered:

- **sample C:** a parameterized catalog of radio-galaxies [122] (42 galaxies at distances up to 300 Mpc selected on the basis of a theoretical description of the energy of jets, acceleration of cosmic rays, their relativistic focusing, and chemical composition);

- **sample D:** a catalog of magnetars in our Galaxy and in the Magellanic Clouds [123] contain-

Tab 4: Considered in this work survey of EHECR events. This also includes including doublet ($\dagger\dagger$), triplet (\dagger), and detected by TA events with assigned energy $E = 100$ eV ($*$)

E	E_{calibr}	RA	Dec	Gal l	Gal b	E	E_{calibr}	RA	Dec	Gal l	Gal b
EeV	EeV	deg	deg	deg	deg	EeV	EeV	deg	deg	deg	deg
PAO											
127.1	152.5	192.8	-21.2	-57.1	41.7	92.8	111.3	343.3	-71.6	-44.9	-42.6
118.3 \dagger	141.9	287.7	1.5	36.5	-3.6	89.3	107.1	116	-50.6	-96.4	-12.9
118.3	141.9	340.6	12.0	80.1	-39.9	89.1	106.9	218.8	-70.8	-48.7	-9.7
111.8	134.1	352.6	-20.8	47.5	-70.5	89.0	106.8	349.9	9.3	88.4	-47.3
108.2	129.8	45.6	-1.7	179.5	-49.6	85.3	102.3	123.3	-6.2	-131.7	15.1
100.1	120.1	150.1	-10.3	-110.9	34.1	84.8	101.7	154.5	-46.9	-82.4	8.3
99.0	118.8	309.5	-66.7	-31.5	-35.2	84.7	101.6	199.6	-34.8	-50.8	27.7
TA											
162.2		205	20	3.2	76.4	100 $*$		280	56	85	23
154.3		239.8	-0.4	9.3	36.2	100 $*$		15	59	124	-3
139		152.3	11.1	228.6	49.4	100 $*$		300	13	52	-8
135.3 \dagger		288.3	0.3	33.2	-4.1	100 $*$		158	57	152	51
124.8		295.6	43.5	76.4	9.2	100 $*\dagger\dagger$		157	58	151	50
122.2		347.7	39.4	101.4	-19.7	100 $*\dagger\dagger$		195	40	115	77
120.3		285.4	33.6	63.5	12.3	100 $*$		69	11	185	-23
106.8		37.6	13.9	156.3	-42.7	100 $*$		52	34	156	-18
101.4 \dagger		285.7	-1.7	32.6	-3.1	100 $*$		338	29	89	-24
101		219.6	38.5	65.8	64.3	100 $*$		298	70	102	20
100 $*$		118	40	179	28	100 $*$		6	33	116	-29
100 $*$		278	33	61	18	100 $*$		144	-9	243	30
Fly's Eye											
320		85	48	163	9						

ning 29 magnetars (23 confirmed, six candidates), including three magnetars with observable giant flares in the hard X-ray and soft gamma-ray ranges, which can be accompanied by the acceleration of UHECRs (from SGR 0526-66 on March 5, 1979, from SGR 1900+14 on August 27, 1998, and from SGR 1806-20 on December 27, 2004);

- **sample E**: massive clusters and superclusters of galaxies at a distance of up to 100 Mpc.

2.8 EHECR trajectory recovery

For a more realistic estimate of the correlation of the UHECR arrival directions with potential sources, was determined the direction of the EHECR velocity vectors as they enter the Galactic magnetic field. For this purpose, for each event with a recorded energy E , its inverse trajectory in the Galactic magnetic field is constructed: for a selected Ze particle charge, a particle with a $-Ze$ charge is launched from the Earth in the direction of the recorded event, and its trajectory is calculated in the Galactic magnetic field represented by regular and random components according to the Jansson–Farrar model [101; 117].

At distances over $R_{gal} = 20$ kpc from Galactic center, the particle moves in a random extragalactic field with amplitude $B_{rms} = 10^{-10}$ G and coherence length $l_B = 1$ Mpc [124; 70; 125]. A cosmic ray with energy E from the source at distance D is deflected in this field by angle θ_{rms} and delayed for time τ_{rms} that can be calculated using expressions 27 and 25.

Starting from the detected direction of the CR arrival on the celestial sphere, was tracked the trajectory of the charged particle through the Galaxy and IGM up to the boundaries of the sphere radius 50 Mpc. As a result, the direction to the exit of the charged particle from this region was obtained. This direction can be the pointer to the source of this particle, if it was accelerated at the distance 50 Mpc. This recovered directions was then compared with the positions of the potential sources on the celestial sphere.

Trajectory recovery was divided into several parts, depending on the atomic mass of the particle. The relative positions of UHECRs and the selected classes of astrophysical objects — candidates for their sources — are shown in Figs. 23...30. Figures 23 and 24 show the correlations of the coordinates of the light nuclei fluxes (H and He) with potential sources. Magnetic fields (mainly Galactic) deflect light nuclei relatively weakly, and there are no explicit correlations with extragalactic sources (taking into account distances to them that often exceed the EHECR range); however, Galactic magnetars can be potential sources for the case of H and He nuclei, in particular, in the region of the galactic plane $60^\circ > l > 30^\circ$. It is important to note that magnetars are considered here together with extragalactic objects since presumable EHECR sources in all the

objects are jets with high kinetic (L_{kin}) and magnetic ($L_{mag} \leq L_{kin}$) luminosities, for which the maximum energies of accelerated particles are [126]:

$$\frac{E_{max}}{10^{20}eV} \lesssim \frac{Ze}{10^{20}eV} \left(\frac{L_{kin}\beta}{c\Gamma^2} \right)^{1/2} = 0.1Z \left(\frac{L_{kin}}{10^{45.5}erg/s} \right)^{1/2} \left(\frac{\Gamma^2/\beta}{100} \right)^{-1/2} \quad (29)$$

where e is the elementary charge, c is the speed of light, $\beta = v/c$ is the dimensionless speed of the jet, and $\Gamma = (1-\beta^2)^{-1/2}$ is its Lorentz factor. For typical jet luminosities $lg(L_{kin}/(erg/s))$, both ultrarelativistic ($\Gamma \gg 1$) and weakly relativistic ($\beta \approx 0.1$) jets can accelerate nuclei (especially with large Z) up to energies of more than 10^{20} eV. This assumption is considered in more detail in the section 4. In addition, according to Eq. 27, EHECRs from both Galactic and extragalactic sources will move quasi-ballistically, deviating in magnetic fields only slightly and not entering the diffusion propagation mode. Therefore, to identify their sources, we can compare individual recorded events with specific astrophysical objects.

The deviation of light H and He nuclei from ballistic trajectories is minimal; therefore, their identification is the most informative. However, Figs. 23, 24 and Table 5 indicate that their fraction in the detected EHECRs is insignificant.

In addition, the small range of He nuclei significantly limit their possible presence in the recorded events in comparison with H nuclei.

Nuclei of intermediate masses (C-N-O groups) with $Z = 6-8$ are more strongly deflected mainly by Galactic and, in part, extragalactic magnetic fields (Fig. 27, 28).

An increase in the scatter of the trajectories by random components of the Galactic and extragalactic magnetic fields with increasing charge Z leads to an increase in the number of potential sources; however, the small energy loss lengths of the nuclei of the intermediate masses of the EHECRs significantly reduce their possible fraction in the observed events (Table 5).

The scatter in the positions of large mass nuclei with $Z = 14-26$ (Si-Ca-Fe groups) reaches tens of degrees and provides a significant number of potential sources for the observed EHECRs of this mass group (Figs. 6-9), although the relationship with the sources remains quite clearly determined: the transition to the diffusion mode is not yet achieved. An additional favorable factor is the large (over 100 Mpc) range of the nuclei of this mass group (Table 5).

The effect of magnetic lensing in the GMF is clearly visible on the example of the deflection of the trajectories of the nuclei of heavy groups. And one can see that the distribution of circles roughly follows the large-scale distribution of matter - the so-called supergalactic plane, which may be additional evidence of the extragalactic nature of these particles.

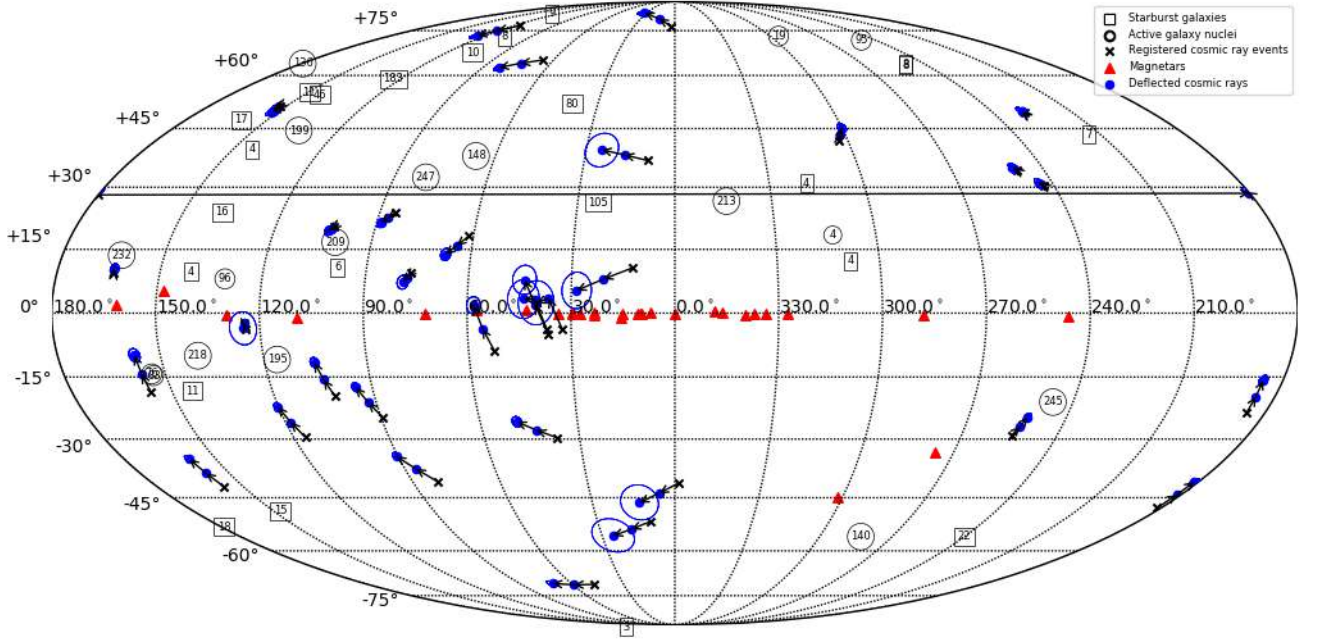


Fig. 23: Observed distribution of EHECRs (crosses), the directions of their entry into the Galactic magnetic field (arrowheads), and the 1σ circles of the total deviation in the random Galactic and extragalactic magnetic fields up to 50 Mpc for H and He nuclei. Also shown are the positions of SBGs (squares), magnetars (triangles), and γ AGN (circles) with the indicated distances (in Mpc)

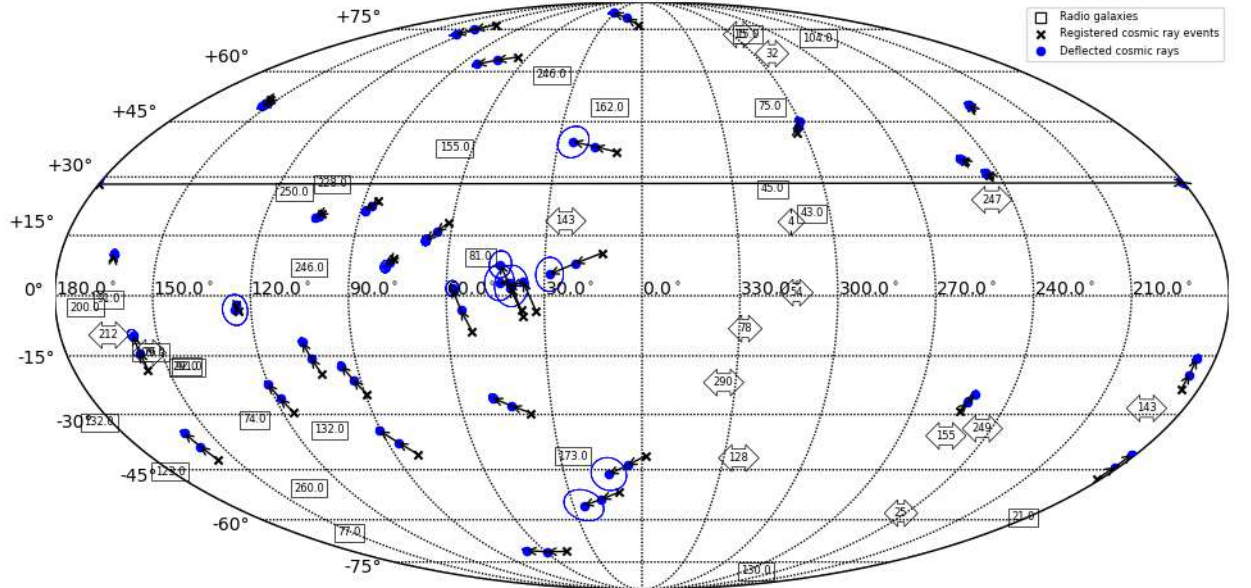


Fig. 24: Same as in Fig. 23, for the case of H, He nuclei, and radio-galaxies

2.9 Correlation of EHECR events with potential sources

The observational data of EHECR events are among the most promising for identifying physical sources and acceleration mechanisms of a wide class of extragalactic cosmic rays with ultrahigh energies $E > 10^{18}$ eV. CRs of such energies propagate in the Galactic and extragalactic magnetic

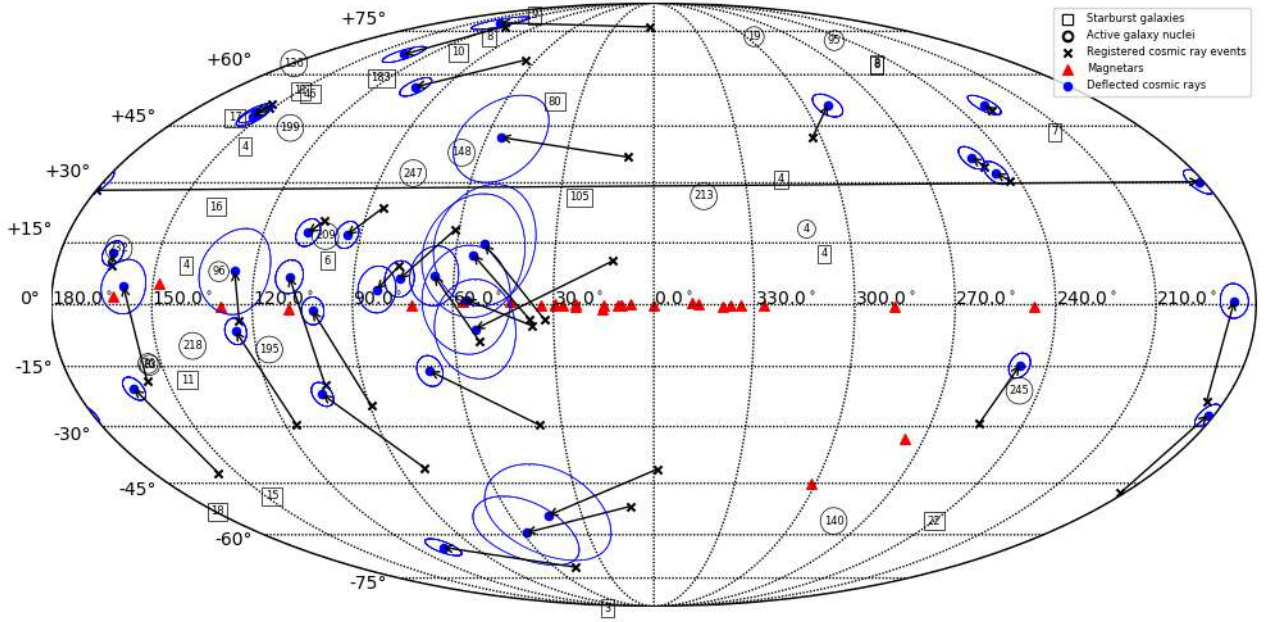


Fig. 25: Same as in Fig. 23 for the case of C nuclei

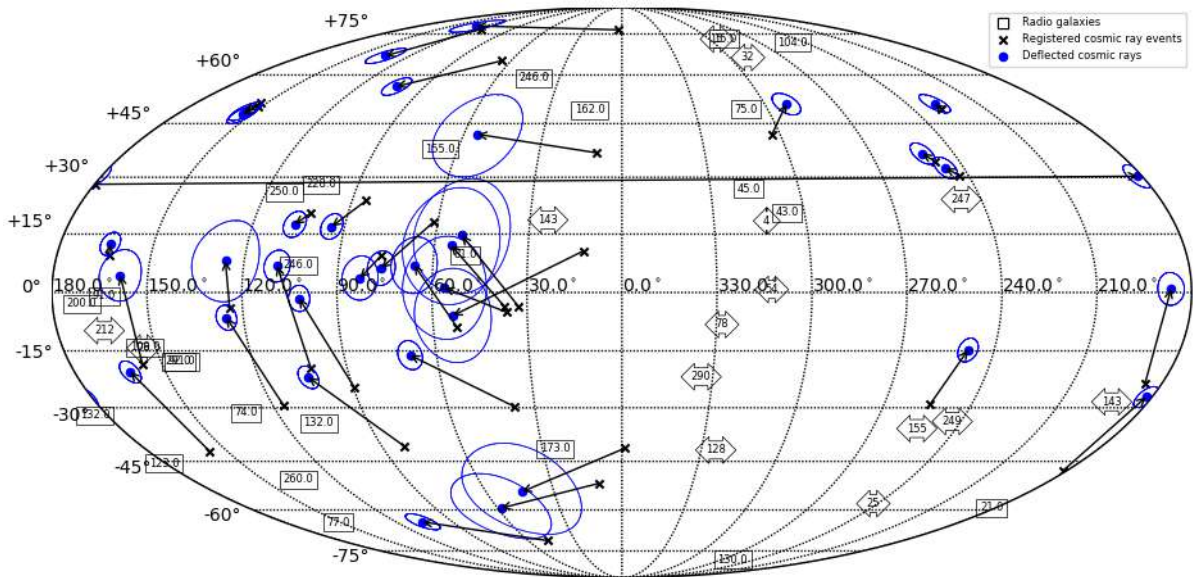


Fig. 26: Same as in Fig. 25 for the case of C nuclei and radio-galaxies.

fields quasi-ballistically, without entering the diffusion mode of propagation even for heavy nuclei of the iron group. In addition, their path is reduced to 100 Mpc due to an increase in energy loss with increasing energy (for photodisintegration in the case of complex nuclei and photopionic loss in the case of protons). These two circumstances make it possible to search for sources of detected EHECRs by searching for matches between the EHECR arrival directions corrected for the influence of the magnetic field and the positions of potential sources on the celestial sphere for each of the events and each of the potential sources.

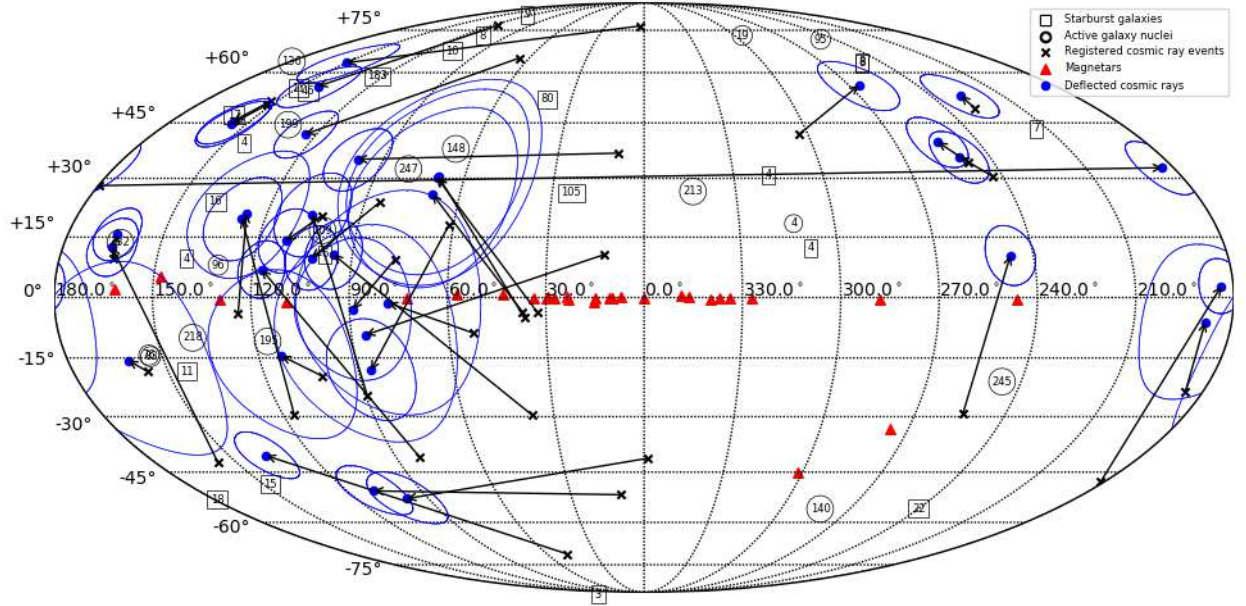


Fig. 27: Same as in Fig. 23 for the case of Si nuclei.

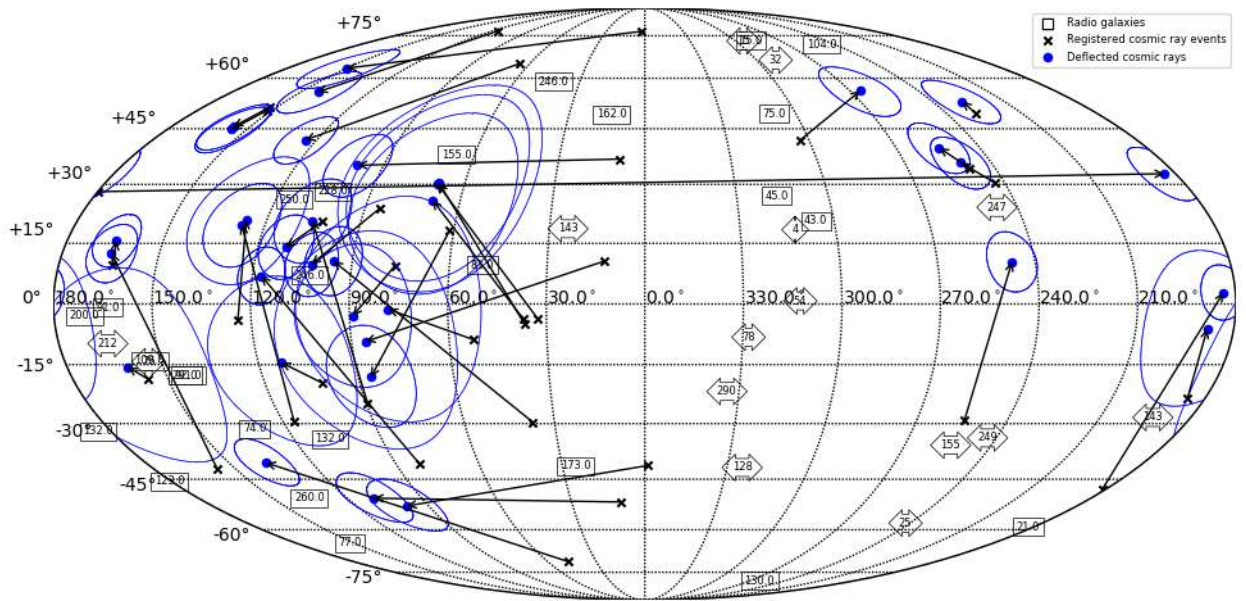


Fig. 28: Same as in Fig. 24 for the case of Si nuclei and radio-galaxies.

Such analysis is expected to be the most effective for light nuclei ($Z = 1-2$), which are least deflected by the magnetic field. It was noted in a number of studies [121; 119] that the light component with $E > 50$ EeV in the UHECR flux can account for a significant proportion of events. In particular, the analysis of the Auger data of the observed flux for $E > 50$ EeV performed in [119] opens up chances for EHECR astronomy. However, Figs. 23 and 24 show no connection of the H and He components with potential sources.

As already noted above, the PAO data regarding the chemical composition indicate the domi-

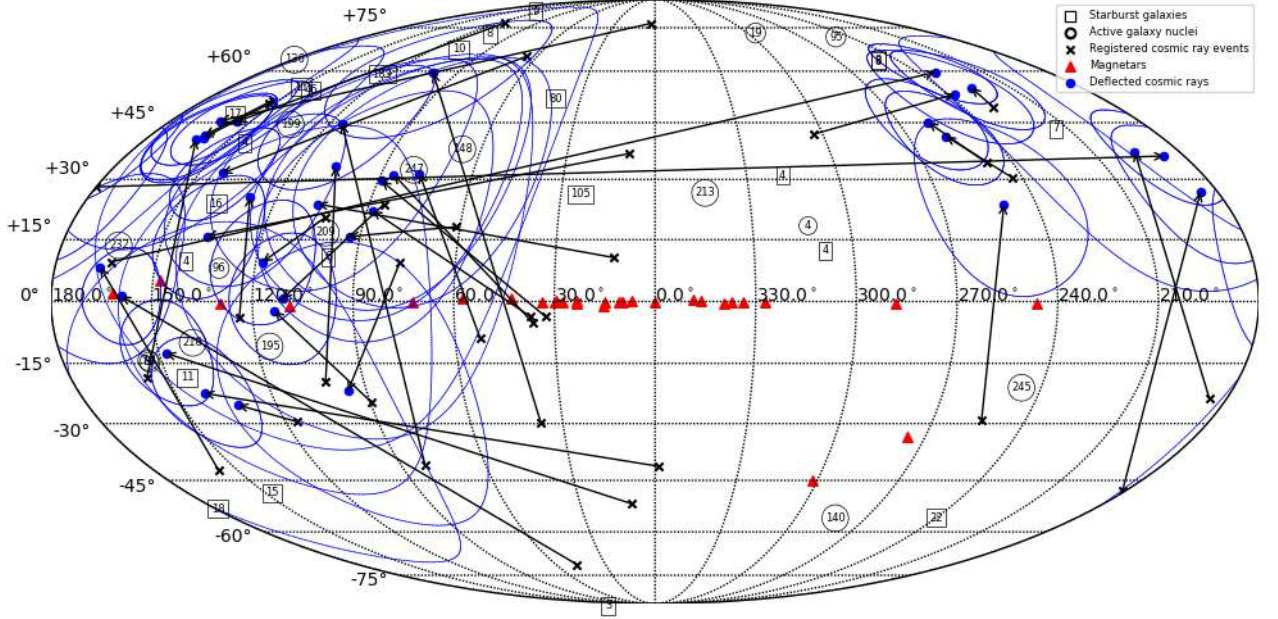


Fig. 29: Same as in Fig. 23 for the case of Fe nuclei.

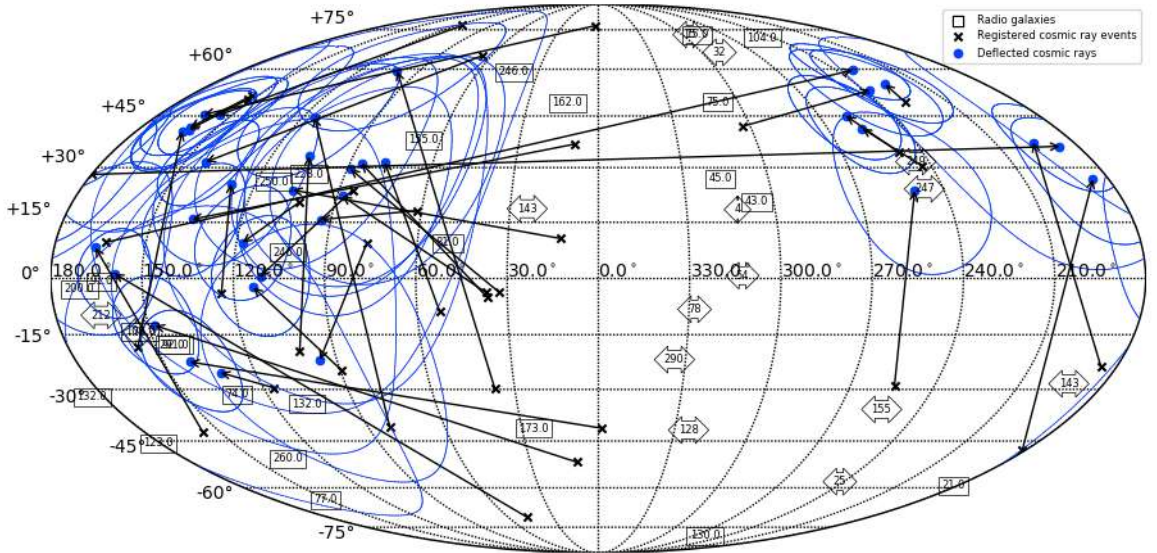


Fig. 30: Same as in Fig. 24 for the case of Fe nuclei and radio-galaxies.

nance of intermediate mass nuclei in a UHECR flux with $E > 10^{19}$ eV. In particular, for 34 Auger events with $lg(E/eV) > 19.9$ the average atomic mass is $\langle lnA \rangle = 2.6$ (C-N-O group) in the QGSJetII-04 model and $\langle lnA \rangle = 4.1$ (Fe group) in the EPOS-LHC model [46]. However, for the nuclei of the C-N-O group, the range of which is less than 10 Mpc, there are no potential sources for almost all the observed EHECR events. At the same time, theoretically, these nuclei could be formed in the vicinity of 10 Mpc from the Earth due to the photodisintegration of heavy nuclei of the iron group; however, a more intense flux of these heavy nuclei should be observed in this case at energies above 10^{20} eV (A_{Fe}/A_C).

Tab 5: Potential sources of EHECR based on the backtracking trajectory calculations.

CR Nuclei	Mean Free Path EHECR $10^{20}/3 \cdot 10^{20}$ eV, Mpc	Potential sources		
		Sample A	Sample C	Sample E
H	120 / 20	IC310, NGC1275	-	Pavo-Indus
He	3 / 3.5	-	-	-
C	4 / 0.9	-	-	Ursa-Major
N	6 / 0.8			
O	7.5 / 0.7	3XMM J185246+ 0033176, SGR 1900+14		
Si	100 / 2.5	TXS 0149+710, IC310, NGC1275	3C386, 3C129, Perseus A	Ursa-Major, Coma
Ca	150 / 4.5	TXS0149+ 710	Hydra, Perseus-Pisces	Perseus A, Ursa-Major, Coma
Fe	270 / 18	IC310, NGC1275	3C66B, 3C31, 3C386	

Elements of the Si group and, especially, the Fe group have quite a few potential sources (Table 5). This is mainly due to large ranges and a significant deviation of the trajectories in random magnetic fields (mainly in the Galactic field). At the same time, the method of individual comparisons of arrival directions and positions of the objects becomes significantly less effective.

The dominance of intermediate and heavy nuclei in the EHECR flux can also be indicated by another fact. It can be seen from Figs. 23, 24 that the distribution of the EHECR arrival directions has a gap in the region of the Galactic center, while the distribution of their potential sources is fairly isotropic. A change in the arrival directions through the influence of the Galactic magnetic field enhances this anisotropy: the directions of the entry of EHECRs into the magnetic field of our Galaxy are concentrated in an extended region of $40^\circ < l < 270^\circ$, $b > 0^\circ$ with an increase in their charge Z (which is equivalent to a decrease in their rigidity $R = E/Ze$, which determines the deflection of a particle in the magnetic field from $R = 10^{20}$ V for $R = 3.8 \cdot 10^{18}$ V for Fe at $E = 10^{20}$ eV). This property of magnetic lensing of the Galactic magnetic field to enhance the

Tab 6: Potential sources of EHECR

Element	$L_{loss}[Mpc]$ $\lg(E/eV)=20/20.5/21$	Galactic Magnetars	Starburst galaxies
H	20/3.5/5	SGR 1935+2154	NGC5055, 3XMM J185246+003317
He	0.5/2/1	SGR 1900+14	-
N	2/0.1/0.3	4U 0142+61, SGR 0501+4516, SGR 1935+2154, SGR1900+14 3XMM J185246+0033176	NGC5055, NGC4631
Si	50/0.15/0.3	1E2259+586, SGR 2013+34, 4U 0142+61, SGR 0501+4516, SGR 1935+2154	NGC 3079, NGC2146, NGC891, NGC6946, NGC3628, NGC3627
Fe	60/10/0.3	SGR 0418+5729, 4U 0142+61 1E2259+586, SGR 2013+34, SGR 0501+4516, SGR 1935+2154	NGC6946, M51, NGC5055 NGC2146, IC342, NGC891, M82, NGC660, Arp299, NGC4631 NGC3556, NGC3079, NGC1068

contribution of some parts of the sky to the total flux of extragalactic UHECRs and weaken the contribution of others is discussed in [23]. For the proton component of EHECRs with $E > 10^{20}$ eV ($R > 10^{20}$ V), this effect is insignificant, and all parts of the sky will contribute to the flux in accordance with the sources available there.

2.10 Conclusions

In this section was calculated the effect of EGMF and background radiation on the propagation of UHECR ($E > 5 \cdot 10^{19}$ eV) from potential sources in the Local Universe, in particular, from the AGN and SBGs in the galaxy superclusters of Virgo, Perseus-Pisces, and the Great Attractor. EGMF significantly deflect the trajectories of UHECR up to their entry into the diffusion regime, while the interaction of UHECR with background radiation leads to energy losses and photodisintegration of nuclei. Both processes erase the signs of the connection for the detected UHECR with their astrophysical sources. I have investigated the values the UHECR trajectory deflection and optical thicknesses, that are characterizing the weakening of the UHECR flux from their potential sources. This work was done for selected groups of nuclei, the detection of which can serve as confirmation of their connection with potential sources in the Local Universe. It is shown that in most cases only protons maintain contact with their sources.

Another part of this section is dedicated to searching of potential sources of EHECR using the technique of backtracking trajectories. Available data on observations of CR with energies exceeding 10^{20} eV was taken and I made corrections to their trajectories based on Galactic magnetic field model JF12. For every CR was obtained new coordinates on celestial sphere, which denote position where charged particle entered the Galaxy. Deflection in random extragalactic magnetic fields was also calculated. This deflection manifested itself as smearing angles around positions where CR entered the Galaxy. The size of such smearing circles strongly depends on charge number of particle. Due to this effect, it was obtained more potential sources for heavier nuclei than for lighter. But in all cases the distribution based on corrected trajectories remains nearly isotropic.

This results demonstrate that it is still difficult to make cross-correlation analysis of CR with its potential sources, even in the case of the highest detected energies. But based on this analysis one can make constrains on models of potential sources of EHECR or even clarify some of them for future investigations. Under “constraining models” I mean that there are clear evidence that corrected distribution of EHECR on celestial sphere follows the distribution of extragalactic objects, while center of Galaxy remains empty. One of the most promising extragalactic candidates for EHECR are galaxy clusters due to their enormous large sizes and the possibility to contain AGN. Particularly, here is a closer look to the GCs possibility to accelerate CRs and considered deposit from AGN to total gamma ray flux from GCs in the next section.

But not only extragalactic objects can contribute to the observed EHECR flux. During doing this work, particular attention was attracted by good candidate for Galactic accelerator - magnetar SGR1900+14, that is spatially coincident with triplet of events. There are evidence about giant magnetar flare that took place on this object in 1998. It is believed that in such events can be produced EHECR.

Of course, the number of EHECR events analyzed in the study (31 events) is insufficient to obtain more rigorous conclusions about their potential sources. The accumulation of new observational data, in particular, updated by the Auger and TA detector arrays, may help identify the long-awaited EHECR sources even before the commissioning of new detectors (JEM-EUSO, GRAND, POEMMA).

3 Galaxy clusters as reservoirs of cosmic rays

3.1 Introduction

In the large-scale structure of the universe, GCs are the largest and most massive gravitationally bound objects. GCs are powerful sources of non-thermal leptonic (synchrotron) radio emission and thermal X-ray radiation due to the temperatures of keV order of the gas in the intracluster medium (ICM) and the presence of CRs. GCs are also repositories for hadronic CRs, however non-thermal hadronic gamma-ray emission from GCs (mostly due to pp collisions and subsequent pion decay) has not yet been identified. In this section I simulated the expected neutrino and non-thermal hadronic γ -ray emission from dominant part of Hercules cluster (GC A2151), Coma cluster (A1656) and investigated feedback influence of AGN inside GC. Based on received results was estimated a perspective of detection of this emission by existing (Fermi-LAT, IceCube, LHASSO) and future (IceCube-Gen2, CTA) space-based and ground-based detectors. Due to backreaction input to expected gamma-ray flux from AGN was decided to investigate properties of AGN in more detail. For this reason was considered 55 blazars and Seyferts from the Planck all-sky survey that have been cross-correlated using the Swift-BAT 105-Month Hard X-ray Survey and Early Release Compact Source Catalog (ERCSC). X-ray Swift/XRT+BAT spectra vs Radio Planck spectra of the AGN sample were fitted with the broken and simple power law (Galactic neutral absorption was taking into account in case of in case of X-ray spectra) to test the connection between the photon indices of synchrotron self-Compton (SSC) or IC emission (in X-rays) and synchrotron emission (in radio range). In the end is demonstrated that, for the majority of AGN in considered sample, there is a relationship between SSC and synchrotron photon indices (one of two for the broken power-law model) that is compatible with error levels. This provides a valuable perspective for identifying the jet base counterpart from the one emitted by the disk-corona AGN “central engine” for such items.

3.2 Formation of galaxy clusters

Due to the modern theories about structure of the Universe, it consists from hierarchically build objects. This hierarchy are differentiate by mass - from the smallest to the biggest. Starting from the planet systems, through sizes as galaxies and to the galaxy clusters - the biggest virialised objects in the Universe. GCs are the largest virialized structures in the Universe at the present cosmological time $t_0 = 13.8$ Gyr (a redshift $z_0 = 0.0$)[127]. A rise in initial density fluctuations as a result of gravitational instability led to the production of the primary building blocks of large-scale

structure: Galaxy clusters and superclusters are sheet-like formations connected to high-density nodes by filaments and low-density voids [128]. The total gravitational masses $M_{cl} \sim 10^{14} - 10^{15} M_{\odot}$ of GCs include small amount of baryonic matter ($\sim 5\%$ of mass in stars/galaxies and $\sim 15\%$ of mass in intracluster medium (ICM) gas) and dominant contribution of dark matter (about 80 % of mass) [129], [130], [131]. Virial temperatures of ICM plasma $k_B T \sim GM_{cl} m_p / R_{cl}$ in GCs with typical size $R_{cl} \sim 2 - 3$ Mpc are of the order of 1 – 10 keV, therefore GCs are powerful sources of thermal X-ray emission, with typical luminosity $L_X \sim 10^{44} - 10^{46}$ erg s⁻¹.

Formation of gravitationally bound and virialized GCs is a long, violent process of primary halo collapse and substructures' union that is frequently unfinished yet. The majority of clusters have not yet reached full equilibrium, and accretion and merging processes are still occurring. Magnetohydrodynamic (MHD) flows from AGN and in ICM, rich in shock waves, efficiently accelerate CRs and generate/enhance magnetic fields in ICM. Once more, in observed $B_{cl} \sim 1 - 10 \mu\text{G}$ GC magnetic fields the time of diffusive escape of CR from GCs $t_{dif} \sim R_{cl}^2 / D(E)$ is of order or larger than the age of Universe for typical value of diffusion coefficient $D(E) \sim 10^{28} (E/10\text{GeV})^{0.5} \text{cm}^2 \text{s}^{-1}$. Consequently, GCs are efficient repositories for accelerated CRs [130]; consequently, GCs are anticipated to be promising sources of non-thermal leptonic (synchrotron) radio emission as well as of hadronic radio emission (due to proton-proton collisions and subsequent neutral pion decay) [132], [133].

Indeed, a non-thermal synchrotron radio emission in MHz – GHz range from relativistic electrons ($E_e \sim 10$ GeV) in clusters' magnetic fields ($\nu_{syn} \sim 4(B_{cl}/1\mu \text{G})(E_e / 10 \text{GeV})^2$ GHz) is commonly observed in GCs [134], but non-thermal γ -ray emission from GCs has not been detected yet [135], [136].

Non-thermal radio- and thermal X-ray emission, augmented by data of the *Planck* thermal Sunyaev-Zeldovich (SZ) phenomenon, provide vital information regarding the distribution of dark/baryon matter and physical processes in the interstellar medium (ISM) of galaxies.

3.3 Galaxy cluster content and distribution parameters

Lets take a closer look to GC from biggest scale to the inner parts. Whole cluster and filamentary structure around it describes by a definition of the IGM. Such regions can extends up to the tens of Mpc. Ambient gas that is falling into the filaments is heated to the high temperatures $kT \sim 10 - 1000\text{eV}$ ($T \sim 10^5 - 10^7$) K, and therefore producing an ionized plasma. But the inner regions of cluster, so-called ICM, are filled with a much more heated and rarefied (electron density $10^{-4} - 10^{-1} \text{cm}^{-3}$) gas. This gas mainly consist of ionized hydrogen, helium, partially ionized

heavier elements and of the electrons. Due to presence of a lot of heated electron plasma, the main manifestation of cluster is thermal bremsstrahlung and free-free emission.

Physical conditions and spherically-symmetric distribution of dark/baryonic matter in the ICM of GC are primarily dictated by two global GC parameters: its size R_{cl} and total mass M_{cl} . Various sorts of characteristic masses have been utilized in modeling. M_{500} represents the mass contained within the radius R_{500} where the mean density (averaged over volume) surpasses the critical density by 500 times $\rho/\rho_{crit} = 500$. Corresponding values are linked by the following relationship:

$$M_{500} = \frac{4\pi}{3} 500 \rho_{crit} R_{500}^3 \quad (30)$$

Total mass M_{tot} of GC can be expressed as $M_{tot} = M_{HSE}/(1 - b_{HSE})$, where M_{HSE} is the hydrostatic mass derived from hydrostatical equilibrium and $b_{HSE} \sim 0.2$ is the hydrostatic mass bias [137], [138]. Spatial distribution of gas mass fraction in GC $f_{gas}(r)$ is determined as the ratio of the gas mass $M_{gas}(r)$ and the total mass $M_{tot}(r)$ $f_{gas}(r) = M_{gas}(r)/M_{tot}(r)$.

Gas electron density profile $n_e(r)$ is an important parameter for estimating gamma-ray emission, because it is proportional to total gas density $n_{gas}(r)$, that describes the intensity of proton-proton interactions. There are several theoretical models to describe $n_e(r)$, particularly, analytical beta model [139] that was used in this work:

$$n_e(r) = n_{e,0} \left[1 + \left(\frac{r}{r_c} \right)^2 \right]^{-3\beta_{dens}/2} \quad (31)$$

where $n_{e,0}$ is the normalisation factor, r_c is the core radius of density distribution, β_{dens} is the density index.

The thermal gas pressure is also essential since it permits the number of CR to be normalized. Electron thermal pressure $P_e(r)$ can be expressed by Generalized Navarro Frank White (GNFW) profile [140]. Universal pressure profile (UPP) for electrons $\mathbb{P}_e(r)$ depends on four parameters: the normalization factor P_0 , the scale radius $r_p = R_{500}/c_{500}$ (where c_{500} is the concentration parameter for region bounded by R_{500}), and three power indices a_p, b_p, c_p , which denote distribution slope for different spatial regions ($r < r_s$, $r \approx r_s$ and $r > r_s$, respectively):

$$\mathbb{P}_e(r) = P_0 \cdot (r/r_p)^{-c_p} \cdot (1 + (r/r_p)^{a_p})^{(c_p - b_p)/a_p} \quad (32)$$

For describing of the physical processes in any particular GC, one need to multiply UPP (32) by several scale factors: $P_e(r) = \mathbb{P}_e(r) \times P_{500} \times F_{500}$, where P_{500} is the characteristic pressure [140],

[141], which can be determined by mass and cosmological parameters:

$$P_{500} = 1.65 \times 10^{-3} E(z)^{8/3} \left(\frac{M_{500}}{3 \times 10^{14} h_{70}^{-1} M_{\odot}} \right)^{2/3} h_{70}^2 \quad (33)$$

and the corrective factor F_{500} makes modification by mass due to the self-similarity of GC:

$$F_{500} = \left(\frac{M_{500}}{3 \times 10^{14} h_{70}^{-1} M_{\odot}} \right)^{0.12} \quad (34)$$

Here $H_0 = 100h$ km/s/Mpc, $h_{70} = h/0.70$, and $E(z) = H(z)/H(0)$ or $E^2(z) = \Omega_M(1+z)^3 + \Omega_{\Lambda}$.

For ICM with helium $Y=0.270$ and hydrogen $X=0.725$ and heavy elements' mass fraction $Z = 1-X-Y = 0.005$, the mean molecular weights are $\mu_{gas} = 0.60$, $\mu_e = 1.15$, and now one can express the density, pressure and temperature of ICM gas through the pressure and number density of ICM electrons [142]:

$$P_{gas}(r) = (\mu_e/\mu_{gas})P_e(r), \quad \rho_{gas}(r) = (\mu_e/\mu_{gas})m_H n_e(r), \quad k_B T_{gas}(r) = \mu_{gas} m_H (P_{gas}(r)/\rho_{gas}(r)) \quad (35)$$

Magnetic field distribution is following matter distribution [143], [144]. Based on magnetic freezing conditions, spatial distribution of magnetic field can be expressed as proportional to some power η_B of density profile: $B(r) = B_0(n_e(r)/n_{e,0})^{\eta_B}$. Normalisation factor B_0 is set to $5\mu G$, as typical value for GCs, that was measured for Coma cluster based on Faraday rotation data. [143].

Spatially-energetic distribution of CR - nuclei (mainly protons, $i=p$) and electrons ($i = e_1$ for primary ICM electrons, $i = e_2$ for secondary electrons produced in inelastic collisions) in ICM can be divided into the product of energetic and spatial distributions:

$$dN_i(E, r)/dE = A_i f_i(E) \phi_i(r) \quad (36)$$

ICM protons and electrons accelerated by shock waves within GCs develop a power law energy distribution. In this study, the standard power law with exponential cut-off energy spectrum was utilized:

$$f_i(E) = A_i \times \left(\frac{E}{E_{0,i}} \right)^{-\alpha_i} \times \exp\left(-\frac{E}{E_{cut,i}}\right) \quad (37)$$

where α_i is the spectral index, and cut-off occurs at energies $E_{cut,i}$ ($i = p, e1$). Normalization factor A_i is determined by the ratio of CR energy to thermal energy inside sphere with radius $r = R_{500}$. This ratio can be calculated as $X_{CR,i,th} = U_{CR,i}(R_{500})/U_{th}(R_{500})$, where U_{CR} and U_{th} are CR and thermal energy, respectively. Typical values are $X_{CR,p,th} \approx 0.02 - 0.10$, $X_{CR,e,th} \approx 0.0001 - 0.001$. The spatial distribution of CRs in the ICM is dependent on the distribution of gas and can be approximated by power law dependency:

$$\phi_i(r) = \left(\frac{n_e(r)}{n_e(0)} \right)^{\eta_{CR,i}} \quad (38)$$

Important parameters include the truncation radius R_{trunc} , which is used to represent the physical boundaries of the region containing the complete GC volume, outside of which the density goes to zero. The thermodynamic parameters are discontinuous at this distance from the center of the GC. It denotes the region of the accretion shock radius where the kinetic energy of accretion is transformed into thermal energy [145]. This region's size is dependent on the characteristic radius $R_{trunc} = 3R_{500}$.

3.4 Dark matter in galaxy clusters

First evidences of some hidden mass that resides in GC was obtained by Fritz Zwicky in 1933 [146]. He found out that total amount of matter in Coma cluster exceeds the luminous matter by around of 400 times. After that, many other experiments and observations have been performed that confirmed primary assumption about some hidden mass. This type of matter are called now Dark Matter, because it doesn't interact through EM forces. Moreover, due to the latest observations, it is interacting only by gravitational forces and it has to be non-baryonic to be consistent with observations and theoretical predictions.

As was mentioned in the Introduction to this section, the biggest part of GC by mass is in the form of DM. Galaxy clusters have density contrast of $\delta \sim 10^3$ which can not be explained only by growing of baryon fluctuations. There must be a large amounts of DM which behave like potential wells for usual matter. One of the main ways to investigate non-linear evolution of structures in the Universe is numerical N-body simulations. They give the exceptional profit in reproduction of matter distribution in DM halo [147].

Recent decades observations of weak gravitational lensing confirmed the results of N-body simulations about matter distribution. Due to this, the dark matter density profile in the virialised objects obey the universal law [148; 149]. Lets consider in more details the most relevant recent models of DM distribution. First of all lets begin from the distribution that was obtained as a result of N-body simulations - above mentioned NFW profile [150]. They show that all density profiles of DM halo can be approximated by some universal profile:

$$\rho(r) = \frac{\delta_c \rho_{crit}}{\frac{r}{r_s} \cdot \left(1 + \frac{r}{r_s}\right)^2} \quad (39)$$

where $r_s = r_{vir}/c$ - is scale radius, that depends on the virial radius and concentration parameter. Virial radius r_{vir} is the quantity that defines the region where mean density of matter

is in Δ_{vir} times larger than critical - $\Delta_{vir} = \frac{\rho(r)}{\rho_{crit}}$. For example in literature and in simulations is often used a value r_{200} or r_{500} - that denotes regions, where density of matter is higher than critical in 200 or 500 times respectively. This is the same type of parameters that we used in previous paragraph in UPP definition. Characteristic density δ_c is defined by:

$$\delta_c = \frac{\Delta}{3} \frac{c_{\Delta}^3}{\ln(1 + c_{\Delta}) - \frac{c_{\Delta}}{1+c_{\Delta}}} \quad (40)$$

The improved variant of NFW profile, so-called generalised NFW profile was described in previous section. But NFW profiles have problems with describing very center of GC. Einasto profile can be used to reduce this issue and for better modelling inner slope of distribution :

$$\rho(r) = \rho_{-2} \exp\left(-\frac{2}{a} \left[\left(\frac{r}{r_{-2}}\right)^{\alpha} - 1\right]\right) \quad (41)$$

There are many other models in addition to this mentioned above. Every model have its pros and cons, and limits of application. Except of models of distribution, it is important to know what exactly are DM particles, but unfortunately that still remains one of the main problems of modern physics. There are couple of theories about what it can be. The most promising one consider DM as substance that is composed by Weakly Interacting Massive Particles (WIMPs) with typical masses in the GeV-Tev range. This particles should be electrically neutral and interact with Standart Model only via weak nuclear forces. I send the interested reader to the recent review by Roszkowski et al. [151].

As one can see DM plays crucial role in GC evolution, but CR are more important if we talk about manifestations of GC in EM or neutrino band. In the next section we briefly discuss signatures of CR acceleration in GC and how they reveal itself.

3.5 Signatures of cosmic ray acceleration in galaxy clusters

Galaxy clusters manifest themselves in different ways through the wide EM spectrum. Extended radio emission of ICM demonstrate the fact that thermal plasma is mixed with non-thermal components. The interaction of relativistic electrons and large-scale magnetic field produces synchrotron emission. Other independent evidence for existence of magnetic field in GC is measuring of Faraday rotation in the polarised radio galaxies. The density of relativistic particles is around 10^{10} cm^{-3} , and their Lorentz factor significantly exceeds 10^3 . The magnitude of magnetic fields lies within $\sim 0.1 - 1 \text{ } \nu G$, and energy density of relativistic plasma is $\leq 1\%$ of thermal gas [152].

Overview over the different physical processes can be seen on the Fig. 31. This figure can be divided into two parts - upper and lower, thermal and non-thermal respectively. For us the

Cluster observables:

Physical processes in clusters:

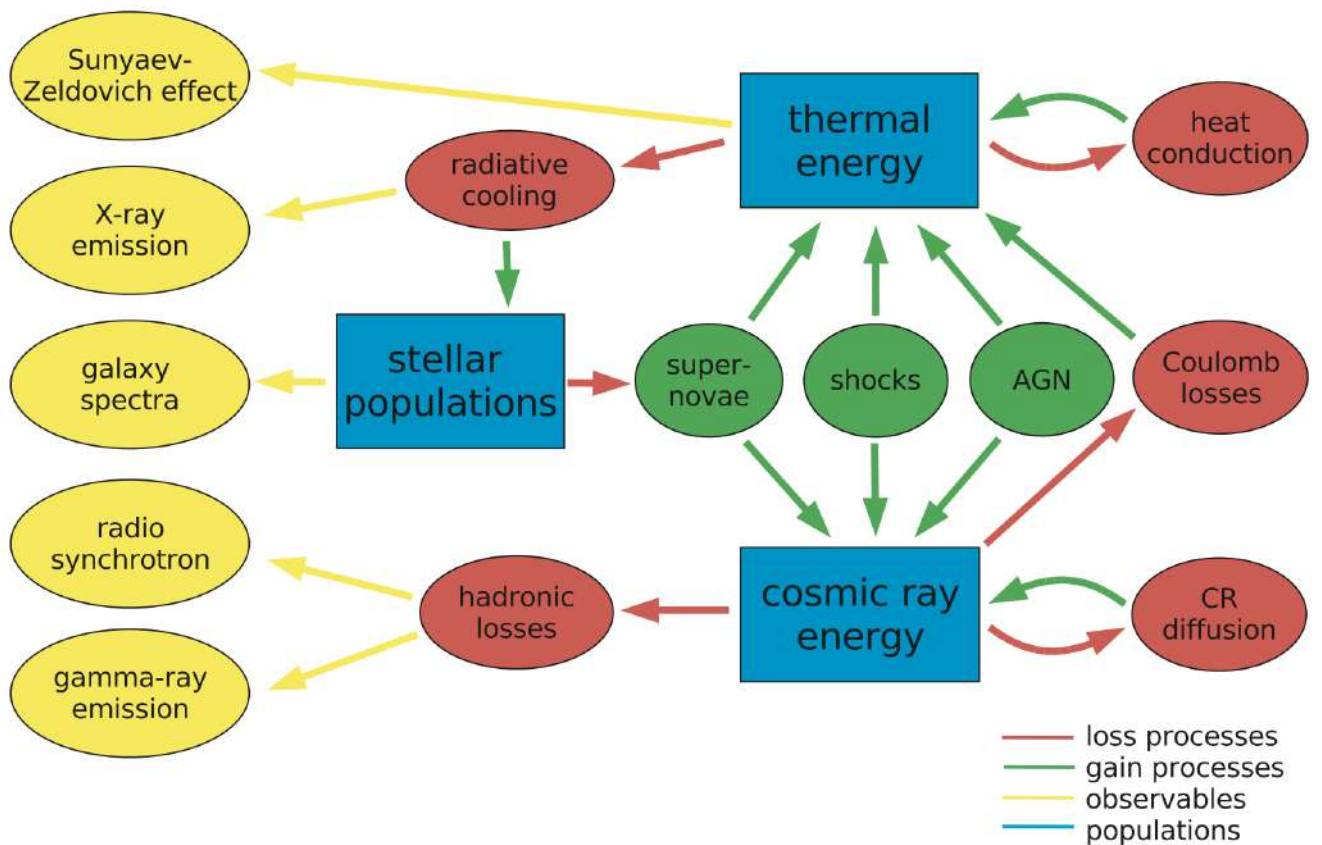


Fig. 31: Overview of different physical processes that take place in galaxy clusters. Fig. from [153].

particular interest has lower part, where is sketched the CR physics within clusters. In general, CRs behave in different way compared to the thermal gas. They have possibilities to spread over macroscopic distances and their energy loss time are typically much larger than for the thermal gas.

Observations of extended radio emission (in the halo and radio relics) in GCs that are merged, demonstrate existence of electrons with energies exceeding ~ 10 GeV, which in turn generate synchrotron emission [154; 155].

Galaxy clusters are the reservoirs for CR that was accelerated on the shock waves by processes of merging, accretion and AGN feedback. Registration of diffuse radio synchrotron emission confirms the existence of high energy electron and all-permeating magnetic fields in the inner parts of GC. As long we don't have any direct evidence for the acceleration of protons, but registration of gamma-rays that were produced by decay of neutral pions can approve this fact. The most of the GC are still in the phase of merging. That means there are a lot of released energy during this processes of merging, accretion and turbulence. This processes must accelerate electrons and

protons to the high energies. Cooling time of protons is quite high, so they can be gathered in GC volume by the Hubble time. Gamma emission that are produced by the interaction of protons with hot ICM gas must dominate IC and bremsstrahlung [156].

$$\begin{aligned}
p + p &\rightarrow \pi^0 + \pi^+ + \pi^- + \textit{anything} \\
\pi^0 &\rightarrow \gamma\gamma \\
\pi^\pm &\rightarrow \mu^\pm + \nu_\mu, \\
\mu^\pm &\rightarrow e^\pm \nu_\mu \nu_e
\end{aligned}
\tag{42}$$

But it is important to mention, that only CR protons with momentum above the threshold $p \simeq 0.8 GeV/c$ can interact with background photons, and therefore be visible through decay processes like in Eq. 42. This hadronically produced relativistic electrons can also be respective for radio synchrotron halo by interaction with intra-cluster magnetic fields.

3.6 AGN in galaxy clusters and their influence on cosmic rays

As it will be justified in the next subsections about modelling of non-thermal content of GCs, AGN in GCs play important role in total energy distribution. Due to the feedback by their energetic jets, they can strongly change shape of the spectrum of the non-thermal emission. Due to this, here comes section where described investigation of the model for generation of non-thermal emission in the centers of AGN.

3.6.1 Physics of radio-loud AGN

The blazars are radio-loud AGN with one jet pointing along the observer's line of sight. Due to the jet observed configuration, an observer will detect near-pure jet base emission at the center of an AGN, as the disk-corona "central engine" emission is often much less than the jet base emission and nearly invisible in the blazar's X-ray spectrum. This makes blazars extremely intriguing when we plan to explore the features of the jet base emission. Here, was analyzed the relationship between the jet base direct synchrotron emission in the radio spectrum and its IC or SSC emission in X-rays. Taking into consideration that non-blazar type, radio loud (RL) AGN demonstrate the same non-thermal component in their spectra, this feature can provide some opportunities to differentiate between jet base and nuclear (corona+disk) components in their high energies spectra by extrapolating certain parameters of the jet base synchrotron radio spectra to IC/SSC ones.

The size of the jet base is a percentage of pc. It is made up of ultrarelativistic plasma, either electron-proton (hadronic) or electron-positron (leptonic); the nature of this plasma is currently a matter of contention. Plasma particles are produced at relativistic bulk velocities from the central region of an AGN, and as they are accelerated along shock fronts within the jet, they emit synchrotron radiation at wavelengths ranging from radio to ultraviolet and beyond.

Depending on the peak frequency ν_S of the Synchrotron power (of peak intensity) $\nu_S F(\nu_S)$ two classes of BL Lacs were introduced in [157]: High-frequency peaked BL Lacs (HBL) and Low-frequency peaked BL Lacs (LBL). In [158] the same classification was introduced to the sample of all blazars: Intermediate Synchrotron Peaked blazars (ISP, $10^{14} \leq \nu_S \leq 10^{15}$ Hz), Low Synchrotron Peaked blazars (LSP, $\nu_S \leq 10^{14}$ Hz) and High Synchrotron Peaked blazars (HSP, $\nu_S > 10^{15}$ Hz) (see also discussion in [159; 160; 161]).

In addition to the overwhelming non-thermal jet-driven emission, accretion-driven thermal disk radiation, Comptonized to power-law X-ray emission by a hot ~ 100 keV corona, can in some situations contribute significantly to the overall X-ray flux (3C120, 3C273, etc.) [162; 158; 163]. In LSP blazars where IC (SSC) jet components predominate, such a disk-corona contribution should be detectable in X-ray spectra. Some ISP blazars with the junction of dropping synchrotron and rising SSC/IC spectra in the X-ray band (such as IBL S5 0716+714) are also attractive candidates for studying jet-disk-corona interactions in the X-ray band [158; 164].

As it was shown in [165], The synchrotron from the jet and X-ray IC (SSC) spectra are related because they are generated by the same population of leptonic cosmic rays. In particular, there is a correlation between photon indices in the radio band Γ_R and the X-ray band Γ_X .

In this study, was examined how this dependence manifests itself in the radio and X-ray spectra of a sample of radio-loud AGN derived from the cross-correlation with the Swift BAT 105-Month Hard X-ray Survey³ and the Planck Early Release 353-GHz Compact Source Catalog (ERCSC, [166]). For this reason, we compare the photon indices the Swift/XRT+BAT spectra and the 24-240 GHz Planck spectra of the same objects in X-rays.

3.6.2 Spectral energy distribution of the radio loud AGN

In the majority of circumstances, the cosmic-ray electrons and positrons (hereinafter electrons) of the jet are dispersed throughout energies $E > Em$. (Lorentz factor $\gamma = E/m_e c^2 > \gamma_m$) following a single power-law dependency $N(E) \propto E^{-p} \exp(-E/E_{cut})$ of the injected electron spectrum with the spectral index p and an exponential cut-off at $E \sim E_{cut}$ [165; 167]. Such a distribution of ultra-

³<https://swift.gsfc.nasa.gov/results/bs105mon/>

relativistic electrons ($\gamma_m \gg 1$) produces a two-hump spectrum composed of the high-frequency component due to IC of synchrotron photons (synchrotron-self-Compton (SSC)) or external low energy photons (CMB or other background radiation) and low-frequency synchrotron component by the same electron population [168]. The two-hump spectra of two HSPs (Mrk 501 and Mrk 421) and two LSPs (3C273 and 3C279) are displayed in Fig. 32. In the case of 3C273, the thermal contribution of the accretion disk is also apparent in the optical-UV band.

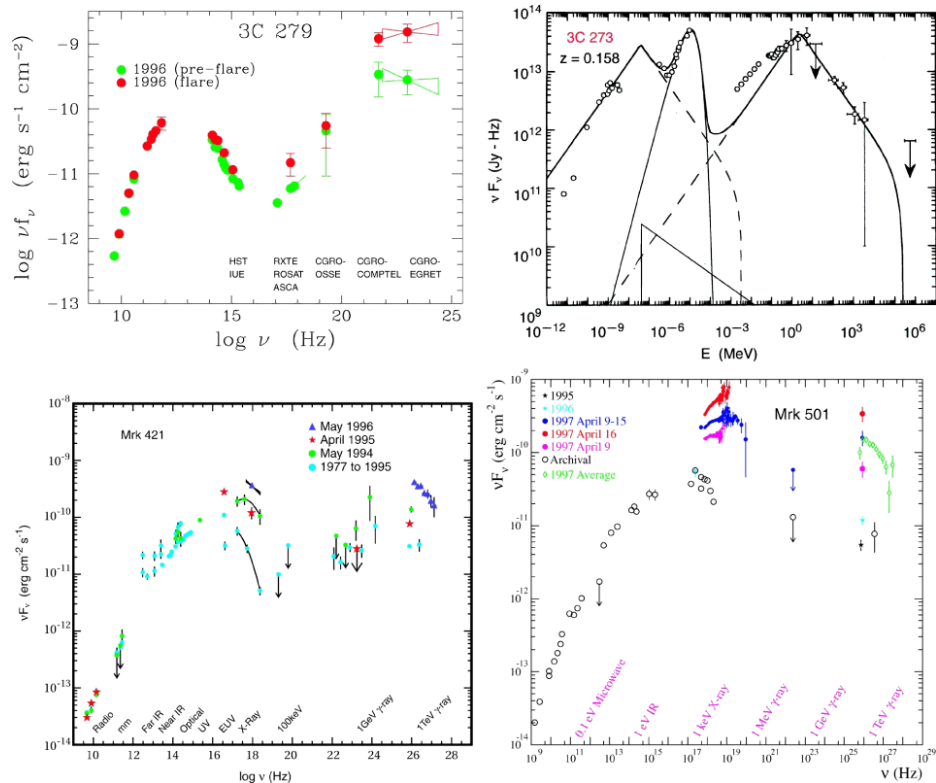


Fig. 32: Two-hump typical multiwavelength spectra of HSP (Mrk 421 and Mrk 501) and LSP (3C273 and 3C279) blazars. Disk thermal contribution in optical-UV band is also visible in the 3C273 case. Credit: A.E. Wehrle/J.H. Buckley/M.A. Catanese/Whipple Collaboration.

The broken power law spectrum of the final emitting electrons with a spectral index of $p+1$ for $\gamma > \gamma_c$ is the result of the rapid radiation cooling of high-energy relativistic electrons (if present). For such a two-parts power law electron spectra, the corresponding synchrotron spectrum in the case of slow cooling ($\gamma_c > \gamma_m$) is determined as four-segment power law $F_\nu \propto \nu^{-\alpha}$ with the spectral indices α_s (the photon index $\Gamma_s = \alpha_s + 1$) equal to -2.0 , $-1/3$, $(p-1)/2$, and $p/2$ for $\nu < \nu_a$, $\nu_a < \nu < \nu_m$, $\nu_m < \nu < \nu_c$, and $\nu > \nu_c$, correspondingly. Here ν_a is the self-absorption frequency, ν_m is the frequency of synchrotron emission of electrons with minimum Lorentz factor $\gamma = \gamma_m$, ν_c is the same for electrons at the edge of fast cooling with $\gamma = \gamma_c$ and the typical case $\nu_a < \nu_m < \nu_c$ with the weak self-absorption regime $\nu_a < \nu_c$ is considered [165]. Synchrotron

frequencies ν_i ($i = a, m, c$) are radiated by electrons with γ_i via γ^2 -scattering of virtual photons with gyrofrequency $\nu_g = \omega_g/2\pi = eB/(2\pi m_e c)$ in magnetic field B : $\nu_i \sim \gamma_i^2 \nu_g$.

The real photons of newly generated synchrotron (SSC) or background (IC) radiation are γ^2 -scattered by the relativistic electrons, and moreover, the distinctive frequencies of SSC spectra rely on those of synchrotron spectra $\nu_{ij}^{IC} \sim \gamma_i^2 \nu_j$. Hence, the SSC spectra profiles are comparable to those of the synchrotron spectra and for the above-mentioned instance $\nu_a < \nu_m < \nu_c$ the four-parts power law spectrum has the spectral indices α_{IC} (the photon index $\Gamma_{IC} = \alpha_{IC} + 1$) equal to -1.0, -1/3, $(p - 1)/2$, and $p/2$ for $\nu < \nu_{ma}^{IC}$, $\nu_{ma}^{IC} < \nu < \nu_{mm}^{IC}$, $\nu_{mm}^{IC} < \nu < \nu_{cc}^{IC}$, and $\nu > \nu_{cc}^{IC}$, correspondingly [165].

The multiwavelength spectral energy distributions of blazars (FSRQs and BL Lacs) exhibit a two-hump structure (Figure 33, taken from [160]). As it is discussed in detail in [160], at low frequencies $\nu < \nu_t$ up to the self-absorption frequency $10^{11} \leq \nu_t/\text{Hz} \leq 10^{12}$ a plausible approximation of all observable spectra in the radio range corresponds to a power law with $\alpha_R = -0.1$ or photon index $\Gamma_R = 0.9$. In $\log(\nu L_\nu) - \log \nu$ representation where L_ν is the spectral luminosity, the peak frequency ν_S of the synchrotron determines the aforementioned classes (HSP, LSP and ISP) of blazars. At frequency $\nu_{cut,S}$ the switch to emission dominated by IC occurs. In a similar way, the peak frequency ν_C determines Compton-dominated hump and at $\nu_{cut,C}$ Compton-dominated emission decays. Between limiting frequencies ν_t and $\nu_{cut,C}$, the two-segment power law approximations for the humps of SSC/IC (photon indices $\Gamma_4 = \Gamma_2$ and Γ_3) and for humps of the synchrotron (photon indices Γ_1 and Γ_2) are presented and analysed in [160]. In Figure 33, parameters of the hump are indicated for the FSRQs with $44 < \log(L_\gamma/\text{erg s}^{-1}) < 45$. In some situations, the connectivity between synchrotron radio-spectra at frequency $\nu_t < \nu < \nu_S$ and IC/SSC X-ray spectra at frequencies $\nu > \nu_{cut,S}$ as traces of emission produced by a shared cosmic-ray electron population is apparent, as shown in Table 7 [160]. Specifically, in the situations of FSRQs with $44 < \log(L_\gamma/\text{erg s}^{-1}) < 47$, the photon indices are $\Gamma_1 \approx 1.5$, while $1.4 < \Gamma_1 < 1.75$ and IC/SSC X-ray emission dominates at $\nu > \nu_{cut,S} \approx 10^{16}$ Hz. There are other potential sources among BL Lacs with $46 < \log(L_\gamma/\text{erg s}^{-1}) < 48$ for which $1.5 < \Gamma_1 < 1.65$ whereas $1.45 < \Gamma_3 < 1.62$ and $\nu > \nu_{cut,S} \approx 6 \times 10^{15}$ Hz IC/SSC X-ray emission dominates.

3.6.3 Spectral Fitting of the AGN Sample

This study incorporates all Swift/XRT+BAT datasets accessible in the public data archive HEASARC for the sample objects designated as beamed AGN. ⁴

⁴<https://swift.gsfc.nasa.gov/results/bs105mon/>

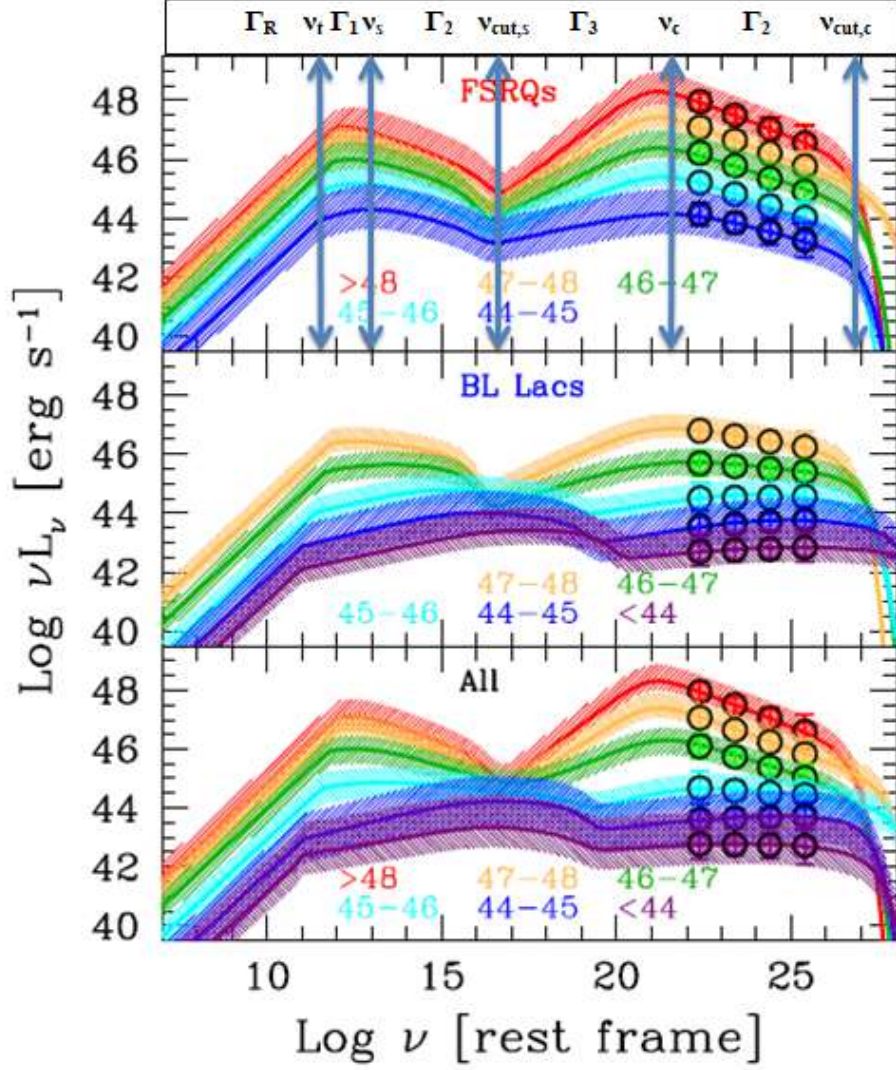


Fig. 33: Spectral characteristics of the two-hump multi-wavelength spectra for the novel phenomenological Fermi blazar sequence, substantiated in [160]. The upper, middle, and lower sections of the diagram depict the spectra of FSRQs, BL Lacs, and all sources, respectively. Different hues correspond to distinct bins of the $\log(L_\gamma/\text{erg s}^{-1})$. The characteristic frequencies and photon indices for the FSRQs example with $44 < \log(L_\gamma/\text{erg s}^{-1}) < 45$ are reported. More details in the text. Figure taken from [160].

Nonetheless, other sources are identifying these objects as BL Lacs (Table 7), FSRQs (Table 8), and Seyferts 1 (Table 9). Following the SIMBAD data⁵, we present the source type, location, and redshift, as well as the neutral hydrogen absorption column in the Galaxy in these Tables.

The Planck spectra within the frequency range of 24 to 240 GHz were extracted from the ERCSC of compact sources detected by Planck during its 2009-2010 survey of the entire sky.

⁵<https://simbad.u-strasbg.fr/simbad/>

These Planck spectra are accessible to the public on the HEAVENS website⁶.

Swift/XRT spectra were produced utilizing observations made by the University of Leicester's UK Swift Science Data Centre (UKSSDC). We used single-pass centroid method with the maximum of 10 attempts and 6 arcmin search radius.

Swift/BAT spectra were collected from the official website of the Swift BAT 105-Month Hard X-ray Survey⁷.

The XSPEC module of the NASA HeaSoft version 6.27.2 program for astronomical data processing and analysis⁸ was used to fit spectra.

Tab 7: Subsample of blazars of BL Lac type

Object	RA [h, m, s]	Dec [$^{\circ}$, $'$, $''$]	N_H [cm^{-2}]	z	Type
PKS 0426-380	04 28 40.42	-37 56 19.58	2.3×10^{20}	1.11	LSP
PKS 0521-36	05 22 57.98	-36 27 30.84	4.1×10^{20}	0.05	LSP
PKS 0537-441	05 38 50.36	-44 05 08.93	3.5×10^{20}	0.89	LSP
S5 1803+784	18 00 45.68	+78 28 04.01	4.1×10^{20}	0.68	LSP
S5 0716+714	07 21 53.44	+71 20 36.36	3.5×10^{20}	0.3	ISP
PKS 2331-240	23 33 55.23	-23 43 40.65	1.7×10^{20}	0.05	ISP
Mrk 501	16 53 52.21	+39 45 36.6	3.5×10^{20}	0.03	HSP
PKS 2005-489	20 09 25.39	-48 49 53.72	4.1×10^{20}	0.07	HSP

To fit the spectra in the radio and X-ray ranges (neutral hydrogen absorption is also included in our model), we used the broken or simple power-law model, with taking into account that the flattening frequency ν_t due to self-absorption may be in the Planck range and the dip frequency $\nu_{cut,S}$ of the transition between synchrotron to IC component may be in the Swift range or higher (Figure 33). The two-segment power law approximation yields two photon indices: $\Gamma_{1,l} < 1$ for $\nu < \nu_t$ and $\Gamma_{1,h} > 1$ for $\nu > \nu_t$, if the self-absorption frequency ν_t falls within the Planck range $24 \text{ GHz} < \nu_t < 240 \text{ GHz}$.

Similarly, simple power law Swift X-ray spectra with $2 > \Gamma_3 \approx \Gamma_1 > 1$ are anticipated for the LSP and some ISP blazars with $\nu_{cut,S} \leq 10^{17} \text{ Hz}$, or below the Swift range. Otherwise, the approximation of X-ray spectra by a two-segment power law will result in two photon indices: $\Gamma_{3,l} > 2$ for $\nu < \nu_{cut,S}$ and $2 > \Gamma_{3,h} > 1$ for $\nu > \nu_{cut,S}$. If $h\nu_{cut,S}$ surpasses the Swift/BAT range

⁶<https://www.isdc.unige.ch/heavens>

⁷<https://swift.gsfc.nasa.gov/results/bs105mon/>

⁸<https://heasarc.gsfc.nasa.gov/lheasoft/>

Tab 8: Sub-sample of blazars of FSRQ type

Object	RA	Dec	N_H [cm^{-2}]	z	Type
S5 0212+735	02 17 30.81	+73 49 32.61	3.9×10^{21}	2.36	FSRQ - LSP
PKS 0312-770	03 11 55.25	-76 51 50.84	8.0×10^{20}	0.22	FSRQ
4C +32.14	03 36 30.1	+32 18 29.34	2.7×10^{21}	1.26	FSRQ
4C +50.11	03 59 29.74	+50 57 50.16 2.7×10^{21}	1.52		FSRQ
PKS 0402-362	04 03 53.74	-36 05 01.91	6.1×10^{19}	1.42	FSRQ
PMN J0525-2338	05 25 06.50	-23 38 10.8	2.4×10^{20}	3.1	FSRQ
PKS 0528+134	05 30 56.46	+13 31 55.14 2.4×10^{20}	2.07		FSRQ - LSP
PKS 0537-286	05 39 54.28	-28 39 55.94	2.4×10^{20}	3.1	FSRQ
B2 0552+39A	05 55 30.80	+39 48 49.16	2×10^{21}	2.37	FSRQ
PMN J0623-6436	06 23 07.69	-64 36 20.71	4.7×10^{20}	0.12	FSRQ
PKS 0723-008	07 25 50.63	-00 54 56.54	1.7×10^{21}	0.12	FSRQ
4C +71.078	08 41 24.35	+70 53 42.28	3.1×10^{20}	2.21	FSRQ
S5 1039+81	10 44 23.06	+80 54 39.44	2.7×10^{20}	1.26	FSRQ
PKS 1127-14	11 30 07.05	-14 49 27.38	3.8×10^{20}	1.18	FSRQ - LSP
4C +49.22	11 53 24.46	+49 31 08.83	3.8×10^{20}	0.33	FSRQ - LSP
FBQS J1159+2914	11 59 31.83	+29 14 43.82	3.8×10^{20}	0.72	FSRQ - LSP
PG 1222+216	12 24 54.45	+21 22 46.38	2.3×10^{20}	0.43	FSRQ
3C 273	12 29 06.69	+02 03 08.59	2.3×10^{20}	0.15	FSRQ - LSP
3C 279	12 56 11.16	-05 47 21.53	2.3×10^{20}	0.53	FSRQ -LSP
PKS 1329-049	13 32 04.46	-05 09 43.3	2.4×10^{20}	2.15	FSRQ
PKS 1335-127	13 37 39.78	-12 57 24.69	6.5×10^{20}	0.54	FSRQ
PMN J1508-4953	15 08 38.94	-49 53 02.32	3.4×10^{21}	-	FSRQ
PKS 1510-08	15 12 50.53	-09 05 59.82	9.3×10^{20}	0.36	FSRQ
PKS 1622-29	16 26 06	-29 51 26.97	2.6×10^{21}	0.81	FSRQ
3C 345	16 42 58.81	+39 48 36.99	2.6×10^{21}	0.59	FSRQ - LSP
PKS 1830-21	18 33 39.92	-21 03 39	2.6×10^{21}	2.5	FSRQ - LSP
B1921-293	19 24 51.05	-29 14 30.12	2×10^{21}	0.35	FSRQ
4C +73.18	19 27 48.49	+73 58 01.57	1.1×10^{21}	0.3	FSRQ
PKS 2008-159	20 11 15.71	-15 46 40.25	2×10^{21}	1.18	FSRQ
QSO B2013+370	20 15 28.72	+37 10 59.51	1.3×10^{22}	0.85	FSRQ
B2 2023+33	20 25 10.84	+33 43	7.7×10^{21}	0.22	FSRQ
PKS 2052-47	20 56 16.35	-47 14 47.62	3.2×10^{20}	1.49	FSRQ
[HB 89] 2142-758	21 48	-75.575	7.7×10^{21}	1.13	FSRQ
PKS 2145+06	21 48 05.45	+06 57 38.6	5.6×10^{20}	1	FSRQ
PKS 2149-306	21 51 55.52	-30 27 53.69	1.8×10^{20}	2.35	FSRQ - LSP
4C +31.63	22 03 14.97	+31 45 38.26	1.2×10^{21}	0.29	FSRQ - LSP
II Zw 171	22 11 53.88	+18 41 49.85	5.1×10^{20}	0.06	FSRQ
[HB 89] 2230+114	22 31 48	+11.721	5.1×10^{20}	1.03	FSRQ
PKS 2227-088	22 29 40.08	-08 32 54.43	5.0×10^{20}	1.55	FSRQ - LSP
3C 454.3	22 53 57	+16 08 53	8.6×10^{20}	0.85	FSRQ

(175 keV), two photon indices describe the falling portion of the synchrotron spectra of HPS blazars: $\Gamma_{3,l} \geq 2$ for $E < E_{br}$ and $\Gamma_{3,h} \geq \Gamma_{3,l}$ for $E > E_{br}$.

In Table 10, we present the model parameters that best suit the Planck and Swift/XRT+BAT spectra of 55 blazars and Seyferts. These were the models used to suit them:

- *po* (Planck spectra - simple power-law,);
- *bknpo* (Planck spectra - broken power-law);
- *po*tbabs* (Swift/XRT+BAT spectra - absorbed power-law);
- *bknpo*tbabs* (Swift/XRT+BAT spectra - absorbed broken power-law).

Tab 9: Sub-sample of AGN of Seyfert 1 type

Object	RA	Dec	$N_H [cm^{-2}]$	z	Type
Mrk 1501	00 10 31.00	+10 58 29.5	7.1×10^{20}	0.09	Seyfert 1
QSO B0309+411	03 13 01.96	+41 20 01.18	1.7×10^{21}	0.13	Seyfert 1
PKS 0405-12	04 07 48.43	-12 11 36.66	4.2×10^{20}	0.57	Seyfert 1
PKS 1143-696	11 45 53.62	-69 54 01.79	2.8×10^{21}	0.24	Seyfert 1
3C 309.1	14 59 07.58	+71 40 19.86	2.4×10^{20}	0.9	Seyfert 1
3C 380	18 29 31.78	+48 44 46.15	2.4×10^{20}	0.69	Seyfert 1
8C 1849+670	18 49 16.07	+67 05 41.68	6.0×10^{20}	0.66	Seyfert 1
NGC 7213	22 09 16.21	-47 10 00.08	1.1×10^{20}	0.005	Seyfert 1

In the Appendix 7, we describe the finer details of our Planck spectrum fitting and data statistics.

In columns 2–4 of Table 10, we provide the results of best fitting photon indices and break energies for the X-ray (XRT+BAT/Swift) spectra for the objects listed in the first column; in the last three columns, we display photon indices and break energy for the Planck spectra. If the difference between the broken power-law and simple power-law is statistically significant (i.e., the null-hypothesis probability $P_{null} < 10\%$, where P_{null} corresponds to the simple power-law model), we provide the broken power-law model parameters that best fit the data. If there is no significant difference between these two models based on χ -statistics and parameter values, we merely display the simple power-law photon index.

3.6.4 Interconnection of Radio and X-ray Spectra in the AGN Sample

As shown in Table 10, 33 of 55 AGN have at least one photon index in the Planck spectrum model that coincides with one of the photon indices in the X-ray spectral model. 23 AGN of this subsample exhibit the pattern in which the single Γ_1 or upper $\Gamma_{1,h}$ photon index of the Planck spectrum coincides within error limits with the lower $\Gamma_{3,l}$ or single Γ_3 photon index in the X-ray spectrum, i.e., in both the radio and X-ray ranges, we observe the lower knees of the synchrotron and SSC/IC components.

This is the case for PKS 2331-240, S5 0212+735, PMN J0623-6436, PKS0312-770, 3C 309.1, PKS0537-441, 4C +31.63, 4C +50.11, 4C +32.14, PKS 1329-049, 4C +73.18, PKS 2227-088, PKS 2005-489, PKS 0426-380, PKS 0405-12, PKS 0723-008, PKS 0528+134, S5 1039+81, B2 0552+39A, S5 1803+784, B2 2023+33, B1921-293, PMN J1508-4953, and others. PG1222+216, PKS 1143-

Tab 10: The best-fit parameters of the model for the Swift (XRT+BAT) and Planck spectra.

Object	X-rays			Radio			
	parameter ->	E_b , keV	$\Gamma_{3,l}$	$\Gamma_{3,h}$	$\Gamma_{1,l}$	E_b , 10^{-4} eV	$\Gamma_{1,h}$
Mrk 1501		74±69	1.62±0.03	2.91±0.16	0.4±0.8	1.6±0.4	1.47±0.09
S5 0212+735		-	1.41±0.08	-	1.57±0.08	4.0±0.6	2.0±0.3
PKS 0312-770		2.7±0.3	2.15±0.08	1.41±0.09	0.4±0.3	2.0±0.2	1.95±0.15
QSO B0309+411		1.2±0.2	2.7±0.6	1.8±0.07	1.0±0.2	-	-
4C +32.14		25±4	1.47±0.07	1.8±0.3	1.62±0.14	-	-
4C +50.11		-	1.66±0.07	-	1.60±0.05	-	-
PKS 0402-362 ²		9.5±9.3	1.58±0.04	2.0±0.5	1.13±0.08	6.0±0.6	1.45±0.05
PKS 0405-12		21±4	1.79±0.15	2.7±0.3	1.64±0.09	-	-
PKS 0426-380		4.1±1.9	1.66±0.07	1.35±0.07	0.7±0.4	2.0±0.6	1.57±0.08
PKS 0521-36		4.8±1.8	1.58±0.03	1.86±0.06	1.11±0.09	4.1±0.7	1.32±0.03
PMN J0525-2338		-	1.5±0.8	-	0.6±0.6	2.5±0.3	2.5±0.5
PKS 0528+134		1.5±0.9	0.9±0.3	1.49±0.07	1.9±0.1	-	-
PKS 0537-441		0.9±0.2	2.0±0.2	1.68±0.03	2.0±0.4	-	-
PKS 0537-286		10.9±5.2	1.20±0.06	1.36±0.04	1.10±0.08	4.1±0.8	1.43±0.03
B2 0552+39A		-	1.45±0.11	-	2.5±0.3	1.9±0.5	1.78±0.10
PMN J0623-6436		-	1.63±0.11	-	0.87 ^{+0.17} _{-0.23}	2.1±0.1	1.59±0.08
S5 0716+714		6.1±0.4	2.02±0.09	1.13±0.06	0.75±0.29	3.4±0.6	1.28±0.07
PKS 0723-008		-	1.62±0.05	-	0.85±0.06	3.7±0.6	1.48±0.06
S5 1039+81		2.7±1.8	1.25±0.35	1.65±0.12	1.38±0.15	-	-
PKS 1127-14		18.4±9.9	1.49±0.06	2.7±1.6	0.6±0.4	2.9±0.6	1.70±0.08
PKS 1143-696		unc.	2.5±1.4	1.79±0.14	1.12±0.35	3.3±1.5	1.85±0.27
4C +49.22		5.4±2.8	1.68±0.05	1.84±0.04	1.29±0.05	-	-
FBQS J1159+2914		47 ⁺⁹⁰ ₋₁₉	1.53±0.04	>1.6	1.17±0.06	-	-
PG 1222+216		1.1±0.1	2.16±0.17	1.43±0.03	0.28±0.22	2.4±0.6	1.62±0.12
3C 273		2.5±0.3	1.52±0.03	1.72±0.01	0.96±0.01	3.8±0.2	1.76±0.03
3C 279		2.5±0.3	1.49±0.05	1.67±0.03	1.12±0.08	4±1	1.60±0.03
PKS 1329-049		-	1.33±0.09	-	1.22±0.09	-	-
PKS 1335-127		6.4±0.7	1.42±0.02	2.1±0.3	1.13±0.04	3.5±0.8	1.64±0.06
3C 309.1		-	1.48±0.07	-	1.41±0.13	-	-
PMN J1508-4953		-	1.32±0.07	-	0.6±0.5	3.5±0.7	1.5±0.3
PKS 1510-08		10.7±6.5	1.31±0.02	1.39±0.05	1.13 ± 0.06	3.3±0.4	1.85±0.09
PKS 1622-29		7.1±0.9	1.39±0.03	1.91 ^{+0.4} _{-0.2}	1.08±0.08	-	-
3C 345		1.2±0.2	1.97±0.22	1.64±0.04	1.33±0.02	3.8±0.8	1.80±0.04
Mrk 501		21±14	2.09±0.01	2.46±0.13	1.57±0.10	-	-
S5 1803+784		-	1.52±0.04	-	1.17±0.04	4.0±0.8	1.51±0.06
3C 380		2.3±0.9	1.67±0.17	2.1±0.3	1.53±0.09	3.7±0.5	1.95±0.15
PKS 1830-21		5.3±0.7	1.40±0.03	1.21±0.05	1.74±0.04	-	-
8C 1849+670		6.3±5.3	1.72±0.10	1.49±0.1	1.26±0.19	3.7±1.6	1.53±0.11
B1921-293		-	1.82±0.10	-	1.32±0.01	4.9±0.3	1.72±0.03
4C +73.18		-	1.76±0.05	-	1.04±0.55	2.2±0.7	1.75±0.08
PKS 2005-489		7.1±0.6	1.42±0.02	2.4±0.3	1.13±0.12	5.5±0.9	1.9±0.3
PKS 2008-159		6.4±0.9	1.40±0.02	2.0 ^{+0.5} _{-0.3}	1.64±0.14	-	-
QSO B2013+370		22±18	1.16±0.20	2.2±0.8	1.51±0.20	-	-
PKS 2052-47		11.0±0.4	1.38±0.02	2.2 ^{+0.5} _{-0.4}	1.39±0.04	4.5±1.5	1.41±0.07
PKS 2145+06		2.0±0.5	1.28±0.06	1.43±0.01	1.35±0.04	3.9±0.4	1.97±0.05
[HB 89] 2142-758		1.8±0.3	0.8±0.3	1.49±0.11	0.7±0.2	2.0±0.2	1.46±0.05
4C +31.63		-	1.62±0.06	-	1.0±0.4	3.0±0.9	1.49±0.154
II Zw 171		-	1.81±0.05	-	1.27±0.16	-	-
PKS 2149-306		14±5	1.22±0.03	1.61±0.13	1.12±0.09	-	-
NGC 7213		-	1.69±0.03	-	-1.67±0.15	-	-
PKS 2227-088		<85	1.3±1.5	1.69±0.32	0.97±0.06	4.2±0.9	1.61±0.08
[HB 89] 2230+114		7.1±2.1	1.40±0.02	1.96±0.11	1.39±0.04	5.7±0.8	2.0±0.2
3C 454.3		1.2±0.3	1.92±0.20	1.62±0.03	0.37±0.05	3.0±0.2	1.21±0.03
PKS 2331-240		7.6±2.2	1.64±0.04	2.4±0.3	0.9±0.07	3.6±0.3	1.57±0.12
4C +71.078		6.7±1.8	1.33±0.03	1.73±0.07	0.73±0.05	3.2±0.5	1.20±0.15
B2 2023+33		-	1.46±0.17	-	1.37±0.15	7.4±0.8	-0.2±0.8

696, 3C 279, 3C 273, and others are among the eight objects of this subsample that exhibit the pattern where the single Γ_1 or upper $\Gamma_{1,h}$ photon index of the Planck spectrum coincides with the upper $\Gamma_{3,h}$ photon index of the X-ray spectrum within the error limits. [HB 89] 2230+114, PKS 0537-286, and 3C 380 contain lower and upper photon indices for the Planck spectrum that correspond with the X-rays; this can be read as the presence of the $\Gamma_{1,l,h}$ and $\Gamma_{3,l,h}$ segments in the Planck and Swift spectra, respectively. Nonetheless, for some of them, like [HB 89] 2142-758, 3C 273, etc., the values of the lower photon indices are below 1, which can be read for the radio range as an indication of self-absorption (see Figure 32 for the 3C273 case).

The subsample of 22 blazars with no correlation between the photon indices is also extremely noteworthy. There are a variety of possible explanations for each of these objects. As demonstrated in [169], the single synchrotron zone model is unsuitable for 3C 454.3. HSP blazar Mrk 501 for which the lower portion of the synchrotron hump is visible in the Planck spectrum and the higher one is visible in X-rays. Mrk 501's SSC/IC spectrum is located above the energies considered here (see Figure 32). Similarly, the two-zone SSC model describes the spectrum features of 4C +49.22 needed [170]. Gravitationally lensed blazar PKS 1830-21 has the spectra that can be distorted by a lensing object [171]. Therefore, the accretion corona/disk counterpart in its X-ray spectrum could be rather large. S5 0716+714 is an ISP type blazar for which most of the Planck spectrum lies in the self-absorbed region. In X-rays, we observe primarily the upper synchrotron knee, a dip-like junction of the synchrotron and SSC spectra at $E_b \approx 6$ keV [164].

3.7 Modelling of gamma-ray emission using MINOT

In this research, I modeled the emission of non-thermal hadronic gamma rays and neutrinos from the Abell cluster A2151 (a dominant part of Hercules cluster) and A1656 (so-called Coma cluster). Based on obtained results was estimated prospects for gamma-ray observations of A2151 by existing and planned ((LHASSO, Fermi-LAT, CTA, IceCube, IceCube-Gen2) ground-based and space-based detectors. For calculations I used code MINOT ⁹ and Λ CDM cosmological model with $H_0 = 70 \text{ km s}^{-1} \text{ Mpc}^{-1}$, $\Omega_M = 0.3$, $\Omega_\Lambda = 0.7$ [172]. In this paragraph I will discuss in more details this code and its limits of applications.

MINOT (Modeling of the Intra-cluster medium (Non-)thermal content and Observables prediction Tools) is a software aimed for the self-consistent modeling of the non-thermal and thermal diffuse components of GCs and is based on the Python language. With help of this code one can compute multi-wavelength predictions for wide range of electromagnetic bands and even for neutri-

⁹<https://github.com/remi-adam/minot>

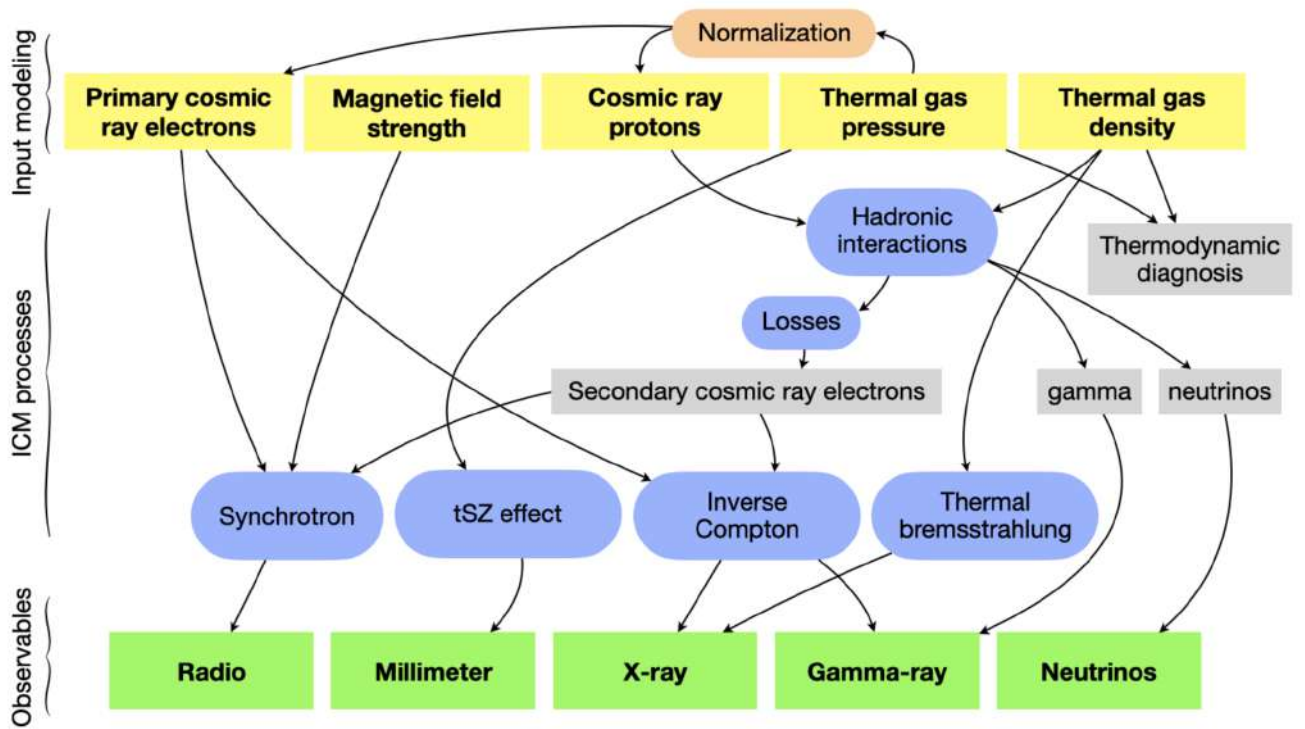


Fig. 34: Overview of the MINOT input parameters, relevant ICM processes and resulting observables. Figure taken from [142]

nos. MINOT includes different radial and spectral profiles that can explain various components of the clusters. It directly models the spectral and spatial distributions of the thermal gas and cosmic rays. Based on their characteristics we can get predictions for observables for the radio to γ -ray bands. But not only predictions in EM range is available, but also neutrino emissions, that was generated by hadronic processes. All these output data are made in the form of surface brightness profiles, integrated flux and spectra.

Figure 34 demonstrates how different input parameters evolve inside the code into what we get as output. So as we can see from figure, we need to have knowledge about thermal gas density and CR profiles for modeling hadronic interactions. This modeling is based on the modern theoretical predictions based on Naima software [173]. As a result we can get gamma-ray and neutrino spectra that can be used to further analysis of GC observables.

3.8 Hercules galaxy cluster

The nearby Hercules supercluster ($z=0.0367$) is one of the largest formations in the Local Universe. It is composed by Abell clusters A2147, A2152 and A2151 (the Hercules cluster) [174], schematic overview of this sky region can be seen at Fig. 35. The most prominent GC A2151 with

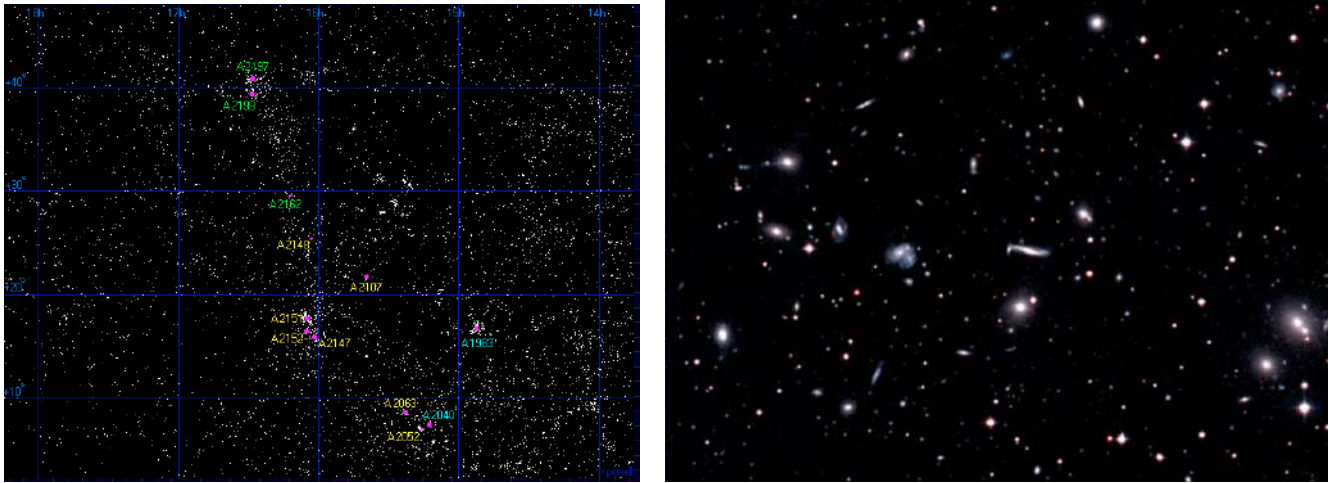


Fig. 35: Left: morphology of region on the sky around Hercules supercluster. Right: image of Hercules cluster made by VST, Image credit ESO/INAF-VST/OmegaCAM/A

mass $M_{200} = 4.00 \times 10^{14} M_{\odot}$ and size $R_{200} = 1.45$ Mpc includes three subclusters and is still in the processes of collapsing and mergers [175]. There are 7 galaxies with active nuclei in central part of A2151, including NGC 6050 - a pair of interacting galaxies NGC 6050 and IC 1179.

Considered in this work GC A2151 contains nearly 360 galaxies. Its optical center lies at R.A. = 241.34° and Dec = 17.75° [175]. This cluster is significantly subdivided into a number of substructures, including the bright center bimodal subclump A2151C and two fainter substructures, A2151N and A2151E. Based on XMM-Newton and Chandra observation, A2151C also can be divided into two substructures - fainter lateral A2151C(F) and bright central A2151C(B)[176]. According to state of the art sensitivity of our γ -ray detectors, only A2151C has enough powerful flux to be detected, so in this work was investigated such possibility.

The spatial distribution of matter (barionic and dark), magnetic fields, and CRs (leptonic and hadronic components) within the ICM determines the thermal and non-thermal emission characteristics of GCs. To recover this distributions one can use observational data about thermal X-ray emission and CMB distortions due to the thermal SZ effect. These data allow to recover a spatial distribution of partial pressure of electrons $P_e(r)$ and of total pressure of baryonic gas $P_{tot}(r)$ inside ICM. The distributions of magnetic fields and CR within the ICM can be constructed based on the formulas described above.

Recent research [176] reveals fresh observational findings about thermal X-ray emission and the recovery of thermodynamic characteristics of ICM plasma in the brightest subclumps A2151CB and A2151CF. Table 11 displays the parameters of the ICM in subclumps A2151CF and A2151CB that we utilized to model their γ -ray and neutrino emission. Based on these data, I calculated normalization factor P_0 (in Table its denoted by star) for pressure profile from Eq. (32). Other

pressure distribution characteristics were obtained from Planck Universal Profile 2013 [177]. It was also necessary to calculate the γ -ray flux absorption that rises from the photon interactions with an extragalactic background light (EBL) [178]. Python package `ebtable`¹⁰ was used for this purpose.

Using described above parameters of GCs and CRs as input ones, I used open available software MINOT for performing the modelling.

Tab 11: Simulation parameters

Global Parameters	A2151CB	A2151CF	A1656 (ICM only)	A1656 (with AGN)
z	0.0368	0.0368	0.0231	0.0231
M_{500} in [$10^{13} M_{\odot}$]	9.08 ± 5.24	3.01 ± 2.11	6.13	6.13
R_{500} in [kpc]	$803.38^{+113.18}_{-172.13}$	$566.09^{+89.09}_{-158.26}$	1310	1310
R_{trunc} in [kpc]	2410.15	1698.28	3930	3930
helium mass fraction	0.2735	0.2735	0.2735	0.2735
metallicity	0.0153	0.0153	0.0153	0.0153
abundance	0.43	0.13	0.3	0.3
hydrostatic mass bias	0.2	0.2	0.2	0.2
$X_{cr,p} = U_{cr,p}/U_{th}$ inside R_{500}	0.1	0.1	0.02	0.06
$X_{cr,e1} = U_{cr,e1}/U_{th}$ inside R_{500}	0.01	0.01	0.00002	0.00006
$E_{p,min}$ in [GeV]	1.21	1.21	1.21	1.21
$E_{p,cut}$ in [TeV]	30	30	30	30
$E_{p,max}$ in [TeV]	10^6	10^6	10^6	10^6
Spectral index α_p (Model)	1.5 (PLEC)	1.5 (PLEC)	2.3 (PLEC)	1.8 (PLEC)
$E_{e1,min}$ in [keV]	511	511	511	511
$E_{e1,break}$ in [GeV]	-	-	-	-
$E_{e1,cut}$ in [TeV]	10^6	10^6	-	-
$E_{e1,max}$ in [TeV]	10^6	10^6	10^{-2}	10^{-2}
Spectral index α_{e1} (Model)	2.3 (PL)	2.3 (PL)	3.0 (PL)	3.0 (PL)
Density CR_p model				
$n_{CR,p}(r) \propto n_e(r)^{\eta_{CR,p}}$	$\eta_{CR,p} = 1.0$	$\eta_{CR,p} = 1.0$	$\eta_{CR,p} = 1.0$	$\eta_{CR,p} = 2.0$
Density CR_{e1} model				
$n_{CR,e}(r) \propto n_e(r)^{\eta_{CR,e}}$	$\eta_{CR,e} = 1.0$	$\eta_{CR,e} = 1.0$	$\eta_{CR,e} = 1.0$	$\eta_{CR,e} = 1.0$
Pressure gas model (GNFW):	$P_0 + PUP$	$P_0 + PUP$	$P_0 + PUP$ (Eq.(1) Remi paper)	$P_0 + PUP$
P_0 [keV/cm^3]	0.009*	0.0077*	0.022	0.02
a_p	1.33	1.33	1.8	1.8
b_p	4.13	4.13	3.1	3.1
c_p	0.31	0.31	0.0	0.0
c_{500}	1.81	1.81	-	-
r_p in [kpc]	-	-	466.8	466.8
Density gas model (beta)				
n_0 [cm^{-3}]	0.00875	0.0049	3.36×10^{-3}	3.36×10^{-3}
r_c [kpc]	19.35	10.43	310	310
β_{dens}	0.38	0.28	0.75	0.75
Magnetic field (Eq.(31))				
B_0 [μG]	5	5	4.7	4.7
η_B	2/3	2/3	0.5	0.5

Main results for the neutrino and γ -ray emission for A2151CF and A2151CB subclumps are presented in Fig 36-39. The most promising cases for detection by CTA derectors correspond to hard CR spectrum (spectral index $\alpha_p < 2$). In particular, Fig. 36 demonstrates expected gamma-ray flux from the central brightest subclump A2151CB for $\alpha_p = 1.5$ and for three values of cluster

¹⁰<https://github.com/me-manu/ebtable/>

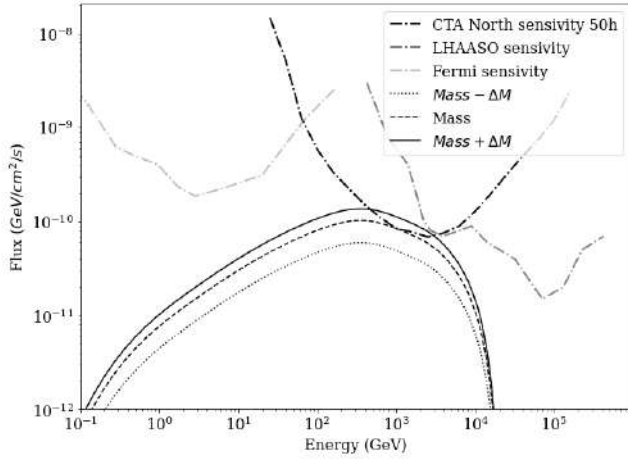


Fig. 36: Spectral flux from A2151CB for three values of cluster mass M_{500} and $M_{500} \pm \Delta m$. Other parameters as in Table 11

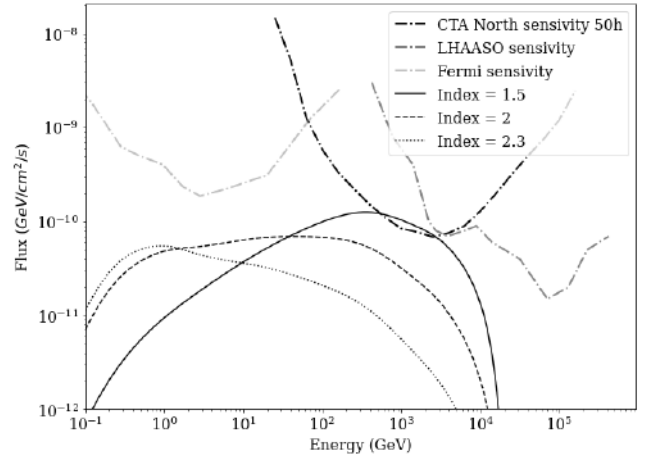


Fig. 37: Spectral flux from A2151CB for three values of spectral index. CRs distribution $CR_p \propto n_e(r)^2$. Other parameters as in Table 11

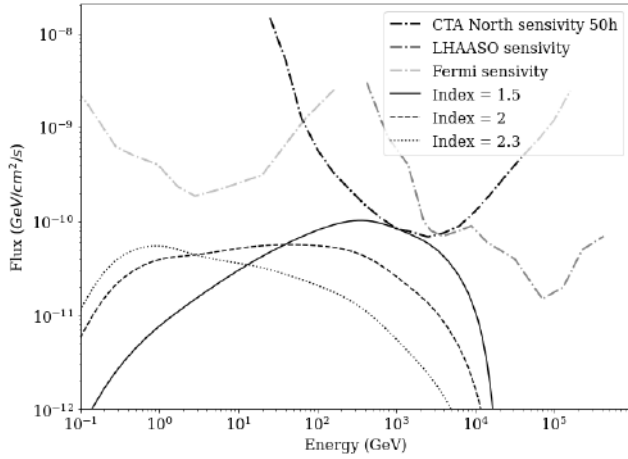


Fig. 38: Spectral flux from A2151CB for three values of spectral index. Other parameters as in Table 11

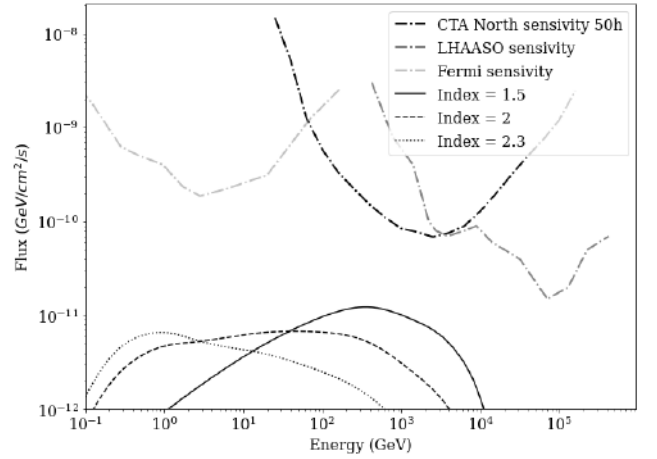


Fig. 39: Spectral flux from A2151CF for three values of spectral index. Other parameters as in Table 11

mass - average mass and $\pm \Delta m$ from Table 11. Meantime, there is no significant increase in flow due to more compact CR distribution (a result of magnification of $\eta_{CR,p}$ twice is shown in Fig. 37).

For comparing different models of CR distribution in ICM, I simulated γ -ray flux for three values of spectral index - see Fig. 38 and Fig. 39. As one can see from these figures, there is a possibility for CTA to detect the brightest subclump A2151CB in case of hard CR spectrum, instead of A2151CF, that has relatively low flux for all CR distribution models (Fig. 39). Calculated neutrino flux from the brightest subclump A2151CB together with IceCube discovery potential [179] at significance level 5σ is shown in Fig. 40. This figure demonstrates that neutrinos do not

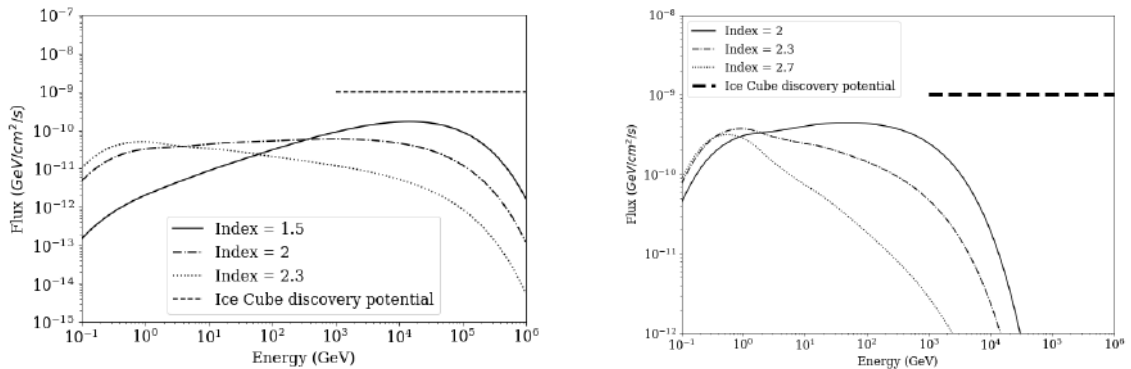


Fig. 40: Left: Neutrino flux from the brightest subclump A2151CB. Right: Neutrino flux from the A1656 together with IceCube 5σ discovery potential at 1-1000 TeV

suffer by energy losses due to EBL absorption, unlike photons. This can make neutrino emission an effective GC probe in the future.

3.9 Coma galaxy cluster

The Coma GC (A1656) has the redshift $z = 0.0231$. Recently, gamma radiation in the A1656 direction has been detected for the first time with the help of the Fermi-LAT telescope [180; 181]. Both the Coma GC and the Fermi-LAT point source 4FGL J1256.9+2736 (radio galaxy NGC 4839) can be its source. Therefore, this GC is a good candidate for the further study of the generation of non-thermal gamma radiation and neutrinos in the harder (TeV) gamma spectral interval. Besides the proton-proton interactions in the ICM, one may expect that the active nucleus of the galaxy NGC 4839 should also make a contribution to the total radiation flux [181]. For instance, the arrival direction of high-energy neutrinos detected by IceCube (event IC200921A) coincides with the AGN of NGC4839 within a localization error of 90%.

As was mentioned in the previous case of Hercules cluster, we can restore the spatial distributions of the temperature $T_e(r)$, electron concentration $n_e(r)$, partial pressure of electrons $P_e(r)$, and total pressure of baryonic gas $P_{gas}(r)$ inside the ICM. Using the formulas presented in the section 3.3, we can simulate the distributions of magnetic fields and CRs in the ICM. The recent work [182] contains new observational results on thermal X-ray radiation and the restoration of the thermodynamic plasma parameters of the ICM of A1656 that were obtained from observations of the new SRG/eROSITA X space X-ray mission.

Taking the available data into account, a set of parameters necessary for modeling gamma and neutrino radiation from the Coma GC making use of MINOT software code has been formed (see Table). As in the case of Hercules cluster, the absorption of gamma-ray flux owing to the

interaction with intergalactic background radiation was made allowance for with the help of the Python software package `ebtable`¹¹.

At first, was calculated the expected spectra of gamma (Fig. 41) and neutrino (Right Fig. 40) emission for physical models neglecting the contributions made by the AGN and the merging processes to the total CR stock. While comparing various models of CR distribution in the ICM, was simulated the gamma-ray flux using three values for the spectral index, $\alpha_p = 2, 2.3, \text{ and } 2.7$ (See Fig. 41). The cases that are the most promising for CTA detection correspond to the hard CR spectrum (the spectral index $\alpha_p \approx 2$). The sensitivity of the CTA experiment was taken from this webpage¹² and the sensitivity of the LHAASO one from work [183]. At the same time, a twofold enhancement of the gamma-ray flux occurring owing to a more compact spatial distribution of CRs is observed only at low energies (not higher than tens of GeVs, Fig. 41). Therefore, it follows from Fig. 41 that the Coma cluster (A1656) can be detected in the TeV spectral interval using the CTA array only if the CR spectrum is hard. The calculated neutrino flux from A1656 is shown in Fig. 40 together with the observed IceCube potential at a statistical significance level of 5σ .

We are expecting that the AGN in A1656 can substantially contribute to the total CR amount in the ICM of this GC. Taking into account the processes of active merging of two GCs associated with the NGC4839 group and A1656 [182], let us consider a model with a harder radiation spectrum, which is formed owing to the additional contribution to the total CR amount from the AGN and the merging processes. As a result of CR acceleration in AGN jets - in particular, owing to magnetic switching - the expected spectral index of such CRs will be hard with typical values $\alpha_p = 1.4 - 1.8$ for strongly magnetized plasma. The corresponding spectrum of gamma radiation from pp-collisions in CRs accelerated in the jets is depicted in Fig. 42 for three values of the spectral index, $\alpha_p = 1.4, 1.6, \text{ and } 1.8$.

The most promising for the CTA detection is the CR spectrum with the hardest spectral index ($\alpha_p = 1.4$ in our calculations). In Fig. 4, a neutrino flux calculated in the hard spectrum case is exhibited. One can see that in our model, IceCube can register neutrino events already if the CR energy fraction in the thermal ICM energy equals $X_{cr,p} \approx 0.05$. It is important to note that, unlike photons, neutrinos do not undergo energy losses due to their interaction with the CMB at TeV energies: the neutrino spectrum, which reproduces the CR spectrum with the energy shift $E_\nu \approx 0.1E_p$, is exponentially cut at energies $E_{\nu,cut} \approx 0.1E_{p,cut} \approx 3 \text{ TeV}$ only due to the high-energy cut-off of the CR spectrum at $E_{p,cut} = 30 \text{ TeV}$ in the considered case (Figs. 2 and 4). For the CR spectrum with $E_{p,cut} = 300 \text{ TeV}$, we have $E_{\nu,cut} \approx 30 \text{ TeV}$. At the same

¹¹<https://github.com/me-manu/ebtable/>

¹²<https://www.cta-observatory.org/science/cta-performance>

time, owing to $\gamma + \gamma \rightarrow e^+ + e^-$ annihilations, the path length of 10-100 TeV photons equals $\lambda_{\gamma\gamma} \approx 200 \times (E_\gamma/10\text{TeV})^{-2}$ Mpc [182] and gives rise to an additional abrupt cut-off of the gamma radiation spectrum from the Coma GC (at the distance of about 100 Mpc) at energies of about 20 TeV (Figs. 41 and 42). This fact confirms the prospects of neutrino studies of physical processes running in GCs.

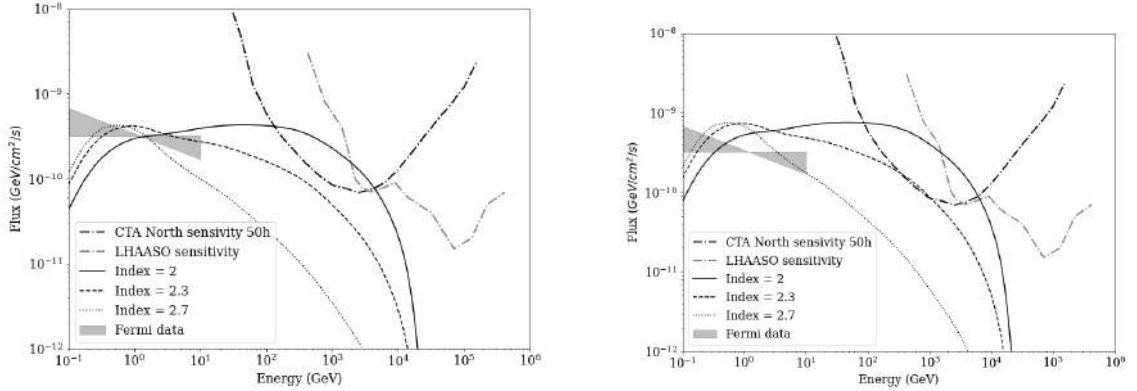


Fig. 41: The spectral flux of gamma radiation from A1656 for three values of the spectral index. Left: for CR distribution $CRp \propto n_e(r)$. Right: for CR distribution $CRp \propto n_e(r)^2$. Other parameters as in Table 11.

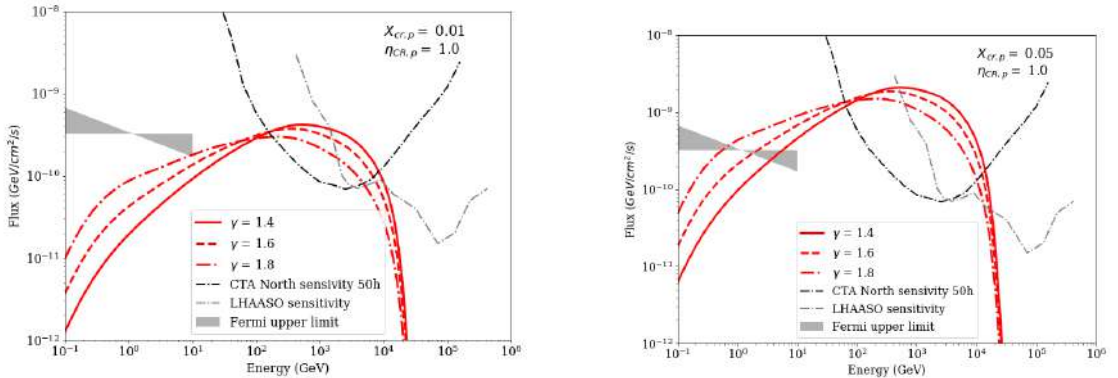


Fig. 42: The spectral flux of gamma radiation from A1656 with AGN feedback for different values of parameter $X_{cr,p} = 0.01$ (Left) and 0.05 (Right). Other parameters as in Table 11.

3.10 Conclusions

Due to a long time for cosmic rays diffusion escape, GCs should be a luminous extragalactic sources of neutrino and non-thermal gamma-rays, but such emission has not been detected yet. Using the recent data from [176] about thermal X-ray emission of brightest subclumps A2151CB and

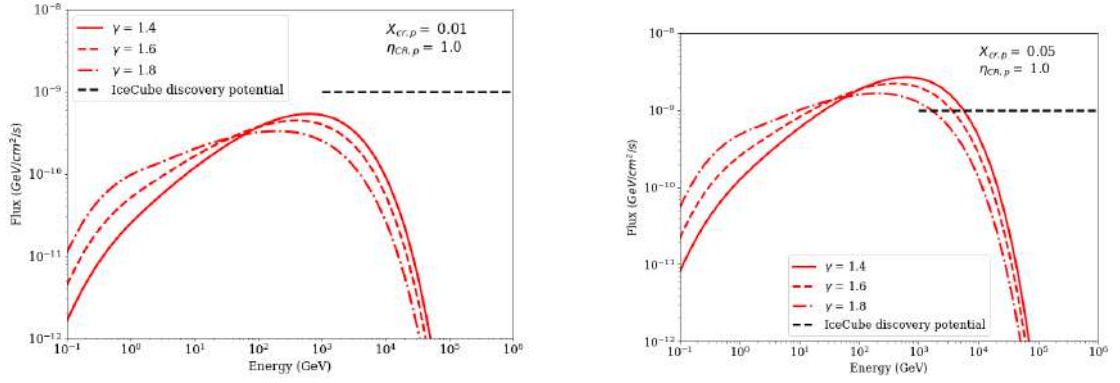


Fig. 43: Neutrino spectrum from A1656 with AGN feedback for different values of parameter $X_{cr,p} = 0.01$ (Left) and 0.05 (Right). Other parameters as in Table 11.

A2151CF in GC A2151 I have carried out a modelling of non-thermal hadronic γ -ray and neutrino emission for these subclumps using MINOT code [142]. Results of this simulations show that under the typical parameters of CR distribution (CR proton to thermal energy ratio $X_{cr,p} \approx 0.04 - 0.06$, spectral index of proton power-law energy spectrum $\gamma = 2.5$) both non-thermal hadronic γ -ray and neutrino emission of subclumps A2151CF and A2151CB are still undetected by existing and planned detectors. Meantime, backreaction of 7 AGN-type galaxies in subclumps A2151CB and A2151CF and other unaccounted for sources of CRs (accretion flows, merging, turbulence etc.) can increase $X_{cr,p} \approx 0.1$ and provide harder spectral index $\gamma = 1.5 - 2.0$. In these cases brighter subclump A2151CB can be detected by CTA at 5σ level. The hard CR proton spectrum is also promising for neutrino flux detection from GCs in future neutrino detectors (IceCube-Gen2 etc.). Contrary to γ -ray fluxes, neutrino fluxes do not attenuate by interaction with the EBL, therefore, there are promising possibilities to detect PeV- neutrinos in case of GCs - cosmic PeVatrons with hard ($\gamma < 2.0$) spectra.

On the basis of current data obtained for thermal X-ray radiation and thermodynamic parameters of plasma inside the GC A1656, was simulated non-thermal gamma and neutrino radiation using the MINOT software. The simulation of hadronic gamma radiation emitted from the Coma GC as a result of pp-collisions of CR protons with ICM plasma is consistent with Fermi-LAT observational data (100 MeV - 300 GeV) at typical CR parameters; namely, the ratio between the CR energy and the plasma thermal energy $X_{cr,p} \approx 0.02$, the spectral index $\alpha_p = 2.3 - 2.7$, and the spatial distribution of CRs insignificantly increases the spectral flux (by a factor of two for $\eta_{cr,p} = 2$). Owing to large values of the spectral index (they correspond to small values of the Mach number M for the shock waves at the fronts of which CRs accelerate), the spectral fluxes of TeV gamma emission are insufficient for reliable detection. The situation can be better for CRs

with a hard spectrum, i.e., with small values of the spectral index, $\alpha_p \leq 2$ (Fig. 42). The hard CR spectrum is expected for the CR acceleration at the fronts of strong shock waves ($M \geq 10$, $\alpha_p \approx 2$) or at the switching of the magnetic field lines in the AGN jets ($\alpha_p < 2$). In GCs - in particular, the Coma GC - strong shock waves can accompany the processes of substructure merging, and jets are certainly present in the radio-loud AGN inside GCs. Figure 42 demonstrates that CRs with a hard spectrum can provide a detectable spectral flux of TeV gamma emission even at a relatively small fraction of CR energy, $X_{r,p} \approx 0.01$.

To summarise, I would like to note that the simulation results obtained for the fluxes of non-thermal gamma emission and neutrinos from the Coma GC testify to a real possibility of its registration with available (Fermi-LAT, LHAASO, Ice-Cube) and planned ground-based (CTA, IceCube-Gen2) detectors.

During above mentioned modelling was recognized strong influence of AGN energetic flux on the overall energy deposit in the GC. In this work were considered radio loud AGN and compared spectrum indices for radio and x-ray emission. In the simple one-zone model of multi-wavelength radiation of radio-loud AGN the observable two-hump spectra with νL_ν -maxima in low-energy ($\sim 10^{-1} - 10^4$ eV) and high-energy ($\geq 10^7$ eV) bands can be naturally explained by the non-thermal synchrotron and SSC/IC emission of relativistic leptons, accelerated at relativistic shocks, and during magnetic field reconnections in relativistic jets. Typical power-law spectra of accelerated leptonic cosmic-rays result in similar predicted slopes or photon indices of high energy X-ray and γ -ray and low-energy radio emission. In the meantime, the Comptonised thermal X-ray luminosity of the accretion disk+corona complex in some radio-loud AGN can be comparable to the non-thermal X-ray jet luminosity. The investigation of radio and X-ray spectra of such AGN enables the separation of jet and disk-corona contributions and the clarification of AGN radiative processes. Planck radio and Swift /XRT+BAT X-ray spectra are compared for a sample of 55 beamed AGN (Seyferts 1 and Blazars) from the Swift-BAT 105-Month Hard X-ray Survey. There are found confirmation of expected one-zone model coincidences between radio and X-ray photon indices for 33 of 55 AGN. As anticipated, comparing radio and X-ray data can assist in distinguishing jet and disk-corona contributions in the case of LSP and some ISP radio-loud AGN, in which the switch from synchrotron to SC/SSC dominant contribution occurs in the sub-keV range.

4 Transient sources of EHECR in the Galaxy and Local Universe based on example of magnetar SGR1900+14

4.1 Introduction

In modern astrophysics CR acceleration sources can be separated into individual classes, in one of which the acceleration occurs in the transient jets. Such sources don't have enough permanent energetic stock to accelerate particles to the highest energies. But this class of objects can eject enormous amounts of energy during transient jets events, and therefore accelerate EHECR. Such objects are present in our Galaxy and in other galaxies.

Prime candidates for PeVatrons are star formation regions (SFRs), SNRs, and PWNe. Nonthermal high-energy (HE, $\varepsilon > 100$ MeV) and very high-energy (VHE, $\varepsilon > 100$ GeV) γ -ray emission from these sources should be indicative of acceleration processes. In this work was investigated the possibility that the HE and VHE γ -ray emission from the sky region around magnetar SGR 1900+14's is a signature of CRs accelerated in the aforementioned sources. In order to accomplish this, in this work was simulated the γ -ray emission from the extended VHE H.E.S.S. source candidate HOTS J1907+091, the Fermi-LAT HE extended source 4FGL J1908.6+0915e and the point HAWC TeV source 3HWC J1907+085. This sources are spatially coincident with the magnetar SGR 1900+14, the SNR G42.8+0.6 and the SFR W49A. Simulations are conducted within the framework of the hadronic and leptonic models. Here is demonstrated that the observed γ -ray emission from the magnetar SGR 1900+14 region can, in principle, include contributions of varying intensities from three types of potentially confused sources. The most promising one is considered in detail case of a magnetar-connected, but undetected SNR and a PWN, but have a severe requirement on the energy reserve of radiated CR particles - on the order of $10^{51} d_{10\text{kpc}}^2$ erg for sources at a distance of $d \sim 10$ kpc. Such an energy reserve can be supplied by the Hypernova or MWN remnant created by the newly-born millisecond magnetar's abundant supply of rotational energy $E_{\text{rot}} \sim 10^{52}$ erg.

In addition, here was reconstructed the evolutionary path of the magnetar from its birthplace in a young compact cluster Cl 1900+14 to its outburst as Hypernova and subsequent Hypernova remnant (HNR) evolution.

As it will be shown in subsequent section, this particular magnetar can be the source of triplet of EHECR events.

4.2 Looking for Galactic transient sources of UHECR

Galactic ($E_{\text{cr}} \lesssim 10^{18}$ eV) and extragalactic ($E_{\text{cr}} \gtrsim 10^{17}$ eV) cosmic ray sources and acceleration mechanisms are among the major unsolved problems in contemporary astrophysics. As mentioned previously, UHECR are believed to be of extragalactic origin, but it is also possible that transient Galactic sources contribute.

In potential Galactic sources of CRs – SNRs, PWNe and Star formation regions (SFRs) – powerful shock waves can provide an effective DSA of protons, heavier nuclei with a charge $Z > 1$, and electrons/positrons up to multi-PeV energies $E > 10^{15}Z$ eV.

Nonthermal HE and VHE γ -ray emission and neutrino messenger from CR sources' neighbourhoods due to CR nuclei-target ISM nuclei inelastic collisions with subsequent pion decay (thereafter pp -collisions, (hadronic scenario)) and inverse Compton (IC) scatter (leptonic scenario).

Consequently, the observed spectra and morphology of γ -ray sources provide unique information regarding both the physical processes occurring in the sources and the mechanisms of CR acceleration.

Recent observations of the sky region surrounding magnetar SGR 1900+14 have uncovered a number of unidentified sources, particularly in the γ -ray band. It includes three point-like sources from the 4FGL Catalogue (J1908.7+0812, J1910.0+0904, J1911.0+0905) and the 4FGL J1908.6+0915e extended source, based on the first eight years of observations from the *Fermi*-LAT Gamma-ray Space Telescope [184]. Also the extended source candidate (hotspot) HOTS J1907+091 that was detected by the High Energy Spectroscopic System (H.E.S.S.) and the point-like source 3HWC 2HWC J1907+084*/J1907+085 from the 3HWC catalog of sources which have energies higher than several TeV of the High Altitude Water Cherenkov (HAWC) observatory [185] and [186].

The magnetar SGR 1900+14 itself is one of the possible candidates for these γ -ray sources. Magnetars are young neutron stars with extremely strong magnetic fields on their surfaces. $B_s \sim 10^{14} - 10^{15}$ G [187; 188; 189; 190; 191; 192; 193]. Magnetars exhibit persistent X-ray – γ -ray activity as repeated hard X-ray – soft γ -ray flares (soft gamma repeaters, SGRs) [194; 188; 189; 195] and persistent/transient quiescent super-luminous X-ray emission, in addition to short bursts (milliseconds/seconds) and longer outbursts (weeks/months), named AXPs - anomalous X-ray pulsars [196; 189; 197]. The total magnetar luminosity is supported primarily by the decay of magnetar's magnetic energy during the evolution of a neutron star's magnetic field or the reconfiguration of magnetospheric fields [188; 189].

In comparison to a typical pulsar, the evolution of magnetars is characterized by a unique set of characteristics due to their large magnetic fields. Dissipation of a dipolar magnetic field's energy

($E_{\text{mag}} \approx B_s^2 R_{\text{NS}}^3 / 6 \approx 3 \times 10^{47} B_{s,15}^2$ erg for a neutron star's radius of $R_{\text{NS}} = 12$ km) a source of X-ray – γ -ray activity in magnetars, including rare giant flares - short (~ 0.1 s) hard X-ray – soft gamma-ray bursts with luminosities $\sim 10^{44} - 10^{47}$ erg s $^{-1}$ and energies that are released $\sim 10^{44} - 10^{46}$ erg (SGR 1900+14 case on 27 August 1998 , from SGR 0526–66 on 1979 March 5, and SGR 1806–20 case on 27 December 2004)[198]. Unless otherwise specified, in this section the physical quantities will be expressed as $Q = 10^n Q_n$ in cgs units. A sudden release of magnetic energy in over-twisted magnetospheres through solar flare-like fast reconnections generates a GRB-like fireball and an ultrarelativistic (Lorentz factor $\gamma_j \lesssim 10$) outflow [188; 199], observed as afterglows in radio range of the SGR 1900+14 [200] and the SGR 1806–20 [201] giant flares.

Absence of reliable signs of unquestionably existing MWN and magnetar-connected SNR can be explained by both the great distance of $d_{\text{mag}} \sim 12.5$ kpc and the great absorption in the Galactic plane [198]. Magnetars are again promising UHECR accelerators due to the anticipated presence of magnetar giant flares, relativistic shock waves and reconnection processes in newborn millisecond magnetar winds [202; 203; 204; 205; 206; 207; 208; 209]. As previously argued in [210], the magnetar SGR 1900+14 can be a potential source of $E_{\text{cr}} > 10^{20}$ eV EHECR triplet [211] in view of joint data of Telescope Array (TA) [212] and Auger [213] detectors. This fact can be proven after calculating backtracking trajectories of EHECR in the GMF model (Fig. 44).

Reasonable association between the distant magnetar SGR 1900+14 and the "po star" of 4 BCE [214] implies a Hypernova type of a magnetar-connected SN with favorable conditions for UHECR acceleration [207]. If this is the case, then the magnetar SGR 1900+14 should also manifests as a PeVatron with nonthermal emission from radio to TeV-range [215; 216].

In addition to SGR 1900+14, other possible source candidates includes two SNRs: SNR G 43.3-0.2 and SNR G42.8+0.6 from the Galactic Supernova Remnants Catalogue and the SFRs magnetar host stellar clusters W49A and Cl 1900+14 (Fig. 44). The possibility of source confusion should also be considered.

4.3 Sky region around the magnetar SGR1900+14 in different bands

4.3.1 Sky region around SGR 1900+14 in the γ -ray band

Search for persistent and pulsed γ -ray emission from 20 magnetars (including SGR 1900+14) in six years of *Fermi*-LAT data was unsuccessful with upper limits $\sim 10^{-12} - 10^{-11}$ erg cm $^{-2}$ s $^{-1}$ in the 0.1 – 10 GeV band [217]. Simultaneously, a positive result of this search revealed an extended

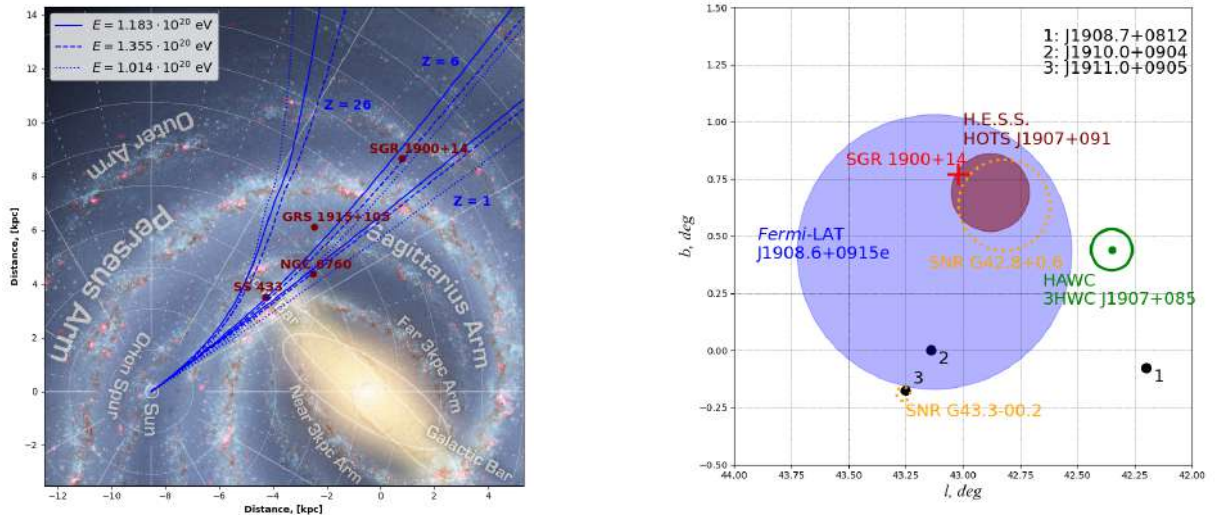


Fig. 44: Magnetar SGR 1900+14 vicinity. Left (a): backward trajectories of the $E > 10^{20}$ eV triplet in the magnetar region. NASA/JPL-Caltech/R. Hurt, SSC/Caltech kindly provided the background image. Right (b): γ -ray sources emitting HE and VHE in the magnetar region. The extended *Fermi*-LAT source 4FGL J1908.6+0915e (blue circle), the H.E.S.S. extended source HOTS J1907+091 (brown circle), the HAWC point-like source 3HWC J1907.8+085 (the green bullet with a 1σ error box) and three extragalactic point-like 4FGL sources (black points) are shown. Two SNRs (orange rings) in the field are not physically connected to the region that are under consideration.

γ -ray source that coincides in position with SGR 1900+14 and the neighboring SNR G042.8+00.6. 4FGL J1908.6+0915e coordinates - RA = $287^{\circ}.16$, Dec = $9^{\circ}.26$ ($l = 43^{\circ}.1249$, $b = 0^{\circ}.4301$), and radius of $\Theta_{\text{HE}} = 0^{\circ}.6$ from *Fermi*-LAT 4FGL Catalogue [184] are extended and has an overall significance only 4.58σ (5.8σ in 4FGL, v.27) (Fig. 44). In the 50 MeV – 1 TeV energy range, 4FGL J1908.6+0915e photon flux density can be approximated by a power-law

$$F_{\text{ph}}(\varepsilon) = F_{\text{ph}}(\varepsilon_0)(\varepsilon/\varepsilon_0)^{-\Gamma}, \quad (43)$$

with the photon index $\Gamma = 2.23 \pm 0.098$, the reference (pivot) energy $\varepsilon_0 = 4.52$ GeV and normalization $F_{\text{ph}}(\varepsilon_0) = (1.01 \pm 0.19) \times 10^{-13}$ ph cm $^{-2}$ s $^{-1}$ MeV $^{-1}$. SNR G42.8+0.6 from this catalogue is noted as a likely associated source.

There are recent [218] report about the connection of a point-like source 4FGL J1910.2+0904c (Fig. 44) with the γ -ray emission from a massive SFR – W49A.

In the VHE γ -ray domain, the HGPS [186] reveals a candidate source (hotspot) HOTS J1907+091 with test statistics above 30 (TS > 30) detection threshold in one (TS = 43) of 2 analyses (significance TS = 18).

Two potential counterparts of HOTS J1907+091 coincide spatially with the hotspot: the SNR G42.8+0.6 and the magnetar SGR 1900+14 [186].

Using blind search techniques for γ -ray source detection in [219] authors discovered potentially valuable objects in the HGPS significance map. Bunch of objects around the SGR 1900+14 position recovered by edge detection and Hough circle transform correspond to the expanded structure with circular symmetry of the TeV source (Fig. 44).

TeV point-like source 3HWC J1907+085 from 3HWC HAWC Observatory Gamma-Ray Catalog [185], with coordinates RA = 286°.79, Dec = 8°.57 ($l = 42°.35$, $b = 0°.44$), (all with $1\sigma_{\text{stat}} = 0°.09$) is the nearest source to SGR 1900+14 (a separation of approximately $\approx 0°.75$), a relatively low TS = 75.5 peak on a large background spot [220].

There are no additional spatially coincident sources of 3HWC J1907+085. The nearest pulsar ($\sim 0°.3$) in the Australia Telescope National Facility Pulsar Catalogue (ATNF) of 1509 pulsars [221] PSR J1908+0839 (period $P = 0.185$ s, distance $d = 8.27$ kpc, characteristic age $\tau_c = 1.23$ Myr, spin down power $\dot{E} = 1.5 \times 10^{34}$ erg s $^{-1}$) is too slow rotating and too old in order to support the necessary TeV luminosity of putative PWN [222].

In recent work [223], the H.E.S.S. Collaboration published new analysis for the H.E.S.S. data where revealed that the hotspot HOTS J1907+091 is a genuine new source HESS J1907+089, i.e., it is the H.E.S.S. detection of the HAWC J1907+085 source.

It is confirmed from observations that in the magnetar SGR1900+14 region, only extended HE and VHE γ -ray sources can be considered: the H.E.S.S. source HESS J1907+089/HOTS J1907+091, the hotspot around the HAWC point-like source 2HWC J1907+084* / 3HWC J1907+085 and *Fermi*-LAT source 4FGL J1908.6+0915e (Fig. 44).

4.3.2 Sky region around SGR 1900+14 in the radio band

The radio observation of SGR 1900+14 sky region does not display any signatures of any magnetar, and of a magnetar-connected SNR or a MWN, only 3σ limits on an extended emission of 6.2mJy arcmin $^{-2}$ (1.4 GHz) and 6.1mJy arcmin $^{-2}$ (332 MHz) were found [224] (Figs. 46–50). In the vicinity of SGR 1900+14, only shell-type SNR has been detected in radio band - G42.8+0.6 (of 24' size, $l = 42°.820$, $b = 0°.635$, spectral flux density $F_\nu = 2.0 \pm 0.2$ Jy at 2.695 GHz, 2.4 ± 0.6 Jy at 1.420 GHz, 1.5 ± 0.2 Jy at 4.750 GHz, spectral index $\alpha = 0.4$) [225]. The angular separation between the magnetar and the SNR G42.8+0.6 centre (boundary) is of order of $\sim 15'$ ($3'$) (Fig. 44). Young ($\tau_c \approx 38$ kyr) $P = 226$ ms pulsar PSR J1907+0918 ($l = 43°.024$, $b = 0°.730$ $d = 8.2$ kpc), is the neighbour of SGR 1900+14, the separation between the pulsars $\approx 2'$ [226; 224]. Despite the young age of both pulsars, they can not be physically connected to the SNR G42.8+0.6 because

of very high necessary transverse velocity $v_t = 4 \times 10^3 (d_p/10 \text{ kpc}) / (t_p/10^4 \text{ yr}) \text{ km s}^{-1}$ for observer distances $d_p \sim 5 - 15 \text{ kpc}$ and ages $t_p \sim 10^3 - 4 \times 10^4 \text{ yr}$ of pulsars [227; 226].

Another one, more distant from the magnetar ($\sim 1^\circ$), shell-type SNR G43.3-0.2 (W49B), of $4' \times 3'$ size at distance $d = 11.3 \text{ kpc}$, $l = 43^\circ.275$, $b = -0^\circ.190$, spectral flux density $F_\epsilon = 38 \text{ Jy}$ at 1 GHz , spectral index $\alpha = 0.46$) [228] is detected also in X-ray and γ -ray range as a young (age $t \approx 6 \text{ kyr}$) compact (radius $R \approx 8 \text{ pc}$) SNR is powerfull cosmic ray accelerator with the proton CR energy $W_{\text{cr,p}} \approx 2 \times 10^{49} \text{ erg}$, which is evolving in a dense molecular cloud (number density $n_{\text{mc}} \approx 650 \text{ cm}^{-3}$) [229]. Due to the large separation (greater than 1 kpc), W49B can not be spatially connected to the neighborhood of SGR 1900+14.

4.3.3 Sky region around SGR 1900+14 in the optical/infrared band

Initial searches for an optical/infrared (IR) counterpart to SGR 1900+14 were unsuccessful: Keck J/Ks-band and HST/STIS images placed only upper limits of $m_{50\text{CCD}} \gtrsim 29.0 \text{ mag}$, $J \gtrsim 22.8 \text{ mag}$, $K_s \gtrsim 20.8 \text{ mag}$ [224]. Only in [230] a newly detected variable “object # 7” with $K_s \approx 19.7 \text{ mag}$ and $\Delta K_s = 0.47 \pm 0.11 \text{ mag}$, due to observations with NACO/ESO-VLT inside error circle of the radio position of SGR 1900+14, proposed as a prospective IR candidate corresponding to SGR 1900+14. Keck 2 LGS-AO/NIRC2 observation later confirmed "Star 7" as the IR counterpart [231].

[231] confirmed claimed in [232; 233] physical connection between the magnetar and the young, $R_{\text{cl}} \approx 0.4 - 0.6 \text{ pc}$ -radius cluster of massive stars Cl 1900+14, also known as the SGR 1900+14 Star Cluster [234], with a few Blue Supergiant (BSG) stars and two luminosity-dominated M5 Red Supergiant (RSG) improved in [235] distance $d_{\text{cl}} = 12.5 \pm 1.7 \text{ kpc}$ and extinction $A_V = 12.9 \pm 0.5 \text{ mag}$.

The IR elliptical shell around SGR 1900+14 (Fig.45), discovered by [236] in Spitzer $16 \mu\text{m}$ and $24 \mu\text{m}$ images, provides additional confirmation of a physical connection between the magnetar and the cluster. [236] suggests that this shell is a dust-free cavity produced by the magnetar giant flare on SGR 1900+14 on August 27, 1998 in the stellar cluster-connected dusty gas.

Observed shell dust IR flux of $0.4 \pm 0.1 \text{ Jy}$ and $1.2 \pm 0.2 \text{ Jy}$ at $16 \mu\text{m}$ and $24 \mu\text{m}$, respectively, and temperature of $80 - 120 \text{ K}$, with the absence of ring signatures at X-ray, optical, near-IR, or radio- bands can be explained in model of dust heating by the intrinsic star cluster without the need for SN explosion shock wave presence. The 3D dust radiative transfer modeling [237] reproduces observational data in model of a low density cavity in the circumcluster medium with a molecular cloud-like extinction and sharp intrinsic boundary, and two RSG stars illuminating the cavity. Cluster Cl1900+14, where SGR 1900+14 resides, is categorized as “OC2: open cluster

without ATLASGAL counterpart and without gas” in the Catalog of 695 open and embedded stellar clusters in the inner part of the Galaxy (VizieR J/A+A/560/A76) [234]. In a complete sample of ~ 8000 $M_{\text{mc}} \gtrsim 10^3 M_{\odot}$ dense clumps located in the Galactic disc ($5^{\circ} < l < 60^{\circ}$) ATLASGAL [238] angle separation with the nearest clump is around $0^{\circ}.8$ (G043.141-00.01), at the same time in the CO survey of all-Galaxy ($M_{\text{mc}} \gtrsim 3 \times 10^3 M_{\odot}$ in the outer Galaxy) [239] the closest molecular cloud with $l = 43^{\circ}.553$, $b = 0^{\circ}.567$ is of $0^{\circ}.57$ away.

4.3.4 Sky region around SGR 1900+14 in the X-ray band

In the X-ray band, after the giant magnetar flare (in 1998) and two brightenings (in 2006 and 2001), SGR 1900+14 has returned to its minimum quiescent flux level with a two-component spectrum typical of magnetars: a hard power-law component with a photon index of $\Gamma = 1.21$ and a black body component with a temperature of $k_{\text{B}}T = 0.52$ keV.

For a column density of $N_{\text{H}} = 1.9 \times 10^{22} \text{ cm}^{-2}$, the quiescent bolometric luminosity is of $L_{\text{bol}} = 5.6 \times 10^{35} \text{ erg s}^{-1}$ [190; 240; 241; 242]. Recent analysis of XMM-Newton and NuSTAR data [242] has revealed the spin-down rate \dot{P} and monotonic decrease in the 1 – 10 keV flux in 2006-2016. Newly obtained values $P = 5.22669(3) \text{ s}$, $\dot{P} = 3.3 \times 10^{-11} \text{ s s}^{-1}$ correspond to the value of magnetic field on the magnetar $B_{\text{s}} = 4.3 \times 10^{14} \text{ G}$ and the characteristic age $\tau_{\text{c}} \approx 2.4 \text{ kyr}$ (cf. the old value $\tau_{\text{c}} \approx 700 \text{ yr}$). In the X-ray band, no signatures of an adjacent SNR or MWN have yet been detected.

For SGR 1900+14 was adopted the intrinsic 2 – 10 keV flux (unabsorbed) $F_{2-10\text{keV}} = 1.8 \times 10^{-12} \text{ erg cm}^{-2}\text{s}^{-1} = 1.1 \times 10^{-9} \text{ GeV cm}^{-2}\text{s}^{-1}$ [242] as an upper limit for expected MWN/SNR 2-10 keV flux.

4.4 Expected signatures of PWNe, SNRs and SFRs in the sky region around SGR1900+14

HE and VHE γ -ray sources detected in the SGR 1900+14 region: extended 4FGL J1908.6+0915e and extended HOTS J1907+091, and point-like peaks on enhanced background 2HWCJ1907+084* / 3HWCJ1907+085 and HESS J1907+089 can correspond to three potential acceleration sites of relativistic leptons and hadrons: PWNe, SNRs, and SFRs. Due to the presence of powerful shock waves with effective diffusive shock acceleration of CRs, this objects are prominent Galactic PeVatrons — accelerators of electrons/positrons, heavier nuclei and protons with energies up to PeV. In addition, observations indicate that they manifest as nonthermal radiation, specifically

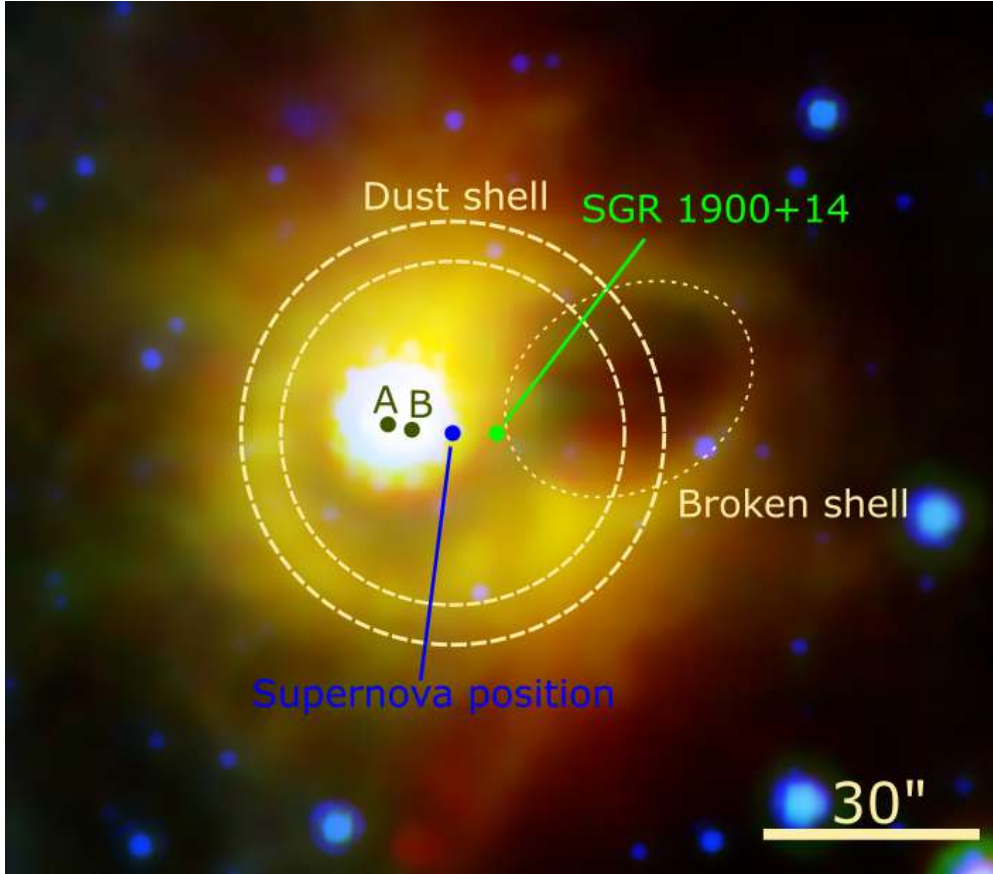


Fig. 45: Red ($24 \mu\text{m}$), blue ($8 \mu\text{m}$) and green ($16 \mu\text{m}$), are the colors used on the Spitzer IR map of the SGR 1900+14 environment. We denoted the present magnetar position with the green dot and the positions of two RSGs at the center in the open cluster Cl 1900+14 with the black dots A and B. In our model, the blue bullet in the center of the dust shell (yellow dash ring) represents the location of the Supernova 2 kyr years ago, while the broken shell (the yellow dotted ellipse) was caused by the anisotropic giant flare on August 27, 1998. Text for more details. Courtesy NASA/JPL/Caltech/S. Wachter (Caltech-SSC)

HE and VHE γ -ray emissions.

4.4.1 PWNe, SNRs and SFRs as CR accelerators

At least two SNRs exist in the region of SGR 1900+14: SNR of an unidentified SN that gave birth to a magnetar (Fig. 44) and SNR G042.8+0.6. Like other neutron stars, magnetar SGR 1900+14 is a compact remnant of a core collapse SN explosion.

In the case of a typical SN explosion, SN ejecta with a typical kinetic energy of $W_{\text{ej}} \sim 1$ Bethe (where B is 10^{51} erg (varies from 0.09 to 2.3 B for the masses around 9-27 M_{\odot} progenitors) interacts with ISM, forming a shock-bounded bubble of swept ISM gas with energy reserve of $W_{\text{SNR}} \sim W_{\text{ej}} \sim 10^{51}$ erg (SNR). A newborn neutron star - a typical radio pulsar with a magnetic

field of $B_s \sim 10^{12}$ G, a rotational period of $P_i \sim 0.01 - 0.1$ s, and a rotational energy of $E_{\text{rot}} \sim 10^{48} - 10^{50}$ erg - generates a TS-bounded PWN that resides inside the SNR with energy reserve about $W_{\text{PWN}} \lesssim E_{\text{rot}} \lesssim 10^{50}$ erg [243].

SNRs are effective accelerators of both leptonic (electrons) and hadronic (nuclei and protons) components of Galactic CRs by DSA of ISM particles on the SNR shocks.

Anticipated spectra of shock-accelerated nuclei (primarily protons, $i = p$) and electrons ($i = e$) are power-law (PL) or exponential cut-off power-law (ECPL) in nature:

$$N_i(E_i) = N_{0,i}(E_i/E_{0,i})^{-\Gamma_{\text{cr},i}} \exp(-E_i/E_{\text{cut},i}), \quad (44)$$

where $E_{0,i}$ is the CR reference energy, $N_{0,i}$ is the normalisation, $N_{0,e}(E) = K_{ep}N_{0,p}(E)$, K_{ep} is the electron-to-proton energy fraction, $E_{\text{cut},i}$ and $\Gamma_{\text{cr},i}$ are the cut-off energy and the spectral index for i -th component, respectively. Standard value for spectral index in 1st order Fermi nonrelativistic DSA is $\Gamma_{\text{cr},i} = 2$, in case of parallel shocks with relativistic speed $\Gamma_{\text{cr},i} = 2.2$ [244; 245]. Observations of Galactic CR sources, e.g. radio-sources with spectral energy flux $F_\varepsilon \propto \varepsilon^{-\alpha}$ with $\alpha = \Gamma + 1 = (\Gamma_{\text{cr},e} - 1)/2 \approx (0.6 - 0.8)$ and diffuse Galactic CR background correspond to $\Gamma_{\text{cr},i} = 2.2 - 2.5$ [246; 247; 248; 249; 250; 251; 252; 253].

The total energy of CR $W_{\text{cr},i}$ ($i = p, e$) is

$$W_{\text{cr},i} = \int_{E_{\text{min},i}}^{E_{\text{max},i}} EN_{0,i}(E/E_{0,i})^{-\Gamma_{\text{cr},i}} \exp(-E/E_{\text{cut},i}) dE, \quad (45)$$

and CR components, that was accelerated at SNR shock, including hadrons with overall energy $W_{\text{cr},p} = \eta_{\text{cr}} W_{\text{SNR}}$ and leptons with total energy $W_{\text{cr},e} = K_{ep} W_{\text{cr},p}$, where $\eta_{\text{cr}} \sim 0.1$ is the CR acceleration efficiency.

In typical SNR ($W_{\text{SNR}} \sim 10^{51}$ erg) we expect $W_{\text{cr},p} \sim 0.1\eta_{p,-1}W_{\text{SNR}} \sim 10^{50}\eta_{p,-1}$ erg, $W_{\text{cr},e} \sim 0.01K_{ep,-2}W_{\text{cr},p} \sim 10^{48}K_{ep,-2}$ erg for young SNR (with age $t_{\text{SNR}} \lesssim 10^4$ yr and radius of $R_{\text{SNR}}(t \sim 10^3 \text{ yr}) \lesssim 10$ pc) [254; 255]. Hereafter the physical quantities are expressed by $Q = 10^n Q_n$ in units of cgs (if not specified otherwise).

Maximum energy of the CRs accelerated by DSA in the SN, with particle charge Ze , velocity $V_{\text{sh}} = \beta_{\text{sh}} \cdot c$ and shock-compressed magnetic field of ISM $B_{\text{sh}} = \sqrt{11}B_{\text{ISM}}$ is [253]:

$$E_{\text{max}} \approx Ze\beta_{\text{sh}}R_{\text{SNR}}B_{\text{sh}} \approx 3 \times 10^2 Z\beta_{\text{sh},-2}R_{\text{SNR},19}B_{\text{sh},-5} \text{ TeV}, \quad (46)$$

or $E_{\text{max}} \approx 0.9Z$ PeV in our case.

Accelerated CRs that have collected in a downstream region are vulnerable to adiabatic losses because of the nonzero divergence of the SNR plasma expansion velocity (\bar{v}). [256]:

$$\dot{E}_{i,\text{ad}} = -\frac{1}{3}(\nabla \cdot \bar{v})E_i. \quad (47)$$

In a spherically symmetric SNR $E_i \propto R_{\text{SNR}}^{-1} \propto t_{\text{SNR}}^{-0.4}$, therefore adiabatic loss time $t_{\text{ad}} = (E_i/\dot{E}_i)_{\text{ad}} = 2.5t_{\text{SNR}}$ exceeds the SNR age. During the same time, CRs of hadronic origin diffusively escapes into upstream region where occurs density enhancement ($n_{\text{ISM}} \gtrsim 1 \text{ cm}^{-3}$), and are noticeably losing energy in collisions with ISM nuclei and protons. For pp collisions cross-section $\sigma_{pp} = 40 \text{ mb}$ and the coefficient of inelasticity - part of proton energy lost in interaction - $\kappa \approx 0.5$ the cooling time is $t_{pp} = (\kappa n_{\text{ISM}} \sigma_{pp} c)^{-1} \approx 1.7 \times 10^{15} n_{\text{ISM}} \text{ s}$ [215]. Produced in collisions secondary pions fastly decay into leptons, in particular, hadronic mechanism of γ -ray generation is consequent for neutral pion decay $pp \rightarrow \pi^0 \rightarrow \gamma\gamma$. In the hadronic $E_p \gtrsim 10 \text{ GeV}$ scenario CR protons with energy $E_p \gtrsim 10 \text{ GeV}$ produce γ -ray photons with energy $\varepsilon \approx 0.1E_p$ and CR protons with power-law spectrum (44) produce power-law spectrum of γ -ray photons (43) with the spectral photon index $\Gamma = \Gamma_{\text{cr},p}$. Time scale for γ -ray production is $t_{pp,\gamma} = (\kappa_{\pi^0} n_{\text{ISM}} \sigma_{pp} c)^{-1} \approx 5 \times 10^{15} n_{\text{ISM}} \text{ s}$, where $\kappa_{\pi^0} \approx 0.17$ is the transferred to π^0 fraction of proton kinetic energy [246; 248; 257].

Ultra high energy protons with Lorentz factor γ_p such that energy of background photon ε in proton rest frame $\varepsilon' = \gamma_p \varepsilon > 145 \text{ MeV}$ produce mesons (pions) in proton-photon collisions $p + \gamma \rightarrow p + \pi^0$, $p + \gamma \rightarrow n + \pi^+$. For CMB photons with $\varepsilon_{\text{CMB}} \approx 3k_B T_{\text{CMB}} \approx 7 \times 10^{-4} \text{ eV}$, where k_B is the Boltzmann constant, $\gamma_p \geq 10^{11}$. Cooling time for photopion production is $t_{p\gamma} = (\kappa_{p\gamma} n_{\gamma} \sigma_{p\gamma} c)^{-1} \approx 1.2 \times 10^{15} (n_{\gamma}/n_{\text{CMB}})^{-1} \text{ s}$, where $\kappa_{p\gamma} \approx 0.2$ is the coefficient of inelasticity and $\sigma_{p\gamma} \approx 340 \text{ } \mu\text{b}$ is the cross-section for the photopion production [246; 248]. Photopion production is strongly negligible for Galactic CRs that was accelerated at SNR shocks.

Proton energy losses due to nonthermal (synchrotron and IC) radiation are $(m_p/m_e)^4 \approx 1.1 \times 10^{13}$ times less than electron energy losses of the same energy.

Observable spectra of hadronic γ -ray emission are determined by parameters of hadronic CR spectra (44) and number densities of target ISM particles n_{ISM} [258; 259; 186].

Galactic SFRs, that include OB associations, stellar clusters, and superbubbles, are also promising sources of Galactic CRs and potential Galactic PeVatrons [260; 261; 262].

There are two SFRs in the SGR 1900+14 region: W49 complex which contains star forming region W49A with SNR W49B and a magnetar-connected star cluster Cl 1900+14 (Fig. 44).

In SFRs, a common interaction between the powerful winds of massive stars and SN ejectas results in the formation of a collection of powerful individual and large-scale TS. Similar to the preceding SNR case, DSA is effective here and provides power-law CR spectra with spectral indexes of $\Gamma_{\text{cr}} = 2 - 2.3$. Again, the presence of multiple shocks increases the acceleration efficiency of CR and their maximum energies [260]. Some SFRs, including the magnetar SGR 1806-20-connected

star cluster Cl*1806-20, have been detected emitting VHE γ -rays [263; 264; 261].

Another type of effective accelerators of CRs are PWNe, but mainly due to their leptonic (positron and electron) components as dominant pulsar wind constituents via DSA at the relativistic TS [265; 266; 267; 268; 269; 270; 263; 271; 272], as well as via an ion-cyclotron waves resonant absorption and driven magnetic reconnection (MR) [267; 272].

In the PWN case, the complex nature of lepton CR acceleration makes it impossible to reliably determine CR spectral characteristics. The evident CRs relativistic leptonic component in PWNe is due to time-dependent MR/TS acceleration and cooling/escaping/advection processes [263; 271]. The total leptonic contributions from various injection epochs and spatial localization make up the observable SED in PWNe. In this case we observe leptonic exponential cut-off broken power-law (ECBPL) spectrum:

$$N_e(E_e) = \begin{cases} N_{0,e}(E_e/E_{0,e})^{-\Gamma_{1,\text{cr},e}}, E_e < E_{\text{br},e} \\ N_{0,e}(E_{\text{br},e}/E_{0,e})^{\Gamma_{2,\text{cr},e}-\Gamma_{1,\text{cr},e}}(E_e/E_{0,e})^{-\Gamma_{2,\text{cr},e}} \\ \quad \times \exp(-E_e/E_{\text{cut},e}), E_e \geq E_{\text{br},e} \end{cases} \quad (48)$$

with characteristic break energy $E_{\text{br},e}$ and two PL spectra with $\Gamma_{1,\text{cr},e} < 2$ for $E_e \leq E_{\text{br},e}$ and $\Gamma_{2,\text{cr},e} > 2$ for $E_e \geq E_{\text{br},e}$ is widely used in PWN modelling [273; 274].

Acceleration of leptonic components in young ($t \lesssim t_{\text{sd},i}$) PWNe is very efficient. Considerable part η_e of spin-down luminosity L_{sd} is converted into CR lepton energy $W_{\text{cr},e}$: $\eta_e = \dot{W}_{\text{cr},e}/L_{\text{sd}} \lesssim 1$, but energy losses produced by accelerated leptons result in an observed value of $W_{\text{cr},e} \lesssim 10^{49}$ erg [263].

Maximum energy of CR leptons, accelerated in the PWN with the radius of PWN $R_{\text{PWN}} \sim 10^{19}$ cm, at relativistic TS with the TS velocity $\beta_{\text{TS}} = V_{\text{TS}}/c \approx 1$, and the magnetic field inside it $B_{\text{PWN}} \sim 100 \mu\text{G}$ is significantly smaller than ~ 300 PeV, predicted by (44) due to their large energy losses inside PWN.

Relativistic electrons in the SFR/SNR case and electrons/positrons the PWN case (hereafter in this work are used the term electrons to the both positrons and electrons) interact with magnetic fields of energy density $w_B = B^2/8\pi$ and with background radiation components, each of them with energy density $w_{\text{rad},i}$: infrared (i = IR), cosmic microwave background (i = CMB), star light (i = SL) radiation, producing IC – synchrotron self-Compton (SSC) (in the GeV – TeV band) and synchrotron (in the radio – X-ray band) emission. [265; 268; 271; 272].

For typical relativistic electron with Lorentz factor $\gamma_e \gg 1$ and energy $E_e = \gamma_e m_e c^2$ the rate of energy losses is

$$P(E_e) = -\frac{dE_e}{dt} = \frac{4}{3}\sigma_{TC}(w_B + \sum_i w_{\text{rad},i} f_{\text{KN},i}(E_e, T_i))\gamma_e^2, \quad (49)$$

where σ_T is Thomson cross-section and

$$f_{\text{KN},i} = \frac{45K^2/64\pi^2}{45K^2/64\pi^2 + \gamma_e^2}, \quad (50)$$

where $K = m_e c^2 / k_B T_i$ and T_i is the background i -th component temperature ($i = \text{SL}, \text{IR}, \text{CMB}$), describes transition to Klein-Nishina scattering [275]. From (49) it follows that electron energy loss time for synchrotron emission in Thomson regime

$$t_{\text{syn}}(\gamma_e) = \frac{E_e}{P_{\text{syn}}(E_e)} = \frac{6\pi m_e c}{\sigma_T B^2 \gamma_e} = 2.4 \times 10^1 B_{-5}^{-2} \gamma_{e,7}^{-1} \text{ kyr}, \quad (51)$$

while the energy loss time in case of IC emission is

$$t_{\text{IC},i}(\gamma_e) = \frac{3m_e c}{4\sigma_T w_{\text{rad},i} \gamma_e} = 2.6 \times 10^2 \frac{w_{\text{rad,CMB}}}{w_{\text{rad},i}} \gamma_{e,7}^{-1} \text{ kyr}. \quad (52)$$

Here $B_{\text{CMB}} = (8\pi w_{\text{rad,CMB}})^{1/2} = 3.2 \mu\text{G}$ and $w_{\text{rad,CMB}} = 0.26 \text{ eV cm}^{-3}$.

CR electrons that are advecting in downstream flow suffer also from adiabatic losses that characterize by adiabatic time loss (47) determined by flow velocity V_{PWN} : $t_{\text{ad,PWN}} = R_{\text{PWN}}/V_{\text{PWN}}$ and PWN radius R_{PWN} [256].

Maximum energy of CR electrons in PWNe is characterised by the balance of loss and acceleration processes. Characteristic acceleration time of CR with energy E and Larmor radius $r_L = E/ZeB$ in magnetic field B in DSA at SNR shock wave of velocity $V_{\text{sw}} = \beta_{\text{sw}}c$ in Bohm diffusion (with diffusion coefficient $D_B = r_L c/3$) is $t_{\text{acc}} = 8D_B/V_{\text{sw}}^2 = 8r_L/3\beta_{\text{sw}}^2 c$ [252]. Similar value $t_{\text{acc}} \approx r_L/c$ is expected in PWNe with relativistic TS [251]. For the most significant synchrotron losses, the CR electron's maximum energy $E_{e,\text{max}} = \gamma_{e,\text{max}} m_e c^2$ follows from equality $t_{\text{acc}} = t_{\text{syn}}$:

$$\gamma_{e,\text{max}} = \frac{3m_e c^2}{2e^{3/2} B^{1/2}} = 3.8 \times 10^{10} B_{-5}^{-1/2}. \quad (53)$$

Observable spectra of leptonic γ -ray emission are determined by parameters of CR leptonic spectra (48) and background radiation [263].

Worth to note also that in young SNRs, including one connected to a magnetar, hadronic and leptonic emission is produced under a slow cooling regime. Both the leptonic cooling time for IC channels and synchrotron $t_i \approx 1.3 \times 10^2 (w_{\text{rad,CMB}}/w_{\text{rad},i})(E_e/10 \text{ TeV})^{-1} \text{ kyr}$ ($i = \text{IR}, \text{CMB}, \text{SL}$) and the hadronic energy loss time for inelastic pp collisions $t_{pp,\gamma} \approx 1.7 \times 10^5 (n_{\text{ISM}}/1 \text{ cm}^{-3})^{-1} \text{ kyr}$ exceed the age of magnetar $t_{\text{mag}} \approx 2 \text{ kyr}$ for $E_e \lesssim 100 \text{ TeV}$.

4.4.2 Energy requirements for γ -ray sources in the region of SGR 1900+14

First, was evaluated the energy requirements of potential sources for explaining observed GeV/TeV emission from the SGR 1900+14 outskirts.

To achieve this, was employed the recipe presented in [257]. In the leptonic scenario, only the Thomson regime IC emission from CMB photon scattering is considered.

Considering the hadronic scenario of emission, the γ -ray emission from HOTS J1907+091 is explained as a result of pp interactions of SNR/SFR shock-accelerated protons and heavy nuclei with the ISM plasma.

For the aforementioned HOTS J1907+091 integral photon flux $F_{\text{ph}}(\varepsilon > 1 \text{ TeV}) = 4.3 \times 10^{-13} \text{ cm}^{-2} \text{ s}^{-1}$ the corresponding integral energy flux is $F_\varepsilon(\varepsilon > 1 \text{ TeV}) = 2.3 \text{ TeV} \times F_{\text{ph}}(\varepsilon > 1 \text{ TeV}) = 9.9 \times 10^{-13} \text{ TeV cm}^{-2} \text{ s}^{-1}$ in case of spectral index $\Gamma = 2.3$. Required energy for accelerated CR protons with $E_p > 10 \text{ TeV}$ is:

$$\begin{aligned} W_{\text{cr},p}(E_p > 10 \text{ TeV}) &\sim 4\pi d^2 F_\varepsilon(\varepsilon > 1 \text{ TeV}) t_{pp,\gamma} \\ &\sim 1.3 \times 10^{50} d_{10\text{kpc}}^2 (n_{\text{ISM}} / (1 \text{ cm}^{-3}))^{-1} \text{ erg}, \end{aligned} \quad (54)$$

or the total CR proton energy

$$\begin{aligned} W_{\text{cr},p} &= W_{\text{cr},p}(E_p > 1 \text{ GeV}) \\ &\sim (1 \text{ GeV} / 10 \text{ TeV})^{2-\Gamma_{\text{cr},p}} \times W_{\text{cr},p}(E_p > 10 \text{ TeV}) \\ &\sim 1.9 \times 10^{51} d_{10\text{kpc}}^2 (n_{\text{ISM}} / 1 \text{ cm}^{-3})^{-1} \text{ erg} \end{aligned} \quad (55)$$

for $1 \text{ GeV} < E_p < 1 \text{ PeV}$ CR bubble with power-law spectrum (44) and with the spectral index $\Gamma_{\text{cr},p}$ equal to the spectral photon index Γ , what is exactly what we expect in hadronic mechanism. In this work was used value $\Gamma = 2.3$ that are the same as the average index of known Galactic VHE γ -ray sources [186] and the typical distance to the sources $d = 10 \text{ kpc}$.

Similar estimate of $W_{p,\text{tot}}$ for HOTS J1907+091 flux follows from the conventional formula for the chemical composition of CRs and ambient gas [215] $F_{\text{ph}}(\varepsilon > 1 \text{ TeV}) \approx 0.2 \times 10^{-11} A \text{ cm}^{-2} \text{ s}^{-1}$ for $\Gamma_{\text{cr},p} = 2.3$, where A is the scaling parameter

$$A = \frac{W_{\text{cr},p}}{10^{50} \text{ erg}} \left(\frac{d}{1 \text{ kpc}} \right)^{-2} \frac{n_{\text{ISM}}}{1 \text{ cm}^{-3}}. \quad (56)$$

In the leptonic scenario of emission with IC scattering of CMB by PWN/SFR/SNR accelerated electrons for the HOTS J1907+091 energy flux, the necessary energy of accelerated leptons is expected to be

$$\begin{aligned} W_{\text{cr},e}(E_e > 10 \text{ TeV}) &\sim 4\pi d^2 F_\varepsilon(\varepsilon > 1 \text{ TeV}) t_{\text{IC,CMB}} \\ &\sim W_{\text{cr},p}(E_p > 10 \text{ TeV}) (t_{\text{IC,CMB}} / t_{pp,\gamma}) \\ &\sim 1.3 \times 10^{47} d_{10\text{kpc}}^2 \text{ erg}, \end{aligned} \quad (57)$$

or the total CR lepton energy

$$\begin{aligned} W_{\text{cr},e} &= W_{\text{cr},e}(E_e > 1 \text{ GeV}) \sim 16 W_{\text{cr},e}(E_e > 10 \text{ TeV}) \\ &\sim 1.9 \times 10^{48} d_{10\text{kpc}}^2 \text{ erg}. \end{aligned} \quad (58)$$

In the HE band, the *Fermi*-LAT extended source 4FGL J1908.6+0915e is modeled by a power-law spectrum with photon index $\Gamma = 2.2$ and integral energy flux $F_\varepsilon(\varepsilon > 100 \text{ MeV}) = 2.75 \times 10^{-11} \text{ erg cm}^{-2} \text{ s}^{-1}$ [184]. This source overlaps the SGR 1900+14 position. In the hadronic emission scenario with photon energy $\varepsilon \approx 0.1E_p$ a requirement for the total CR proton energy

$$\begin{aligned} W_{\text{cr},p} &= W_{\text{cr},p}(E_p > 1 \text{ GeV}) \\ &\sim 1.3 \times 10^{51} d_{10\text{kpc}}^2 (n_{\text{ISM}}/1 \text{ cm}^{-3})^{-1} \text{ erg} \end{aligned} \quad (59)$$

is comparable to the considered before HOTS J1907+091 case due to an spectra agreement of SGR 1900+14 (Fig. 46).

In the leptonic emission scenario the HE γ -ray band corresponds to $200 \text{ GeV} \lesssim E_e \lesssim 6 \text{ TeV}$ and a requirement for the CR $E_e > 200 \text{ GeV}$ electron energy is

$$\begin{aligned} W_{\text{cr},e}(E_e > 200 \text{ GeV}) &\sim 4\pi d^2 F_\varepsilon(\varepsilon > 100 \text{ MeV}) \\ &\times t_{\text{IC,CMB}}(E_e = 200 \text{ GeV}) \sim 6.4 \times 10^{49} d_{10\text{kpc}}^2 \text{ erg}, \end{aligned} \quad (60)$$

and we have $W_{\text{cr},e} = W_{\text{cr},e}(E_e > 1 \text{ GeV}) \sim 1.9 \times 10^{50} d_{10\text{kpc}}^2 \text{ erg}$ for the total CR electron energy.

The calculated CR energy requirements in the detected HE – VHE sources, particularly, $W_{\text{cr},e} \sim 1.9 \times 10^{50} d_{10\text{kpc}}^2 \text{ erg}$ for leptons and $W_{\text{cr},p} \sim 1.3 \times 10^{51} d_{10\text{kpc}}^2 (n_{\text{ISM}}/1 \text{ cm}^{-3})^{-1} \text{ erg}$ for hadrons correspond to a ordinary SNR/PWN case for sources at 2-5 kpc, but propose an HNR-type energy reserve for distances beyond 10 kpc.

4.4.3 Modelling of the spectral energy distribution (SED) for the SGR 1900+14 region in SNR model

In SFR and SNR models of the SED of the SGR 1900+14 neighbourhood the observed γ -ray emission consists of leptonic contribution from electron ($i = e$) and hadronic contribution from proton ($i = p$) CRs with spectrum (44) and with its parameters $E_{\text{cr},i,\text{max}}$, $E_{\text{cr},i,\text{min}}$, $E_{\text{cr},i,\text{cut}}$, $N_{0,i}$, $E_{\text{cr},i,0}$, $\Gamma_{\text{cr},i,1}$. Additional parameters are external shell number density n_{sh} and electron-to-proton energy ratio K_{ep} .

Shock-accelerated CR electrons will contribute to the synchrotron radio to X-ray emission as well as the observed VHE γ -ray emission by IC scattering off background photons in both upstream and downstream regions.

Besides the CMB component with energy density $w_{\text{CMB}} = 0.26 \text{ eV cm}^{-3}$ and temperature $T_{\text{CMB}} = 2.7 \text{ K}$ we consider a starlight ($w_{\text{SL}} = 1.92 \text{ eV cm}^{-3}$, $T_{\text{SL}} = 7906 \text{ K}$, SL) and an infrared ($w_{\text{IR}} = 1.19 \text{ eV cm}^{-3}$, $T_{\text{IR}} = 107 \text{ K}$, IR) ones as the representative values for the population of TeV PWNe in the HGPS [263].

In order to explain observed by *Fermi*-LAT (extended object 4FGL J1908.6+0915e) and HESS (extended object HOTS J1907+091/HESS J1907+089) fluxes was used the NAIMA package [276]. NAIMA carries out Markov Chain Monte Carlo (MCMC) fitting of emission models to observed X-ray - γ - ray spectra and calculates the uncertainty and best-fit distributions of spectral model parameters by sampling their likelihood distributions using MCMC. In this case, *Fermi*-LAT observations consist of just seven bins with an overall significance of 4.58σ . There are analytical approximation in the 50 MeV – 10 TeV energy range for 4FGL J1908.6+0915e differential flux density. H.E.S.S. observations of HOTS J1907+091/HESS J1907+089 are of even poorer quality – there are published only the measured integral photon flux $F_{\text{ph}}(\varepsilon > 1 \text{ TeV})$, which we approximated by power-law differential flux density in 1 – 10 TeV (see Section 4.3.1 and Fig. 46-50 for details). As input data for NAIMA fitting, was thus used fluxes and their uncertainties for 20 bins of H.E.S.S. approximation in the energy range 1 TeV – 10 TeV, and 20 bins of *Fermi*-LAT approximation in the range of 50 MeV – 1 TeV . CR spectra that was fitted has form of a an exponential cut-off power-law (ECPL) and power-law (PL) type (44) with fixed values of parameters $E_{\text{cr},i,\text{max}}$, $E_{\text{cr},i,\text{min}}$ and K_{ep} (only for PL spectrum) (Table 12).

Best-fit CR parameters and wind shell nucleon density that was estimated are shown in (Table 12), and the associated best-fit spectral energy distribution is shown in Fig. 46-47. As it was expected from analytical approximations, main contributor to the observed γ -ray flux corresponds to the hadronic mechanism with a typical for ordinary relatively close ($d \lesssim 5 \text{ kpc}$) SNR value of CRs energy reserve, but in this case with high – of Hypernova type – value of CR energy for distant ($d > 10 \text{ kpc}$) SNR $W_{\text{cr},p} \approx 3 \times 10^{50} d_{10\text{kpc}}^2 (n_{\text{sh}}/10 \text{ cm}^{-3})^{-1} \text{ erg}$ even with increased density for swept-up shell ($n_{\text{sh}} \sim 10 \text{ cm}^{-3}$). This conclusion is only somewhat sensitive to the electron contribution (K_{ep}), as the majority of energy losses occur between 1 and 10 GeV. In contrast, for softer (rising $\Gamma_{\text{cr},i}$) spectra, the contribution of electron CR could be significant or perhaps dominant in the TeV band. As one can find in (50), KN depression in background radiation of temperature T starts at IC photon energy $\varepsilon_{\text{IC,KN}} \approx 4k_B T \gamma_{e,\text{KN}} \approx 73.3 \times 10^{13} (T/T_{\text{CMB}})^{-1} \text{ eV}$ or at electron Lorentz factor $\gamma_{e,\text{KN}}$ such that $f_{\text{KN}} \lesssim 0.5$. In our situation, the contribution of IC scattering off SL photons to the TeV band is negligible.

Synchrotron radiation of electron CRs in the radio to X-ray spectrum is determined by the magnetic field strength in the CR-filled area. Excluding a tiny acceleration zone surrounding the shock front, the magnetic field in the rarefied wind bubble and within the HNR is predicted to be of interstellar order $B \lesssim 3\mu\text{G}$ or less. Corresponding flux does not exceed existing observational limits (Fig. 46-50).

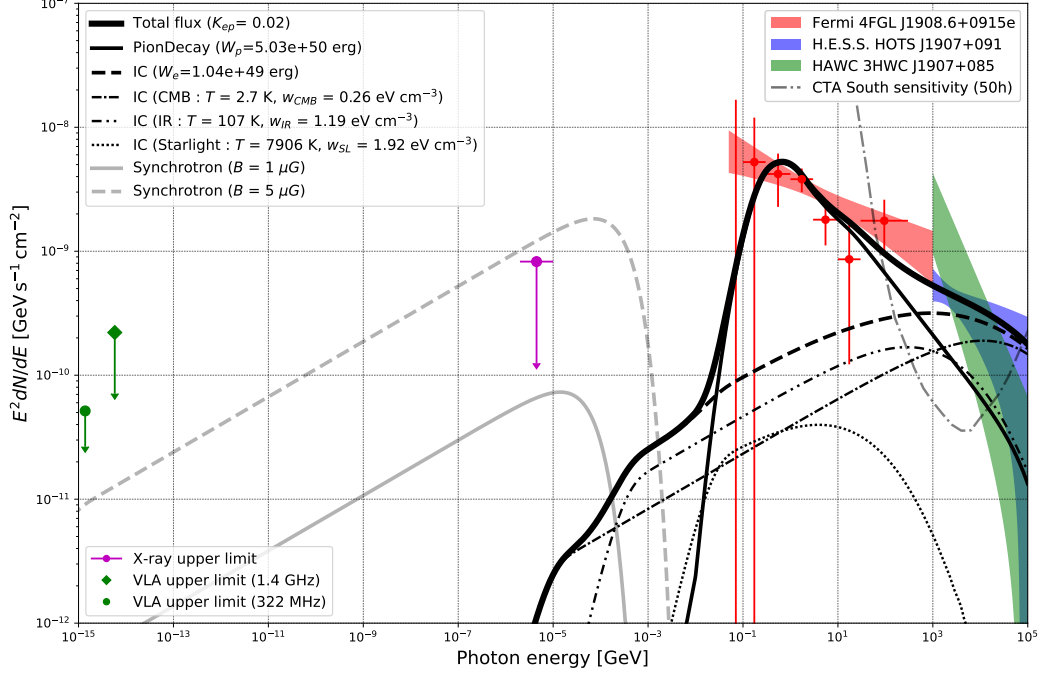


Fig. 46: Simulated SED of the magnetar SGR 1900+14 area using the SNR model. Table 12 contains the NAIMA-fitted parameters (in the case of SNR at distance $d = 12.5$ kpc and shock-accelerated electron and proton PL spectra with $K_{ep} = 0.02$). Observations of H.E.S.S. HOTS J1907+091 (in blue), *Fermi*-LAT 4FGL J1908.6+0915e (red colour), , and HAWC 3HWC J1908.6+085 (green colour) are given with radio (green colour) and X-ray (magenta colour) band upper limits. The entire γ -ray flux is a sum of leptonic contributions (IC scattering of electrons on IR, CMB and SL background photons) and hadronic (pp collisions with subsequent neutral pion decay). The calculation of synchrotron emission is performed for two values of the ambient magnetic field: 1 and 5 μG . The grey dash-dot line depicts the CTA’s South array sensitivity at a zenith angle of 40 degrees.

4.4.4 Modelling of the SED for the SGR 1900+14 region in PWN model

The results of the NAIMA-fitting of the SED of the SGR 1900+14 neighborhood in the PWN model for the ECBPL spectrum are shown in Fig.48, while the predicted leptonic CR parameters are shown in Table 12.

Fig. 49 shows the results of the NAIMA-fitting for the SGR 1900+14 neighbourhood in the PWN model in case of ECBPL spectrum form. One can see leptonic CR parameters that are necessary for such model in Table 12. As we can see, similarly to the SNR case, required reserve of leptonic CR energy $W_{cr,e} \approx 2.3 \times 10^{50} d_{10\text{kpc}}^2$ erg is typical for ordinary relatively close ($d \lesssim 5$ kpc) PWNe, but increases by the several orders – up to Hypernova-related MWN type – for distant ($d > 10$ kpc) PWNe.

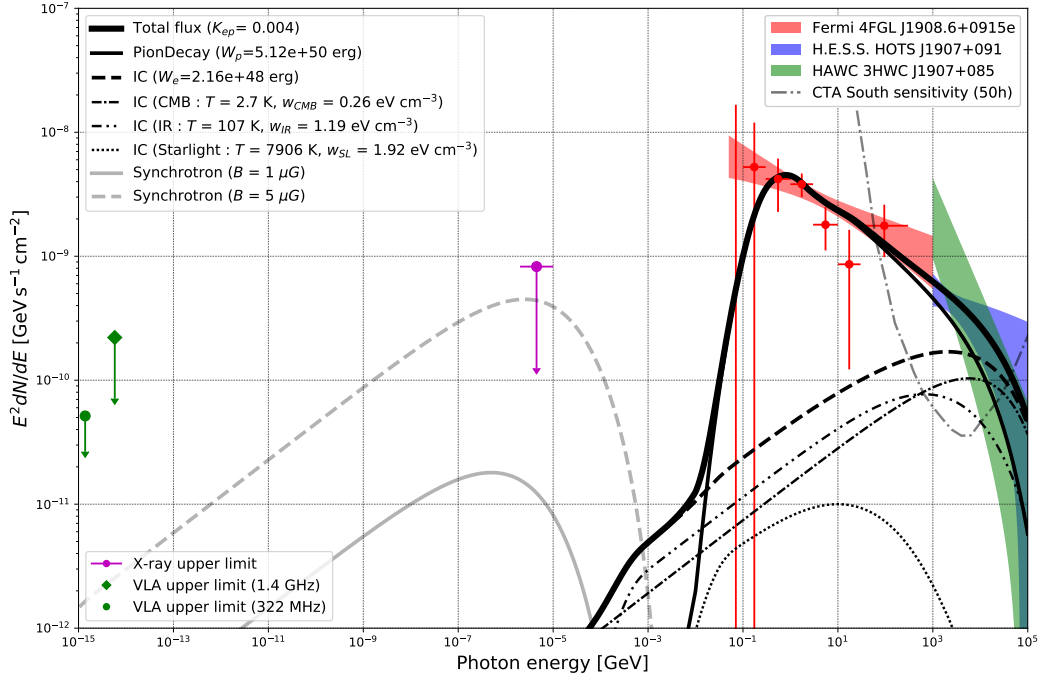


Fig. 47: Same as in Fig. 46 but for ECPL spectra with free K_{ep} .

For a decreasing $\varepsilon^2 F_{\text{ph}}(\varepsilon)$ flux in TeV region (photon index $\Gamma > 2$) an average spectral index for electrons of CR should be $\Gamma_{\text{cr},e,2} = 2\Gamma - 1 > 3$. In our situation, we only witness this post-maximum drop $\varepsilon^2 F_{\text{ph}}(\varepsilon)$ in flux in the all GeV – TeV region with $\Gamma \sim 2.2 - 2.9$ (GeV – TeV band respectively). So we used for modelling the PWN broad band spectrum also an inspired by “alternative model” of [274] ECPL electron spectrum with $E_{\text{min}} = E_{\text{br},e} \sim 10$ GeV and $\gamma_{2,e} > 3$ in order to estimate the minimum energy in leptonic CR, that are necessary to explain observations. Results of the NAIMA-fitting of SED for different ECPL lepton spectra are shown on Fig. 49, and the required leptonic CR parameters are shown in Table 12. Minimum leptonic CR energy reserve $\sim 6 \times 10^{49} d_{10\text{kpc}}^2$ erg exceeds an order of magnitude below what was anticipated in millisecond magnetar-related MWN model.

It was considered also the case of two lepton populations ($i = 1, 2$) with ECPL spectra in order to examine a two lepton population model:

$$N_i(E) = N_{0,i}(E/E_{0,i})^{-\gamma_{i,e}} \exp(-E/E_{\text{cut},i}), \quad (61)$$

with $\gamma_{1,e} < 2$ typical for PWN lepton CR spectra and $\gamma_{2,e} > 2$ typical for SNR electron CR spectra. Fig. 50 demonstrates SED for this case and Table 12 contains leptonic CR parameters. As it follows from Table 12, explanation of TeV γ -ray emission necessitates six times greater electron CR energy than can be supplied by externally accelerated electron CRs with $K_{ep} = 0.02$; hence, it cannot dominate in our scenario. However, it is still detectable by CTA-like detectors.

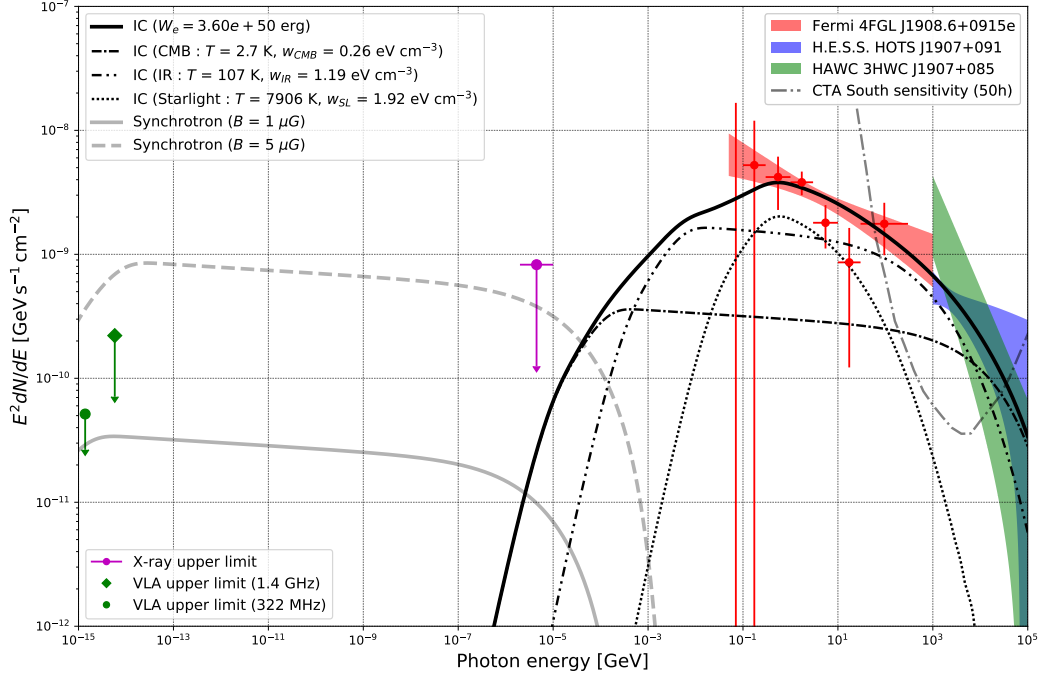


Fig. 48: Modeled SED of the region around magnetar SGR 1900+14 using the PWN model. Table 12 presents NAIMA-fitted parameters (in the case of PWN at distance $d = 12.5$ kpc and TS/reconnection) accelerating leptons with ECPL). The total gamma-ray flux is the sum of contributions from IC scattering of leptons on the IR background photons, CMB, and SL background photons. All other data are identical to those in Fig. 46.

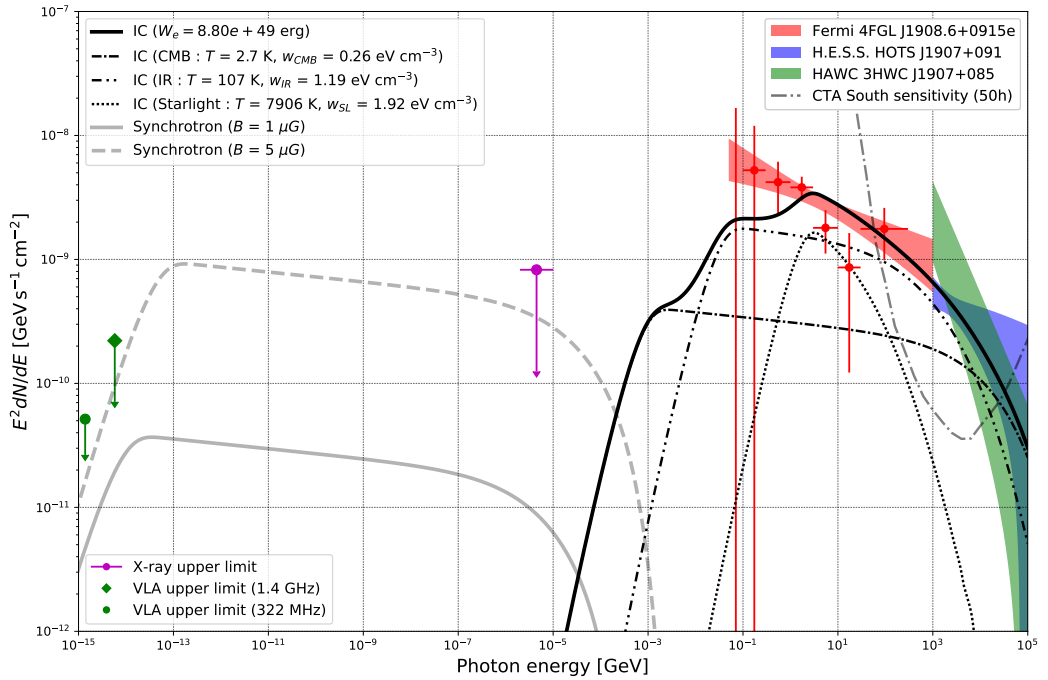


Fig. 49: Same as in Fig. 48 but for alternative ECPL with $E_{\min} = 10$ GeV.

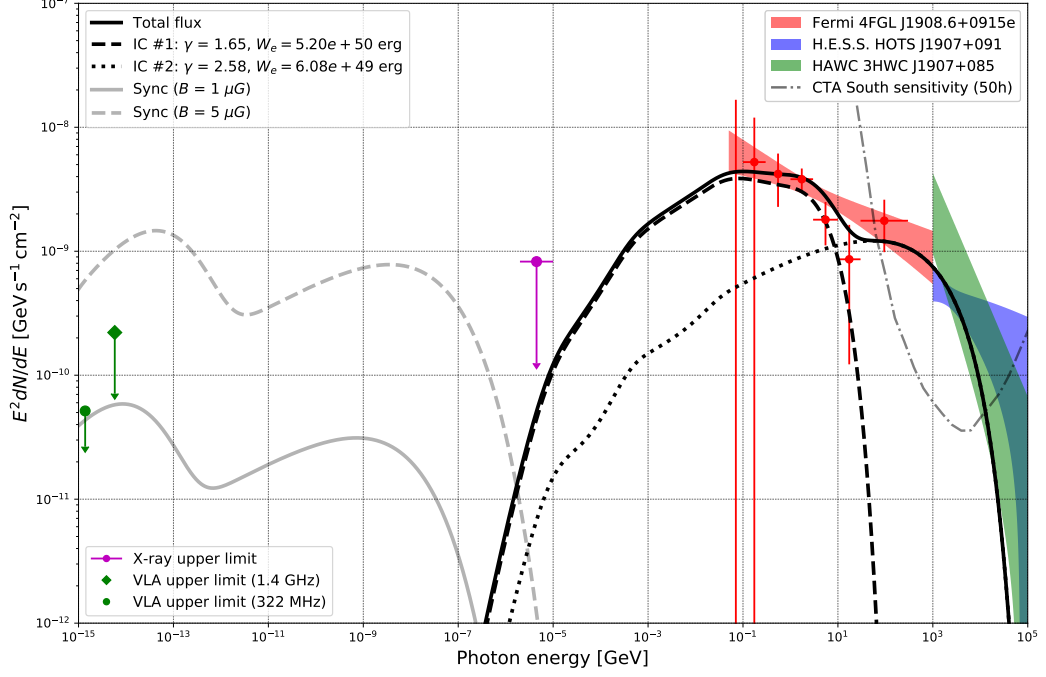


Fig. 50: Same as in Fig. 48 but for two electron populations with ECPL spectra. Only overall γ -ray fluxes as total amount contributed by parts from IC scattering of leptons on IR, CMB, and SL background photons are presented.

4.5 HE – VHE gamma-ray emission from SGR 1900+14 region - possible sources

4.5.1 Supernova Remnants

Regular SNR with an energy of explosion $E_{\text{SN}} \sim 10^{51}$ erg and mass that was ejected $M_{\text{ej}} \sim 5M_{\odot}$ in a dense ($n_{\text{mc}} = \rho_{\text{mc}}/\mu \sim 10^4 \text{ cm}^{-3}$) molecular cloud of radius of $R_{\text{mc}} \sim 0.5$ pc and with the mean molecular weight $\mu = 1.4m_{\text{H}}$ is considered to be in an adiabatic (Sedov - Taylor, ST) stage of evolution at the present time.

At the ST stage, the time-dependent exterior (forward) shock wave radius R_{ST} and velocity D_{ST} are calculated as follows:

$$\begin{aligned}
 R_{\text{ST}}(t) &= (2.026E_{\text{SN}}/\rho_{\text{mc}})^{1/5}t^{2/5} \\
 &= 0.791(E_{\text{SN},51}/n_{\text{mc},4})^{1/5}t_{\text{kyr}}^{2/5} \text{ PC},
 \end{aligned}
 \tag{62}$$

Tab 12: NAIMA-fitted models in the case of PWN and SNR. SED for the region around magnetar SGR 1900+14

Parameter	SNR: PL and ECPL spectra ($i = p$)		PWN: ECBPL and alternative ECPL spectra ($i = e$)		PWN: Two electron population spectra ($i = e$)	
	PL	ECPL	ECBPL	ECPL	ECPL #1	ECPL #2
$E_{cr,i,min}$ [GeV](fixed)	1	1	1	10	1	1
$E_{cr,i,max}$ [GeV](fixed)	1e6	1e6	1e6	1e6	1e6	1e6
$N_{0,i}$ [1/ eV]	(1.18±0.04)e35	(1.42±0.05)e37	(1.90±0.12)e40	(8.91±0.50)e37	(4.41±0.51)e38	(8.81±0.44)e34
$E_{cr,i,0}$ [TeV]	3.93±0.1	0.78±0.01	0.19±0.01	0.175±0.003	1.91±0.19	1.81±0.19
$E_{cr,i,br}$ [TeV]	-	-	0.0047±0.0003	-	-	-
$E_{cr,i,cut}$ [TeV]	-	185.2±9.5	396.7±41.7	424.3±21.1	0.0096±0.0008	9.99±1.06
$\Gamma_{cr,i,1}$	2.55±0.01	2.41±0.03	1.49±0.07	-	1.65±0.11	-
$\Gamma_{cr,i,2}$	-	-	3.04±0.06	3.08±0.03	-	2.58±0.17
W_p [erg] (calculated [†])	5.03e50	5.12e50	-	-	-	-
W_e [erg] (calculated [†])	1.04e49	2.16e48	3.60e50	8.80e49	5.20e50	6.08e49
n_{sh} [cm ⁻³]	11.42±0.66	9.81±0.35	-	-	-	-
K_{ep}	0.02 (fixed)	0.0041±0.0002	-	-	-	-
χ^2/ndf^*	42.10/36	30.74/34	16.54/34	40.24/36		36.64/32

* Best fit of 20 bins of *Fermi*-LAT PL 0.05-1000 GeV spectrum and 20 bins of HOTS PL 1-10 TeV spectrum approximation
[†] for distance to the source $d = 12.5$ kpc

$$\begin{aligned}
 D_{ST}(t) &= (2/5)R_{ST}(t)/t = (2/5)(2.026E_{SN}/\rho_{mc})^{1/2}R_{ST}(t)^{-3/2} \\
 &= 2.15 \times 10^7 R_{ST,pc}(t)^{-3/2} (E_{SN,51}/n_{mc,4})^{1/2} \text{cm s}^{-1} \\
 &= 3.07 \times 10^7 (E_{SN,51}/n_{mc,4})^{1/5} t_{kyr}^{-3/5} \text{cm s}^{-1}
 \end{aligned} \tag{63}$$

[254; 255].

Observations, however, do not establish the occurrence of SNR within molecular clouds. In addition, not even the molecular cloud itself is observed. Recent modeling of star formation indicates that in a young compact cluster that contains massive stars and is similar to Cl 1900+14, at the time of first explosion of SN, the gas component is almost entirely expelled from the cluster by stellar winds of the cluster's stars and is concentrated in the wind shell to a concentration of ~ 40 pc. Magnetar-connected SN erupted in a rarefied mixture of stellar winds and, in addition to being energized by new millisecond magnetar, has attained a massive size by now.

The HNR with energy $E_{HNR} \sim 10^{52}$ erg develops within the low-density wind bubble with density ($n_w \sim 10^{-3}$ cm⁻³, $B_w \lesssim 3 \mu\text{G}$) in our Hypernova model, and now ($t_{HNR} \approx 2$ kyr) is with the shock velocity $V_{HNR} = 0.4R_{HNR}/t_{HNR} \approx 7 \times 10^3$ km s⁻¹ and with the radius $R_{HNR} \approx 35$ pc at the ST stage. This HNR is approaching an extended shell-like halo ($R \sim 40$ pc) with $n_{sh} \sim 10$ cm⁻³. Also the total swept up mass of HNR are equal approximately $\sim 10^4 M_\odot$.

Similar to the SNR scenario stated above, the HNR shock is an effective proton and electron CR accelerator. For total energy that resides in HNR shock, $W_{HNR} = 10^{52}$ erg, we expect $W_{cr,p} \sim 0.1\eta_{p,-1}W_{SNR} \sim 10^{51}\eta_{p,-1}$ erg in proton CRs and $W_{cr,e} \sim 0.01K_{ep,-2}W_{cr,p} \sim 10^{49}K_{ep,-2}$ erg in

electron CRs.

According to (46), the maximum energy of accelerated CRs with the charge Ze at the HNR shock due to DSA, with post-shock value of magnetic field $B_{\text{HNR}} = \sqrt{11}B_w$ is around $9Z$ PeV. For proton CRs, energy losses are negligible throughout the HNR age, however for electron CRs, radiative cooling is significant for energies greater than 100 TeV.

We expect the major contribution to the observed VHE γ -ray emission of the SGR 1900+14 region are originating due to inelastic interaction between shock-accelerated protons or heavier nuclei and target protons or heavier nuclei of the dense shell-like boundary of the stellar wind bubble halo, followed by neutral pion decay. Since the shock wave is near the bubble boundary but still within the bubble $R_{\text{HNR}} \lesssim R_{\text{swb}}$, only CR from the upstream shock area will significantly collide with target shell material. Therefore, this discrepancy was disregarded.

In the studied HNR model, a natural explanation can be given for the huge size of the young ~ 2 kyr GeV-TeV source. In the wind bubble shell with an increased number density n_{sh} and a radius $R_{\text{sh}} \approx 40$ pc, the hadronic component of TeV *gamma*-ray emission is generated. Accelerated at the shock front proton and electron CRs diffusively expand at a characteristic distance [215]:

$$L_{\text{dif}} \approx 2(D \times t)^{1/2} \approx 35 \left(\frac{E_{\text{cr}}}{10Z \text{ GeV}} \times \frac{3\mu\text{G}}{B} \right)^{0.24} t_{\text{kyr}}^{1/2} \text{ pc}, \quad (64)$$

where the best fitted diffusion coefficient D is taken from the Galactic model that includes diffusion-reacceleration-convection [247] and dependence on magnetic field inside source B [248]

$$D = D_0 \left(\frac{\mathcal{R}}{4 \text{ GV}} \cdot \frac{3\mu\text{G}}{B} \right)^\delta, \quad (65)$$

with $D_0 = 6.14 \times 10^{28} \text{ cm}^2 \text{ s}^{-1}$, $\delta = 0.48$, and with the slope of injection spectrum $\Gamma_{p,e} = 2.37$ for CR rigidity $\mathcal{R} = E_{\text{cr}}/Ze > 16 \text{ GV}$ ($E_{\text{cr}} > 16Z \text{ GeV}$).

Eq.(64) indicates that diffusion of electron and proton CRs in the upstream region is efficient and that proton CRs can pierce the wind bubble shell and create hadronic γ -ray emission even if the magnetic field B in the shock outskirts is tenfold stronger.

4.5.2 Star formation region

As previously indicated, two SFRs – W49A and Cl 1900+14, are likely contributors to the detected gamma-ray emission from the SGR 1900+14 area. However, a quantitative examination of expected gamma-ray fluxes from these sources reveals that their contributions are small.

In star cluster Cl 1900+14, that is connected to the young magnetar SGR 1900+14, there are only two luminosity dominated M5 Red Supergiant stars with masses $M \sim 14 - 18M_\odot$ and most

likely only one SN outburst from progenitor of similar mass, we do not anticipate the presence of powerful CR accelerated shocks in addition to the SNR shock.

Contrary to Cl 1900+14, SFR W49A is the most luminous Galactic SFR at a comparable distance of ~ 11 kpc in the very massive gigantic molecular cloud complexes, W49 with $M_{\text{gas}} \sim 10^6 M_{\odot}$ [277].

However, H.E.S.S observations of W49A only detected γ -ray emission with the primary analysis, while the supplementary cross-check analysis did not verify the detection level (above 5 σ) [278].

4.5.3 Pulsar wind nebulae

Only a remnant MWN that is tied to a magnetar is a possible source in the SGR1900+14 region because there are no active pulsars there.

Newborn magnetar with millisecond rotational period and initial spin-down time-scale $t_{\text{sd}} \sim 10^4$ s generates gamma-ray emission of HNR driven by the spin-down luminosity $L_{\text{sd}} \sim 10^{48}$ erg s^{-1} . The total energy released, $E_{\text{sd}} \sim 10^{52}$ erg, is converted into electron-positron pairs of energy at the TS, where it is accelerated and then gathered in MWN within the SN ejecta that is still expanding at that moment. Adiabatic expansion of MWN provides an additional acceleration for SN ejecta up to a Hypernova signature due to the expense of MWN cooling $E_{\text{MWN}} \propto R_{\text{HNR}}^{-1}$ for a number of weeks.

Lets consider case when the magnetar wind is jet-like and well-collimated [279; 280]. In such case it can drill the expanding ejecta and manifest itself as Type I superluminous SN (SLSN I) and long gamma-ray burst (LGRB) [203; 281; 282]. The main part of magnetar rotational energy will be transferred in the relativistic Poynting-flux dominated jet, that have initial magnetization parameter $\sigma_{\text{j,ini}}(r) = B^2/4\pi\rho c^2 \gg 1$, the initial Lorentz factor $\Gamma_{\text{j,ini}}(r) \gg 1$, and the isotropic luminosity:

$$L_{\text{j}}^{\text{iso}} \approx L_{\text{sd}}\omega^{-1} \approx 4\pi r^2 \rho c^3 \gamma_{\text{j,ini}}^2 (1 + \sigma_{\text{j,ini}}), \quad (66)$$

where $\rho = n_l m_e$ is the lepton rest mass density (all B , σ_j and ρ in the comoving frame), $\omega = \theta_j^2/4$ is the isotropic correction, θ_j is the jet half-opening angle, $t_j = t_{\text{sd}}$ and $\Delta = ct_j$ are duration and length of the jet, correspondingly. The interaction of the jet with the ISM is similar to that of the GRB jet [283], with the exception that in our situation the jet's predominant constituents are leptons as opposed to baryons (protons) and electrons as they are in the classical fireball model. In the fireball model, jet with isotropic energy $E^{\text{iso}} = L_{\text{j}}^{\text{iso}} t_j = \omega^{-1} E_{\text{rot}}$ creates a jet-like analog of MWN because of interaction with ISM. It includes undisturbed ISM (region **1**) with the baryon

(proton) number density n_1 , then region shocked by relativistic external shock (region **2**) with proton number density n_2 , moving closer to the center occurs region where relativistic reverse shock playing its role (region **3**, (MWN)) with the lepton number density $n_{l,3}$ (the equivalent proton number density $n_3 = (m_e/m_p)n_{l,3}$ and the undisturbed jet region **4** (in our case its the free magnetar wind), the lepton number density in the region **4** is $n_{l,4}$ (the equivalent proton number density $n_4 = (m_e/m_p)n_{l,4}$ (all number densities are given in comoving frames).

Here are employing the numerical values of those parameters as fiduciary estimates of the determinative parameters: the ISM number density $n_w = n_1 = 10^{-3} \text{ cm}^{-3}$, the spin down energy $E_{\text{sd}} = 10^{52} \text{ erg}$, jet duration $t_{\text{sd}} = t_j = 10^4 \text{ s}$, the Lorentz factor of magnetar wind jet $\gamma_j = 10^3$, the isotropic correction $\omega = 10^{-3}$ (all values are in the centre of explosion frame(COE)), the comoving magnetic field in MWN $B_3 = 2 \times 10^{-2} \text{ G}$ and the fraction of magnetic energy in MWN $\epsilon_B = 10^{-3}$.

Reverse shock reaches the inner limit of the jet-like magnetar wind at a distance of $R_\Delta = 6.5 \times 10^{18} \text{ cm}$ from COE cm at a given moment in time $t_\Delta = R_\Delta/c = 3.2 \times 10^8 \text{ s}$. At this time, the total leptonic plasma of the magnetar wind has crossed TS and become the MWN plasma. Both regions shocked and swept up (region **2**) by external shock ISM and regions separated by contact discontinuity MWN (region **3**) move in accordance with the Lorentz factor $\gamma_2 = \gamma_3 \sim f^{1/4}\gamma_j^{1/2}/\sqrt{2} \sim 5.8 \times 10^1$. In contrast, the Lorentz factor of the MWN plasma relative to the unperturbed magnetar wind is $\bar{\gamma}_3 = f^{-1/4}\gamma_j^{1/2}/\sqrt{2} \sim 8.6$, which corresponds to the TS Lorentz factor $\gamma_{\text{TS}} = \sqrt{2}\bar{\gamma}_3 \sim 1.2 \times 10^1$. Electron-positron CR acceleration at the TS accompanies all phases of MWN creation up until the time when all lepton plasma from magnetar wind crosses the TS and fills the MWN. Similar to the ordinary PWN case, almost all magnetar wind kinetic energy is converted to accelerated particles with the comoving post-shock energy density $w = w_e + w_B$ as the sum of the electron $w_e = \epsilon_e w$ and magnetic field energy densities $w_B = \epsilon_B w$, where $\epsilon_B \ll 1$ and $\epsilon_e \simeq 1$ are the fractions of magnetic field and electron energy densities, respectively. In our example, the energy densities in areas **3** and **2** are identical, hence $w_3 = w_{e,3} + w_{B,3} = w_2 = 4\gamma_2 n_1 m_p c^2 \sim 2.0 \times 10^{-2} \text{ erg cm}^{-3}$ with a little amount of magnetic field energy density $\epsilon_{B,3} \sim 10^{-3}$ for $B_3 = 2 \times 10^{-2} \text{ G}$.

After all stages of MWN formation the transverse radius of MWN was $R_\Delta \theta_j \sim 4 \times 10^{17} \text{ cm}$, the comoving radial size was of $\Delta_3 \sim 8.5 \times 10^{15} \text{ cm}$, the comoving volume $V_3 = \pi \Delta (R_\Delta \theta_j)^2 \sim 4.3 \times 10^{51} \text{ cm}^3$, the transverse radius - $R_\Delta \theta_j \sim 4 \times 10^{17} \text{ cm}$, and comoving age $t_3 \sim 3\Delta_3/c \sim 8.5 \times 10^5 \text{ s}$. The maximum energy of accelerated CRs is equal to $E_{\text{cr},e,\text{max}} = 4.4 \times 10^{14} \text{ eV}$, which is defined by the balance of the synchrotron energy loss and acceleration times. The energy spectrum of accelerated CR is predicted to be similar to the standard PWN situation described above, i.e., an exponential cut-off broken power-law spectrum (48). $E_{\text{cr},e,\text{fc}} \sim 1 \text{ TeV}$ is the minimum energy of electrons that

radiate in the rapid cooling regime when the comoving age is comparable to energy loss time. Total MWN energy reserve in the comoving frame $W_{\mathbf{3},\text{tot}} \sim w_{\mathbf{3}}V_{\mathbf{3}} \sim 8.6 \times 10^{49}$ erg is comparable to the energy reserve of the ISM when it is shocked (region **2**). The total energy of regions **2** and **3** is the same in the COE frame, and equal to $W_{\mathbf{3}}^{\text{obs}} \sim W_{\mathbf{2}}^{\text{obs}} \sim \gamma_{\mathbf{3}}W_{\mathbf{3},\text{tot}} \sim E_{\text{rot}}/4$ for each of the two jets, as predicted by the rule of energy conservation.

To summarise, after approximately 1.3×10^7 seconds after its launch, the jet-like magnetar wind pulse (time of the pulse $\sim 10^4$ s), is traveling distance $\sim 4 \times 10^{17}$ cm, and totally decelerates due to interactions with ISM. Due to deceleration it transferred its energy to the two-layer structure: decelerated and shocked by reverse TS magnetar wind plasma i.e. MWN, and accelerated and shocked by external shock ISM. In each jet, MWN are composed of accelerated leptonic CRs with a comoving energy reserve of $\sim E_{\text{rot}}/4\gamma_{\mathbf{3}} \sim 4 \times 10^{49}$ erg and travel with a Lorentz factor of $\gamma_{\mathbf{3}} \sim 57$. Similar energies and Lorentz factors characterize layers of accelerating ISM. After the above-mentioned time, when the reverse shock reaches the inner boundary of the jet, the magnetar wind pressure vanishes, the MWN enters the stage when it is free expanding in vacuum, and the CRs of the MWN expand freely without adiabatic losses and diffusely feel a magnetar's periphery. In the COE frame, their average energy grows $\sim \gamma_{\mathbf{3}} \sim 57$ times. According to (64), we can now anticipate the appearance of these MWN-born leptonic CR bubbles with a PWN-typical ECBPL spectrum, a total energy of $\sim 0.5E_{\text{rot}}$ from both jets, and a radius of ~ 40 pc in magnetar outskirts. We can compare these predictions with the parameters of CRs required by the MWN model to explain gamma-ray emission from SGR 1900+14 region.

It is essential to note that the estimations of CR parameters presented above are rather upper bounds, as they correspond to the minimal energy losses of leptonic CRs in MWN.

Approximately half of the energy that was deposited by jets in the ISM and is part of the thermal and kinetic energy of the above-mentioned layers of shocked ISM will continue to support a collimated jet-like plasma flow (mainly baryons) with decreasing Lorentz factor $\gamma_{\mathbf{2}}$ until $\gamma_{\mathbf{2}}\theta_{\mathbf{j}} \gtrsim 1$, after which the jet loses its collimation and the flow begins to spherize and enters the Sedov stage at a distance of order of $l_{\text{Sed}} \sim 2 \times 10^{20}$ cm according to Eq. (62)–(63). Currently, the non-relativistic jet-created shock has parameters identical to the preceding HNR example, but with a lower energy $E_{\text{JCS}} \sim E_{\text{rot}}/2$ (contributions of both jets are merged), a shock radius $R_{\text{JCS}} \approx 30$ pc, and a velocity $V_{\text{JCS}} \approx 6 \times 10^3$ kms $^{-1}$. In this case we expect $W_{\text{cr},p} \sim 5 \times 10^{50}\eta_{p,-1}$ erg in proton CRs and $W_{\text{cr},e} \sim 5 \times 10^{48}\eta_{p,-1}K_{ep,-2}$ erg in electrons.

Contrary to the classical PWN scenario of HE-VHE gamma-radiation producing, where only accelerated CRs of leptonic origin generate γ -ray emission, in this case of the MWN scenario we inevitably get accelerated proton and electron CRs at an external shock created by a magnetar

wind jet along with accelerated MWN leptonic CRs. Therefore, the leptonic scenario in the MWN example include contributions from the two lepton populations — the MWN leptons (electron-positron pairs) and the externally accelerated ISM electrons (Eq.61)..

In conclusion, the observational data can only be explained by the PWN model if the total energy of radiated electrons is $W_{e,\text{tot}} \approx (1 - 5) \times 10^{50} d_{10\text{kpc}}^2$ ergs. Such energy much surpasses the predicted CR energy for typical remote PWNe, but it can be produced by a newborn magnetar with a millisecond rotation time (Table 12). Similar to the HNR model, the magnetic field inside the stellar wind bubble $B_w \lesssim 2\mu\text{G}$ does not affect the upper radio band limitations due to synchrotron emission(Fig. 48-50).

4.5.4 Source confusion

Source confusion is a significant issue for γ -ray sources in the Galactic plane, especially for extended sources. 36 of the 47 unidentified HGPS sources have indications of source uncertainty [284].

One of the causes of source confusion in the SGR 1900+14 region may be TeV halos. Observations of this halos surrounding several middle-age pulsars [285; 286] can be explained due to IC emission of high energy positrons and electrons accelerated at the pulsar wind TS but diffusively penetrating outside PWNe at distances ~ 10 -30 pc and continuously interacting with background radiation fields (SL, IR, etc). TeV halos are anticipated to be common, with 10–50 TeV halos amounting to discovered unexplained sources and PWN candidates, and up to 50–240 halos in future CTA and HAWC observations [286].

In ATNF Pulsar Catalogue [221] among pulsars of moderate age (40-500 kyr) in a circle with a radius of $0^\circ.5$ degree around HESS J1907+089 are PSR J1908+0909 and PSR J1907+0918, while in a circle of radius 1° there are also PSR J1909+0912, PSR J1903+0925 and PSR J1908+0909, in addition to 15 more pulsars with unknown ages listed in The FAST Galactic Plane Pulsar Snapshot survey [287]. Notable is the fact that total population of pulsars with middle-age, including “invisible pulsars” with misaligned beaming angles, is around four times as abundant as young pulsars [285]. It is possible for local ($\lesssim 1$ kpc) unseen pulsars with TeV halos to contribute to or perhaps dominate the observed TeV output.

Fluxes and spectra of observed γ -ray sources towards the SGR 1900+14 region in the Fermi Large Area Telescope Fourth Source Catalog [184], particularly the extended source 4FGL J1908.6+0915e, can also be affected by source confusion. This extended source overlaps with the SNR G42.8+0.6 and the SGR 1900+14. However, as stated previously, this SNR is only discovered as a faint radio source devoid of any other non-thermal activity and is unlikely to produce a significant gamma-ray emission. In this location, there are also three unidentified 4FGL sources:

J1910.2+0904c, J1908.7+0812, and J1911.0+0905 (Fig. 44). 4FGL J1910.2+0904c carries a flag 5 as a warning to confusion and is very likely physically linked to the SFR W49A (coincident with an interstellar cluster) [218].

The SFR W49A has a large number of young massive stars and HII regions encased in a dense molecular cloud with favorable conditions for γ -ray emission of stellar wind shock-accelerated CRs, but no SNR signals. It may contribute to the gamma-ray emission from the western hemisphere of the extended 4FGL J1908.6+0915e (one can find it on Fig. 3 in [217]). 4FGL J1911.0+0905 is related with the SNR W49B (G043.3-00.2), also known as the TeV source HESS [186]; nevertheless, because to its point-like form and large spacing, we do not anticipate a significant source misunderstanding with the SGR 1900+14 area.

4.6 Conclusions

In this section was modeled the observed HE and VHE γ -ray emission from the region of the sky around magnetar SGR 1900+14 as result of contributions from individual sources, particularly the SNRs W49B and G42.8+0.6, the SFRs W49A and Cl 1900+14, as well as undetected magnetar-connected SNR and potential MWN. Source misunderstanding with TeV halos is likely as well.

Main conclusions connected to the main topic of the thesis can be summarised as follows. A set of multiwavelength observational data may be explained by a scenario of a magnetar-connected supernova that exploded approximately 2,000 years ago at a distance of 12,5 kpc and was documented in ancient Chinese records on April 24, 4 BC. The SN should be of the Hypernova type, with high explosion energy $E_{\text{HNR}} \sim 10^{52}$ erg obtained from the rotational energy $E_{\text{rot}} \approx 2 \times 10^{52} P_{i,3}^{-2}$ erg of strongly magnetized newborn millisecond X-ray pulsar — magnetar SGR 1900+14. The fallback accretion is anticipated to result in a magnetar with an equilibrium millisecond period of $B_s = 4.3 \times 10^{14}$ G. Very high initial magnetar spin-down luminosity will energize Hypernova ejecta and development of the MWN. Model-dependent estimates of the relative proportions of energy input into the Hypernova ejecta and the MWN can be derived from the study of recent observations. The energy-dominated Hypernova ejecta with $E_{\text{HNR}} \approx E_{\text{rot}} \approx 10^{52}$ evolves inside the low-density wind bubble (that is now producing the HNR at the ST stage) in the so-called HNR model. Shock accelerated nuclei and electrons are diffusely distributed over the observed γ -ray sources, and γ -ray emission is primarily generated by the hadronic mechanism (pp collisions with subsequent neutral pion decay) in a dense ($n_{\text{sh}} \sim 10 \text{ cm}^{-3}$) extended shell-like halo of swept up mass of $\sim 3 \times 10^4 M_{\odot}$. In the TeV band, the leptonic process (IC scattering of SL, IR and CMB photons by electrons accelerated on the shock) can be the dominating contri-

butor (IC scattering of background CMB, SL and IR photons by shock-accelerated electrons). The intense relativistic collimated jet-like magnetar wind can efficiently pierce the Hypernova ejecta, producing twin GRB-like jets within a rarefied star wind bubble. Due to the deceleration of the leptonic jet, two transient MWNe with $E_{\text{MWN}} \lesssim 0.5E_{\text{rot}} \approx 10^{52}$ erg are produced, and a portion of the jet's energy is transferred to reconnection/Ts accelerated positrons and electrons. After a jet shutdown, accelerating leptons disperse over the detected gamma-ray sources and the leptonic mechanism produces gamma-ray emission. Such energetic processes can be responsible for acceleration of EHECR, especially the observed triplet of events.

Undoubtedly, a more realistic model would incorporate contributions from both hadronic and leptonic models, but the lack of observational data prevents us from developing a fully quantitative model for the γ -ray emission of the SGR 1900+14 region.

In the future years, new broadband observations in γ -ray (LHAASO, MAGIC, HAWC, and H.E.S.S.), X-ray (eROSITA) and radio (FAST) bands can clarify source characteristics and increase our knowledge of the physical processes in MWNe/SNRs and nature of the γ -ray emission from the region surrounding the magnetar SGR 1900+14.

5 Overall conclusions

In this thesis was investigated the influence of the intergalactic and interstellar medium on the propagation of UHECR from potential sources, were determined the potential sources of extremely high energy cosmic rays, as well as was investigated the processes of acceleration of UHECR in galaxy clusters and magnetars based on the analysis of secondary non-thermal gamma-ray and neutrino emission. The following results have been obtained:

1. Based on the analysis of EHECR energy loss lengths and deviations in magnetic fields the estimation of characteristic maximum distances to the EHECR sources in the Local Universe was carried out.
2. The potential sources of EHECR events in the Local Universe were determined based on the calculation of the backward trajectories of the detected by Auger and TA EHECR events in the Galactic and extragalactic magnetic field. A list of potential sources based on correlation with restored directions is provided.
3. Was estimated and justified prospects for observations of Coma and Hercules galaxy clusters in existing (Fermi-LAT, LHAASO, IceCube) and future (CTA, IceCube-Gen2) observatories based on numerical modeling of non-thermal gamma and neutrino radiation from these objects.
4. Was investigated signatures of CRs in AGN jets and selected the subsample of radio loud AGN with similar spectral indices of radio synchrotron and X-ray inverse Compton emission as a signature of multiwavelength leptonic CR jet emission.
5. Was substantiated the connection of the Galactic magnetar SGR1900+14 with the detected by Auger and TA EHECR triplet and explained the observed multiwavelength emission from the magnetar SGR1900+14 region in the frame of the magnetar- connected Hypernova remnant/magnetar wind nebula.

6 References

- [1] K. Olive *Chinese Physics C* **40** (2016) 100001.
- [2] J. H. Boyer, B. C. Knapp, E. J. Mannel and M. Seman *Nuclear Instruments and Methods in Physics Research Section A: Accelerators, Spectrometers, Detectors and Associated Equipment* **482** (2002) 457.
- [3] R. Baltrusaitis, R. Cady, G. Cassiday, R. Cooperv, J. Elbert, P. Gerhardy et al. *Nuclear Instruments and Methods in Physics Research Section A: Accelerators, Spectrometers, Detectors and Associated Equipment* **240** (1985) 410.
- [4] J. Adams, S. Ahmad, J.-N. Albert, D. Allard, M. Ambrosio, L. Anchordoqui et al. *Astroparticle Physics* **44** (2013) 76.
- [5] R. A. Batista, J. Biteau, M. Bustamante, K. Dolag, R. Engel, K. Fang et al. *Frontiers in Astronomy and Space Sciences* **6** (2019) .
- [6] K. Olive *Chinese Physics C* **38** (2014) 090001.
- [7] M. S. Longair, *High Energy Astrophysics*. Cambridge University Press, 2, 2011, 10.1017/CBO9780511778346.
- [8] T. Antoni, W. Apel, A. Badea, K. Bekk, A. Bercuci, J. Blümer et al. *Astroparticle Physics* **24** (2005) 1.
- [9] W. D. Apel, J. C. Arteaga-Velázquez, K. Bekk, M. Bertaina, J. Blümer, H. Bozdog et al. *Physical Review Letters* **107** (2011) 171104.
- [10] D. J. Bird, S. C. Corbato, H. Y. Dai, B. R. Dawson, J. W. Elbert, B. L. Emerson et al. *The Astrophysical Journal* **424** (1994) 491.
- [11] D. ALLARD, E. PARIZOT and A. OLINTO *Astroparticle Physics* **27** (2007) 61.
- [12] V. S. Berezinsky and S. I. Grigor'eva *Astron. Astrophys.* **199** (1988) .
- [13] V. Berezinsky, A. Gazizov and S. Grigorieva *Physical Review D* **74** (2006) 043005.
- [14] T. Wibig and A. W. Wolfendale *Journal of Physics G: Nuclear and Particle Physics* **30** (2004) 525.
- [15] K. Greisen *Physical Review Letters* **16** (1966) 748.
- [16] G. T. Zatsepin and V. A. Kuzmin *JETP Lett.* **4** (1966) 78.
- [17] D. Allard, E. Parizot, A. V. Olinto, E. Khan and S. Goriely *Astronomy & Astrophysics* **443** (2005) L29.
- [18] M. Takeda, N. Sakaki, K. Honda, M. Chikawa, M. Fukushima, N. Hayashida et al. *Astroparticle Physics* **19** (2003) 447.
- [19] O. Adriani, G. C. Barbarino, G. A. Bazilevskaya, R. Bellotti, M. Boezio, E. A. Bogomolov

- et al. *Nature* **458** (2009) 607.
- [20] M. Aguilar, G. Alberti, B. Alpat, A. Alvino, G. Ambrosi, K. Andeen et al. *Physical Review Letters* **110** (2013) 141102.
- [21] J. Nishimura *Advances in Space Research* **26** (2000) 1313.
- [22] D. Gaggero, L. Maccione, G. D. Bernardo, C. Evoli and D. Grasso *Physical Review Letters* **111** (2013) 021102.
- [23] A. IBARRA, D. TRAN and C. WENIGER *International Journal of Modern Physics A* **28** (2013) 1330040.
- [24] A. A. Abdo, B. T. Allen, T. Aune, D. Berley, S. Casanova, C. Chen et al. *The Astrophysical Journal* **698** (2009) 2121.
- [25] R. Abbasi, Y. Abdou, T. Abu-Zayyad, J. Adams, J. A. Aguilar, M. Ahlers et al. *The Astrophysical Journal* **718** (2010) L194.
- [26] A. H. Compton and I. A. Getting *Physical Review* **47** (1935) 817.
- [27] J. Abraham, P. Abreu, M. Aglietta, C. Aguirre, D. Allard, I. Allekotte et al. *Astroparticle Physics* **29** (2008) 188.
- [28] P. Abreu, M. Aglietta, E. Ahn, D. Allard, I. Allekotte, J. Allen et al. *Astroparticle Physics* **34** (2010) 314.
- [29] A. Aab, P. Abreu, M. Aglietta, E. J. Ahn, I. A. Samarai, I. F. M. Albuquerque et al. *The Astrophysical Journal* **804** (2015) 15.
- [30] F. M. Rieger and F. A. Aharonian *Astronomy & Astrophysics* **506** (2009) L41.
- [31] P. Tinyakov, H. Sagawa, S. Troitsky, G. Thomson, K. Kawata, T. Okuda et al., *Ta anisotropy summary*, p. 326, Sissa Medialab, 8, 2016, DOI.
- [32] R. U. Abbasi, M. Abe, T. Abu-Zayyad, M. Allen, R. Anderson, R. Azuma et al. *The Astrophysical Journal* **790** (2014) L21.
- [33] P. D., *Particle Astrophysics*. Oxford University Press, 2009.
- [34] G. Sigl, *Astroparticle Physics: Theory and Phenomenology*, vol. 1. Atlantis Press, 2017, 10.2991/978-94-6239-243-4.
- [35] G. Kowal, A. Lazarian, E. T. Vishniac and K. Otmianowska-Mazur *The Astrophysical Journal* **700** (2009) 63.
- [36] E. M. de Gouveia Dal Pino, G. Kowal and A. Lazarian.
- [37] T. W. Speiser *Journal of Geophysical Research* **70** (1965) 4219.
- [38] E. M. de Gouveia Dal Pino and A. Lazarian *Astronomy & Astrophysics* **441** (2005) 845.
- [39] A. Lazarian and E. T. Vishniac *The Astrophysical Journal* **517** (1999) 700.
- [40] D. Giannios *Monthly Notices of the Royal Astronomical Society: Letters* **408** (2010) L46.

- [41] E. M. de Gouveia Dal Pino, P. P. Piovezan and L. H. S. Kadowaki *Astronomy & Astrophysics* **518** (2010) A5.
- [42] J. F. Drake, P. A. Cassak, M. A. Shay, M. Swisdak and E. Quataert *The Astrophysical Journal* **700** (2009) L16.
- [43] J. F. Drake, M. Swisdak, K. M. Schoeffler, B. N. Rogers and S. Kobayashi *Geophysical Research Letters* **33** (2006) L13105.
- [44] A. Lazarian and M. Opher *The Astrophysical Journal* **703** (2009) 8.
- [45] J. F. Drake, M. Opher, M. Swisdak and J. N. Chamoun *The Astrophysical Journal* **709** (2010) 963.
- [46] M. V. del Valle, G. E. Romero, P. L. Luque-Escamilla, J. Martí and J. R. Sánchez-Sutil *The Astrophysical Journal* **738** (2011) 115.
- [47] B. Zhang and H. Yan *The Astrophysical Journal* **726** (2011) 90.
- [48] E. M. D. G. D. PINO, G. KOWAL, L. H. S. KADOWAKI, P. PIOVEZAN and A. LAZARIAN *International Journal of Modern Physics D* **19** (2010) 729.
- [49] B. Cerutti, G. R. Werner, D. A. Uzdensky and M. C. Begelman *The Astrophysical Journal* **770** (2013) 147.
- [50] P. O. Lagage and C. J. Cesarsky *Astronomy & Astrophysics* **125** (1983) 249.
- [51] W. I. Axford *The Astrophysical Journal Supplement Series* **90** (1994) 937.
- [52] A. M. Hillas *Journal of Physics G: Nuclear and Particle Physics* **31** (2005) R95.
- [53] F. Aharonian, A. Bykov, E. Parizot, V. Ptuskin and A. Watson *Space Science Reviews* **166** (2012) 97.
- [54] M. Ackermann, M. Ajello, A. Allafort, L. Baldini, J. Ballet, G. Barbiellini et al. *Science* **339** (2013) 807.
- [55] F. Aharonian, A. G. Akhperjanian, G. Anton, U. B. de Almeida, A. R. Bazer-Bachi, Y. Becherini et al. *Astronomy & Astrophysics* **508** (2009) 561.
- [56] S. Sahu, B. Zhang and N. Fraija *Physical Review D* **85** (2012) 043012.
- [57] E. M. D. G. D. PINO, G. KOWAL, L. H. S. KADOWAKI, P. PIOVEZAN and A. LAZARIAN *International Journal of Modern Physics D* **19** (2010) 729.
- [58] P.-H. T. Tam, Q.-W. Tang, S.-J. Hou, R.-Y. Liu and X.-Y. Wang *The Astrophysical Journal* **771** (2013) L13.
- [59] C. A. Norman, D. B. Melrose and A. Achterberg *The Astrophysical Journal* **454** (1995) 60.
- [60] P. P. Kronberg *Reports on Progress in Physics* **57** (1994) 325.
- [61] T. Stanev, *High Energy Cosmic Rays*. Springer Berlin Heidelberg, 2010, 10.1007/978-3-540-85148-6.

- [62] T. E. Clarke, P. P. Kronberg and H. Böhringer *The Astrophysical Journal* **547** (2001) L111.
- [63] H. Kang, D. Ryu and T. W. Jones *The Astrophysical Journal* **456** (1996) 422.
- [64] T. A. Collaboration, R. U. Abbasi, T. Abu-Zayyad, M. Allen, Y. Arai, R. Arimura et al.
- [65] J. G. Hills *Nature* **254** (1975) 295.
- [66] M. J. Rees *Nature* **333** (1988) 523.
- [67] B. T. Zhang, K. Murase, F. Oikonomou and Z. Li *Physical Review D* **96** (2017) 069902.
- [68] R. A. Batista and J. Silk *Physical Review D* **96** (2017) 103003.
- [69] R. Jansson and G. R. Farrar *The Astrophysical Journal* **757** (2012) 14.
- [70] R. Jansson and G. R. Farrar *The Astrophysical Journal* **761** (2012) L11.
- [71] P. P. Kronberg *Physics Today* **55** (2002) 40.
- [72] R. Durrer and A. Neronov *The Astronomy and Astrophysics Review* **21** (2013) 62.
- [73] A. D. Angelis and M. J. M. Pimenta, *Introduction to Particle and Astroparticle Physics*. Springer Milan, 2015, 10.1007/978-88-470-2688-9.
- [74] K. Dolag, D. Grasso, V. Springel and I. Tkachev *Journal of Experimental and Theoretical Physics Letters* **79** (2004) 583.
- [75] K. Dolag, D. Grasso, V. Springel and I. Tkachev *Journal of Experimental and Theoretical Physics Letters* **79** (2004) 583.
- [76] G. Sigl, F. Miniati and T. A. Enßlin *Nuclear Physics B - Proceedings Supplements* **136** (2004) 224.
- [77] J. L. Puget, F. W. Stecker and J. H. Bredekamp *The Astrophysical Journal* **205** (1976) 638.
- [78] K. Kotera and A. V. Olinto *Annual Review of Astronomy and Astrophysics* **49** (2011) 119.
- [79] T. Abu-Zayyad, R. Aida, M. Allen, R. Anderson, R. Azuma, E. Barcikowski et al. *Astroparticle Physics* **61** (2015) 93.
- [80] R. Aloisio, V. Berezhinsky, P. Blasi, A. Gazizov, S. Grigorieva and B. Hnatyk *Astroparticle Physics* **27** (2007) 76.
- [81] D. J. Bird, S. C. Corbato, H. Y. Dai, J. W. Elbert, K. D. Green, M. A. Huang et al. *The Astrophysical Journal* **441** (1995) 144.
- [82] F. Halzen, R. Vázquez, T. Stanev and H. Vankov *Astroparticle Physics* **3** (1995) 151.
- [83] A. Neronov *Physical Review Letters* **119** (2017) 191102.
- [84] P. L. Biermann, L. I. Caramete, F. Fraschetti, L. A. Gergely, B. C. Harms, E. Kun et al.
- [85] V. Berezhinsky *Astroparticle Physics* **53** (2014) 120.
- [86] M. Nagano and A. A. Watson *Reviews of Modern Physics* **72** (2000) 689.
- [87] G. R. Farrar and A. Gruzinov *The Astrophysical Journal* **693** (2009) 329.
- [88] N. Globus, D. Allard, R. Mochkovitch and E. Parizot *Monthly Notices of the Royal*

- Astronomical Society* **451** (2015) 751.
- [89] S. Horiuchi, K. Murase, K. Ioka and P. Mészáros *The Astrophysical Journal* **753** (2012) 69.
- [90] B. T. Zhang, K. Murase, S. S. Kimura, S. Horiuchi and P. Mészáros *Physical Review D* **97** (2018) 083010.
- [91] P. Mészáros *Nuclear Physics B - Proceedings Supplements* **256-257** (2014) 241.
- [92] J. Arons *The Astrophysical Journal* **589** (2003) 871.
- [93] K. Fang, K. Kotera and A. V. Olinto *The Astrophysical Journal* **750** (2012) 118.
- [94] K. Kotera, E. Amato and P. Blasi *Journal of Cosmology and Astroparticle Physics* **2015** (2015) 026.
- [95] G. R. Farrar and T. Piran.
- [96] C. Guépin and K. Kotera *Astronomy & Astrophysics* **603** (2017) A76.
- [97] C. J. T. Peixoto, *Estimating the depth of shower maximum using the surface detectors of the pierre auger observatory*, p. 440, Sissa Medialab, 9, 2019, DOI.
- [98] A. Yushkov, *Mass composition of cosmic rays with energies above $10^{17.2}$ ev from the hybrid data of the pierre auger observatory*, p. 482, Sissa Medialab, 8, 2019, DOI.
- [99] W. Hanlon, *Telescope array 10 year composition*, p. 280, Sissa Medialab, 7, 2019, DOI.
- [100] L. Merten, M. Boughelilba, A. Reimer, P. D. Vela, S. Vorobiov, F. Tavecchio et al. *Astroparticle Physics* **128** (2021) 102564.
- [101] T. Fitoussi, G. Medina-Tanco and J.-C. D’Olivo, *Legacy from fly’s eye: Making sense of the highest energy cosmic ray ever observed*, p. 256, Sissa Medialab, 7, 2019, DOI.
- [102] D. Hooper, S. Sarkar and A. M. Taylor *Physical Review D* **77** (2008) 103007.
- [103] A. M. Taylor *EPJ Web of Conferences* **53** (2013) 06007.
- [104] A. M. Taylor, M. Ahlers and F. A. Aharonian *Physical Review D* **84** (2011) 105007.
- [105] X. H. Sun, W. Reich, A. Waelkens and T. A. Enßlin *Astronomy & Astrophysics* **477** (2008) 573.
- [106] H. M. Courtois, D. Pomarède, R. B. Tully, Y. Hoffman and D. Courtois *The Astronomical Journal* **146** (2013) 69.
- [107] D. Pomarède, Y. Hoffman, H. M. Courtois and R. B. Tully *The Astrophysical Journal* **845** (2017) 55.
- [108] E. Carlesi, J. G. Sorce, Y. Hoffman, S. Gottlöber, G. Yepes, N. I. Libeskind et al. *Monthly Notices of the Royal Astronomical Society* **458** (2016) 900.
- [109] R. B. Tully, H. M. Courtois, A. E. Dolphin, J. R. Fisher, P. Héraudeau, B. A. Jacobs et al. *The Astronomical Journal* **146** (2013) 86.
- [110] N. I. Libeskind, Y. Hoffman, R. B. Tully, H. M. Courtois, D. Pomarède, S. Gottlöber

- et al. *Monthly Notices of the Royal Astronomical Society* **452** (2015) 1052.
- [111] *Nuclear Instruments and Methods in Physics Research Section A: Accelerators, Spectrometers, Detectors and Associated Equipment* **798** (2015) 172.
- [112] T. Abu-Zayyad, R. Aida, M. Allen, R. Anderson, R. Azuma, E. Barcikowski et al. *Nuclear Instruments and Methods in Physics Research Section A: Accelerators, Spectrometers, Detectors and Associated Equipment* **689** (2012) 87.
- [113] A. di Matteo, T. Bister, J. Biteau, L. Caccianiga, O. Deligny, T. Fujii et al., *Full-sky searches for anisotropies in uhecr arrival directions with the pierre auger observatory and the telescope array*, p. 439, Sissa Medialab, 8, 2019, DOI.
- [114] O. Deligny, *The energy spectrum of ultra-high energy cosmic rays measured at the pierre auger observatory and at the telescope array*, p. 234, Sissa Medialab, 9, 2019, DOI.
- [115] L. Caccianiga, *Anisotropies of the highest energy cosmic-ray events recorded by the pierre auger observatory in 15 years of operation*, p. 206, Sissa Medialab, 7, 2019, DOI.
- [116] A. Aab, P. Abreu, M. Aglietta, E. J. Ahn, I. A. Samarai, I. F. M. Albuquerque et al. *The Astrophysical Journal* **804** (2015) 15.
- [117] M. Fukushima.
- [118] H. Dembinski, R. Engel, A. Fedynitch, T. Gaisser, F. Riehn and T. Stanev.
- [119] M. S. Muzio, M. Unger and G. R. Farrar *Physical Review D* **100** (2019) 103008.
- [120] K. Kawata, A. di Matteo, T. Fujii, D. Ivanov, C. Jui, J. Lundquist et al. *EPJ Web of Conferences* **210** (2019) 01004.
- [121] A. Aab, P. Abreu, M. Aglietta, I. F. M. Albuquerque, I. Allekotte, A. Almela et al. *The Astrophysical Journal* **853** (2018) L29.
- [122] J. P. Rachen and B. Eichmann.
- [123] S. A. Olausen and V. M. Kaspi *The Astrophysical Journal Supplement Series* **212** (2014) 6.
- [124] H. Takami, K. Murase and C. D. Dermer *The Astrophysical Journal* **817** (2016) 59.
- [125] A. di Matteo, T. Bister, J. Biteau, L. Caccianiga, O. Deligny, T. Fujii et al., *Full-sky searches for anisotropies in uhecr arrival directions with the pierre auger observatory and the telescope array*, p. 439, Sissa Medialab, 8, 2019, DOI.
- [126] D. Kuempel.
- [127] G. M. Voit *Reviews of Modern Physics* **77** (2005) 207.
- [128] V. Springel, C. S. Frenk and S. D. M. White *Nature* **440** (2006) 1137.
- [129] J. J. Mohr, B. Mathiesen and A. E. Evrard *The Astrophysical Journal* **517** (1999) 627.
- [130] V. S. Berezinsky, P. Blasi and V. S. Ptuskin *The Astrophysical Journal* **487** (1997) 529.
- [131] S. W. Allen, A. E. Evrard and A. B. Mantz *Annual Review of Astronomy and Astrophysics*

- 49 (2011) 409.
- [132] C. Pfrommer and T. A. Enßlin *Astronomy & Astrophysics* **413** (2004) 17.
- [133] A. Pinzke and C. Pfrommer *Monthly Notices of the Royal Astronomical Society* **409** (2010) 449.
- [134] R. J. van Weeren, F. de Gasperin, H. Akamatsu, M. Brüggen, L. Feretti, H. Kang et al. *Space Science Reviews* **215** (2019) 16.
- [135] M. Ackermann, M. Ajello, A. Albert, A. Allafort, W. B. Atwood, L. Baldini et al. *The Astrophysical Journal* **787** (2014) 18.
- [136] D. Wittor *New Astronomy* **85** (2021) 101550.
- [137] P. A. R. Ade, N. Aghanim, C. Armitage-Caplan, M. Arnaud, M. Ashdown, F. Atrio-Barandela et al. *Astronomy & Astrophysics* **571** (2014) A20.
- [138] R. Piffaretti and R. Valdarnini *Astronomy & Astrophysics* **491** (2008) 71.
- [139] A. Cavaliere and R. Fusco-Femiani *Astronomy & Astrophysics* **70** (1978) 677.
- [140] D. Nagai, A. V. Kravtsov and A. Vikhlinin *The Astrophysical Journal* **668** (2007) 1.
- [141] M. Arnaud, G. W. Pratt, R. Piffaretti, H. Böhringer, J. H. Croston and E. Pointecouteau *Astronomy & Astrophysics* **517** (2010) A92.
- [142] R. Adam, H. Goksu, A. Leingärtner-Goth, S. Ettori, R. Gnatyk, B. Hnatyk et al. *Astronomy & Astrophysics* **644** (2020) A70.
- [143] A. Bonafede, L. Feretti, M. Murgia, F. Govoni, G. Giovannini, D. Dallacasa et al. *Astronomy & Astrophysics* **513** (2010) A30.
- [144] M. Murgia, F. Govoni, L. Feretti, G. Giovannini, D. Dallacasa, R. Fanti et al. *Astronomy & Astrophysics* **424** (2004) 429.
- [145] G. Hurier, R. Adam and U. Keshet *Astronomy & Astrophysics* **622** (2019) A136.
- [146] Z. F. *Helvetica Physica Acta* **6** (1933) 110.
- [147] A. Pinzke, *Gamma-ray emission from galaxy clusters, doctoral thesis in physics, stockholm university*, 2010.
- [148] K. Umetsu, T. Broadhurst, A. Zitrin, E. Medezinski and L.-Y. Hsu *The Astrophysical Journal* **729** (2011) 127.
- [149] K. Umetsu *The Astronomy and Astrophysics Review* **28** (2020) 7.
- [150] J. F. Navarro, C. S. Frenk and S. D. M. White *The Astrophysical Journal* **462** (1996) 563.
- [151] L. Roszkowski, E. M. Sessolo and S. Trojanowski *Reports on Progress in Physics* **81** (2018) 066201.
- [152] L. Feretti, G. Giovannini, F. Govoni and M. Murgia *The Astronomy and Astrophysics Review* **20** (2012) 54.

- [153] C. Pfrommer, T. A. Ensslin, V. Springel, M. Jubelgas and K. Dolag *Monthly Notices of the Royal Astronomical Society* **378** (2007) 385.
- [154] L. Feretti *Matter and Energy in Clusters of Galaxies, ASP Conference Proceedings* **301** (2003) 143.
- [155] C. Ferrari, F. Govoni, S. Schindler, A. M. Bykov and Y. Rephaeli *Space Science Reviews* **134** (2008) 93.
- [156] *Science with the Cherenkov Telescope Array*. WORLD SCIENTIFIC, 3, 2019, 10.1142/10986.
- [157] P. Padovani and P. Giommi *MNRAS* **277** (1995) 1477 [astro-ph/9511065].
- [158] A. A. Abdo, M. Ackermann, I. Agudo, M. Ajello, H. D. Aller, M. F. Aller et al. *ApJ* **716** (2010) 30 [0912.2040].
- [159] P. Giommi, G. Polenta, A. Lähteenmäki, D. J. Thompson, M. Capalbi, S. Cutini et al. *A&A* **541** (2012) A160 [1108.1114].
- [160] G. Ghisellini, C. Righi, L. Costamante and F. Tavecchio *MNRAS* **469** (2017) 255 [1702.02571].
- [161] Z. Pei, J. Fan, J. Yang, D. Huang and Z. Li *arXiv e-prints* (2021) arXiv:2112.00530 [2112.00530].
- [162] P. Grandi and G. G. C. Palumbo *Science* **306** (2004) 998.
- [163] E. Fedorova, B. I. Hnatyk, V. I. Zhdanov and A. Del Popolo *Universe* **6** (2020) 219.
- [164] S. F. Zhu, W. N. Brandt, B. Luo, J. Wu, Y. Q. Xue and G. Yang *MNRAS* **496** (2020) 245 [2006.13226].
- [165] H. Gao, W.-H. Lei, X.-F. Wu and B. Zhang *MNRAS* **435** (2013) 2520 [1204.1386].
- [166] Planck Collaboration and C. R. Lawrence, *The Planck Early Release Compact Source Catalog*, in *American Astronomical Society Meeting Abstracts #217*, vol. 217 of *American Astronomical Society Meeting Abstracts*, p. 243.07, Jan., 2011.
- [167] G. La Mura, G. Busetto, S. Ciroi, P. Rafanelli, M. Berton, E. Congiu et al. *European Physical Journal D* **71** (2017) 95 [1702.06779].
- [168] C. M. Urry *Advances in Space Research* **21** (1998) 89 [astro-ph/9702176].
- [169] M. S. Anjum and J. Tammi, *Nonlinear synchrotron self-compton modelling of blazars*, in *2015 Fourth International Conference on Aerospace Science and Engineering (ICASE)*, vol. 2-4 Sept. 2015, pp. 1–8, 2015, DOI.
- [170] S. Cutini, S. Ciprini, M. Orienti, A. Tramacere, F. D’Ammando, F. Verrecchia et al. *MNRAS* **445** (2014) 4316 [1409.8101].
- [171] S. Nair, D. Narasimha and A. P. Rao *ApJ* **407** (1993) 46.

- [172] P. A. R. Ade, N. Aghanim, M. Arnaud, M. Ashdown, J. Aumont, C. Baccigalupi et al. *Astronomy & Astrophysics* **594** (2016) A13.
- [173] V. Zabalza.
- [174] P. Barmby and J. P. Huchra *The Astronomical Journal* **116** (1998) 1508.
- [175] I. Agulli, J. A. L. Aguerri, A. Diaferio, L. D. Palmero and R. Sánchez-Janssen *Monthly Notices of the Royal Astronomical Society* **467** (2017) 4410.
- [176] J. Tiwari and K. P. Singh *Monthly Notices of the Royal Astronomical Society* **500** (2020) 5524.
- [177] P. A. R. Ade, N. Aghanim, M. Arnaud, M. Ashdown, F. Atrio-Barandela, J. Aumont et al. *Astronomy & Astrophysics* **550** (2013) A131.
- [178] E. Dwek and F. Krennrich *Astroparticle Physics* **43** (2013) 112.
- [179] M. G. Aartsen, M. Ackermann, J. Adams, J. A. Aguilar, M. Ahlers, M. Ahrens et al. *The European Physical Journal C* **79** (2019) 234.
- [180] S.-Q. Xi, X.-Y. Wang, Y.-F. Liang, F.-K. Peng, R.-Z. Yang and R.-Y. Liu *Physical Review D* **98** (2018) 063006.
- [181] R. Adam, H. Goksu, S. Brown, L. Rudnick and C. Ferrari *Astronomy & Astrophysics* **648** (2021) A60.
- [182] E. Churazov, I. Khabibullin, N. Lyskova, R. Sunyaev and A. M. Bykov *Astronomy & Astrophysics* **651** (2021) A41.
- [183] X. Bai, B. Y. Bi, X. J. Bi, Z. Cao, S. Z. Chen, Y. Chen et al. *arXiv e-prints* (2019) arXiv:1905.02773 [1905.02773].
- [184] S. Abdollahi, F. Acero, M. Ackermann, M. Ajello, W. B. Atwood, M. Axelsson et al. *ApJS* **247** (2020) 33 [1902.10045].
- [185] A. Albert, R. Alfaro, C. Alvarez, J. R. A. Camacho, J. C. Arteaga-Velázquez, K. P. Arunbabu et al. *ApJ* **905** (2020) 76 [2007.08582].
- [186] H. E. S. S. Collaboration, H. Abdalla, A. Abramowski, F. Aharonian, F. Ait Benkhali, E. O. Angüner et al. *A&A* **612** (2018) A1 [1804.02432].
- [187] R. C. Duncan and C. Thompson *ApJ* **392** (1992) L9.
- [188] C. Thompson and R. C. Duncan *MNRAS* **275** (1995) 255.
- [189] C. Thompson and R. C. Duncan *ApJ* **473** (1996) 322.
- [190] R. Turolla, S. Zane and A. L. Watts *Reports on Progress in Physics* **78** (2015) 116901 [1507.02924].
- [191] S. Mereghetti, J. A. Pons and A. Melatos *Space Sci. Rev.* **191** (2015) 315 [1503.06313].
- [192] V. M. Kaspi and A. M. Beloborodov *ARA&A* **55** (2017) 261 [1703.00068].

- [193] P. Esposito, N. Rea and G. L. Israel, *Magnetars: A Short Review and Some Sparse Considerations*, in *Astrophysics and Space Science Library* (T. M. Belloni, M. Méndez and C. Zhang, eds.), vol. 461 of *Astrophysics and Space Science Library*, pp. 97–142, Jan., 2021, 1803.05716, DOI.
- [194] B. Paczynski *Acta Astron.* **42** (1992) 145.
- [195] C. Kouveliotou, S. Dieters, T. Strohmayer, J. van Paradijs, G. J. Fishman, C. A. Meegan et al. *Nature* **393** (1998) 235.
- [196] J. van Paradijs, R. E. Taam and E. P. J. van den Heuvel *A&A* **299** (1995) L41.
- [197] V. M. Kaspi, F. P. Gavriil, P. M. Woods, J. B. Jensen, M. S. E. Roberts and D. Chakrabarty *ApJ* **588** (2003) L93 [astro-ph/0304205].
- [198] S. A. Olausen and V. M. Kaspi *ApJS* **212** (2014) 6 [1309.4167].
- [199] K. Parfrey, A. M. Beloborodov and L. Hui *ApJ* **774** (2013) 92 [1306.4335].
- [200] D. A. Frail, S. R. Kulkarni and J. S. Bloom *Nature* **398** (1999) 127 [astro-ph/9812457].
- [201] J. Granot, E. Ramirez-Ruiz, G. B. Taylor, D. Eichler, Y. E. Lyubarsky, R. A. M. J. Wijers et al. *ApJ* **638** (2006) 391 [astro-ph/0503251].
- [202] P. Blasi, R. I. Epstein and A. V. Olinto *ApJ* **533** (2000) L123 [astro-ph/9912240].
- [203] J. Arons *ApJ* **589** (2003) 871 [astro-ph/0208444].
- [204] D. Eichler *arXiv e-prints* (2005) astro-ph/0504452 [astro-ph/0504452].
- [205] K. Asano, R. Yamazaki and N. Sugiyama *PASJ* **58** (2006) L7 [astro-ph/0503335].
- [206] X.-W. Liu, X.-F. Wu and T. Lu *New Astron.* **15** (2010) 292 [0908.4371].
- [207] K. Kotera and A. V. Olinto *ARA&A* **49** (2011) 119 [1101.4256].
- [208] C. Guépin and K. Kotera *A&A* **603** (2017) A76 [1701.07038].
- [209] K. Fang, B. D. Metzger, K. Murase, I. Bartos and K. Kotera *ApJ* **878** (2019) 34 [1812.11673].
- [210] R. B. Gnatyk *Kinematics and Physics of Celestial Bodies* **34** (2018) 167.
- [211] P. Sokolsky *Report on workshop “Multimessenger Astronomy in the Era of PeV Neutrinos”, Nov 10-12, 2014, Annapolis, Maryland* (2014) .
- [212] R. U. Abbasi, M. Abe, T. Abu-Zayyad, M. Allen, R. Anderson, R. Azuma et al. *ApJ* **790** (2014) L21 [1404.5890].
- [213] A. Aab, P. Abreu, M. Aglietta, E. J. Ahn, I. A. Samarai, I. F. M. Albuquerque et al. *ApJ* **804** (2015) 15 [1411.6111].
- [214] Z. Wang, Z. Li and Y. Zhao *ApJ* **569** (2002) L43.
- [215] F. A. Aharonian, *Very high energy cosmic gamma radiation: a crucial window on the extreme Universe*. 2004, 10.1142/4657.

- [216] Cherenkov Telescope Array Consortium, B. S. Acharya, I. Agudo, I. Al Samarai, R. Alfaro, J. Alfaro et al., *Science with the Cherenkov Telescope Array*. 2019, 10.1142/10986.
- [217] J. Li, N. Rea, D. F. Torres and E. de Oña-Wilhelmi *ApJ* **835** (2017) 30 [1607.03778].
- [218] S. E. Xin and X. L. Guo *PoS(ICRC2021)* **626** (2021) .
- [219] Q. Remy, Y. A. Gallant and M. Renaud *Astroparticle Physics* **122** (2020) 102462 [2005.05176].
- [220] A. U. Abeysekara, A. Albert, R. Alfaro, C. Alvarez, J. D. Álvarez, R. Arceo et al. *ApJ* **843** (2017) 40 [1702.02992].
- [221] R. N. Manchester, G. B. Hobbs, A. Teoh and M. Hobbs *AJ* **129** (2005) 1993 [astro-ph/0412641].
- [222] M. L. Ahnen, S. Ansoldi, L. A. Antonelli, C. Arcaro, D. Baack, Babić et al. *MNRAS* **485** (2019) 356 [1901.03982].
- [223] H. Abdalla, F. Aharonian, F. Ait Benkhali, E. O. Angüner, C. Arcaro, C. Armand et al. *arXiv e-prints* (2021) arXiv:2107.01425 [2107.01425].
- [224] D. L. Kaplan, S. R. Kulkarni, D. A. Frail and M. H. van Kerkwijk *ApJ* **566** (2002) 378 [astro-ph/0107519].
- [225] E. Fuerst, W. Reich, P. Reich, T. Handa and Y. Sofue *A&AS* **69** (1987) 403.
- [226] D. R. Lorimer and K. M. Xilouris *ApJ* **545** (2000) 385 [astro-ph/0005389].
- [227] C. Kouveliotou, T. Strohmayer, K. Hurley, J. van Paradijs, M. H. Finger, S. Dieters et al. *ApJ* **510** (1999) L115 [astro-ph/9809140].
- [228] D. A. Green *Journal of Astrophysics and Astronomy* **40** (2019) 36 [1907.02638].
- [229] H. Sano, S. Yoshiike, Y. Yamane, K. Hayashi, R. Enokiya, K. Tokuda et al. *ApJ* **919** (2021) 123 [2106.12009].
- [230] V. Testa, N. Rea, R. P. Mignani, G. L. Israel, R. Perna, S. Chaty et al. *A&A* **482** (2008) 607 [0712.4171].
- [231] S. P. Tendulkar, P. B. Cameron and S. R. Kulkarni *ApJ* **761** (2012) 76 [1210.8151].
- [232] F. J. Vrba, C. B. Luginbuhl, K. C. Hurley, P. Li, S. R. Kulkarni, M. H. van Kerkwijk et al. *ApJ* **468** (1996) 225.
- [233] F. J. Vrba, A. A. Henden, C. B. Luginbuhl, H. H. Guetter, D. H. Hartmann and S. Klose *ApJ* **533** (2000) L17 [astro-ph/0002530].
- [234] E. F. E. Morales, F. Wyrowski, F. Schuller and K. M. Menten *A&A* **560** (2013) A76 [1310.2612].
- [235] B. Davies, D. F. Figer, R.-P. Kudritzki, C. Trombly, C. Kouveliotou and S. Wachter *ApJ* **707** (2009) 844 [0910.4859].

- [236] S. Wachter, E. Ramirez-Ruiz, V. V. Dwarkadas, C. Kouveliotou, J. Granot, S. K. Patel et al. *Nature* **453** (2008) 626 [0805.4815].
- [237] G. Natale, N. Rea, D. Lazzati, R. Perna, D. F. Torres and J. M. Girart *ApJ* **837** (2017) 9 [1701.07442].
- [238] J. S. Urquhart, C. König, A. Giannetti, S. Leurini, T. J. T. Moore, D. J. Eden et al. *MNRAS* **473** (2018) 1059 [1709.00392].
- [239] T. S. Rice, A. A. Goodman, E. A. Bergin, C. Beaumont and T. M. Dame *ApJ* **822** (2016) 52 [1602.02791].
- [240] T. Enoto, S. Shibata, T. Kitaguchi, Y. Suwa, T. Uchide, H. Nishioka et al. *ApJS* **231** (2017) 8 [1704.07018].
- [241] F. Coti Zelati, N. Rea, J. A. Pons, S. Campana and P. Esposito *MNRAS* **474** (2018) 961 [1710.04671].
- [242] T. Tamba, A. Bamba, H. Odaka and T. Enoto *PASJ* **71** (2019) 90 [1906.04406].
- [243] A. Burrows and D. Vartanyan *Nature* **589** (2021) 29 [2009.14157].
- [244] J. G. Kirk and P. Duffy *Journal of Physics G Nuclear Physics* **25** (1999) R163 [astro-ph/9905069].
- [245] J. G. Kirk, A. W. Guthmann, Y. A. Gallant and A. Achterberg *ApJ* **542** (2000) 235 [astro-ph/0005222].
- [246] F. W. Stecker, *Cosmic gamma rays*. 1971.
- [247] Q. Yuan, S.-J. Lin, K. Fang and X.-J. Bi *Phys. Rev. D* **95** (2017) 083007 [1701.06149].
- [248] V. S. Berezhinskii, S. V. Bulanov, V. A. Dogiel and V. S. Ptuskin, *Astrophysics of cosmic rays*. 1990.
- [249] T. Delahaye, J. Lavalley, R. Lineros, F. Donato and N. Fornengo *A&A* **524** (2010) A51 [1002.1910].
- [250] G. Ferrand and S. Safi-Harb *Advances in Space Research* **49** (2012) 1313 [1202.0245].
- [251] G. Pelletier, A. Bykov, D. Ellison and M. Lemoine *Space Sci. Rev.* **207** (2017) 319 [1705.05549].
- [252] C. Evoli, E. Amato, P. Blasi and R. Aloisio *Phys. Rev. D* **103** (2021) 083010 [2010.11955].
- [253] A. M. Hillas *Journal of Physics G Nuclear Physics* **31** (2005) R95.
- [254] J. K. Truelove and C. F. McKee *ApJS* **120** (1999) 299.
- [255] S. P. Reynolds *ARA&A* **46** (2008) 89.
- [256] J. Martín, D. F. Torres and N. Rea *MNRAS* **427** (2012) 415 [1209.0300].
- [257] H. E. S. S. Collaboration, H. Abdalla, A. Abramowski, F. Aharonian, F. Ait Benkhali, E. O. Angüner et al. *A&A* **612** (2018) A3 [1802.05172].

- [258] F. Acero, M. Ackermann, M. Ajello, L. Baldini, J. Ballet, G. Barbiellini et al. *ApJS* **224** (2016) 8 [1511.06778].
- [259] P. Cristofari, S. Gabici, R. Terrier and T. B. Humensky *MNRAS* **479** (2018) 3415 [1803.09728].
- [260] A. M. Bykov, A. Marcowith, E. Amato, M. E. Kalyashova, J. M. D. Kruijssen and E. Waxman *Space Sci. Rev.* **216** (2020) 42 [2003.11534].
- [261] G. Morlino, P. Blasi, E. Peretti and P. Cristofari *MNRAS* **504** (2021) 6096 [2102.09217].
- [262] P. Cristofari *Universe* **7** (2021) 324 [2110.07956].
- [263] H. E. S. S. Collaboration, H. Abdalla, A. Abramowski, F. Aharonian, F. Ait Benkhali, A. G. Akhperjanian et al. *A&A* **612** (2018) A2 [1702.08280].
- [264] H. E. S. S. Collaboration, H. Abdalla, A. Abramowski, F. Aharonian, F. Ait Benkhali, A. G. Akhperjanian et al. *A&A* **612** (2018) A11 [1606.05404].
- [265] B. M. Gaensler and P. O. Slane *ARA&A* **44** (2006) 17 [astro-ph/0601081].
- [266] N. Bucciantini, J. Arons and E. Amato *MNRAS* **410** (2011) 381 [1005.1831].
- [267] E. Amato, *The Theory of Pulsar Wind Nebulae*, in *International Journal of Modern Physics Conference Series*, vol. 28 of *International Journal of Modern Physics Conference Series*, p. 1460160, Mar, 2014, 1312.5945, DOI.
- [268] O. Kargaltsev, B. Cerutti, Y. Lyubarsky and E. Striani *Space Sci. Rev.* **191** (2015) 391 [1507.03662].
- [269] J. M. Blondin and R. A. Chevalier *ApJ* **845** (2017) 139 [1707.07021].
- [270] S. P. Reynolds, G. G. Pavlov, O. Kargaltsev, N. Klingler, M. Renaud and S. Mereghetti *Space Sci. Rev.* **207** (2017) 175 [1705.08897].
- [271] B.-T. Zhu, L. Zhang and J. Fang *A&A* **609** (2018) A110.
- [272] E. Amato *arXiv e-prints* (2020) arXiv:2001.04442 [2001.04442].
- [273] D. F. Torres, A. Cillis, J. Martín and E. de Oña Wilhelmi *Journal of High Energy Astrophysics* **1** (2014) 31 [1402.5485].
- [274] W. Ishizaki, S. J. Tanaka, K. Asano and T. Terasawa *ApJ* **838** (2017) 142 [1703.05763].
- [275] C. Evoli, P. Blasi, E. Amato and R. Aloisio *Phys. Rev. Lett.* **125** (2020) 051101 [2007.01302].
- [276] V. Zabalza, *Naima: a Python package for inference of particle distribution properties from nonthermal spectra*, in *34th International Cosmic Ray Conference (ICRC2015)*, vol. 34 of *International Cosmic Ray Conference*, p. 922, July, 2015, 1509.03319.
- [277] R. Galván-Madrid, H. B. Liu, Z. Y. Zhang, J. E. Pineda, T. C. Peng, Q. Zhang et al. *ApJ* **779** (2013) 121 [1309.4129].

- [278] H. E. S. S. Collaboration, H. Abdalla, A. Abramowski, F. Aharonian, F. Ait Benkhali, A. G. Akhperjanian et al. *A&A* **612** (2018) A5 [1609.00600].
- [279] N. Bucciantini, E. Quataert, J. Arons, B. D. Metzger and T. A. Thompson *MNRAS* **380** (2007) 1541 [0705.1742].
- [280] A. Corsi and D. Lazzati *New Astron. Rev.* **92** (2021) 101614.
- [281] K. Murase, P. Mészáros and B. Zhang *Phys. Rev. D* **79** (2009) 103001 [0904.2509].
- [282] T. Piran, E. Nakar, P. Mazzali and E. Pian *ApJ* **871** (2019) L25.
- [283] T. Piran *Phys. Rep.* **314** (1999) 575 [astro-ph/9810256].
- [284] J. Devin, M. Renaud, M. Lemoine-Goumard and G. Vasileiadis *A&A* **647** (2021) A68 [2101.07775].
- [285] T. Linden, K. Auchetl, J. Bramante, I. Cholis, K. Fang, D. Hooper et al. *Phys. Rev. D* **96** (2017) 103016 [1703.09704].
- [286] T. Sudoh, T. Linden and J. F. Beacom *Phys. Rev. D* **100** (2019) 043016.
- [287] J. L. Han, C. Wang, P. F. Wang, T. Wang, D. J. Zhou, J.-H. Sun et al. *Research in Astronomy and Astrophysics* **21** (2021) 107 [2105.08460].

7 Appendix

Models for Planck Spectra

Two models were utilized to fit the Planck spectra:

- *bknpo* - broken power-law.
- *pow* - simple power-law;

The outcomes of spectra fitting are displayed in Table 13. In some cases when neither of the aforementioned models provided a $\chi^2/\text{d.o.f.} > 2.0$ fit, we attempted to use the more sophisticated model, a three-segment broken power-law model with three different photon indices and two breaks. These instances are denoted by upper-case digits in the Table 13 and are elaborated upon below the Table. As a null-hypothesis for estimating the statistical significance of our models, we assume the simplest one, namely the single power-law. Null-hypothesis probability for each sample object was calculated using the Fisher test (*ftest* in the XSPEC); these probabilities are displayed in the final column of Table 13.

If the likelihood of the null hypothesis is less than 50 percent, we consider the alternative model (i.e., the broken power-law model) to be the best match. In the absence of $P_{null} > 50\%$, the single power-law fit is acceptable and the broken power-law fit is statistically indistinguishable from the power-law fit.

In the case where the double broken power-law model was used (PKS 0402-362, AGN 3C 273, and FBQS J1159+2914), was estimated two "null-hypothesis" probabilities for it: one for the single power-law null hypothesis and the other for the broken power-law model as a null-hypothesis.

¹ *bkn2po* $\Gamma_{1,l} = 0.96 \pm 0.01$, $E_{b1} = 3.8 * 10^{-4}$ eV, $\Gamma_{1,i} = 1.76 \pm 0.02$, $E_{b2} = 10^{-3}$ eV and $\Gamma_{1,h} = 1.88 \pm 0.05$; $\chi^2/\text{d.o.f.} = 4.2/4$; with $P_{Null} = 3\%$ of the *bknpo* model relatively to *bkn2po* one and $P_{Null} < 10^{-4}\%$ relatively to the power-law one;

² *bkn2po* $\Gamma_{1,l} = 0.7 \pm 0.1$, $E_{b1} = 2.5 \pm 0.3 * 10^{-4}$ eV, $\Gamma_{1,i} = 1.13 \pm 0.08$, $E_{b2} = 6.0 \pm 0.6 * 10^{-4}$ eV, $\Gamma_{1,h} = 1.45 \pm 0.05$ and $\chi^2/\text{d.o.f.} = 9.2/3$; with $P_{Null} = 15\%$ of the *bknpo* model relatively to *bkn2po* one and $P_{Null} = 0.1\%$ relatively to the power-law one;

³ *bkn2po* $\Gamma_{1,l} = 0.4 \pm 0.5$, $E_{b1} = 1.9 \pm 0.1 * 10^{-4}$ eV, $\Gamma_{1,i} = 3.4 \pm 0.8$, $E_{b2} = 2.3 \pm 0.2 * 10^{-4}$ eV, $\Gamma_{1,h} = 1.13 \pm 0.07$ and $\chi^2/\text{d.o.f.} = 7.9/4$; with $P_{Null} = 18\%$ of the *bknpo* model relatively to *bkn2po* one and $P_{Null} = 34.7\%$ relatively to the power-law one.

Tab 13: Parameters of the model in case of the Planck spectra.

Object	Broken power-law				Power-law		P_{Null}
	$\Gamma_{1,l}$	$\Gamma_{1,h}$	$E_b, 10^{-4} \text{ eV}$	$\chi^2/d.o.f.$	Γ_1	$\chi^2/d.o.f.$	
[HB 89] 2230+114	1.39±0.04	2.2±0.2	5.7±0.8	5.7/4	1.52±0.05	81.4/5	0.2 %
[HB 89] 2142-758	0.7±0.2	1.46±0.05	2.0±0.2	6.6/4	1.29±0.05	103.4/5	0.2 %
PMN J0525-2338	0.6±0.6	2.5±0.5	2.5±0.3	1.1/1	1.61±0.12	10.8/2	20.7%
PMN J0623-6436	0.87 ^{+0.17} _{-0.23}	1.59±0.08	2.1±0.1	4.9/3	1.38±0.08	26.1/4	3.7%
3C 454.3	0.31±0.05	1.21±0.03	3.0±0.20	6.2/5	0.95±0.03	426.7/7	<0.01%
PMN J1508-4953	0.6±0.5	1.51±0.46	3.5±0.7	1.3/1	0.9±0.2	10.8/2	22.6%
3C 345	1.33±0.06	1.80±0.04	3.8±0.5	3.1/4	1.61±0.03	61.6/6	0.3%
3C 380	1.53±0.09	1.95±0.15	3.7±0.5	6.6/4	1.7±0.05	24.9/5	3%
3C 279	1.12±0.08	1.60±0.03	4±1	7.9/6	1.47±0.03	43.9/7	0.2%
3C 273 ¹	0.96±0.01	1.76±0.03	3.8±0.2	16.6/5	1.35±0.02	4520.6/6	<0.01%
3C 309.1	-	-	-	-	1.41±0.13	0.71/2	-
4C +71.078	0.73±0.05	1.92±0.05	3.2±0.5	0.8/3	1.33±0.05	347.3/5	0.01%
4C +73.18	1.04±0.55	1.75±0.08	2.2±0.7	2.9/3	1.65±0.07	9.4/5	17%
4C +50.11	-	-	-	-	1.60±0.05	-	-
4C +49.22	-	-	-	-	1.29±0.05	-	-
4C +32.14	-	-	-	-	1.62±0.14	2.9/3	-
4C +31.63	1.0±0.35	1.49±0.15	3.0±0.9	4.0/3	1.2±0.2	20.0/5	9%
S5 1803+784	1.17±0.04	1.51±0.06	4.0±0.8	1.8/3	1.3±0.05	32.6/5	1.3%
8C 1849+670	1.25±0.19	1.53±0.11	3.7±1.5	3.6/3	1.26±0.10	24.4/5	5.6%
S5 0716+714	0.75±0.28	1.28±0.07	3.4±0.6	4.3/3	1.18±0.06	22.2/4	3.9%
S5 0212+735	1.57±0.08	2.0±0.3	4±0.6	1.9/2	1.6±0.6	7.0/3	14.6%
PKS 0312-770	0.4±0.3	1.95±0.15	2.0±0.2	2.7/3	1.45±0.08	35.8/4	0.9%
S5 1039+81	-	-	-	-	1.38±0.25	1.3/2	-
PKS 1127-14	0.6±0.4	1.7±0.08	2.9±0.6	0.9/2	1.16±0.08	141.9/4	0.6%
PKS 1143-696	1.12±0.35	1.85±0.27	3.3±1.5	6.0/3	1.3±0.2	17.3/4	10%
PKS 1510-08	1.13±0.06	1.85±0.09	3.9±0.4	7.4/4	1.38±0.04	65.3/5	0.5%
PKS 1329-049	-	-	-	-	1.22±0.09	7.2/4	-
PKS 1830-21	-	-	-	-	1.74±0.04	3.8/4	-
PKS 1335-127	1.13±0.04	1.64±0.06	3.5±0.8	4.5/3	1.35±0.03	52.1/5	2.5%
PKS 2005-489	1.13±0.12	1.9±0.3	5.5±0.9	4.7/2	1.31±0.11	14.5/3	17.8%
PKS 1622-29	-	-	-	-	1.08±0.08	0.9/4	-
PKS 2008-159	-	-	-	-	1.64±0.14	1.9/1	-
PKS 2052-47	1.53±0.04	1.41±0.07	4.5±1.5	8.6/4	1.48±0.03	10.6/5	38.9%
PKS 2227-088	0.97±0.06	1.61±0.08	4.2±0.9	3.2/2	1.22±0.04	15.7/4	20%
PKS 2145+06	1.35±0.04	1.97±0.05	3.9±0.4	4.4/3	1.57±0.2	127.8/5	0.6%
PKS 0402-362 ²	0.65±0.07	1.37±0.05	3.1±0.5	20.9/5	1.13±0.02	316.3/7	0.1%
PKS 2149-306	-	-	-	-	1.52±0.09	0.42/1	-
PKS 0405-12	-	-	-	-	1.64±0.17	1.3/1	-
PKS 2331-240	0.9±0.07	1.57±0.12	3.6±0.3	3.9/2	1.22±0.04	28.0/3	7.2%
PKS 0426-380	0.7±0.4	1.52±0.06	2.0±0.6	7.7/4	1.43±0.06	15.9/6	23%
PKS 0521-36	1.11±0.03	1.32±0.03	4.1±0.7	5.6/3	1.21±0.02	38.1/5	5.6%
PKS 0537-286	-	-	-	-	2.0±0.4	0.5/1	-
PKS 0528+134	-	-	-	-	1.90±0.15	4.5/3	-
PKS 0537-441	1.10±0.08	1.43±0.03	4.1±0.8	9.2/5	1.33±0.02	44.7/7	1.9%
PKS 0723-008	0.85±0.06	1.48±0.06	3.7±0.6	3.4/3	1.17±0.04	91.7/5	0.7%
B2 2023+33	1.37±0.15	-0.2±0.8	7.4±0.8	6.03/2	1.28±0.12	13.8/3	25%
B2 0552+39A	2.5±0.3	1.78±0.10	1.9±0.5	1.2/1	2.0±0.1	7.1/3	41.3%
FBQS J1159+2914 ³	1.24±0.19	1.15±0.08	unconstr.	13.1/5	1.17±0.06	13.4/6	74%
B1921-293	1.32±0.01	4.9±0.3	1.72±0.03	7.9/4	1.43±0.10	509.7/6	0.02%
QSO B2013+370	-	-	-	-	1.51±0.20	0.51/1	-
Mrk 501	-	-	-	-	1.57±0.10	2.6/2	-
II Zw 171	-	-	-	-	1.27±0.16	0.03/0	-
NGC 7213	-	-	-	-	-1.67±0.15	0.59/0	-
Mrk 1501	0.4±0.8	1.47±0.09	1.6±0.4	4.2/4	1.34±0.07	8.6/5	11%
QSO B0309+411	3.9/1	0.5±0.6	1.2±0.3	6.0±2.0	0.23/0	1.0±0.2	15.6%
PG 1222+216	0.28±0.22	1.62±0.12	2.4±0.6	1.3/1	1.17±0.08	35.2/3	19%

Models for X-ray Spectra

Was used this two models to fit Swift/XRT+BAT spectra:

- Simple power-law that uses neutral hydrogen absorption *pow*tbabs* - fitting parameters are absorbing column density N_H and photon index Γ_3 ;
- Broken power-law with absorption of neutral hydrogen, with parameters that was fitted: two photon indices $\Gamma_{3,h}$ and $\Gamma_{3,l}$ (*bknpow*tbabs*), break energy E_b and the neutral absorbing column density N_H . For every particular object lower fitting values for N_H were set to the Galactic absorption values shown in the Tables 7–9. In the Table 14 are shown the absorption excesses respectively to those values.

The outcomes of fitting are displayed in Table 14. To quantify the statistical significance of our models, was assumed the null-hypothesis to be the simplest model of two, much as we did for the Planck spectra. Was calculated the null-hypothesis probability P_{Null} for each object in our sample using the Fisher test; these probabilities are displayed in the final column of Table 14. Optimal model was determined in the same manner as for the Planck spectra.

Tab 14: The model parameters for the Swift spectra.

2 Object parameter ->	Broken power-law					Power-law			P _{Null}
	$\Gamma_{3,l}$	$\Gamma_{3,h}$	E_b^{**}	N_H^*	$\chi^2/d.o.f.$	Γ_3	N_H^*	$\chi^2/d.o.f.$	
[HB 89] 2230+114	1.40±0.02	1.96±0.11	7.1±2.1	7±4	838/700	1.41±0.03	7±4	841/702	100%
[HB 89] 2142-758	0.8±0.3	1.49±0.11	1.8±0.3	<100	68/54	1.44±0.07	<100	74/56	10%
3C 273	1.52±0.03	1.72±0.01	2.5±0.3	3±2	1087/827	1.65±0.01	3±2	1279/829	<0.01%
PMN J0623-6436	-	-	-	-	-	1.63±0.11	<4	85.7/63	-
3C 309.1	-	-	-	-	-	1.48±0.07	<6	54.2/65	-
3C 279	1.49±0.05	1.67±0.03	2.5±0.3	2±1	1087/827	1.59±0.01	2±1	1165/829	<0.01%
3C 380	1.67±0.17	2.1±0.3	2.3±0.9	60±10	702/689	1.89±0.06	90±10	711/691	2%
3C 345	1.97±0.22	1.64±0.04	1.2±0.2	<2	251/268	1.64±0.04	<2	258/270	2.5%
4C +31.63	-	-	-	-	-	1.62±0.06	80±60	118//110	-
3C 454.3	1.92±0.20	1.62±0.03	1.2±0.3	<4	272/268	1.63±0.03	<4	281/270	2%
4C +49.22	1.68±0.05	1.84±0.04	5.4±2.8	<10	202/142	1.78±0.02	<10	219/144	0.3%
4C +32.14	1.47±0.07	1.8±0.3	25±4	<20	114/110	1.54±0.03	<20	121/112	3.8%
4C +71.078	1.33±0.03	1.73±0.07	6.7±1.8	<42	602/496	1.49±0.01	39±4	957/498	<0.01%
4C +50.11	-	-	-	-	-	1.66±0.07	<110	76.1/86	-
8C 1849+670	1.72±0.10	1.49±0.11	6.3±5.3	<50	54.2/40	1.57±0.03	<50	62.1/42	6.6%
4C +73.18	-	-	-	-	-	1.76±0.05	<5	92.4/90	-
PKS 0312-770	2.15±0.08	1.41±0.09	2.7±0.3	<20	659/559	1.81±0.03	<20	862/561	<0.01%
S5 0212+735	-	-	-	-	-	1.41±0.08	170±100	85.5/73	-
PKS 1143-696	2.5±1.4	1.79±0.14	unc.	<7	62.8/66	1.72±0.06	<7	64.3/68	41%
PKS 1127-14	1.49±0.06	2.7±1.6	18.4±9.9	85±16	113/109	1.59±0.05	85±16	140/111	<0.01%
PKS 1335-127	1.42±0.02	2.1±0.3	6.4±0.7	<2	646/617	1.47±0.02	<2	759/619	<0.01%
PKS 1329-049	1.33±0.09	unc.	unc.	<40	32.0/30	1.38±0.08	<55	34.3/32	35%
PKS 1622-29	1.39±0.03	1.91 ^{+0.4} _{-0.2}	7.1±0.9	<2	659/617	1.44±0.02	<2	748/619	<0.01%
PKS 1510-08	1.31±0.02	1.39±0.05	10.7±6.5	<5	661/577	1.32±0.02	<5	666/579	8.8%
PKS 2005-489	1.42±0.02	2.4±0.3	7.1±0.6	6±1	654/617	1.54±0.02	19±4	993/619	<0.01%
PKS 1830-21	1.40±0.03	1.21±0.05	5.3±0.7	<2	689/617	1.33±0.02	<2	769.6/619	<0.01%
PKS 2052-47	1.38±0.02	2.2 ^{+0.5} _{-0.4}	11±4	25±4	737/693	1.39±0.02	25±4	751/695	0.2%
PKS 2008-159	1.40±0.02	2.0 ^{+0.5} _{-0.3}	6.4±0.9	<3	730/693	1.42±0.02	<3	745/695	<0.01%
PKS 2149-306	1.22±0.03	1.61±0.13	13.6±4.3	9±7	285/253	1.35±0.01	9±7	370/255	<0.01%
PKS 2145+06	1.28±0.06	1.43±0.04	2.0±0.5	<6	730/693	1.39±0.02	<6	744/695	<0.01%
PKS 2331-240	1.64±0.04	2.4±0.3	7.6±2.2	14±5	298/291	1.73±0.03	14±5	384/293	<0.01%
PKS 2227-088	1.33±1.50	1.69±0.32	<85	<14	40.2/35	1.46±0.08	<14	43.1/37	29.6%
PKS 0405-12	1.79±0.15	2.7±0.3	21±4	<40	54.2/36	2.5±0.1	<40	94.4/38	<0.01%
PKS 0402-362	1.58±0.04	2.0±0.5	9.5±9.3	24±10	187/166	1.64±0.04	34±10	205/168	<0.01%
PKS 0521-36	1.58±0.03	1.86±0.06	4.8±1.8	<9	357/316	1.70±0.02	<9	434/318	<0.01%
PKS 0426-380	1.66±0.07	1.35±0.07	4.1±1.9	<31	61.8/38	1.43±0.05	<31	93/40	0.03%
PKS 0537-286	1.20±0.06	1.36±0.04	10.9±5.2	15±14	107/84	1.29±0.01	15±14	124/86	0.2%
PKS 0528+134	0.93±0.28	1.49±0.07	1.5 ^{+0.9} _{-0.2}	340±40	168/144	1.53±0.06	430±90	171/146	28%
PKS 0723-008	-	-	-	-	-	1.62±0.05	<3	79.6/90	-
PKS 0537-441	2.0±0.2	1.68±0.03	0.9±0.2	<3	297/290	1.66±0.02	<5	306/292	1.3%
S5 0716+714	2.61±0.09	2.17±0.02	1.24±0.05	20±5	1343/846	2.22±0.15	20±5	1731/848	<0.01%
B2 0552+39A	-	-	-	-	-	1.45±0.11	26±17	20.1/20	-
S5 1803+784	-	-	-	-	-	1.52±0.04	<5	123/131	-
S5 1039+81	1.25±0.35	1.65±0.12	2.7±1.8	<12	44.4/27	1.55±0.07	<12	50.5/29	17.6%
B2 2023+33	-	-	-	-	-	1.46±0.17	<250	8.7/9	-
B1921-293	-	-	-	-	-	1.82±0.10	<4	53.6/73	-
II Zw 171	2.1±1.0	1.82±0.09	unc.	<7	144/134	1.81±0.05	<7	146/136	40%
FBQS J1159+2914	1.53±0.04	>1.6	47 ⁺⁹⁰ ₋₁₉	<11	214/204	1.54±0.04	<13	218/206	15.1%
Mrk 1501	1.62±0.04	2.91±0.16	74±69	<6	169/126	1.63±0.03	<6	172/128	33%
Mrk 501	2.04±0.01	2.7±0.5	56±25	<1	642/455	2.10±0.01	<1	652/457	7.2%
PG 1222+216	2.16±0.17	1.43±0.03	1.1±0.1	<11	285/275	1.41±0.03	<11	739/277	<0.01%
NGC 7213	-	-	-	-	-	1.69±0.03	14±13	72.2/94	-
PMN J1508-4953	>1.0	1.30±0.06	0.9±0.2	20±10	19/21	1.32±0.07	<300	30.3/23	0.7%
PMN J0525-2338	-	-	-	-	-	1.5±0.8	<95	7.2/5	-
QSO B2013+370	1.6±0.2	2.2±0.8	22±18	59±25	65.3/52	1.57±0.08	56±25	75.3/54	2.5%
QSO B0309+411	2.7±0.6	1.80±0.07	1.2±0.1	<60	151.4/126	1.79±0.04	<60	158.9/128	4.8%

* 10¹⁹ cm⁻²; ** keV.

Документ підписано у сервісі Вчасно (продовження)
VoitsekhovskiyThesis_final_compressed.pdf

Документ відправлено: 11:14 11.01.2023

Власник документу

Електронний підпис

11:14 11.01.2023

Ідентифікаційний код: 3403806278

Войцеховський Вадим Вадимович

Власник ключа: Войцеховський Вадим Вадимович

Час перевірки КЕП/ЕЦП: 11:14 11.01.2023

Статус перевірки сертифікату: Сертифікат діє

Серійний номер: 58E2D9E7F900307B040000008418330077479A00

Тип підпису: удосконалений